A Novel Scanned Mask Imaging System for High Resolution Solid State Laser Ablation

David Thomas Edmund Myles

Submitted for the degree of Doctor of Engineering

Heriot-Watt University

School of Engineering and Physical Sciences

March 2016

The copyright in this thesis is owned by the author. Any quotation from the thesis or use of any of the information contained in it must acknowledge this thesis as the source of the quotation or information.

ABSTRACT

A technology gap has emerged between the sub-micron semiconductor manufacturing technologies used in the manufacture of integrated circuits and the semi-additive processes used to manufacture advanced chip packages which are currently limited to feature sizes greater than 10 µm. Embedding conductors in laser ablated circuit features is one of the proposed solutions to address this technology gap in the advanced chip packaging industry. Excimer laser systems are currently the only available production tools capable of the high throughput laser ablation of circuit features down to 2 µm.

In this thesis I have developed an ablative, solid state laser, mask imaging system for the high volume 3D structuring of organic dielectrics. This system enables the ablation of circuit features down to 2 µm which are of comparable quality to excimer laser ablation. The system architecture has a throughput exceeding that of an excimer laser production system. I have developed an illumination system, which I have tested at both a feasibility stage and at a prototype stage, with custom designed optical components. The illumination system consists of a galvanometer scan head which is used to raster scan a solid state laser beam across a binary mask, the image of which is then projected onto the substrate. The system I present enables the use of multimode, UV, solid state lasers in well-developed and high resolution mask imaging optical systems.

Through the use of a less expensive laser technology, the system I have developed has a cost of ownership estimated to be less than 50% of that of an excimer production system, thus reducing the cost of high resolution, high throughput laser ablation.

In Memory of Nigel Butterworth and Geoffrey Lawson

Inspiring Teachers

ACADEMIC REGISTRY
Research Thesis Submission

Name:	David Myles		
School:	Engineering & Physical Sciences		
Version: *(i.e. First, Resubmission, Final)*	Final	Degree Sought:	Doctor of Engineering

Declaration

In accordance with the appropriate regulations I hereby submit my thesis and I declare that:

1) the thesis embodies the results of my own work and has been composed by myself
2) where appropriate, I have made acknowledgement of the work of others and have made reference to work carried out in collaboration with other persons
3) the thesis is the correct version of the thesis for submission and is the same version as any electronic versions submitted*.
4) my thesis for the award referred to, deposited in the Heriot-Watt University Library, should be made available for loan or photocopying and be available via the Institutional Repository, subject to such conditions as the Librarian may require
5) I understand that as a student of the University I am required to abide by the Regulations of the University and to conform to its discipline.
6) I confirm that the thesis has been verified against plagiarism via an approved plagiarism detection application e.g. Turnitin.

* *Please note that it is the responsibility of the candidate to ensure that the correct version of the thesis is submitted.*

Signature of Candidate:		Date:	

Submission

Submitted By *(name in capitals):*	
Signature of Individual Submitting:	
Date Submitted:	

For Completion in the Student Service Centre (SSC)

Received in the SSC by *(name in capitals):*			
Method of Submission *(Handed in to SSC; posted through internal/external mail):*			
E-thesis Submitted (***mandatory for final theses)***			
Signature:		Date:	

Please note this form should be bound into the submitted thesis.
Academic Registry/Version (1) August 2016

TABLE OF CONTENTS

Chapter 1: Introduction ... 1
Chapter 2: Literature review ... 5
2.1 Contact printing and photolithography: the current industry standard for PCB manufacture ... 6
2.2 HDI manufacturing processes ... 9
2.3 Inkjet technologies ... 10
2.4 Lithographic manufacturing processes ... 11
2.4.1 Laser Direct imaging ... 11
2.4.2 Mask projection ... 14
2.4.3 Dynamic mask imaging ... 16
2.5 Ablative laser processes ... 17
2.5.1 Excimer laser processes ... 20
2.5.2 Solid state direct write laser processes for microelectronics interconnections ... 26
2.5.3 Proposed system architecture: scanned mask imaging ... 29
2.6 Solid state laser processing ... 31
2.6.1 Nanosecond 355nm laser ablation ... 31
2.6.2 Ablation mechanisms in pulsed nanosecond UV laser ablation ... 32
2.6.3 Ablation mechanism of polymers ... 32
2.6.4 Ablation of metal films ... 35
2.7 Plume shielding ... 35
2.8 Impact of pulse length ... 36
2.9 Absorption enhancement ... 37
2.10 Summary ... 39
Chapter 3: Scanned Mask Imaging: Proof-of-Concept ... 40
3.1 Preliminary trials with an f103 mm f-theta lens ... 41
3.1.1 Experimental set up ... 41
3.1.2 Preliminary imaging results ... 45
3.2 Tests conducted with a higher NA f-theta lens ... 48
3.2.1 Details of the new opto-mechanical set up ... 48
3.2.2 Image magnification and illumination uniformity ... 50

3.2.3 Fixing the target magnification and setting up a ray tracing model..........53
3.2.4 Distortion correction at the object plane 59
3.2.5 Thermal loading of substrate and lens 62
3.3 Imaging results with the f103 mm f-theta lens..64
3.4 Summary 66
Chapter 4: Custom Imaging Optics: Design and Installation 67
4.1 System schematic and design considerations..68
4.2 Zemax model of the custom imaging lens..72
4.3 System set up with custom projection lens 75
4.4 Ablation results with new lens 82
4.4.1 Alignment and first results...82
4.4.2 Selective mask scanning – samples for TPCA show 87
4.4.3 Resolving the issue with infinity imaging system 92
4.4.4 Aperture imaging from the plane of uniformity and beam stitching effects 93
4.5 Summary 97
Chapter 5: Characterising the SMI System...98
5.1 Imaging Performance of the SMI System 99
5.1.1 Depth of focus...99
5.1.2 Resolution across image field 101
5.2 Variable intensity ablation with the SMI system 105
5.3 Filler size in ABF substrates...111
5.4 Taper angle, fluence and aspect ratio 114
5.5 Imaging from the first plane of uniformity 121
5.5.1 Limiting resolution..121
5.5.2 Overlay of images for micromachining 125
5.6 Selective mask scanning...126
5.7 Via drilling with SMI 130
5.8 SMI compatibility with conventional mask imaging techniques 131
5.8.1 Half tone masks...132
5.8.2 Resist exposure 136
5.9 Summary 137
Chapter 6: Evaluation of SMI...139
6.1 Comparison of SMI and excimer laser systems for high resolution ablation.140
6.1.1 Performance 140

6.1.2 Machine architecture and throughput comparison ... 142
6.1.3 Cost of ownership ... 143
6.2 Cost comparison of SMI with conventional SAP technologies ... 145
6.3 SMI for micro-via drilling and micromachining ... 147
6.4 Summary ... 147
Chapter 7: Further Work and Conclusions ... 149
7.1 Further work ... 150
7.2 Conclusions ... 151
References ... 154

LIST OF PUBLICATIONS BY THE CANDIDATE

International patent: D. Milne, P. Rumsby, D. Myles, "Method and apparatus for forming fine scale structures in dielectric substrate". International patent number: WO2014068274, 2014.

D. Myles, M. Ziyenge, J. Shephard, D. Milne, "Scanned Mask Imaging Solid State Laser Tool for Cost Effective Flip Chip – Chip Scale Package Manufacture," Proc. 15th Int. Symp. on Laser Precision Microfabrication, 2014.

D. T. E. Myles, M. Ziyenge, J. D. Shephard, D. C. Milne, "Scanned Mask Imaging Solid State Laser Tool for Cost Effective Flip Chip – Chip Scale Package Manufacture," Journal of Laser Micro/Nanoengineering **10** 1, p106, 2015.

D. Myles, D. Milne, "UV Solid State Laser Ablation for Embedded Fine Scale Circuitry," Chip Scale Review **19** 1, p32, 2015.

D. Myles, D. Milne, J. D. Shephard, "Scanned Mask Imaging Ablative DPSS UV Laser Process for 2μm L/S RDL," IMAPS Additional Conferences (Device Packaging, HiTEC, HiTEN, & CICMT): January 2015, Vol. 2015, DPC, pp. 000554-000589.

D. Milne, D. Myles, P. Rumsby, "SMI: a new method to allow low cost, high resolution micro-machining using UV solid state lasers," Proc. SPIE 9657, Industrial Laser Applications Symposium (ILAS), 2015.

D. Milne, D. Myles, "Scanned mask imaging: The economical approach to high resolution micro-machining using UV solid state lasers," Proceedings of Lasers in Manufacturing, 2015.

D. Milne, D. Myles, "Scanned Mask Imaging: The economical approach to high resolution micro machining using UV solid-state lasers," commercial micro manufacturing international **8** 5, p20, 2015.

Chapter 1: Introduction

The semiconductor industry continues to meet the targets set by International Technology Roadmap for Semiconductors (ITRS) [1]. The targets follow Moore's law, which predicts that the number of transistors on a chip will double every 2 years, shown in Figure 1.1. With feature sizes down to 11 nm on commercially available Integrated Circuits (ICs), the transistor density in semiconductor devices is increasing rapidly. For a given circuit design, this means the pitch of the input and output (I/O) connection pads must decrease resulting in a higher I/O density. Shannon's law predicts that circuit architecture complexity increases at a faster rate than the transistor number predicted by Moore's law. In combination with Rent's Rule, which describes an exponential relationship between the number of I/Os on a circuit and the circuit complexity, these devices require increasingly higher density interconnects [2]. The need for increasingly more complex interconnections with more I/Os at finer pitches with improved signal integrity and reduced signal latency, all at reduced costs, has driven research into alternative manufacturing technologies that might bridge the interconnection gap between sub-micron scale ICs and millimetre scale Printed Circuit Boards (PCBs).

In addition to this, it is becoming increasingly difficult and costly to maintain Moore's law progression for semiconductors. As a result, the industry is exploring alternatives such as advanced packaging solutions to reduce the demand placed on the performance and yield of semiconductor manufacturing technologies. These include, for example, 2.5D interposers, which break up a large, high performance chip into several chips interconnected by a high performance chip package. This enables the use of higher yield processes for the lower resolution parts of the chip, and limits the chip size of the highest resolution, lowest yield parts [3]. This comes at the cost, however, of requiring high density, low latency interconnects between the chips. This is beyond the capability of current, high volume, package manufacturing technologies which is driving research into cost effective, high resolution manufacturing processes to bridge this gap.

High resolution laser ablation of organic dielectrics has been put forward as one methodology to enable the feature sizes required in the next generation of advanced chip packages. In this thesis I present the development of a new optical system which enables the use of low cost, multimode, nanosecond UV solid state lasers in a high resolution mask imaging system. The key aspect of this development is the use of a galvanometer scan head to raster scan a solid state laser beam across a binary mask, the image of which is then projected onto the substrate. I demonstrate ablation of the

features relevant to the next generation of chip packages with the prototype optical system. More generally, however, the development enables the reduction in cost of high resolution laser ablation for any application. Excimer laser micromachining systems currently offer the highest throughput and best resolution achievable with a laser ablation production tool. The system I have developed matches the quality of excimer laser ablation, but by multiplexing with a less expensive laser technology, can exceed the throughput of a 300 W excimer system at <50% of the cost of ownership.

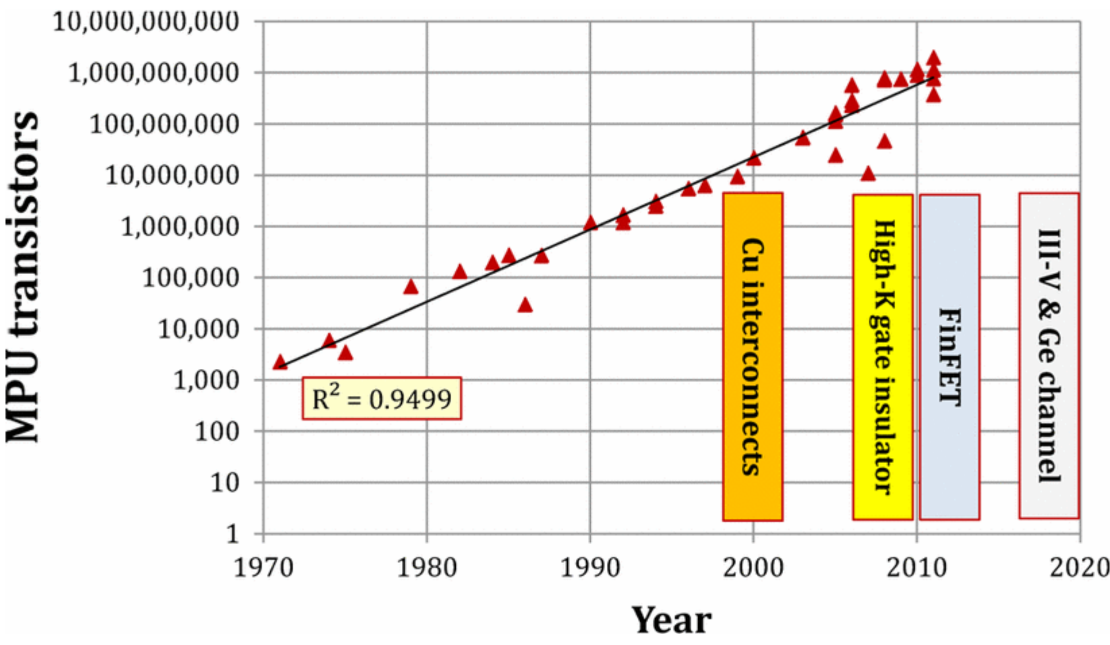

Figure 1.1 Graph showing Moore's law which predicts the number of transistors on MicroProcessor Units (MPU) doubles every two years from [4].

The literature review (Chapter 2) begins by describing the current state of the art in high volume, PCB manufacture. It goes on to present some of the proposed solutions to enable a reduction in feature size for the next generation of chip packages, none of which are currently in high volume production. I make the case for laser ablation as a solution to addressing the technology gap between current, high volume PCB manufacturing technologies and sub-micron semiconductor manufacturing technologies. The current state of the art in cost effective laser micromachining is then presented in the context of chip package manufacture, and the concept for a solid state laser mask imaging system is put forward. Literature relevant to the realisation of this concept is then discussed, with particular focus on the ablation of polymers at 355 nm.

In chapter 3 I describe the development of a test platform to demonstrate the proof of concept of the solid state laser mask imaging system. The results I have obtained with stock f-theta lenses in the proof-of-concept system are shown and the limitations of

using f-theta scan lenses in finite conjugate imaging systems are discussed. I describe a method to mitigate lens distortion across the image field and the first prototype chip packages I laser patterned with the proof-of-concept system are shown.

Having demonstrated the proof-of-concept in chapter 3, I was able to justify the investment in upgrading the system optics and opto-mechanics. Chapter 4 details the design and installation of custom optical components for the system which I specified, including modelling I conducted of the projection optics and descriptions of some of the issues which arose during the installation. I go on to present the first ablation results I obtained with the bespoke optical system, as well as some optimisation of the illumination of the imaging system I performed.

Having detailed the set-up of the system in chapter 4, in chapter 5 I begin by assessing the optical systems imaging performance. I highlight some of the unique features of the imaging system that I discovered, and I demonstrate the system capability to produce the features required for advanced chip packaging. I conclude the chapter by investigating the compatibility of the imaging system with mask imaging techniques developed for other light sources.

In chapter 6 I evaluate the developed system based on metrics of ablation quality, throughput in production and cost. I analyse a throughput model for a production tool and compare this with excimer laser production tools. I use these to form a cost of ownership model for the system, and this is compared with current processes used in the chip packaging industry. Finally, I comment upon the likelihood of the adoption of the technology for advanced chip packaging. In chapter 7 I conclude the thesis and highlight key areas of interest for further work and development.

Chapter 2: Literature review

2.1 Contact printing and photolithography: the current industry standard for PCB manufacture

The current industry standard for the economic production of PCBs is contact printing. A photoresist is exposed and developed on a copper clad laminate, and much of the copper film on the substrate is subsequently etched away to define the conductive pattern. Some of the steps in this subtractive manufacturing process are depicted in Figure 2.1. In (b), the substrate is plated with copper. Photoresist is then coated on the copper in (c), and a pattern transferred to it by use of a phototool and subsequent exposure by UV lamp in (d). Once the resist has been developed in (e), unwanted copper areas are then etched away in a wet chemical process. As can be seen in (f), this results in a raised copper pattern on the substrate. Contact of the phototool with the substrate is essential to avoid unwanted polymerisation of the photoresist, and is normally achieved through use of a vacuum tray with a clear film to draw the silver halide or diazo phototool down onto the substrate [5].

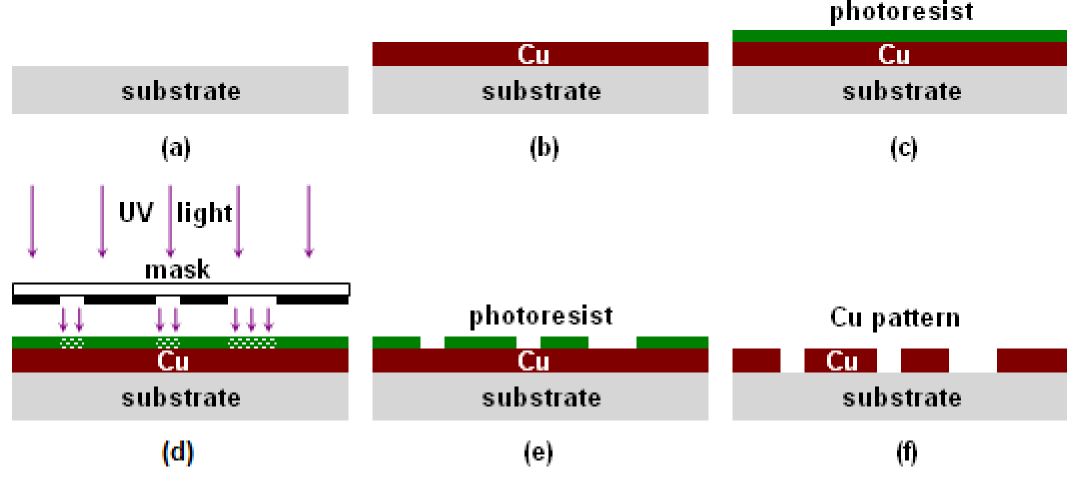

Figure 2.1 Schematic diagram of a contact printing process from [6].

These subtractive manufacturing processes result in a large amount of waste negatively impacting on the environment. The waste in IC packaging contributes to the estimated 1.7 kg of non-renewable resources that go into making a 2 g microchip [7]. This mature technology has been the dominant interconnect fabrication technology for the past 30-40 years. It has developed slowly in comparison with the fast paced advances in the semiconductor industry, and can currently achieve line widths of around 75 μm and pad sizes 100 μm larger than the vias [2, 8]. Vias can be machined down to 50 μm diameters dependent on material, which restricts pad sizes to larger than 150 μm. This

large tolerance is necessary due to the dimensional instability of the phototools and substrates used in the manufacturing process. Phototool expansion and contraction occurs anisotropically and is thus very difficult to compensate for with phototool design. This problem therefore creates a fundamental limit for the technology.

The capital cost of a system whereby the vias are mechanically drilled remains lower than laser drilled via systems. With via sizes less than 150 μm, however, the cost of ownership of such tools becomes much higher due to the cost of small drill bits, and the increased rate at which they need to be replaced. As such, laser drilled vias are the norm in high density interconnect circuits.

These techniques are currently used in Sequential Build-Up (SBU) technologies, where additional resin and conductive layers are added to a core layer. SBU technologies are the current standard [9], and the process steps are outlined in Figure 2.2.

Core	Build-up layers	Finish
Drill	Roughen surface	Roughen surface
De-smear (etch)	Laminate dielectric	Apply solder resist
Plate copper panel	Drill laser vias	Expose resist
Form black copper oxide	Roughen surface	Develop resist
Plug vias	Electroless copper plating	Cure resist
Grind plugs	Apply photoresist	Apply metal finish
Pattern	Apply electrolytic copper	
	Strip resist	
	Etch	

Figure 2.2 Sequential build up manufacturing process steps from [9].

As can be seen in the figure, the process involves many steps, a lot of which have to be repeated every layer. The application and subsequent stripping of the resist and the etching of the copper also involve much material waste. As suggested by the name, SBU technologies are built up sequentially allowing via placement anywhere within a circuit pattern. However this comes at the cost of multiple lamination and plating runs, making many layers prohibitively expensive and time inefficient. Figure 2.3 shows the large gap between current interconnect technologies and the sub-micron scales in ICs. Thin film technologies are considered a technology 'bridge', generally accepted as the best performer in terms of interconnection density and electrical performance. Thin films enable the use of dense interconnection patterning technologies with feature sizes down to 10 μm and below. This allows high density interconnections to be created

using as few as two fine routing layers [10]. Due to the different nature of the manufacturing processes involved in thin film processing, the only challenge in accurately registering vias within landing pads is alignment of the respective machining tools such that landing pads 10μm bigger than vias are sufficient to account for tool misalignment.

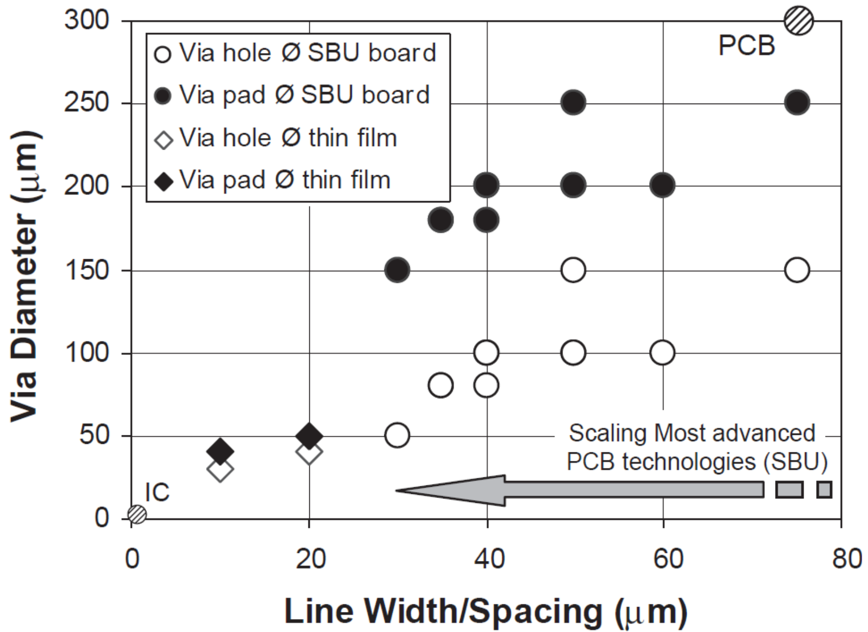

Figure 2.3 Graph comparing the minimum feature sizes on PCBs, interconnects made using SBU technology, interconnects made using thin film technology and ICs from [11].

Thin film technologies allow for the use of low dielectric constant (low k) materials and high conductivity conductors giving good electric performance which is not normally possible due to the high temperatures and chemicals used in conventional manufacturing processes. They also have the finest feature resolution and therefore the highest wiring densities compared to other high density interconnect manufacturing methods. Thin film manufacturing technologies normally suffer from a restricted device size, but are ideal for Wafer Level Packaging (WLP) of ICs and can be readily used in conjunction with other HDI manufacturing technologies to increase the areas of applicability of the technology [12]. WLP technology is whereby the ICs are packaged at the wafer level, before the wafer dicing. Chip scale packages (CSPs), where the package size is on the same scale as the chip, are therefore a requisite for WLP, restricting the device sizes required for the high density interconnect to approximately the size of a chip. The steps typically involved in the manufacture of a two layer interconnect package are outlined in [12] as:

1. Select and prepare substrate.

2. Deposit dielectric (if required, e.g., if using a metal substrate).

3. Deposit first metal layer and define conductor pattern.

4. Deposit second dielectric layer and define vias.

5. Deposit second metal layer and define conductor pattern.

6. Deposit third dielectric (passivation) layer and define openings to expose all bonding pads.

7. Plate bond pads if required.

It is clear that to enable thin film technology on an industrial scale, equipment is required which is able to efficiently and cost effectively accomplish conductive pattern transfer. This equipment must be able to pattern down to 10 µm or less, and work with the materials that ensure good electrical performance.

The IC substrate or interposer market has lagged behind the development of ICs. Profit margins are low and the trend has been to incrementally improve existing technologies to avoid the significant investment required to develop and adopt new technologies. As such the current technology is dated and no longer able to produce the feature sizes demanded by the next generation of ICs without restricting the system performance. The necessary adoption of new technology has driven research into new manufacturing methods that are capable of resolving tracks down to 10µm and below for use in densely wired 2 layer interposers in an effort to move away from the current trend of adding more layers and therefore more process steps in SBU technologies.

The following section details the current state of the art and the proposed system architecture which offers additional advantages in a high volume manufacturing environment. The final section reviews literature particularly relevant to realising the proposed system architecture.

2.2 HDI manufacturing processes

There are a number of advanced packaging manufacturing technologies that exist in either a development stage or in high end, low volume manufacture. The industry has yet to decide on how best to address the aforementioned technology gap. The IC substrate makers are approaching the problem by scaling PCB manufacturing technologies, using panel sized organic substrates which have cost advantages over other formats and materials. The Outsourced Semiconductor Assembly and Test

(OSAT) companies specialise in the backend processing of silicon wafers. As such they have an expertise in silicon handling and manufacturing processes. Their focus has been on using semiconductor technologies such as high resolution steppers using mask projection for WLP. These typically exceed performance requirements in terms of minimum feature size, but the wafer format and the cost of semiconductor processes, as well as the poor electrical properties of silicon, makes these solutions less attractive. There are proponents for other substrates as well, for example glass has much better dielectric properties than silicon, and its coefficient of thermal expansion (CTE) can be tuned to match that of silicon to reduce warpage in the package between the IC substrate or interposer and the silicon chip. Manufacturers of glass interposers may also leverage the existing large glass panel manufacturing infrastructure used in the production of LCDs. However, glass substrates have poor thermal properties which can lead to heat dissipation issues in the chip package. Ceramic substrates have good or reasonable thermal, mechanical and electrical properties but currently lack the existing manufacturing infrastructure of the above mentioned substrates and are consequently too expensive to be attractive for mainstream applications at the time of writing [13].

The advent of relatively cheap, reliable, frequency tripled diode pumped solid state lasers within the past decade or so has led to the development of Laser Direct Imaging (LDI) which is currently the most popular alternative to contact printing for high end PCB applications. Substantial interest has also been shown in LED imaging and inkjet based technologies, as well ablative laser processes such as Laser Direct Write (LDW) or more generally, laser structuring. There are a number of incarnations of each of the various manufacturing methods, some of which were commercial and have already fallen out of use. As such only those technologies widely considered capable of maturing into an economically viable high volume manufacturing process are considered in Sections 2.3-2.5.

2.3 Inkjet technologies

The advantages of inkjet technologies are obvious. They offer a fully additive process, where conductive tracks are only printed in areas where they are required, and the pattern transfer is also fully digitised with no need for the production of a mask or use of photolithographic resist and development. As with all digital techniques, this means changes to circuit designs can be completed and implemented by simply changing a CAD file, and printing can be scaled in x and y to try to optimise the via to pad

registration of boards which have thermally expanded and contracted during the manufacturing process.

As such, inkjet technologies for the printing of conductive inks have been the subject of much research [14-19], but the minimum line widths and spacings achievable limits their applicability to the advanced packaging and IC substrate market. The current state of the art commercially available is around 60 µm line width [20] with some academic groups achieving down to 25 µm line widths with novel printing techniques [21]. Briefly, the size of a printed trace is determined by contact angle, wettability of the surface and volume of the printing nozzle. The smallest printing nozzles currently available, such as the Dimatix Samba printhead, are 2 pL in volume. However, in a practical situation this would still always result in conductive tracks greater than 25 µm. The method used by Meier et al. to achieve 25 µm tracks was through the heating of a 10 pL nozzle such that the volume of liquid within the nozzle was closer to 2 pL.

Although some members of the PCB industry believe inkjet is the technology of the future for the cheap manufacture of printed electronics, the technology has a long way to come, if it is at all possible, before it can achieve the line widths necessary for high density IC substrates and interposers.

2.4 Lithographic manufacturing processes

Lithographic technology has already been used in the manufacture of sub-micron features in commercial chips, and as such is readily adaptable to the fabrication of advanced chip packages. However lithographic processes can be costly, requiring clean rooms with chemical stations for cleaning, developing and etching the substrates as well as the hardware for deposition of thin films, conductive pattern transfer and plating technology required by all IC substrate manufacturing plants. Regardless of the cost and their impact on the environment, the technology is a proven, high volume and high yield industrial process and as such there are a number of tools on the market for the exposure of high density interconnect patterns onto photoresists.

2.4.1 Laser Direct imaging

LDI systems normally consist of raster scanning a UV solid state laser beam across a photoresist and turning the laser on and off, for example through use of an Acousto-Optic Modulator (AOM), to define exposed pixels according to a circuit pattern. The beam is usually scanned across the resist using a scan head. As such the minimum

resolution achievable depends on the optical configuration used to focus the laser, and the laser interaction with the photoresist.

Since the pattern is defined by a digital file on a computer, LDI does not need a mask or phototool. This eliminates printed in defects from the process, as well as reducing costs and lead times associated with producing new circuit designs. It also allows for flexible patterning with on-the-fly changes to circuit designs without affecting throughput.

LDI tools have imaging times close to that of contact printing [22], and can currently achieve line widths and spacings of around 15 µm on large panel formats [23]. Vias are still laser drilled separately and have to be registered with the circuit pattern's landing pads and traces. However one advantage of LDI tools is that the digital pattern can be scaled to compensate for board warping during processing to ensure pads are accurately registered with vias. FR4 is a typical organic core material, and has a CTE of 15-20 ppm K^{-1} [24]. Measuring warping due to CTE mismatches can be done with vision systems measuring the degree of dimensional change in the board by locating and measuring the distance between fiducial marks on the board put down at the same time as the via processing.

The most commonly used, commercially available, LDI tools are manufactured by Orbotech. The Orbotech Paragon Ultra family can process panel sized substrates with specified minimum feature sizes of 12 µm lines on a 30 µm pitch and use a frequency tripled solid state laser as a light source. Figure 2.4 shows the current state of the art achievable with laser direct imaging. As can be seen in the pictures, the paper demonstrates line widths and pitches of approximately 15 µm and 30 µm respectively [25]. LDI tools are compatible with both subtractive processes, and the Semi-Additive Processes (SAP) more commonly used in chip packaging applications.

In SAP processes, ~2 µm of electroless copper is deposited on a substrate through use of a palladium seed layer. A resist is exposed and developed on this thin copper film as shown in the image on the left of Figure 2.4. The substrate is then pattern plated in an electroless copper bath, such that electroless copper growth is only seeded in the areas where the developed resist has been removed from the 2 µm copper film. The resist is then stripped, giving the result seen in Figure 2.4, which would subsequently be etched to remove the 2 µm copper layer. The process flow is depicted on the left of Figure 2.8 [26]. Being a lithographic process, the photoresist still requires development and the

end result is raised copper features on a substrate. This causes issues with the planarity of the board when building up subsequent layers as shown in Figure 2.5. For very fine line space features, it can also cause problems in the trace adhesion, since for a 2 µm track, there is only a 2 µm interface with the substrate. Additionally, etching the 2 µm film used to seed the electroless copper growth also etches the conductive patterning, limiting the minimum feature size the process is able to achieve.

LDI is a high throughput, high yield process already in volume manufacture. Being able to digitally define and change the exposure pattern is seen as a big advantage; however there are fundamental limitations to the resolution limit of the technology which prevent its use to address the technology gap for advanced package substrates.

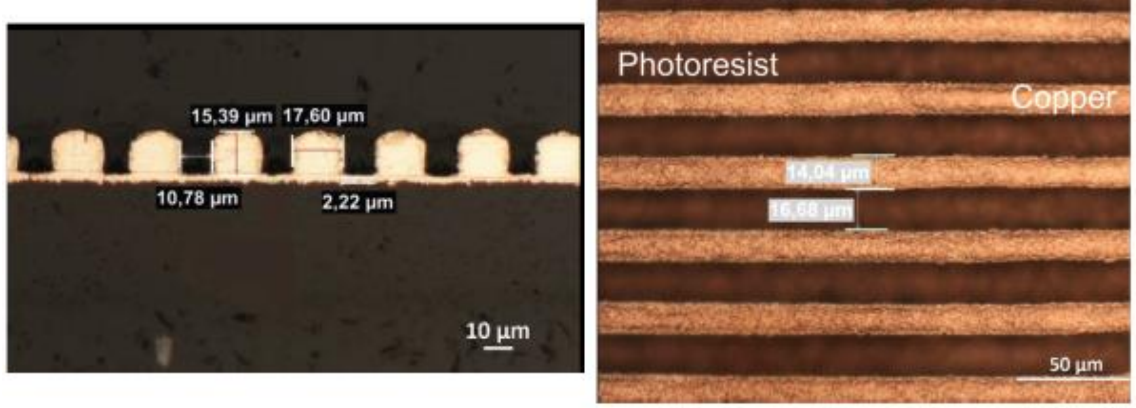

Figure 2.4 Raised copper tracks patterned using an LDI exposure tool on a photoresist [25].

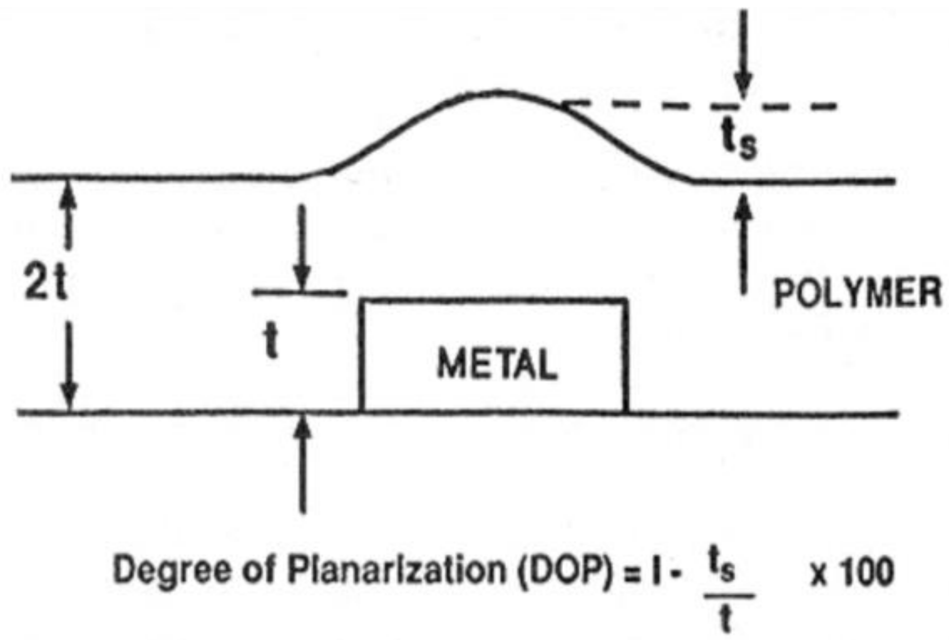

Figure 2.5 Definition of the degree of planarization when adding a polymer layer to raised conductive metal tracks - from [27].

2.4.2 *Mask projection*

Projection imaging, a commonly used step and repeat technology in IC chip manufacture, involves imaging a mask onto a substrate often with a certain feature demagnification. Commercially available immersion lithography tools for IC production, such as Nikon's NSR-S622D, increase the numerical aperture of the imaging lens by immersing it in a medium with a high refractive index such as water. The NSR-S622D has a 1:4 reduction ratio, and can image feature sizes down to 38 nm with an ArF excimer laser 193 nm illumination source. Commercially available extreme UV scanners, such as ASML's Twinscan NXE:3300B, use light sources such as tin based plasmas, which emit at 13.5 nm. The Twinscan NXE:3300B also images with a 1:4 reduction ratio and can be used to image down to 22 nm. The relevance to advanced chip packaging is obvious, with feature sizes well below that required being achievable with commercially available tools for high volume and high yield production.

Illumination sources for projection imaging in advanced packaging vary, with high power mercury lamps, excimer laser sources and LEDs all available. With the need for small feature sizes, masks based on glass are a requisite for dimensional stability of the pattern. The most commonly used type of mask is a chrome on quartz binary mask due to the good transmission of UV through quartz, its dimensional stability and low coefficient of thermal expansion (CTE) [28]. Examples of such projection imaging systems include Ushio's UX-5793SC step and repeat projection exposure system which can achieve 3 μm line widths and spacings across panel sized substrates (510×610 mm); and Suss MicroTec's DSC500 projection scanner, which can resolve 3 μm line widths and spacings across wafers up to 450 mm in diameter and panel substrates up to 450×500 mm. Both systems use high power mercury lamp light sources and as such are compatible with the wide range of resists developed for the mercury i line (365.4 nm). Such projection imaging systems, whether using lamp, LED, excimer or solid state laser illumination sources, are available in commercial tools and able to reach feature sizes down to 2μm.

Figure 2.6 is an cross-sectional Scanning Electron Microscope (SEM) micrograph of a developed resist exposed by a Suss DSC300 projection scanning tool with 3 μm L/S features [29]. The resist is 7 μm thick, and the image demonstrates the steep taper and high resolution acheivable with the system, including an aspect ratio of greater than 2:1. The exposure is of a high quality, however it should be noted that the resist will not

remain in the final product, and must be stripped once the metalization of the channels is complete.

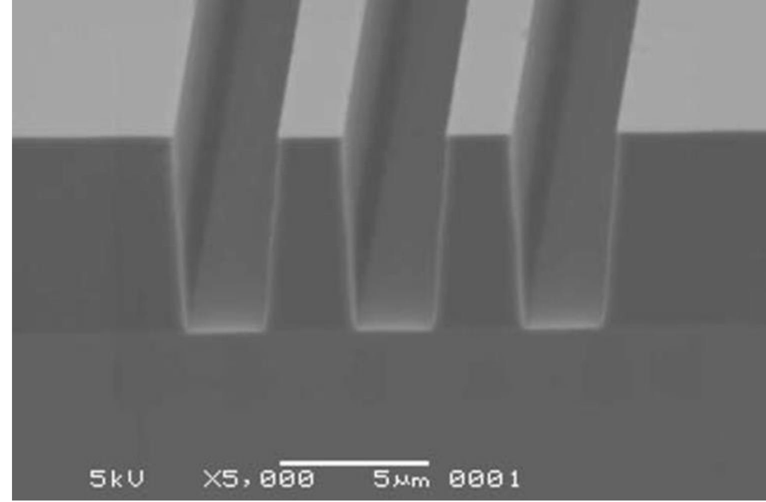

Figure 2.6 SEM micrograph of TOK TMMR P-W1000T resist exposed by Suss MicroTec's DSC300 Projection scanner. The image shows 3 μm L/S channels in the developed resist, which is 7 μm thick [29].

Being lithographic processes, these all require environmentally damaging wet chemical processes and also result in the planarity issues already mentioned and shown in Figure 2.5. Furthermore, in SAP processes it is the adhesion of fine line space copper tracks to the substrate, and the etch of the 2 μm copper seed layer, that limit the minimum feature size, not the exposure of a resist. There are techniques to mitigate these issues, such as Shinko's integrated thin-film high-density organic package (i-THOP) process [30]. This is capable of producing 2 μm L/S features by building the coarser parts of the package by conventional SAP methods, then using chemical mechanical polishing (CMP) to planarize the top surface. This surface is then sputtered with a Ti/Cu seed layer, and a thin film resist is spun onto the package for the fine line space stepper exposure. Once exposed and developed, the fine line space features can be plated up from the sputtered seed layer. Once the resist has been stripped the seed layer can be flash etched without causing significant damage to the 2 μm L/S circuitisation on account of the sputtered metal layer thickness of ~50 nm. This all comes at a cost, since CMP, sputtering and the spin coating of resist layers are all expensive semiconductor processes which the packaging industry has avoided to date.

One proposed solution to alleviate some of these costs is the use of photo-imageable dielectrics. These dielectrics can be structured by exposure and development, and would not require stripping after metallization. This makes them attractive to use,

despite their greater cost and poorer properties than non-photo-imageable dielectrics. Table 2.1 compares a photo-imageable and non-photo-imageable polyimide substrate from the same manufacturer [31]. It can be seen that the CTE of the non-photo-imageable dielectric has been matched to that of silicon to reduce warpage in the chip package, and the non-photosensitive polymer has better mechanical properties as well. Despite inferior material properties, the fact there is no longer the need for a resist, removing a number of process steps, makes the use of photo-imageable dielectrics attractive. Compared with laser ablation, however, the use of steppers with photo-imageable dielectrics still has additional process steps including the development of the imaged polymer, and it uses more expensive materials with inferior mechanical and electrical properties.

Photo/Non-Photo	Non-Photo	Photo
Material	PI	PI
Manufacturer	HD Micro	HD Micro
Product	PI-2611	HD-4100
CTE (ppm/°C)	3	35
Modulus (GPa)	8.5	3.4
Tensile Strength (MPa)	350	200
Elongation (%)	100	45

Table 2.1 Comparison of the properties of photo-imageable (red) and non-photo-imageable (green) polyimide substrates from the same manufacturer. The non-photo-imageable material has a CTE closer to that of silicon, reducing warpage in a package, and better mechanical properties – from [31].

2.4.3 Dynamic mask imaging

Similar in concept to mask projection, dynamic mask projection involves projecting the image of a Spatial Light Modulator (SLM) or Digital Micromirror Device (DMD) onto a substrate [15]. These have the benefit of being able to change in real time to image all or part of a device pattern, and digitise the imaging process. This offers the same advantages as LDI, such as scalable circuit design to improve via to pad registration and the possibility to make on the fly changes to the circuit design without the lead time or

expense of a mask. They most commonly use DMDs illuminated by LEDs or Laser Diodes (LDs).

Such exposure tools can achieve line widths and spacings down to 8 μm [32]. The benefits of digital pattern definition have to be weighed against the higher resolution possible with a binary chrome-on-quartz mask. The minimum feature size limitations currently limit their attractiveness to address the technology gap between PCB and semiconductor manufacturing technologies, since their resolution is comparable to that of LDI systems. Iris AO's water cooled, nitrogen purged, dielectric coated deformable mirrors have currently been damage tested up to ~17W at 355 nm. At the time of writing, this was the highest damage threshold test for an SLM in the UV, limiting its appeal for use in high throughput laser ablation systems with 200-300W average power.

There are a number of lithographic technologies which have evolved from the previous lithography based industry standard, contact printing, or the semiconductor industry. These are capable of feature sizes down to 2 μm or smaller, and include step and repeat mask projection imaging systems that were used to produce the previous generations of ICs. However, all of these technologies involve wet chemical processes to develop photoresists and etch away conductive materials in areas which have been exposed. This leads to a complex, multistep, subtractive manufacturing process which is wasteful and bad for the environment. The process usually results in conductive tracks raised above the substrate surface, which means that subsequent layers in multilayer boards are no longer planar, and there are issues with adhesion of very fine line space tracks. Via drilling must be done separately, normally by laser drilling with a Nd:YAG laser, and as a consequence pad to via registration can also be an issue for this technology.

2.5 Ablative laser processes

Ablative laser processes have several advantages over lithographic methodologies. The ability to process vias at the same time and on the same platform as patterning the pads and traces means that registration between the two features can be improved, facilitating nearly padless vias. This can reduce both the package size and format [33]. There is also no need for an additional via drilling tool. Creating trenches to plate into also means that in a multilayer package the subsequent layers in the build-up are co-planar avoiding the planarity issues shown in Figure 2.7(b) [34]. They also have the advantage of being a dry industrial process. This reduces production cycle time, material waste and the requirement for an infrastructure to handle the wet chemical film development

and etching processes. It also removes the yield and cost sensitive lithography steps from the manufacturing process flow [35]. A comparison of the process flow between conventional SAP technologies and laser embedding features can be seen in Figure 2.8 [26]. Laser embedding conductors involves approximately 8 less process steps for a single build up layer [36, 37]. Embedding features within the substrate also improves the adhesion of the traces to the substrate by increasing the surface area of the trace in contact with the substrate as shown in Figure 2.7(c). Clearly, for large features the difference in surface area in contact with the substrate becomes negligible, but an increase in peel strength by a factor of 3 for 15 μm L/S features has been demonstrated [38].

It is also possible to embed conductors within a dielectric by using a photosensitive material and mask imaging as discussed in Section 2.4.2. The draw backs of this approach when compared to laser ablation are that the material is more expensive, and has less desirable electrical and mechanical properties. It would also require a wet chemistry step to develop the photosensitive dielectric.

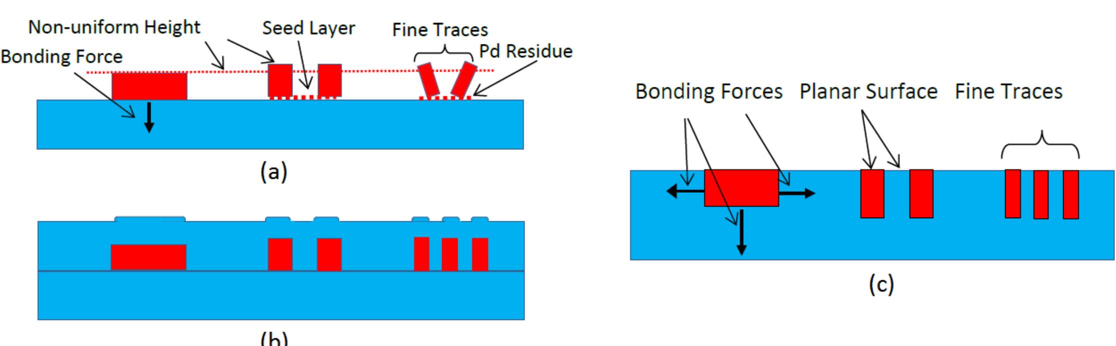

Figure 2.7(a) graphic highlighting the issues with conventional SAP processes in achieving sub 10 μm L/S. These include Pd seed layer residue which can lead to electrical leakage and a reduced bonding force to the substrate compared to embedded structures. This reduced bonding force can lead to delamination of fine traces. (b) graphic highlighting the issues with co-planarity of subsequent layers in a conventional SAP build-up. The depth of focus of high resolution optics is small, so this can lead to issues with fine trace formation in subsequent layers. (c) graphic highlighting the planarity and increased surface area of embedded conductors – from [34].

Laser systems for high resolution ablation of organic dielectrics require high average power laser sources emitting in the UV. This is due to a number of reasons. Firstly, the resolution of an imaging system scales with wavelength, such that shorter wavelengths allow the machining of smaller features. The high energy UV photons are strongly absorbed in the electron absorption bands of many polymers, resulting in absorption

lengths typically shorter than a few microns [39]. This reduces the fluence required for ablation, and limits the size of the heat affected zone. Thirdly, the throughput of a laser micromachining production system scales approximately with the average power reaching the substrate, so a high average power UV laser source is required for high throughput.

Currently there are only two such laser sources: excimer laser sources which are gas lasers characterised by high average power, low repetition rate and high pulse energy emitting at several wavelengths in the UV; 3rd and 4th harmonic frequency converted diode pumped solid state lasers which have higher repetition rates and lower pulse energies. Typical laser parameters are summarised in Table 2.2 [40].

Process Step	Semi Additive Process	LDA Process	Process Step
1. Laminate Dielectric			a. Laminate Dielectric
2. Laser Drill			b. Laser Drill
			c. LDA patterning
3. Desmear / Electroless Cu			d. Desmear / Electroless Cu
4. Apply Resist/Photo exposure/development			
5. Pattern Plate			**e. Panel Plate**
6. Strip Resist			
7. Etch			**f. Planarization / Etch**

Figure 2.8 Comparison of process flows for conventional SAP and Laser Direct Ablation (LDA) methodologies – from [26].

Despite some of the advantages in ablative laser processes, they are still not in commercial use for chip packaging. Step and repeat excimer laser mask projection systems are available and can produce features of the required dimensions, such as the ELP300 from Suss MicroTec, however the high cost of ownership has so far prohibited their uptake in a high volume industrial process. Excimer lasers in a production environment require the infrastructure to handle the toxic gases used as the gain medium in the laser, and the lasers require regular and costly maintenance. Not only do

they need a large capital investment but they are expensive to run. The cost of ownership of commercial excimer laser systems is discussed and quantified in Section 6.1.3.

Characteristic	Excimer Laser	Photon Energy	Diode pumped ND:YAG
Wavelength	 351 nm, 308 nm, 248 nm, 193 nm, 157 nm	1.17 eV 2.33 eV 3.53 eV 4.02 eV 4-66 eV 5.00 eV 6.42 eV 7.90 eV	1064 nm, 532 nm, 355 nm 266 nm
Energy per Pulse	10 .... 1000 mJ		0.1 ... 3 mJ
Repetition Rate	10 .... 4000 Hz		1 kHz ... 100 kHz
Power Range	1 ... 300 W		5 ... 60 W
Pulse Length, FWHM	10 ... 35 ns		15 ... 100 ns
Beam Quality	Large cross section, mutimode		TEM00 $M^2 < 1.2$
Spatial Coherence	Low		High
Max. Energy Density	... 200 J/cm^2		... 2500 J/cm^2
Max. Peak Power Density	... 1000 MW/cm^2		... 200 GW/cm^2

Table 2.2 Comparison of excimer laser and diode pumped Nd:YAG laser parameters from [40].

As a consequence, to try to capitalise on the advantages an ablative laser process can offer, research in laser structuring with frequency tripled solid state lasers has been very active. Laser direct write processes have received the most interest from the research community, where a focused laser beam is scanned across a substrate using a galvanometer scanner and an f-theta lens. There are some UV, solid state commercial systems available, for example Model 5335 from ESI, that employ laser direct write methodologies but the technology has some limitations, which will be discussed in the sections to follow.

2.5.1 Excimer laser processes

Despite the costs mentioned above, excimer laser reliability and pulse energy stability have improved remarkably since their development, and the required maintenance has been drastically reduced [41]. New solid state high power switching technology means they can now operate maintenance free with high duty cycles for around 6 billion pulses, with automatic gas exchanges around every 50 million pulses. This compares with previous systems using thyatron gas switches that would need maintenance every 200-300 million pulses and replacement every 700-1000 million pulses [41]. However

this is still shorter than the operational life time of the diode in a diode pumped solid state laser (~3 years), and an industrial plant would need the infrastructure for the gas replacement.

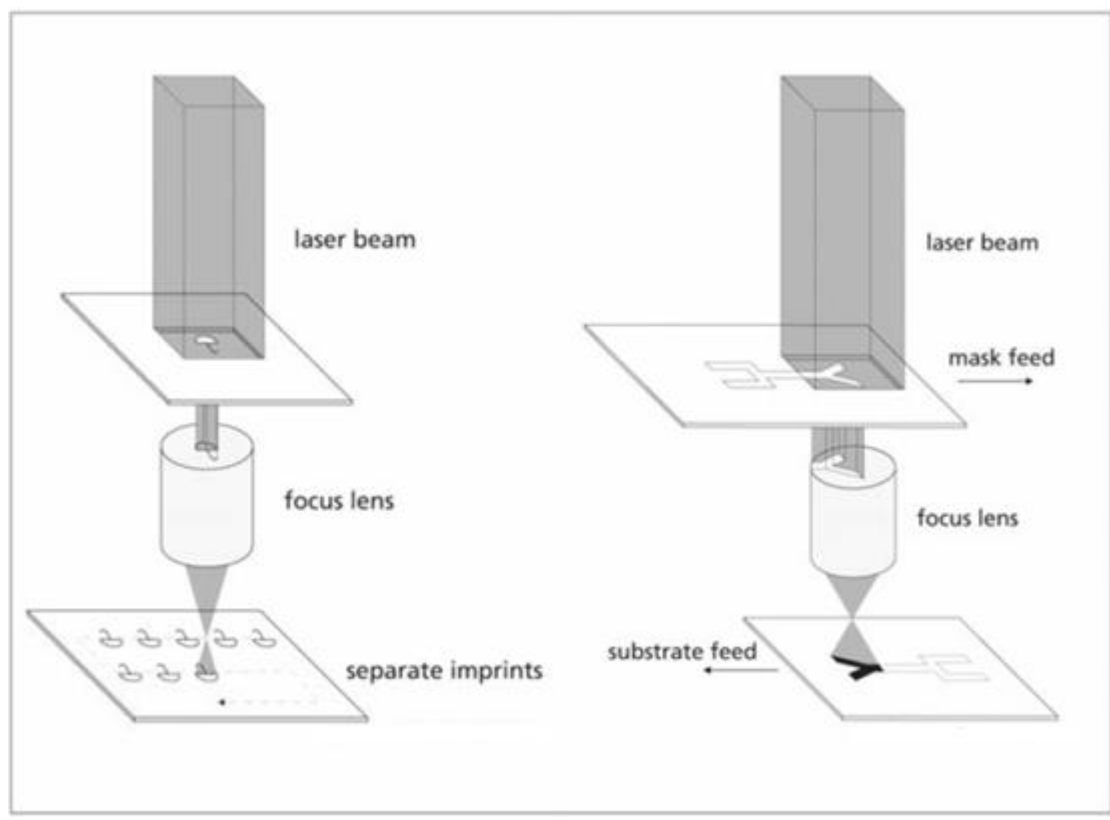

Figure 2.9 The step and repeat (left) and conformal scanning (right) methods of image transfer in ablative excimer laser imaging. The method selected depends on the desired image size and the demagnification of the imaging system – from [42].

Owing to their large pulse energy, excimer lasers can illuminate relatively large areas of a mask with a single pulse. This can either be done in a step and repeat fashion, where the laser beam illuminates a mask to transfer the image of an entire device, or by conformal scanning where both the mask and the substrate stages are moved relative to the beam in opposite directions, as shown in Figure 2.9 [42]. The image of the mask is projected onto the work piece with a projection lens. This is usually with a certain demagnification that allows a low fluence below the damage threshold of the mask at the mask plane, but a fluence above the ablation threshold of the substrate at the work piece. Masks are typically chrome-on-quartz, with quartz offering the required dimensional and thermal stability, and high transmission in the UV. The chrome has a high enough damage threshold to reach the required fluences to ablate most polymers at the substrate with a suitable imaging system. The damage threshold of a chrome on

quartz mask for a 248 nm or 308 nm excimer laser at 300 Hz is around 100 mJ cm^{-2} [43] and the ablation threshold of polyimide thin films is in the region of 45 mJ cm^{-2} [44]. For applications requiring higher fluences, aluminium metal layers can also be used which have damage thresholds of ~250 mJ cm^{-2}.

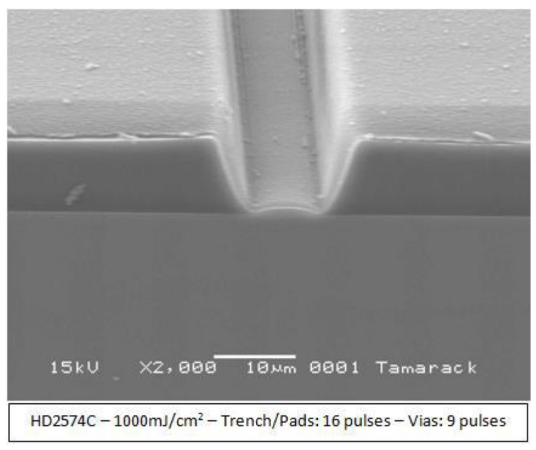

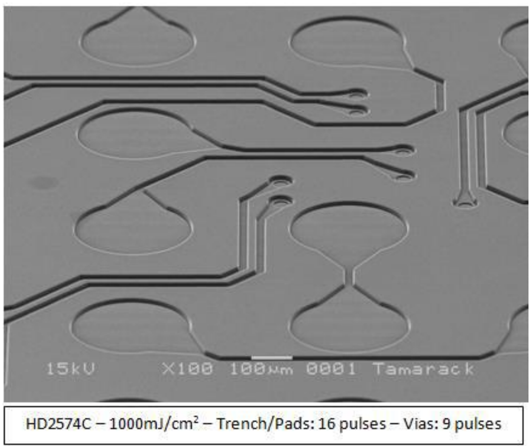

Figure 2.10 SEM micrographs of excimer laser ablation by the Suss MicroTec ELP300 commercial production tool. The image on the left shows the cross-section of an 8 µm track in a proprietary polyimide. The image on the right shows uniform ablation of large pads and traces – from [31].

Figure 2.10 shows excimer laser ablation by the Suss MicroTec ELP300 tool [31]. The 8 µm trace on the left has steep sidewalls and flat trace bottom, and it is clearly well above the resolution limit of the laser ablation. The image on the right of Figure 2.10 shows the ablation of large pads as well as small traces. The uniform ablation of large areas is difficult to achieve with a focused solid state laser beam.

Figure 2.11 is an SEM micrograph of 5 µm channels machined into an Ajinomoto Build-up Film (ABF) by the Suss system [37]. ABF is common substrate in chip packaging, and consists of epoxy resin with silica filler particles. Epoxy resins with glass filler particles made by other manufacturers are commonly called ABF type substrates. The silica particles improve the CTE matching with silicon. The laser cannot machine the glass fillers, so the particles are either ejected from the channels or remain in the substrate and protrude into the channel. This places a restriction on the maximum filler size for a given channel width. For smooth channels without large filler particles protruding into the trace, or voids in the channel wall where silica particles have been ejected, the maximum filler size should be approximately 10% of the minimum channel width [45].

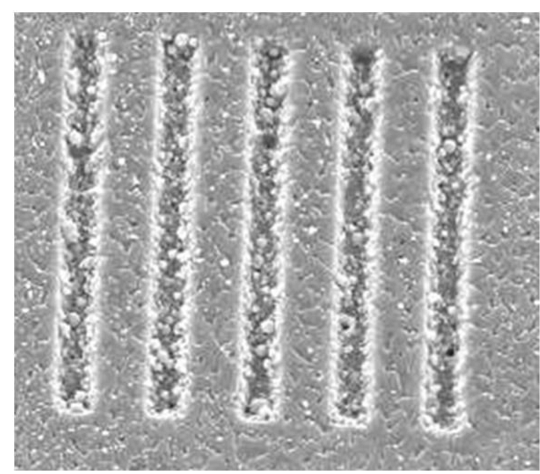

Figure 2.11 SEM micrograph of 5 μm channels machined into ABF GX-13 by the Suss MicroTec ELP300. The ABF substrate is an epoxy resin filled with silica particles which are visible in the channels. The laser cannot machine the glass, so these filler particles are either ejected from channel walls, or protrude into the channels – from [37].

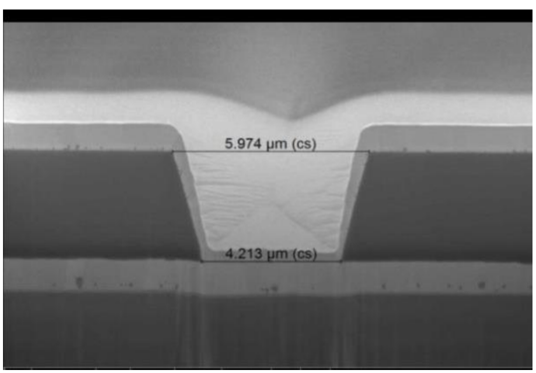

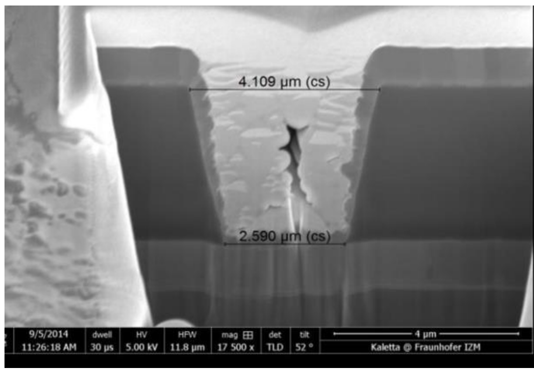

Figure 2.12 SEM micrograph of FIB cross-sections of vias drilled with the Suss Microtec ELP300 excimer platform in Benzocyclobutene (BCB). The images show a 6 μm diameter via (left) and 4 μm diameter via (right) – from [46].

As mentioned at the beginning of Section 2.5, one of the advantages of using as an ablative process to define the routing layer is that the vias can be drilled on the same platform, improving the registration between the two patterns reducing the capture pad size required for the via. In addition to this, excimer laser systems are currently the only available high throughput production tool for laser drilling of sub 5 μm vias. Cross sections of vias down to 4 μm are shown in the SEM micrographs in Figure 2.12 [46]. This further reduces the pad size required to capture the via, meaning more signal routing can be done per layer. Reduction in via size is important to realise the full benefit of 2 μm L/S tracking in the routing layer.

Advanced machining strategies can be employed to machine regular arrays of features over an area much larger than the optical field of the projection lens. Synchronised

Image Scanning (SIS) scans the image of a static mask across a continuously moving substrate [47]. The commanded stage speed of the substrate is equal to the product of the pitch of the objects in the regular array image and the laser repetition rate, such that each part in the array is machined by overlaying the image of different parts of the static photomask. Figure 2.13 illustrates SIS being used to machine a long row of inkjet nozzles. The technique has the benefit that each nozzle is drilled by overlaying images from different parts of the optical field. If the row were formed by a step and repeat process, nozzles drilled at the edge of the optical field can suffer from aberrations in the projection optics such as field curvature and variations in lens telecentricity which both vary with distance from the optical axis. Additionally, each aperture would be exposed to the same part of the laser beam, so variations in intensity across the beam profile could lead to variations in the ablation of the nozzles.

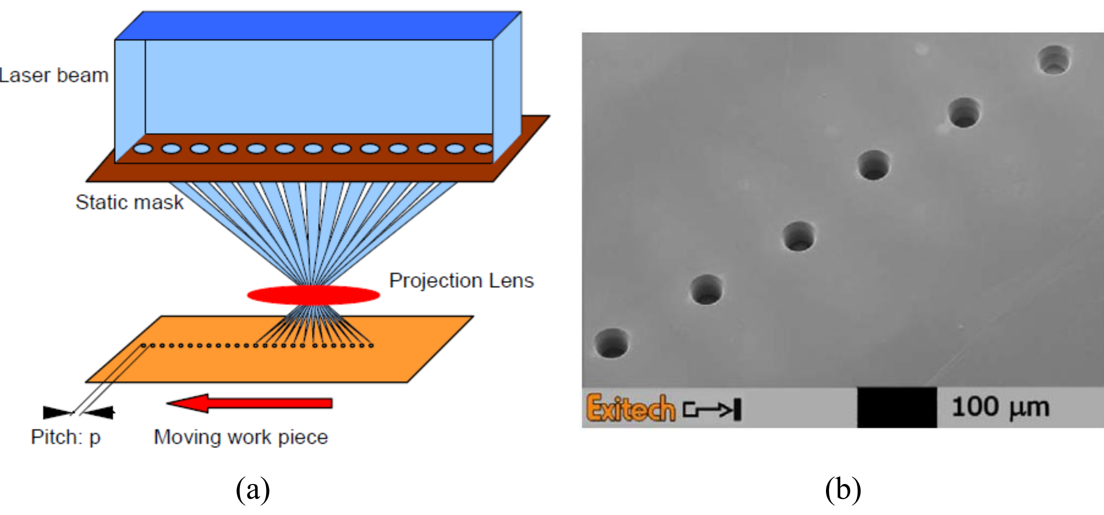

(a) (b)

Figure 2.13 (a) Schematic diagram illustrating synchronised image scanning being used to drill a row of inkjet nozzles much larger than the image field of the projection lens; (b) SEM micrograph of the drilled inkjet nozzles. The speed of the work piece is such that the substrate has moved by the pitch of one nozzle in the period between laser pulses – from [47].

To eliminate edge effects at the start and end of rows in SIS systems, an aperture can be moved across the surface of the photomask to reveal nozzles as the substrate is moved. Figure 2.14 illustrates the principle which can be used to ensure that each nozzle receives the same number of laser pulses at both the start and end of the row.

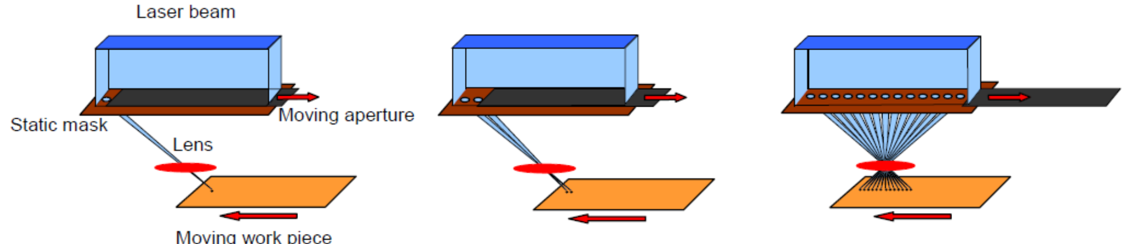

Figure 2.14 Schematic diagram illustrating how to eliminate edge effects in a synchronised mask imaging system. An aperture is moved across the mask is moved across the mask as the substrate is moved in the image plane. The aperture reveals a nozzle between each laser pulse such that each nozzle at the substrate receives the same amount of laser pulses – from [47].

By overlaying the image of different features at the mask in a while defined order, arrays of complex structures can be micro-machined. Figure 2.15 shows SEM micrographs of Fresnel micro-lens arrays machined by overlaying the image of different mask features at the substrate plane using SIS [48]. Although the lenses are not of direct relevance to chip packaging, the images demonstrate the high quality micro-machining possible with excimer mask projection systems. Additionally, they highlight the possibility to use SIS techniques, for example, to efficiently drill large arrays of vias with novel profiles in a chip package.

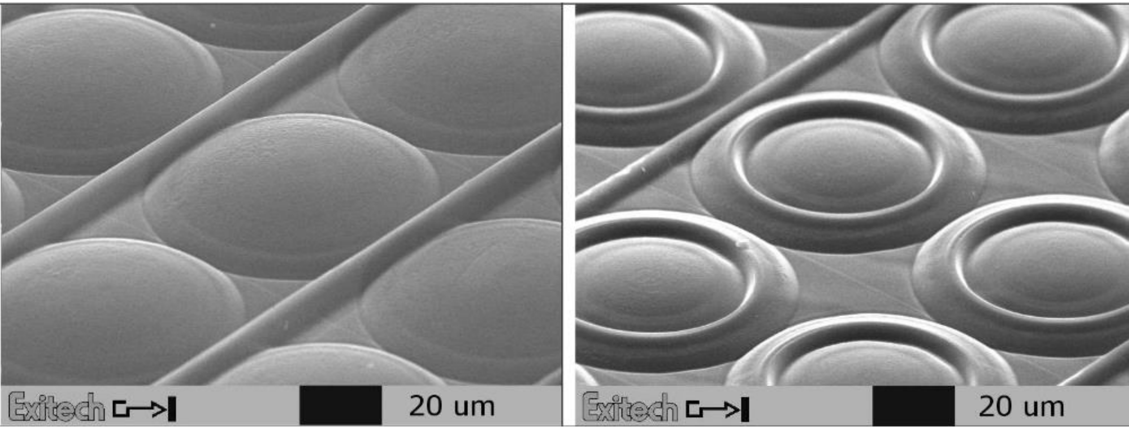

Figure 2.15 SEM micrographs of Fresnel microlens arrays machined using the SIS technique to efficiently overlay the images of different mask features at the substrate plane – from [48].

Excimer laser systems are proven, high throughput and high yield and in regular use in the semiconductor industry in high resolution steppers. They are capable of ablating features down to 2µm over limited device sizes [42], offering higher resolution than current direct write tools using solid state lasers. There has also been some interest and throughput calculations in exploiting excimer lasers in reel to reel systems for patterning and fabricating flexible embedded circuits [41, 49]. However, the

microelectronics industry is both risk averse and slow to adopt different technologies or methodologies, so the cost and infrastructure required to operate an excimer laser production facility and new plating methodologies has proved too great a barrier to its adoption thus far.

2.5.2 Solid state direct write laser processes for microelectronics interconnections

Frequency tripled solid state lasers require less capital to buy and are less expensive to maintain in comparison with excimer lasers. A more detailed cost of ownership comparison of the two laser technologies is presented in Section 6.1.3. Solid state lasers typically have a much higher beam quality than excimer lasers, and their close to diffraction limited performance is exploited in laser direct write systems by focusing the laser to a small spot. Given the cost advantage, laser direct write systems with applications in microelectronics have been the subject of much research, for example [6, 50-55]. Such systems usually pass the laser beam through a galvanometer scan head which deflects the beam across a substrate. An f-theta lens mounted underneath the scan head keeps the beam in focus across a flat substrate regardless of deflection angle. The laser is used to vector mark grooves in a substrate sequentially such that the process time is dependent on the circuit pattern complexity.

As a vector marking system with CAD file input, LDW processes are ideal for low volume prototyping since there is no need for a mask or the longer cycle times associated with lithographic processes [56]. They do, however, suffer from process times dependent on pattern complexity, design rules to keep beam velocity constant across the substrate and some limitations in the circuit features they can process. Complicated control systems have been researched to try to overcome some of these limitations [26, 53], but, for example, it remains challenging and time inefficient to ablate large ground plane areas to a uniform depth by overlapping a comparatively very small focused spot.

Feature resolutions down to around 10μm are currently achievable across approximately 20×20 mm scan fields using commercially available f-theta lenses with direct write laser structuring methods using frequency tripled solid state lasers [57]. SEM micrographs of 9 μm channels machined in an ABF type substrate can be seen in Figure 2.16 [26]. As with the excimer laser, the silica filler particles cannot be machined by the laser and are either ejected from the substrate remain in the channels.

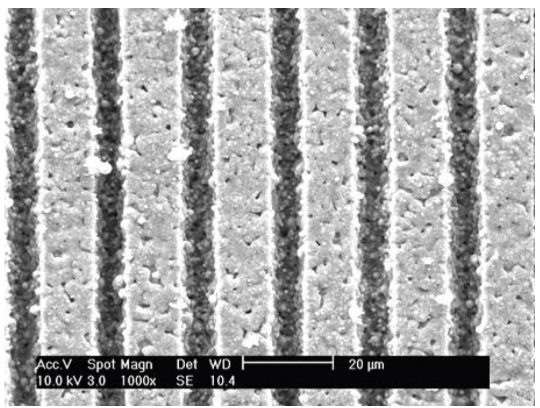

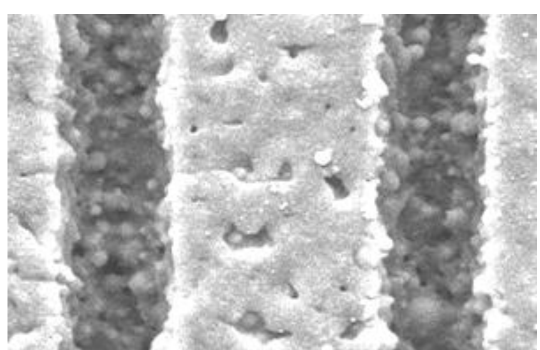

Figure 2.16 SEM micrographs of 9 µm channels machined with a frequency tripled solid state laser and a vector direct write system with galvanometer scanhead and acousto-optic deflector. The ABF type substrate is a glass filled epoxy resin, and the silica particles are visible in the trenches – from [26].

It is possible to extend the area an f-theta lens and scanner can address without stitching scan fields by moving the substrate under the scanner. Bow Tie Scanning (BTS) is a technique where the substrate stage is moved in an axis orthogonal to the scan direction. In addition to scanning the beam across the sample, the galvo-scanner also compensates for the motion of the substrate in the axis orthogonal to the scan direction as depicted in Figure 2.17 [58]. As the laser is scanned across the moving substrate to form parallel lines in the reference frame of the substrate, the commanded moves sent to the scanner outline a bow tie in the static reference frame.

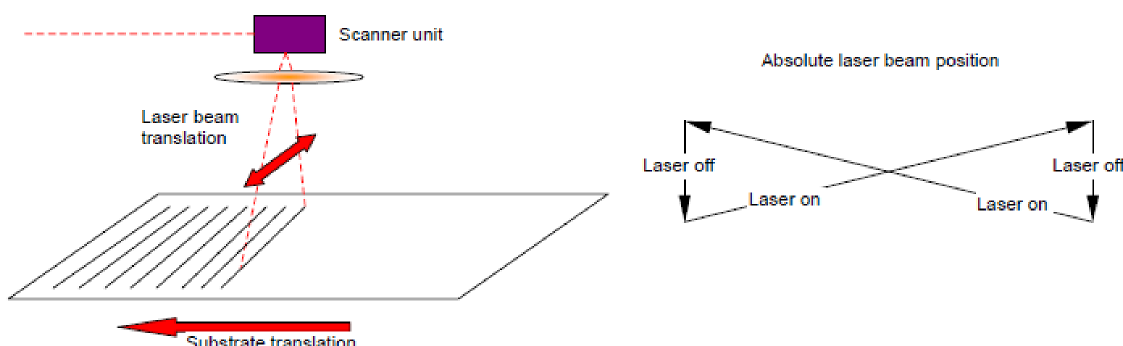

Figure 2.17 Schematic diagram illustrating the bow tie scanning methodology. As the substrate is translated in an axis orthogonal to the scan direction, the scanner compensates for the stage motion such that parallel lines are produced at the substrate – from [58].

When used in conjunction with a silicon mask, this technique can be used to ablate repeating patterns across large substrates. Figure 2.18 shows T bar electrodes ablated into an ITO on glass substrate using a solid state laser in a BTS regime. The image shows a 4×4 array of laser pulses, where each laser pulse contains the image of the

electrodes. This technique could be used to efficiently pattern arrays of repeating features in a chip package across panel sized substrates, for example vias.

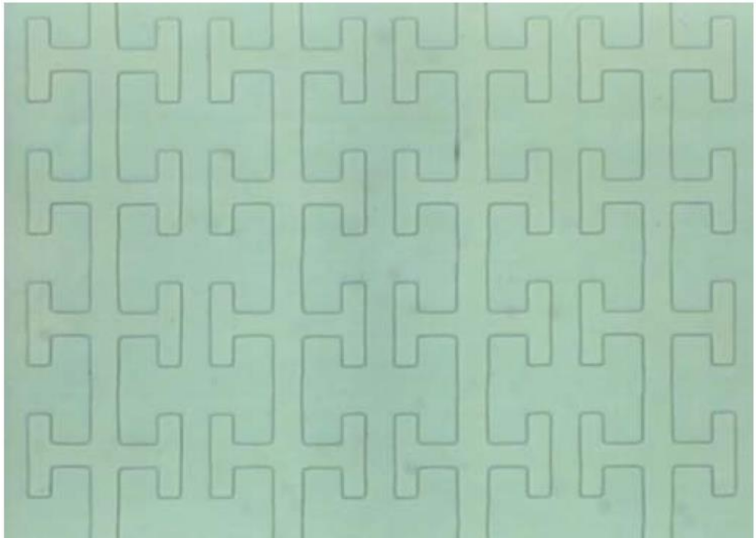

Figure 2.18 Microscope image of electrodes ablated into ITO on glass using the BTS technique. Each element in the 4×4 array contains the image silicon mask projected onto the substrate using the f-theta lens – from [47].

Solid state lasers have long been the industry standard in via drilling below 100μm, where the thermal effects induced by the cheaper CO_2 lasers become too great, and as such vias down to 10μm are the current state of the art [59]. The smallest hole sizes achievable with commercial UV solid state laser systems at throughputs of thousands of holes per second, such as the Orbotech Emerald 150 and ESI 5330 series, is 30 μm and 25 μm diameter respectively. Laser drilling of hole diameters less than 5 μm in diameter in production are only currently achievable with excimer laser systems.

Reference [60] is a simplistic comparison of a frequency tripled solid state laser and a KrF 248nm excimer laser source for the production of fine lines in printed circuits. The excimer laser source is used in a direct write type application. The analogue to the focused spot in solid state systems is achieved by imaging mask apertures of different sizes, since the beam quality of an excimer laser is too low to focus to a small spot. They report a smallest spot size of 25μm achieved by imaging a 100μm aperture to the workpiece where apertures smaller than this result in too little energy reaching the substrate. However this could be easily rectified by changing the beam size at the mask with a telescope. The focused spot of the solid state laser was also 25μm, so the features ablated by the two lasers were of similar dimensions. The excimer laser trench was squarer in profile due to the uniform illumination of the aperture by the laser. In part due to the inefficient use of the beam, since most of it was blocked at the aperture,

the solid state laser process was found to be 120 times faster than the excimer process despite the solid state laser only having 0.12W average power and the excimer laser 7W. They also report larger a resolidification height, the height of the melt relative to the rest of the substrate at the edge of the trench, with the frequency tripled Nd:YAG laser. This could be in part due to the shorter excimer wavelength leading to a more photochemical ablation mechanism, but the repetition rate of the excimer laser being two orders of magnitude smaller than that of the Nd:YAG laser likely contributed significantly as well.

Solid state laser systems are less expensive and more convenient than excimer laser systems. They offer a good solution for marking simple patterns, or low volume prototyping but are less suitable for marking the complex patterns with large areas of uniform ablation required for advanced chip packaging.

2.5.3 Proposed system architecture: scanned mask imaging

Having reviewed the current state of the art in high density interconnection fabrication technology, below is a brief summary of the tools capable of machining high density interconnects for advanced packaging of the next generation of integrated circuit substrates and interposers. LDI exposure tools are the current industry standard for fine line space PCBs. However the feature sizes they are capable of producing are limited to around 15μm by the spot size of the laser beam, the properties of the resist and the etch process of the plating seed layer. Mask projection tools offer resolutions of 2 μm over limited field sizes, making them well suited to chip scale packages. Whilst achieving 2 μm L/S is not challenging for the exposure and development of the resist, transferring this image to metalized features is currently only possible through slow and costly procedures. Ablative laser processes side step the wet chemical processes, however excimer laser processes are prohibitively expensive and frequency tripled Nd:YAG direct write processes have less good feature resolution and, due to their vector write nature, are not well suited to the complex structures required for chip packaging.

The proposed system in this work consists of a mask projection system illuminated by a frequency tripled solid state laser in an ablative laser process. Such a system would have feature resolutions of around 2μm but without the prohibitively high cost of ownership and complicated infrastructure required by an excimer laser production facility. Solid state lasers have lower average powers than excimer laser systems. A system with a single solid state laser would therefore have a lower throughput than an

excimer laser system, assuming the process time scales approximately linearly with power reaching the substrate. However, since solid state lasers have a cost per watt of laser power ~ ⅔ that of an excimer laser, parallel processing with multiple lasers can achieve the same throughput at a lower capital cost. Additionally, the cost of ownership is further reduced by the lower maintenance costs associated with solid state lasers. Such a process could achieve the required throughput and the resolution necessary for the next generation advanced chip packages, as well as avoid the wasteful and expensive, wet chemical lithography processes.

The high repetition rates and comparatively low average powers typical of UV solid state lasers results in pulse energies in the millijoule regime, 2-3 orders of magnitude lower than excimer laser pulse energies. The pulse energy is therefore too low to expand the beam to illuminate an entire device pattern and maintain a fluence above the ablation threshold of the substrate in a step and repeat method similar to that shown in the left of Figure 2.9. Conformal scanning shown on the right side of Figure 2.9 is difficult as well. Since a typical solid state laser has a repetition rate of the order of 10kHz the stage speed and accuracy required at the mask plane in an imaging system where the mask image is demagnified at the substrate would be too high. The proposed solution is therefore to raster scan a spot beam with a galvanometer scan head across a chrome on quartz mask, as shown schematically in Figure 2.19. This reduces the restrictions on the velocity of the beam relative to the mask. Having scanned the mask, the deflected laser light is brought back into the entrance pupil of the imaging lens by the field lens, and the mask image is ablated onto the substrate. The spot size of the beam should be chosen in conjunction with the demagnification of the imaging system such that the fluence is below the damage threshold of the mask at the mask plane, but above the ablation threshold of the substrate at the work piece.

By mounting the mask on a translation stage, 2 mask patterns can be precisely overlaid with a registration equal to the stage accuracy divided by the demagnification of the imaging system. For example, using a stage with 1μm positional accuracy in an imaging system with 3x demagnification, the two mask patterns could be mis-registered by a maximum of 1μm at the mask plane or approximately 300nm at the substrate. If one pattern consisted of traces and pads, and the other pattern consisted of vias - since the two would be patterned consecutively - this allows sub-micron via to pad registration.

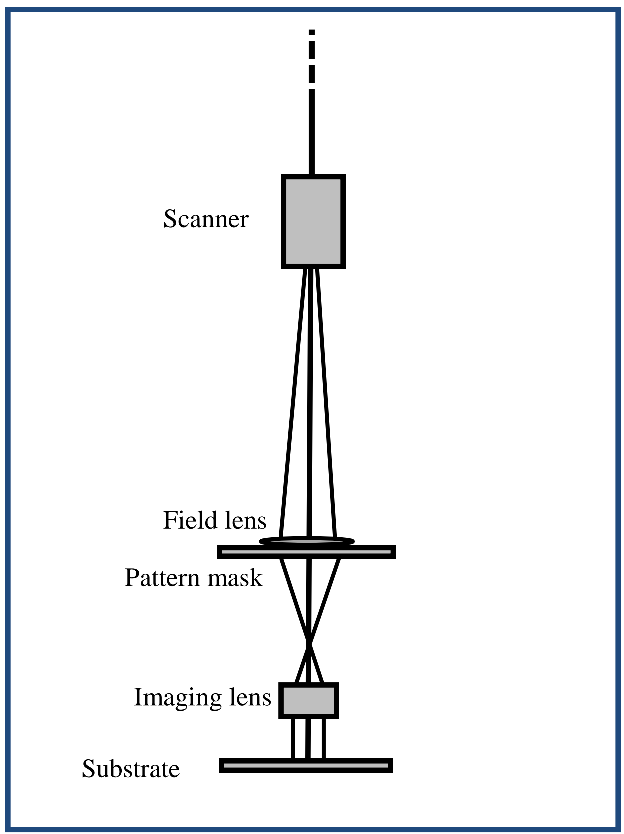

Figure 2.19 Schematic diagram illustrating the scanned mask imaging concept.

2.6 Solid state laser processing

Given the proposed scanned mask imaging concept described above, the following section reviews the literature related to the frequency tripled solid state laser processing of materials relevant to high density interconnect fabrication, namely polymers and thin metal films.

2.6.1 Nanosecond 355nm laser ablation

Working at UV wavelengths offer a number of advantages in laser micromachining, including better resolution of features due to the shorter wavelength, and usually better absorption or a shorter optical penetration depth on account of the higher photon energy [39]. However this comes at a cost. In frequency tripled solid state laser systems, the cost is a reduced power due to the efficiency of the frequency conversion in non-linear crystals. The capital cost of excimer laser system, as well as the cost of ownership, is also high compared to lasers at longer wavelengths (as discussed in Section 6.1.3).

In both the case of frequency tripled solid state laser systems and excimer laser systems, the highest power, lowest cost per watt systems are multimode pulsed lasers with nanosecond pulse lengths. In relation to scanned mask imaging, it is worth noting that multimode lasers are better than single mode lasers in mask imaging applications. This

is because single mode lasers with a long optical coherence length when used to image an aperture or mask show strong interference fringes in the ablation causing undesired depth variation [39]. These diffraction fringes are not present when using multimode lasers due to their short optical coherence length.

2.6.2 Ablation mechanisms in pulsed nanosecond UV laser ablation

Nanosecond pulsed laser ablation can be analysed using thermal, mechanical, photophysical, photochemical and defect models. However, consideration of a single ablation mechanism severely restricts the experimental parameter space over which the model is applicable. A brief description of the relevant ablation mechanisms is given below [39]:

Thermal ablation: incident radiation causes a temperature rise which can cause direct material vaporisation or induce stresses within a substrate which can lead to explosion type ablation or in the case of thin films on a thick substrate, detachment of the film.

Photochemical ablation: if the photon energy of the incident radiation exceeds the bond energy of bonds within the substrate, molecules or fragments of the substrate can desorb from the substrate surface. The breaking of bonds within a substrate can also lead to the build-up of stresses causing mechanical photochemical ablation. These processes need not affect the substrate temperature.

Photophysical ablation: processes resulting from a combination of thermal and photochemical affects, such as enhanced desorption of photochemically broken bonds through a rise in surface temperature.

2.6.3 Ablation mechanism of polymers

The exact ablation mechanism of polymers such as polyimide is still under debate, and depends on the polymer [61]; however they undoubtedly have a larger photochemical contribution than metals. When fluences reach values >10 J/cm2, photochemical models alone can no longer accurately predict the shape and depth of the craters formed during laser ablation so thermal affects should also be considered [62]. The SEM micrographs in Figure 2.20 show the increased thermal effects seen at higher fluences.

The field is relatively young with UV solid state lasers only being commercially available fairly recently, but even the earliest studies on the ablation of polymers at 355nm concluded that thermal effects cannot be ignored [63]. The paper also reports the significance of an absorption coefficient an order of magnitude smaller at 355nm

compared to 248nm, which leads to a larger optical penetration depth and more severe thermal effects, but can also improve the ablation rate.

Ablation of polymers at 355nm depends on a vast parameter space, and hence is complicated to model. Some of the parameters which can affect the ablation include spot size, beam energy profile, pulse length, power distribution of the pulse as a function of time, pulse energy, fluence, repetition rate and shots per area determined by the repetition rate and the beam deflection speed [64]. Material properties also come into play, as well as the proximity of neighbouring features. Balogh et al. report that even with a constant set of controllable parameters, differences in ablation quality are observed depending on the underlying conductive pattern in multilayer boards [65].

Yung et al. report a strong dependence of ablation rate and the composition of Heat Affected Zones (HAZ) on the repetition rate of solid state lasers when ablating Upilex, a proprietary polyimide formula [66]. They report that the ablation rate of Upilex can be increased at higher laser repetition rates due to the accumulation of heat at the substrate.

Gordon et al. attempt to take into account the cumulative build-up of heat after consecutive shots in a given area which occurs with the high repetition rates typical of frequency tripled Nd:YAG lasers [64]. They provide experimental evidence for an increase in ablation rate when raising the substrate temperature before ablation. They introduce a temperature dependent ablation threshold and use a finite elements model to simulate the residual heat dissipation after a laser pulse through 3 modes: conduction, radiation and transfer. They simulate the surface temperature of the polyimide as a function of time and report a 100 °C difference in temperature at a time of 0.02 ms and 1 ms after the laser pulse, which is the time between consecutive shots for repetition rates of 50 kHz and 1 kHz respectively.

They use this analysis to qualitatively explain the difference they observe in ablation rates at 1 kHz and 50 kHz. Quantitative predictions were not possible since the homogenous heating of a sample before laser ablation to a maximum temperature of 186°C cannot be extrapolated to the inhomogeneous, highly localised heating of the substrate by the laser spot to temperatures of the order of thousands of degrees.

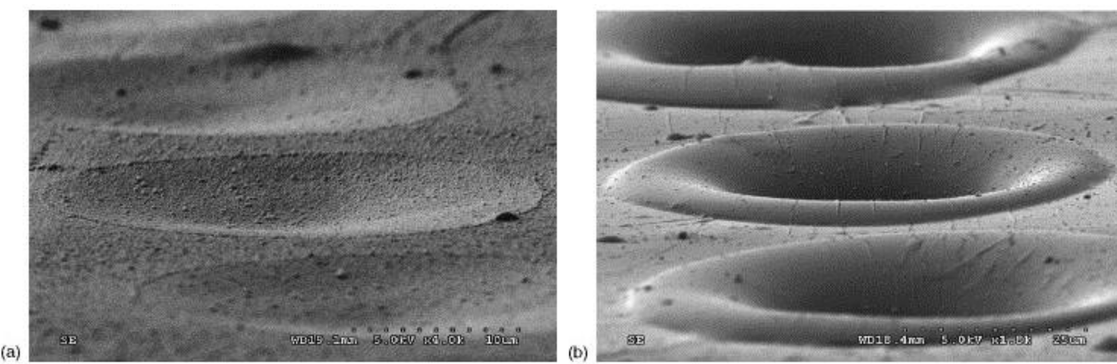

Figure 2.20 Laser ablation of polyimide at (a) a laser fluence of 0.28J/cm^2 (b) a laser fluence of 13.56J/cm^2 [62].

Gordon et al.'s model does not consider many factors such as plume shielding [67, 68], energy transfer by acoustic waves formed in explosion like processes, the effect of scanning the beam across the substrate and more complex heat transfer mechanisms; however it does highlight the importance of the heating of the substrate during 355nm Nd:YAG laser processing. The paper neglects to mention the impact of repetition rate on the HAZ or crater shape, for example re-solidification height, but it is clear that a higher repetition rate would further raise the surface temperature of the polymer and not only increase the ablation rate but possibly cause thermal degradation to areas surrounding the ablation.

Sinkovics in collaboration with Gordon et al. then elaborated on this phenomenological model to include change in morphology of the ablated region after each consecutive pulse, and was able to model the heat dissipation of an ablated region over time [69]. By modelling the temperature increase of one shot, a threshold temperature is used to determine which material is ablated. Knowledge of the ablated volume allows calculation of the new surface topography from which the new thermal simulation based on convection, conduction and radiation is run for the period of time preceding the next laser pulse. The process is then cycled to model a number of laser pulses. The model was successfully corroborated with experimental results by comparison of the depth and shape of ablated vias. An insightful addition to the model would be a material dependent threshold temperature defining the heat affected zone, such that substrate temperatures exceeding this value but below the ablation threshold temperature value could be highlighted as a heat affected zone. This would allow the model to predict the extent of thermal damage around ablated regions as a function of repetition rate, fluence and a number of other easily changeable processing parameters.

Although the low fluence ablation in Figure 2.20(a) is clearly a less thermal process, it would need considerably more shots than the ablation shown in Figure 2.20(b) to reach a given target depth. It is unclear whether the build-up of heat after many consecutive shots at short time intervals would compare favourably to the large thermal effects generated from a relatively small number of high fluence pulses. In terms of implementing the scanned mask imaging concept to reach feature resolutions down to 2μm, the literature is clear in so much as localised heating of the substrate will occur if a high repetition rate 355nm solid state laser fires consecutive shots in a given region of the substrate. The optimum laser parameters to minimise thermal damage in a scanned mask imaging system require investigation and novel mask scanning regimes may have to be employed to increase the time between consecutive shots on a given area of the substrate.

2.6.4 Ablation of metal films

In metals, because the thermal relaxation time of the electrons is short in comparison with a nanosecond pulse length, the predominant ablation mechanism is evaporation from the metal surface and the laser can be considered a heat source [70]. Nanosecond metal ablation usually results in the formation of a burr around the ablated region. This typically has the morphology of recast molten metal. The thermal properties of a thin metal film substrate can also significantly impact on the size of the burr or heat affected zones [62]. With very thin metal films, <1 μm in thickness, the film removal is a single shot process and the threshold fluence, crater diameter and the size of burrs or heat defects become strongly dependent on the film thickness [70].

2.7 Plume shielding

Plasma plume generation and its modelling is a non-trivial research area whose proper treatment is beyond the scope of this review. Plume shielding can, however, impact on ablation rate as a function of fluence and spot size, so is discussed briefly below. It is examined in greater depth in [67]. In the nanosecond pulse length regime, the vapour or plasma plume formed by the material ejected by the incident pulse can shield or screen the substrate from the latter parts of the pulse. For fluences much higher than the ablation threshold, the shielding can be so severe as to remove any further dependence of ablation rate on the fluence [39].

Plume shielding also determines the extent to which the spot size influences the ablation rate. Eyett et al. reported an increase in ablation rate at smaller spot sizes of the same

fluence [71]. The spot size determines the diameter of the ejected crater, changing the volume of material ablated and the expansion of the plume and thus affects the degree of attenuation by the plume. The ablation rate was found to decrease with increasing spot size up to a certain value after which the ablation rate no longer had a measurable dependence on the spot size.

2.8 Impact of pulse length

The pulse length of the laser significantly impacts on the ablation quality and the extent of the heat affected zone. Light impingent on a surface interacts with electrons in the material on a length scale dependent on the materials absorption or optical penetration depth [72]. The transfer of energy from the electrons to the lattice causing a macroscopic temperature rise in the substrate is characterised by the electron-lattice relaxation time, which is typically between 0.5-50ps and is strongly material dependent [73]. The heating of the substrate occurs over several electron-lattice relaxation times, such that if the pulse length is short compared to the electron-lattice relaxation time, very little heat is transferred to the substrate. A comprehensive review of electron-phonon interactions in relation to laser ablation is given in [74]. Ultrashort pulses can also reduce the optical penetration depth through non-linear absorption mechanisms, also minimising the heat affected zone. Heat transfer might still occur as a result of the ejection of molten debris, which might remain molten on the order of 10ns, however the heat affected zone is normally limited to less than a micron for pulses much shorter than the electron lattice relaxation time.

Metals tend to have a shorter electron-lattice relaxation time, on the order of 100 fs, and as a result ablation models of metals in the nanosecond regime are predominantly thermal and the nanosecond laser pulse can be modelled as a heat source in a conductive, convective and radiative heat model [70].

There are many reports on reduced HAZ through use of ultrashort pulse length lasers, for example Le Harzic et al. found the HAZ was reduced from 40μm to less than 2μm when processing aluminium thin films with a femtosecond laser rather than a nanosecond laser [75]. However despite the obvious benefits of shorter pulse lengths, nanosecond lasers are a more mature technology and their reliability, as well as their lower cost per watt, makes them more appealing to industry. Scanned mask imaging requires pulse energies in the millijoule regime to allow a reasonable area of the mask to be illuminated with the desired fluence. Millijoule femtosecond lasers are now

available, however their cost per watt of laser power is of the order of $30k/W, a factor of ~15 higher than a multimode, UV nanosecond system. In designing and implementing a scanned mask imaging system, shorter pulse lengths would restrict the average power of the laser system, reducing the throughput. They may reduce the size of HAZ, however the mask might also be more susceptible to damage at the high peak powers associated with ultra-short pulse length lasers. The choice of laser in such a system would ultimately depend on the material to be processed and the minimum feature size required, with preference for nanosecond, multimode lasers due to a lower cost per watt and shorter optical coherence lengths.

2.9 Absorption enhancement

The absorption of polymers in the UV tends to be high and, as mentioned previously, a smaller optical penetration depth reduces the extent of thermal damage by restricting the volume of material in which the laser pulse is absorbed. It is not possible to machine materials with a low absorption at the laser wavelength to a high resolution using laser pulse lengths in the nanosecond regime because thermal processes begin to dominate. This is not the case in the picosecond or femtosecond regime as the absorption is intensity dependent, not wavelength dependent. Should a material have a low intrinsic absorption, however, it is possible to increase the absorption through the addition of a suitable dopant to achieve results comparable to undoped samples at a wavelength with high intrinsic absorption. The ablation of polymethyl-methacrylate (PMMA) is not normally possible at the 308 nm and 351 nm excimer wavelengths. Bolle et al., however, report the high resolution ablation of PMMA at 308 nm and 351 nm enabled through the addition of a diphenyl triazene dopant [76]. The result is comparable in quality to excimer laser ablation of pure PMMA at 248 nm, a wavelength at which PMMA has strong absorption. The absorption spectrum of pure PMMA and the doped PMMA is shown in Figure 2.21 [76]. The ablation rate was increased by a factor of 10 in the doped substrate at 351 nm compared to the pure PMMA substrate at 248 nm on account of the lower absorption and longer optical penetration depth of the 351 nm laser material interaction.

Studies have also shown that the ablation quality can be improved to the point where thermal damage is no longer observable by the addition of a suitable dopant. Ihlemann et al. demonstrated improvement in the ablation quality of polystyrene by a XeCl 308nm excimer laser by doping it with 2% diphenyl-triazene, which can be seen in Figure 2.22 [77].

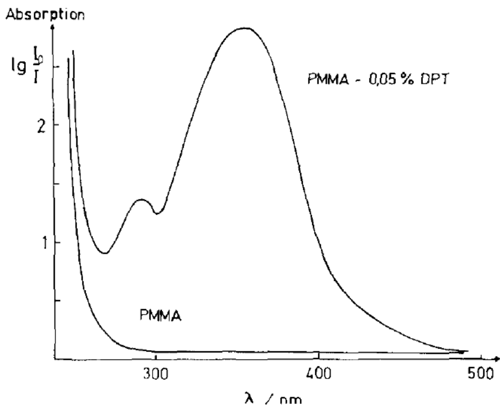

Figure 2.21 Absorption spectrum of PMMA and PMMA doped with 0.05% diphenyl triazene between 250 nm and 500 nm. There is very little absorption in the PMMA at 308 nm and 351 nm. The absorption of the doped PMMA can be tuned to optimise the ablation rate by changing the concentration of the dopant – from [76].

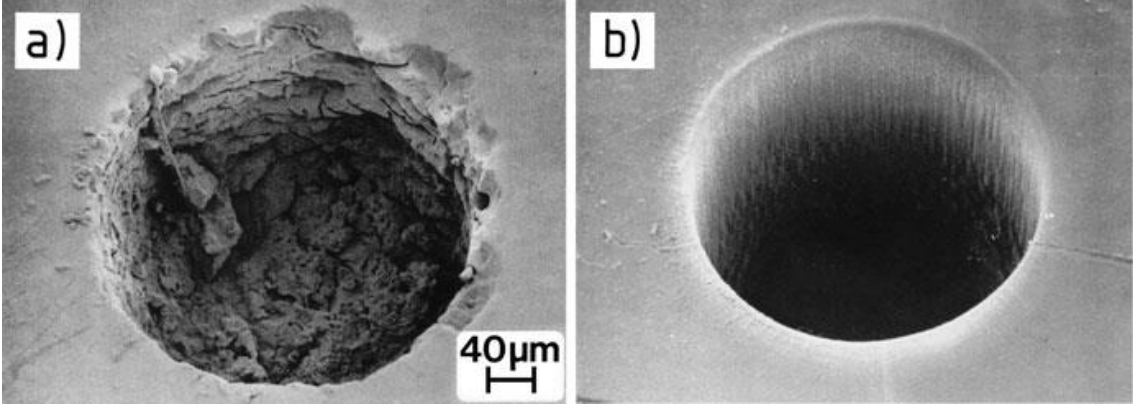

Figure 2.22 (a) SEM micrograph of hole machined in polystyrene with a 308 nm XeCl excimer laser; (b) SEM micrograph of hole machined with the same laser parameters in polystyrene doped with 2% diphenyl-triazene - from [77].

Urech et al. also report on the superior ablation quality of triazene polymers, noting that they have a higher ablation rate, a lower threshold fluence and do not deposit debris on the substrate in comparison with Kapton, a commercially available polyimide [61]. Additionally, the absorption maximum of triazene polymers can be tuned between 290nm and 360nm through the modification of a chemical group in the polymer chain, and exhibits a linear absorption coefficient greater than 10^5 cm^{-1}. They also demonstrate a sharper ablation structure in the triazene polymers compared to Kapton.

If altering the composition of a material is not possible and it has very poor absorption, one can also apply an absorber to the surface of the material to be machined. Ihlemann demonstrated the ablation of fused silica by first coating it in silicon monoxide (SiO),

and showed that by changing the fluence of the incident beam the machined depth could be controlled [78]. After machining, the SiO was removed from the fused silica substrate by irradiating the sample with a lower fluence above the ablation threshold of the SiO, but below the threshold fluence required to machine the fused silica.

For a high volume manufacturing tool, if a sample should show poor absorption or ablation quality, steps should be taken to improve substrate absorption before resorting to shorter pulse lengths. Ultrashort pulse length lasers would have a higher cost for a lower power and therefore a lower throughput.

2.10 Summary

The microelectronics industry is demanding, requiring manufacturing technologies that are capable of producing smaller feature sizes with high yields and high throughputs at reduced costs. The relentless progress in the IC industry has led to the requirement for new technologies that are able to produce high performance IC substrates and interposers that do not restrict or influence the IC design. The boom in handheld and portable devices also means that space is at a premium, and thin film technology is seen as a bridging technology to allow the continued reduction in IC feature size whilst requiring less physical space within the device.

LDI tools and other, new, digital manufacturing technologies such as laser direct write, inkjet and dynamic mask imaging do not have the required resolution for next generation IC substrates. Mask projection tools can reach the required resolution, however price has so far been a barrier to adoption in the cost sensitive IC substrate market. This thesis develops a step and repeat mask imaging system with a frequency tripled solid state laser wherein the mask pattern is ablated onto the substrate. Such an imaging system could achieve high throughput and feature sizes down to around 2 μm in a dry manufacturing process, with the cost benefits of solid state laser technology.

Chapter 3: Scanned Mask Imaging: Proof-of-Concept

The economic motivation behind developing a solid state laser mask imaging system seems clear, since it would allow the laser ablation of high resolution structures at a lower cost compared to excimer laser systems. To demonstrate the feasibility of the idea, a test rig was set up to investigate the optical performance of a scanned mask imaging system. The goal of the initial tests was to determine if it was feasible to image a mask by raster scanning the mask with a galvanometer scan head, with minimal cost, to justify further investment on a more bespoke system. To this end, the first set of experiments was conducted primarily using parts already available in the lab.

3.1 Preliminary trials with an f103 mm f-theta lens

3.1.1 Experimental set up

The first imaging lens used was a Jenoptik f-theta lens with an NA= 0.05 and an effective focal length of 103 mm. The lens is designed to be used with the object at infinity, and has an approximately flat field in its focal plane. Working outside this plane, however, in a finite conjugate imaging system, there is some measurable field curvature and distortion. The laser used was 20 W average power, multimode, diode pumped, frequency tripled Nd:YAG laser (Lee Laser LDP-100MQU). The laser beam was passed through a galvanometer scanner, which scans the beam across a chrome-on-quartz mask. The field lens directly above the mask images the point between the two scanner mirrors to the entrance pupil of the f-theta lens, bringing the beam deviated by the scanner back into the entrance pupil of the projection lens. The mask image is then projected onto the substrate by the f-theta lens, as shown in Figure 3.1.

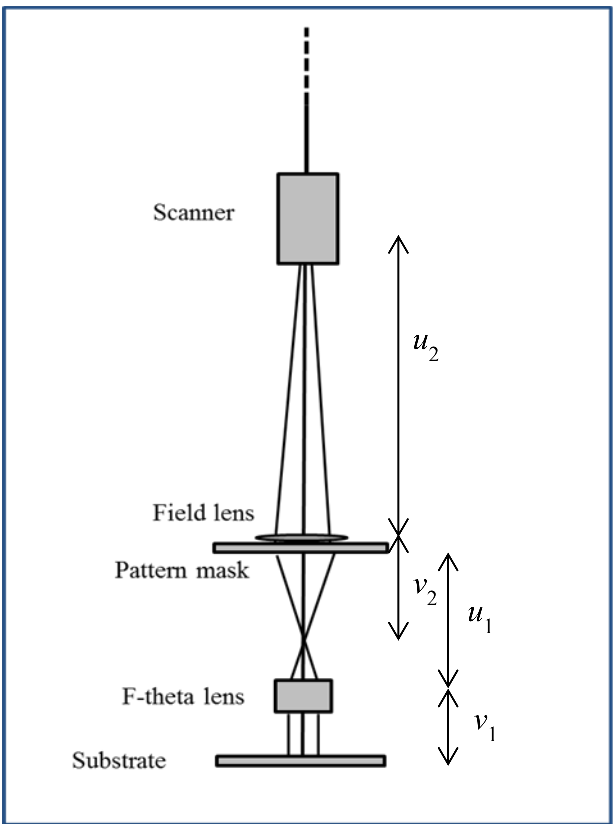

Figure 3.1 Schematic diagram of the SMI pilot test platform.

In designing the system, the separations of the components are defined by two imaging systems. Working from the substrate up, Equation (3.1), the thin lens equation, was used to calculate the approximate separation between the substrate, f-theta lens and chrome on quartz mask in the first imaging system.

$$\frac{1}{f} = \frac{1}{u} + \frac{1}{v} \tag{3.1}$$

where f is the focal of the imaging lens, u signifies the separation between the lens and object, and v is the separation between the lens and the image plane. This fixes the distance between the substrate and the mask, after which various optical arrangements were examined using different focal length, off-the-shelf, field lenses for the second imaging system. The field lenses used were 75 mm diameter to allow the scanning of a reasonable area on the mask. The choice in focal length of the field lens was restricted by the space available on the system, defining the maximum track length from substrate to scanner, and the maximum angular speed of the scanner mirrors which defined the minimum separation between the mask and scanner required to obtain a given scan speed at the mask. The graph in Figure 3.2 plots the required angular speed of the

mirrors to achieve a mark speed of 5 m s^{-1} in the mask plane against the distance between the scanner and the mask. The two red dots represent the position of the scanner required to correctly image the point between the two scanner mirrors to the entrance pupil of the f-theta lens for an f = 150 mm and an f = 200 mm field lens. The solid line represents the angular mark speed of the scanner used as calculated from the scanner data sheet. It is clear from the graph that regardless of other considerations, using the f = 200 mm field lens allows you to attain higher scan speeds at the mask and so was used for the preliminary set of tests.

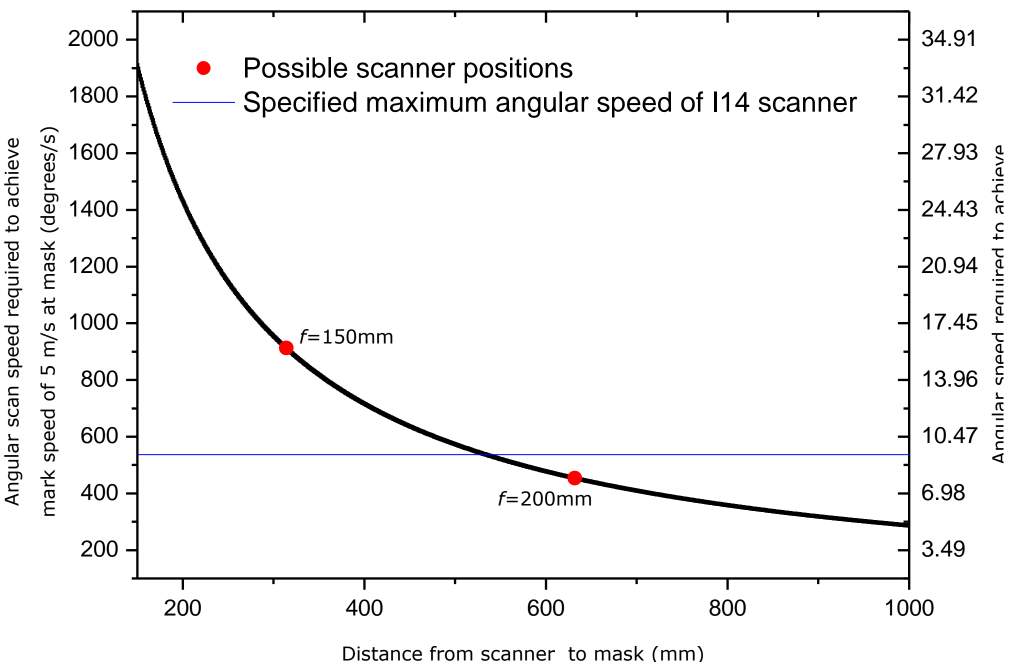

Figure 3.2 Graph plotting the required angular speed of the scanner mirrors to scan a mask at 5 m/s against the separation between the scanner and the mask.

The beam was expanded prior to the scanner using a Keplerian telescope such that the fluence of the collimated beam at the mask was below the damage threshold of the mask. The damage threshold of chrome-on-quartz masks is reported to be 100 mJ cm^{-2} at 248 nm generated by an excimer laser source [43], so the fluence at the mask was kept below this value. It was acknowledged that the damage threshold could in fact be much lower than with the excimer laser due to the higher repetition rate of the laser which could lead to higher intensities and thermal damage of the mask, as well as the higher peak fluence on account of the approximately Gaussian spatial beam profile. However, before damage tests could be conducted, this was the value used for the initial

set up of the system. The magnification of the imaging system was chosen such that the fluence of the beam at the work piece would be above the ablation threshold of the substrate. Due to the regular use of polyimide based materials within the industry, which have an ablation threshold of ~0.1 J cm^{-2} and a high ablation rate above ~0.5 J cm^{-2} at 355 nm [63], this was set as the target fluence.

Prior to any ablation the beam profile was measured below the f = 200 mm field lens using a CCD beam profiler approximately in the plane of the mask. Plots of the beam profile can be seen in Figure 3.3. The manufacturer specified the multimode laser has an M^2 value of 11, however it can be seen that the sum of the transverse electric modes in the beam have a Gaussian profile. The horizontal and vertical beam profiles are essentially the same, meaning the beam has good rotational symmetry. From a fit of the data, the $1/e^2$ beam diameter was determined to be 3.30 ± 0.05 mm. Measuring the average power in this plane with a Nova II Ophir thermopile power detector, the maximum pulse energy at 5 kHz was determined to be 2.12 ± 0.04 mJ, and hence the average fluence 51 ± 1 mJ cm^{-2}. Thus the peak fluence at the centre of the Gaussian beam is 102 ± 3 mJ cm^{-2}, with the possibility to reduce the fluence either by reducing the current to the laser diode pumping the gain medium of the laser, or by increasing the frequency, both of which decrease the pulse energy.

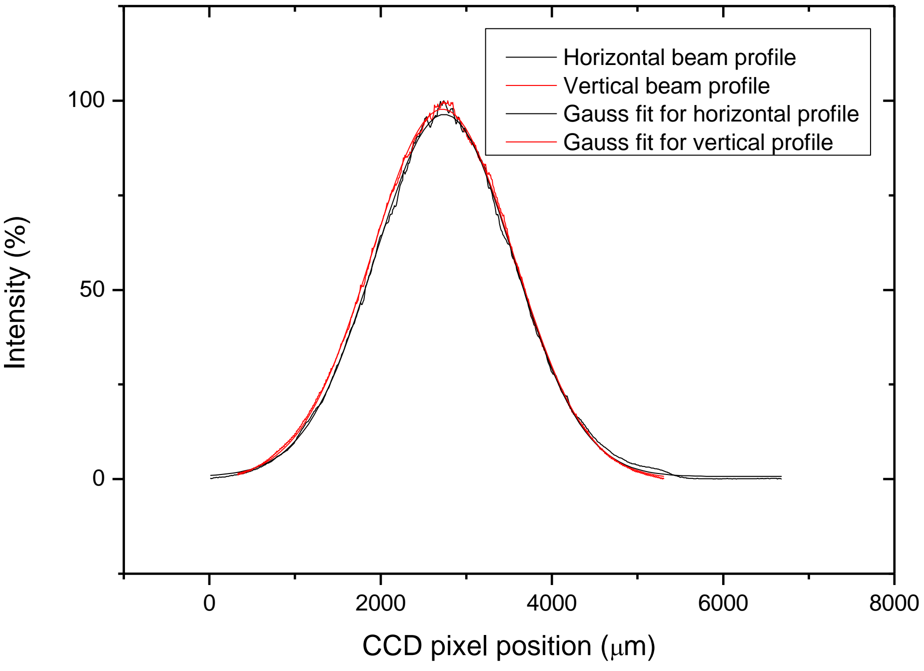

Figure 3.3 Plot of the normalized beam intensity against the profiler CCD pixel position where the horizontal and vertical beam profiles have been overlaid and fitted with a Gaussian function.

3.1.2 Preliminary imaging results

In the initial tests, the 12 mm × 12 mm resolution mask in Figure 3.5 (a) was used to investigate the resolution of the imaging system. The optical components were mounted to a rail fixed vertically above a vacuum chuck on x-y stages. Despite the simplistic optomechanics, efforts were made to ensure the separations and angles of the key components in the imaging system were adjustable, which included mounting the f-theta lens on a micrometer stage to enable fine tuning of the focus of the system. An image of the lab set up can be seen in Figure 3.4.

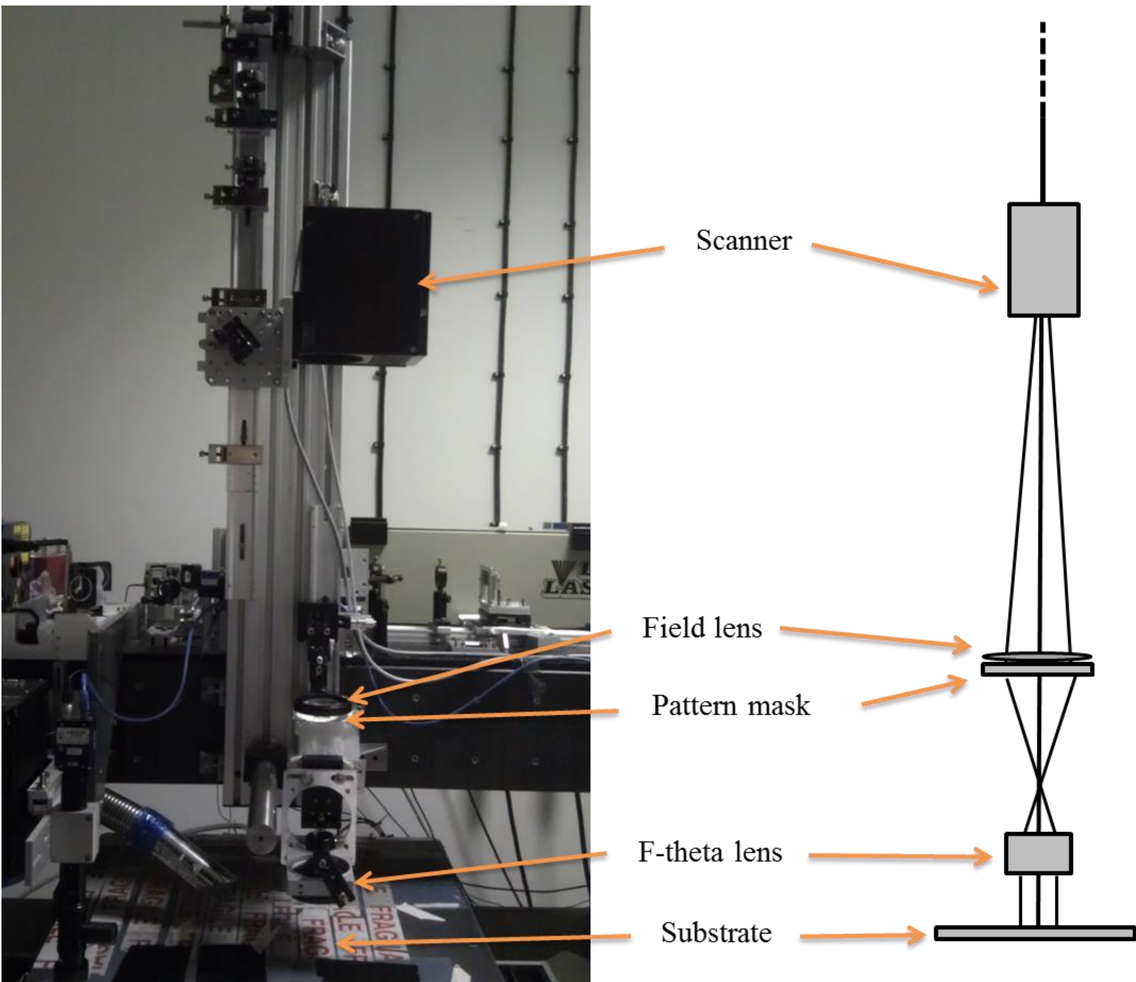

Figure 3.4 The initial lab set up used to demonstrate proof of concept for the SMI process.

The focus of the system was found by scanning the mask then adjusting the f-theta lens height on the micrometer and stepping in x-y with the substrate stage to ablate a series of mask images adjacent to each other each with different f-theta lens positions. The ablation would then be examined using an optical microscope to determine at which lens position the mask image was best in focus and this was repeated with finer increments in the lens position until best focus had been achieved. The demagnification

of the imaging system was empirically determined by comparing the known feature sizes on the chrome-on-quartz and the feature sizes measured using the optical microscope in the ablation. The demagnification was determined to be ~2.5 such that the traces in Figure 3.5 (b) are ~4µm wide. The Rayleigh criterion for the minimum distance between two resolvable points, R, in an image is given by [4]:

$$R = \frac{0.61\lambda}{\mathrm{NA}} \tag{3.2}$$

where λ is the wavelength and NA is the numerical aperture. The imaging system was observed to be operating close to the Rayleigh resolution limit, 4.3µm, at least over a small image field.

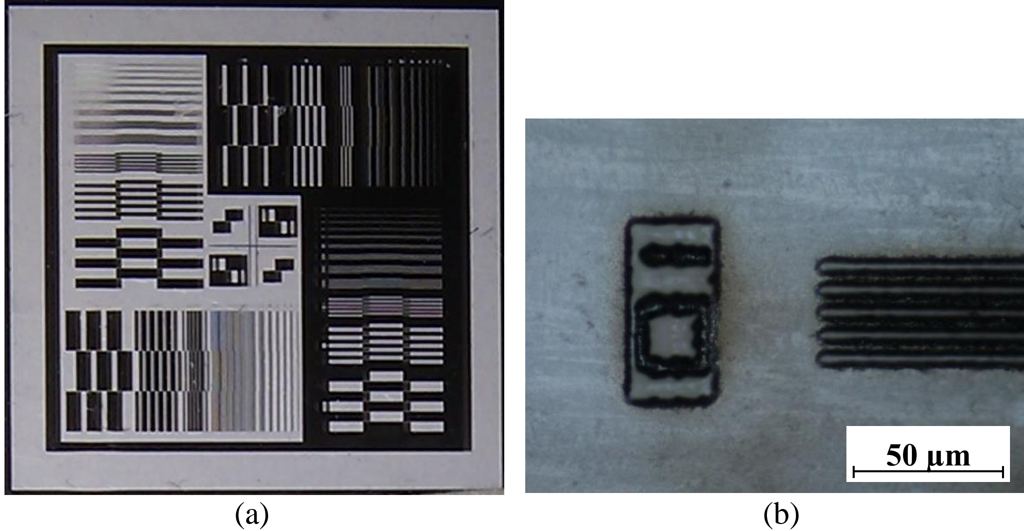

(a) (b)

Figure 3.5 (a) Chrome on quartz resolution mask used to investigate the resolution of the 103 mm focal length f-theta lens; (b) An image taken of the mask with a magnification of ~2.5, such that the lines separated by 10 µm at the mask plane are separated by ~4 µm in the image plane. The substrate is a proprietary material, some component of which is polyimide.

The telescope prior to the scanner was then changed to reduce the beam size allowing a greater range of fluences at the mask. Given that the beam had a Gaussian profile, Equation (3.3) relating the ablation crater diameter, D, the peak fluence, ϕ_0, and the ablation threshold fluence, ϕ_{th}, of a Gaussian beam can be used to calculate w_0, the 1/e^2 spot size [79].

$$D^2 = 2w_0^2 \ln\left(\frac{\phi_0}{\phi_{th}}\right) \tag{3.3}$$

The average power of the laser was measured at different frequencies, and the pulse energy calculated from the power. A series of craters were then formed by firing a single shot of the laser through an open aperture in the mask, and their diameters measured on an optical microscope. A plot of D^2 against the natural logarithm of the pulse energy can be seen in Figure 3.6, from the gradient of which the $1/e^2$ spot size was calculated to be 505 μm.

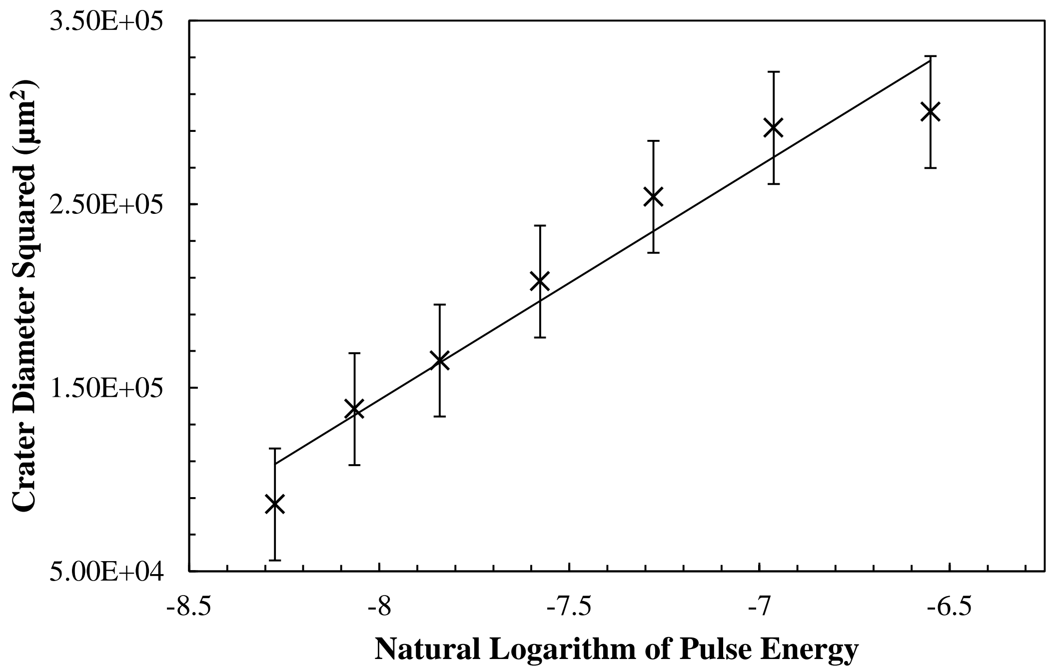

Figure 3.6 Plot of the diameter formed by a single shot of the laser squared, against the logarithm of the pulse energy of the pulse which formed it. The gradient is proportional to the square of the $1/e^2$ beam radius.

From knowledge of the gradient and intercept, the threshold fluence, ϕ_{th}, can also be calculated. The threshold fluence for ablation was determined to be 0.11 J cm^{-2} which is in line with expectations for the substrate at 355 nm [63], which had an unknown composition but was part polyimide. The pulse energy was varied by adjusting the frequency, which also changes the pulse length of the laser. The pulse length can affect the laser-material interaction through complex, non-linear mechanisms such as plume shielding and thermal diffusion and this is thought to be the cause of the non-linear variance in the data.

Varying the mark speed and the pitch of lines used to raster scan the mask, the number of shots per area delivered to the substrate can be controlled. With knowledge of the spot size, the mark speed and pitch of the lines in the vector file sent to the scanner were

adjusted, and the mask was scanned such that ~6 shots were delivered in the x direction and ~6 shots were delivered in the y direction, for a total of ~36 shots per area. Deeper trenches were ablated and their depth measured using the encoder on the z-axis of the optical microscope. By focusing on the top and bottom surfaces of the feature as shown in Figure 3.7, and reading off the value on the z-axis encoder, the depth of the features can be measured. The theoretical depth of focus of the 50x, 0.55 NA objective used on microscope is ±1 μm, which agrees well with the point at which the image from the CCD on the microscope appears to go out of focus. In this manner, the depth of the features was determined to be 8 ± 1 μm, a depth suitable for signal traces in a chip package.

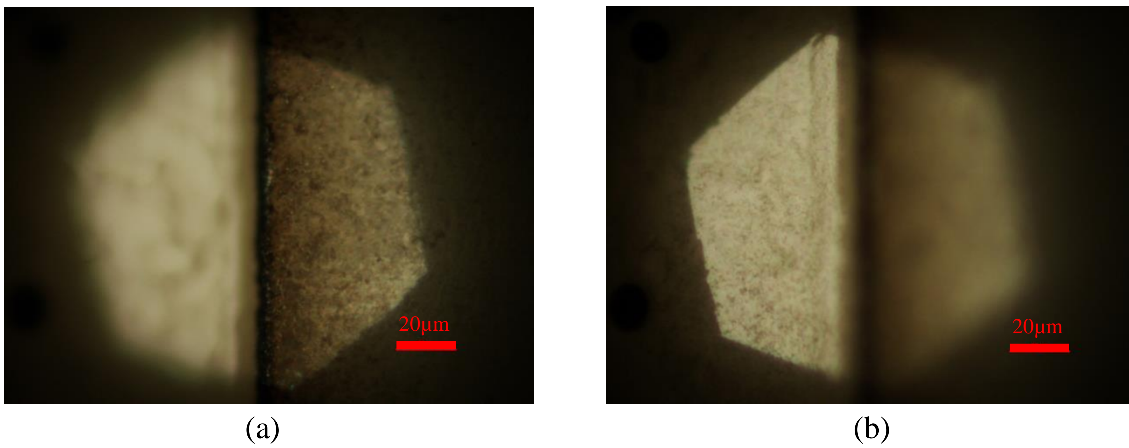

(a) (b)

Figure 3.7 Optical microscope images focused on (a) the top and (b) the bottom surfaces at the edge of an ablated feature illustrating how depth measurements were made using the z-axis encoder on the optical microscope.

3.2 Tests conducted with a higher NA f-theta lens

Having obtained good results with the proof-of-concept system described in section 3.1, including demonstration of feature sizes down to 4 μm L/S, and features 8 μm deep, this justified the acquisition of some additional parts to further demonstrate the SMI process. These included custom designed opto-mechanics, the purchase of a higher NA off-the-shelf f-theta lens and some chrome-on-quartz masks designed to characterise the lens performance.

3.2.1 Details of the new opto-mechanical set up

The custom optomechanics included lens and mask mounts with tip and tilt adjustment, as well as micrometer stages to allow precise adjustment along and perpendicular to the optical axis. One of the primary features of the new 5" mask holder was the inclusion of a linear stage to allow the overlay of the images of two different parts of the mask at the substrate. This allowed the machining of features to two different depths, which

meant with regards to chip packaging, it was now possible to laser ablate the circuitry consisting of the signal traces, landing pads and ground planes, and then overlay the image of microvias well registered to the landing pads in the circuitry layer. The circuitry is conventionally formed lithographically, with the microvias drilled in a subsequent step on a laser drilling tool. This requires large landing pads for the vias to allow for alignment tolerances between the two tools. The SMI process opens the possibility to reduce the landing pad size, giving more space per layer to redistribute the I/O signals from the IC, which can potentially lead to a reduction in the number of layers required. The new mask holder also allowed rotational alignment of the mask to the axis of the linear stage, required for accurate registration of features on different parts of the mask. Alignment of the mask to the linear stage was achieved by using a camera to image fiducials on the mask, which would then be rotated until the two fiducials were overlaid. An image of the CAD model for the upgrade to the SMI system can be seen in Figure 3.8.

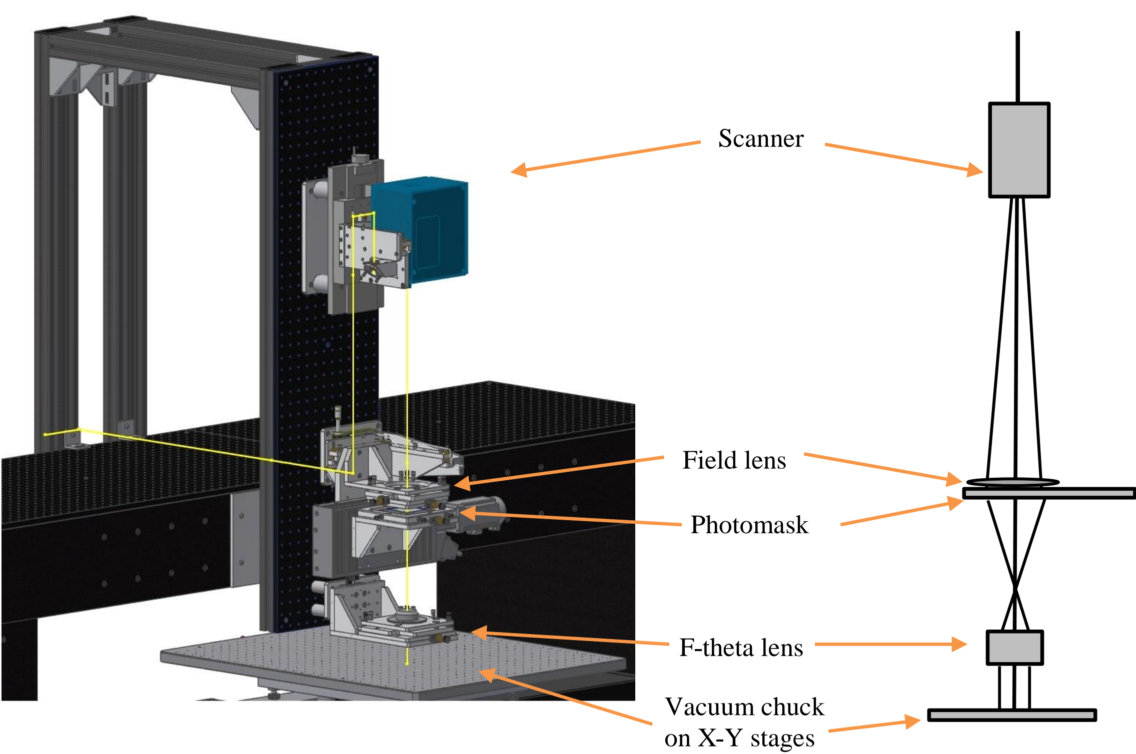

Figure 3.8 CAD model for the opto-mechanical upgrade of the SMI lab system. The upgrade included the opto-mechanical parts necessary for accurate alignment of the system, as well as the mounting of the photomask on a linear stage.

The new Jenoptik f-theta lens had an effective focal length of 53 mm and an NA of 0.08, which improves the theoretical minimum feature resolvable by the lens. The

imaging system was set up with a target magnification of 3, and once installed the magnification measured by plotting the measured feature separation at the substrate against the known feature separation at the mask. The plot is shown in Figure 3.9, and the demagnification determined to be 3.41 ± 0.03. The discrepancy between the target magnification and the measured magnification is attributed to the fact that the physical lens position had not been taken into account when using the thin lens equation. That is to say, the effective focal length of the f-theta lens used in the thin lens equations does not correspond to the back working distance of the lens, and does not correspond directly to the required position of the lens in the setup of the system.

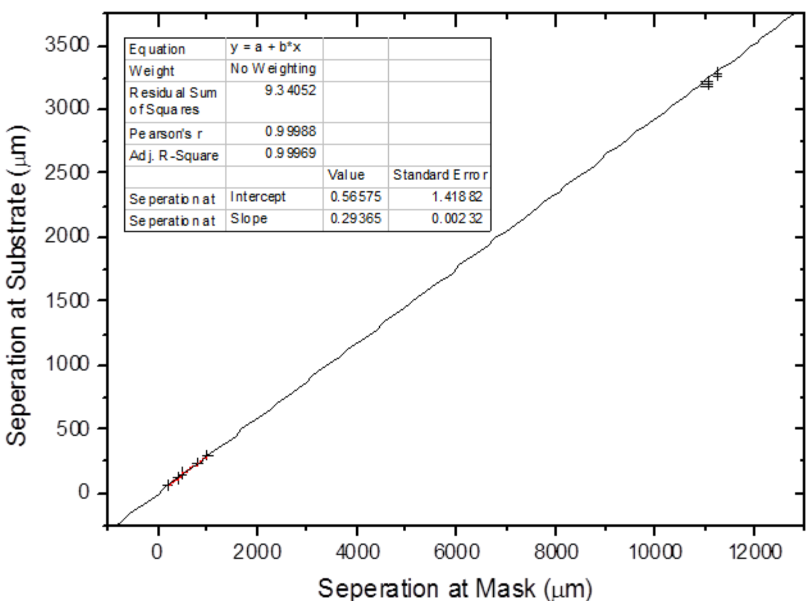

Figure 3.9 Known feature separations at the mask plotted against feature separations measured in the image plane after laser ablation such that the gradient of the fitted line is equal to the magnifcation of the imaging system. Note: the fitted line should be straight and deviations from this are an artifact of the export function in the graph plotting software.

3.2.2 Image magnification and illumination uniformity

Having set up the system and measured the magnification, the spot size at the substrate was calculated using Liu's method [79] as described in Section 3.1.2. The plot of the crater diameter squared against the natural logarithm can be seen in Figure 3.10, and from the gradient the $1/e^2$ spot diameter determined to be 575 μm and the threshold fluence 0.27 J cm^{-2}. However, when scanning the mask such that the pitch of the lines at the substrate was 575 μm giving 1 shot per area in the y-axis, it was noted that there were large gaps in the ablation between the lines. Measurements in Figure 3.11 show

the width of the spot causing uniform ablation to be 360 μm, indicating a reasonably large portion of the $1/e^2$ spot diameter is below the ablation threshold of the substrate. This does not fully explain the discrepancy between the measured spot size and the observed crater size when scanning the beam. Inserting the crater size, 360 μm, into Equation (3.3), as well as the calculated $1/e^2$ spot diameter and threshold fluence, the pulse energy used to form the black lines in Figure 3.11 can be calculated. The calculated pulse energy, ~0.8 mJ, is much lower than that calculated by taking the average power measurement at the substrate (11.9 W) and dividing it by the laser frequency (5 kHz) which gives ~2.4 mJ. Transmission of optics might account for some of this additional loss in pulse energy, however the primary reason for the discrepancy is suspected to be incorrect calibration of the first pulse suppression of the laser when collecting the data in Figure 3.10, which could account for the variance in the data. The first pulses the laser fires after the gain medium has been pumped for a time much greater than the repetition period of the laser can be significantly more energetic than the average pulse. These pulses can be supressed by sending a signal to the laser prior to the trigger signal to leak some of the energy out of the gain medium through use of the acousto-optic modulator (AOM) inside the laser cavity. It is suspected that this first pulse suppression had not been fine-tuned at the time of testing, and thus the pulse energies used to form the craters measured in Figure 3.10 were higher than those calculated by taking the average laser power and dividing by the laser repetition rate. The increased pulse energy would not change the $1/e^2$ spot diameter calculation, but would lead to an underestimation of the threshold fluence for ablation, bringing into question the previously stated value of 0.27 J cm^{-2}. However for uniform ablation depth across a sample, it is clear that the number of interest is the diameter of the spot for which the fluence is above the ablation threshold of the substrate, not the $1/e^2$ spot diameter, which in this case was 360 μm.

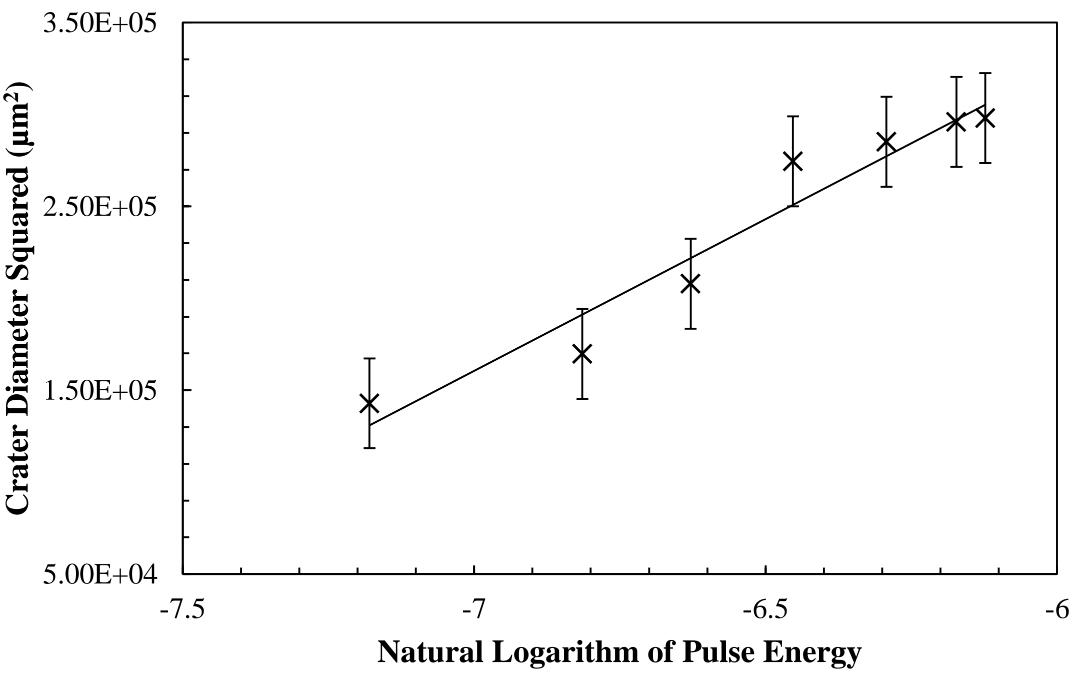

Figure 3.10 Graph plotting the natural logarithm of the pulse energy against the crater diameter squared allowing empirical measurement of spot size and threshold fluence.

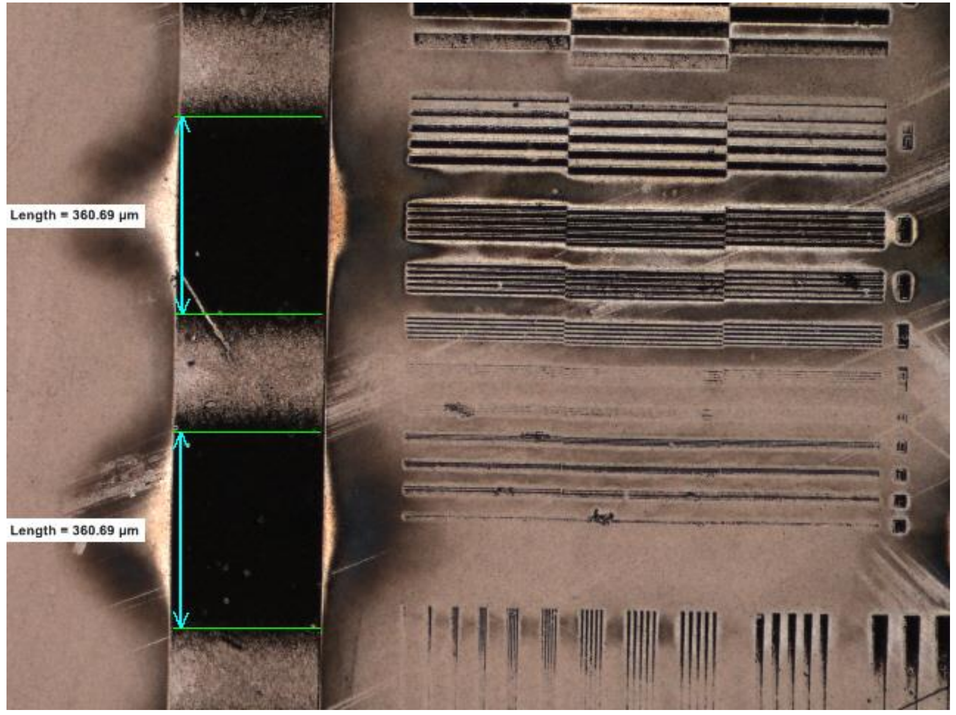

Figure 3.11 Mask scanned with lines at a pitch greater than the diameter of the region of the beam above the ablation threshold of the substrate. The width of the uniformly ablated region was measured to be 360 μm.

Having evaluated the pitch and mark speed required for uniform ablation, different mark speeds and line pitches were programmed into the software to vary the shots per area delivered at the substrate. Figure 3.12 shows the ablated depth measured using the

optical microscope as a function of number of shots. As can be seen, for a given feature this is approximately linear and the depth per shot was found to be 0.44±0.02 µm/shot. To put this into context for chip packaging, the circuitry layers typically required are 5-10 µm deep. The vias within these interconnects are ablated all the way through the thin film to the metallization beneath the film, a further 5-10 µm. The ablation rate (depth per shot) is thus approximately 10% of the target depth, giving good control of depth by varying number of shots. However this would reduce the process throughput significantly.

3.2.3 Fixing the target magnification and setting up a ray tracing model

As stated in Section 3.2.2, the magnification was measured to be 3.41 ± 0.03. To align this value with the target magnification of 3, the separations between the object, lens and image plane were recalculated, this time using the thin lens equation in conjunction with the lens data sheet to calculate where the physical position of the lens should be. In addition, a black box lens file for the f-theta lens was obtained from the supplier to simulate the performance of the elements within the lens using the ray tracing software program Zemax. A Zemax merit function allows the optimisation of certain variables in an optical system based on fixing others. A merit function was created to find the optimum separation between object, lens and image for a 3x imaging system with the f-theta lens. The separation between the bottom surface of the f-theta lens and image plane agreed with that calculated with the thin lens equation to within 150 µm, which is less than the error in separation with which the items were installed on the breadboard using a tape measure, ±2 mm.

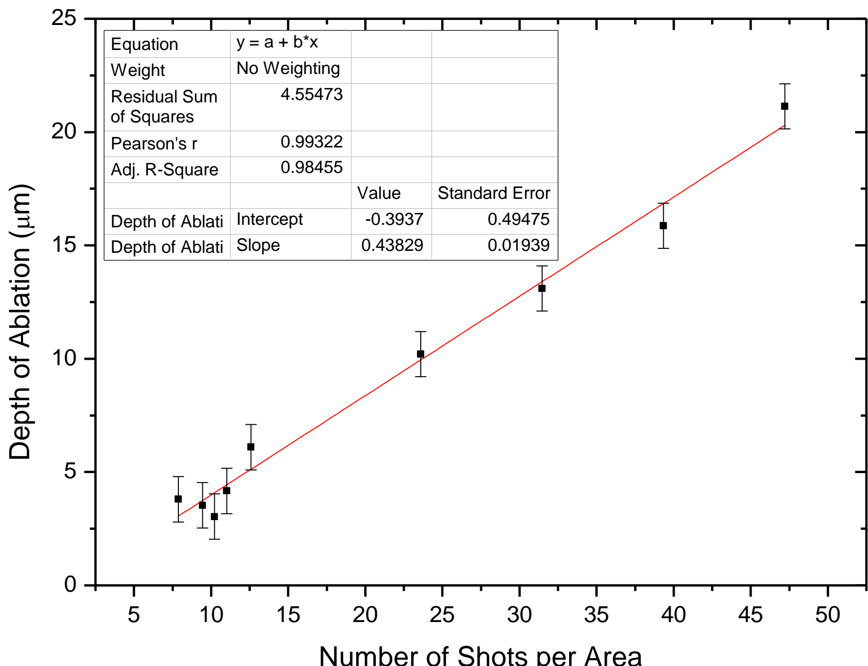

Figure 3.12 Graph of shots per area delivered, by changing the mask illumination pattern, against the ablated depth. The gradient gives the etch rate of the material, 0.44 ± 0.02 µm/shot.

Having attempted to correct the magnification, a new chrome-on-quartz mask was designed to enable accurate measurement of magnification, distortion, and other properties of the imaging system to compare with the Zemax model. Some of the features on the new mask included a grid to map the distortion as a function of position in the image field, various crosses, squares and circles separated on the mask and designed to overlay with each other on adjacent parts of the mask, and resolution features across the image field to determine the minimum feature size that could be kept in focus across one field. An image of the CAD data for the mask can be seen in Figure 3.13.

Figure 3.14 shows two overlaid images of the mask, wherein the "x" features are overlaid on the "+" features on different parts of the mask, and vias are landed within pads. In the figure, the two patterns were scanned with different parameters and it is clear that the parameters have yet to be optimized. However the figure demonstrates the assembly's capability of overlaying two mask images to the necessary degree of accuracy.

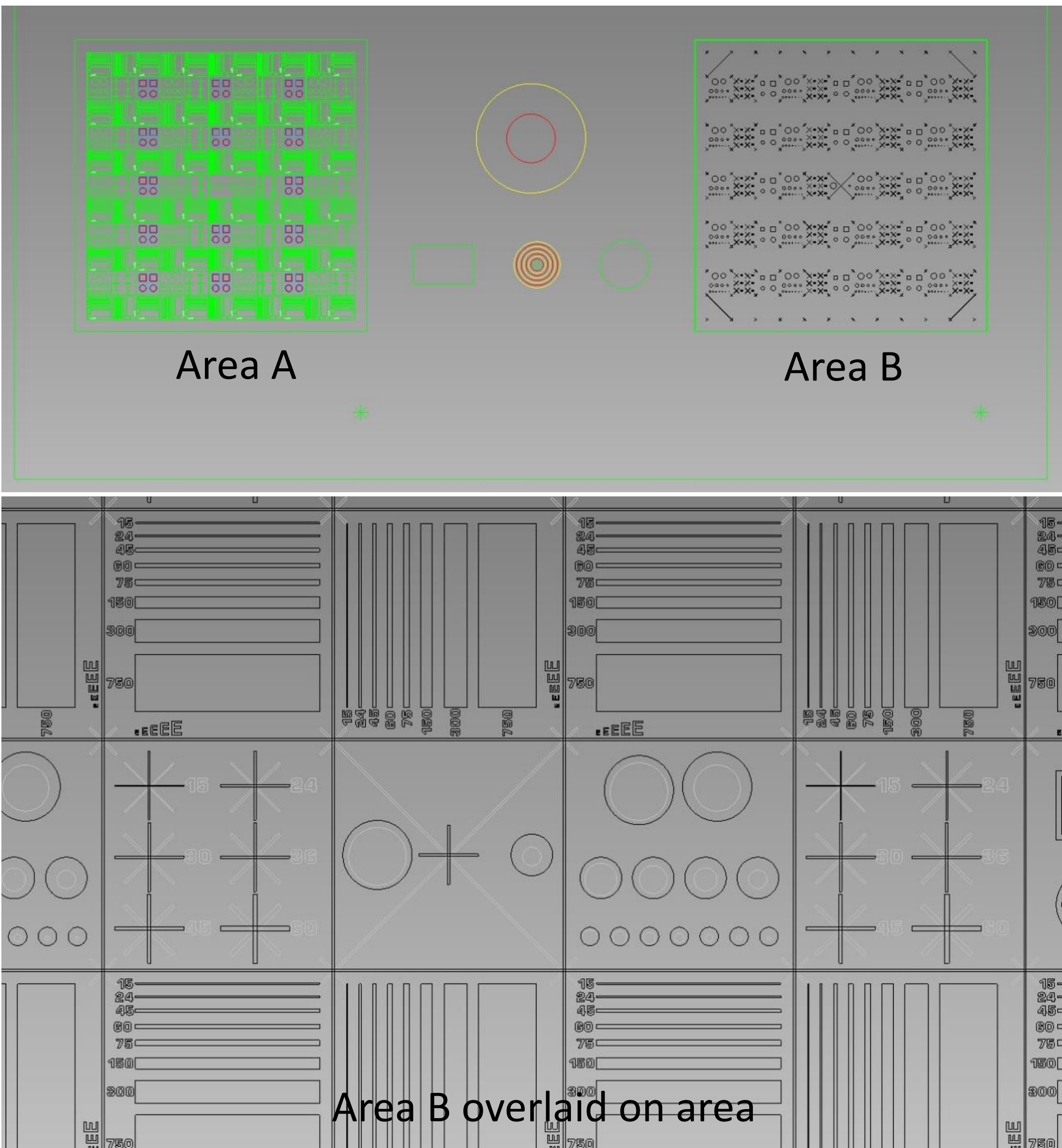

Figure 3.13 An image of the CAD data for a chrome-on-quartz mask designed to measure field curvature and distortion of a lens. The mask contains a regular grid of lines, the nodes of which can be used to measure the distortion in the image of the mask as a function of distance from the optical axis. The fine lines within the grid can be used to determine the smallest feature size which can be successfully machined across the image field of the lens. The two areas of the mask, Area A and Area B can be overlaid at the substrate by mounting the mask on a linear stage. The lower part of the figure shows the features in Area A in black, and the features in Area B in light grey. The areas have been overlaid to show how the features in each area are complimentary, and can be used to test the mask alignment to the linear stage.

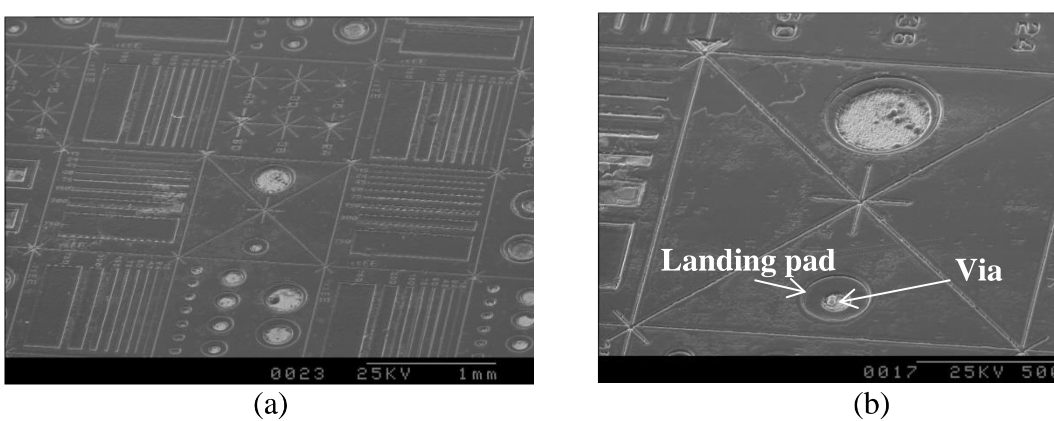

(a) (b)

Figure 3.14 (a) Overlay of two separate chrome-on-quartz mask patterns in which it can be seen that crosses "x" are aligned to the grid and pluses "+", and vias have been landed within pads; (b) a close up of a cross "x" and a plus "+", demonstrating precise overlay of the complimentary features on separate parts of the mask.

Figure 3.16 compares optical microscope photographs of identical patterns at the mask at the centre and at the edge of the lens image field. The geometric distortion and the field curvature are the two aberrations which manifest themselves most obviously in the laser ablation, and these therefore form the focus of the discussion below. Geometric distortion of the image can be seen in Figure 3.16 (b) in the shape of the square. The 17 µm line at the mask (~6 µm at the substrate) which is resolved in Figure 3.16 (a) in the centre of the field is no longer resolved at the edge of the image field, highlighted by the oval in Figure 3.16 (b). This is due to the field curvature of the imaging lens used, which is in part because the lens is designed to have a minimum field curvature when used in an infinite conjugate imaging system where the object is placed at infinity. The result was expected given the field curvature and distortion predicted by the Zemax model of the f-theta lens when used in a finite conjugate 3x imaging system. The plot in Figure 3.15 shows the field curvature and distortion as a function of radial distance from the centre of the object field predicted by the Zemax model. The field curvature plot is generated by plotting the separation of the focal planes of the tangential and sagittal ray bundles from the paraxial focal plane as a function of radial position in the object field. The distortion plot is formed by plotting the separation of the chief and a reference ray in the image plane of the system. The reference ray is generated by tracing a real ray through the optical system at a very small field height and scaling. As can be seen, not only does the lens have several hundred microns of field curvature, it also has significant astigmatism at the edge of the field owing to the difference in field curvature in the sagittal and tangential rays.

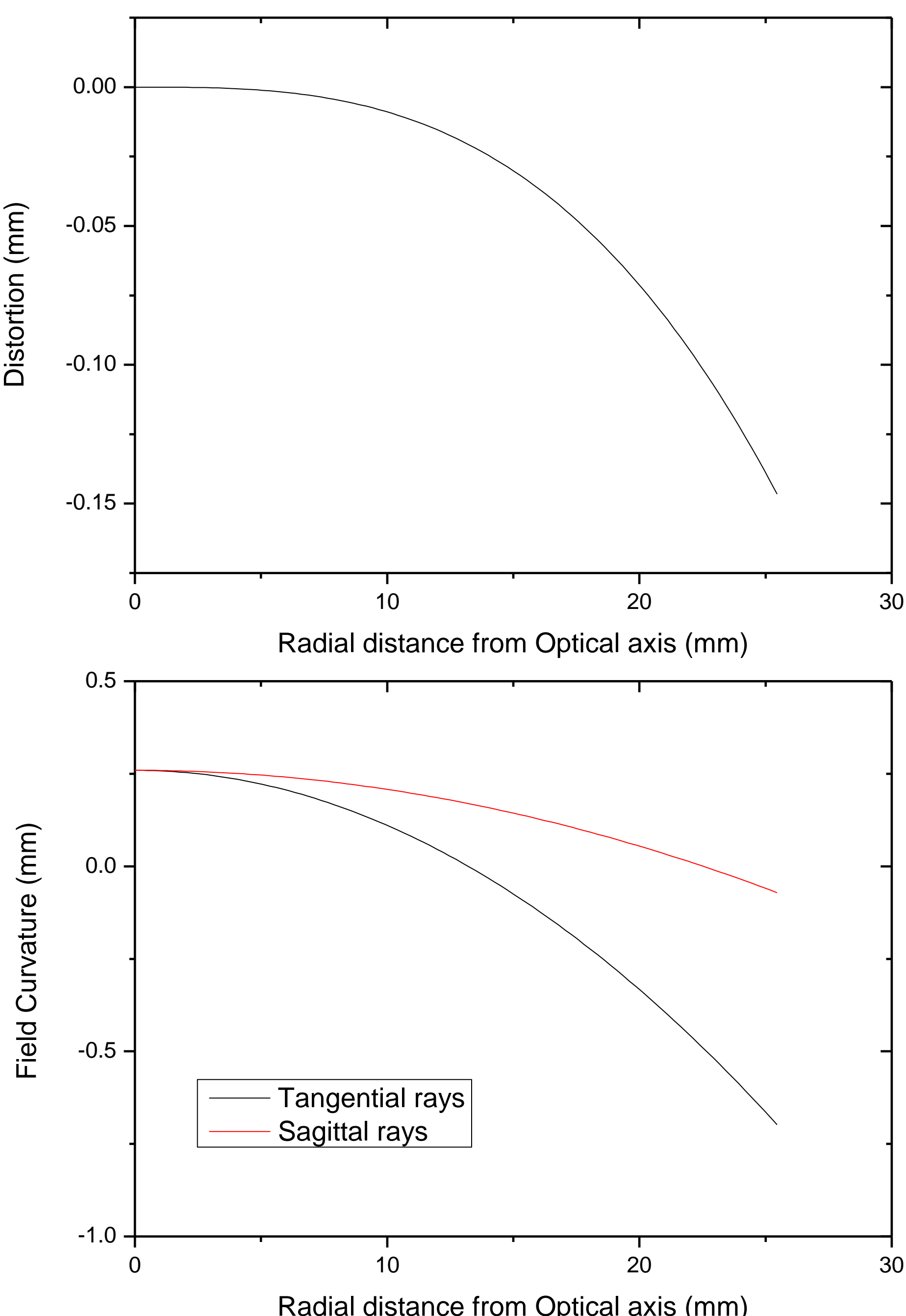

Figure 3.15 Field curvature and distortion as predicted by a Zemax model of the 53mm focal length f-theta lens as used in a 3x imaging system.

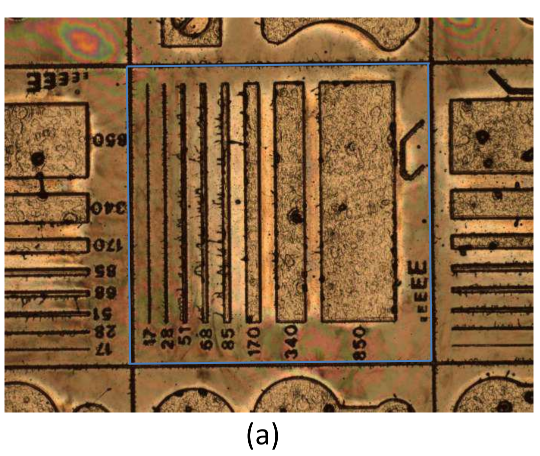

(a)

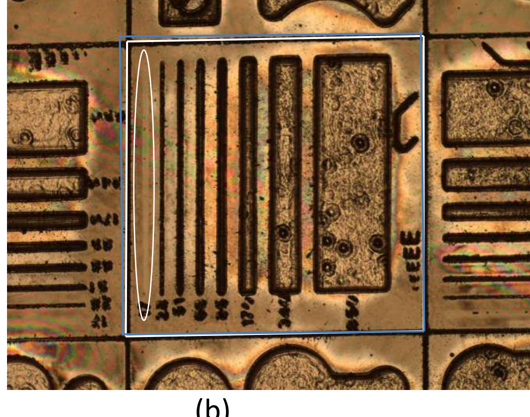

(b)

Figure 3.16 Optical microscope images which highlight the difference in lens performance at the centre (a) and at the edge (b) of the image field. The squares highlight the difference in shape of the grid due to the barrel distortion at the edge of the field. The oval highlights the 6µm feature which is no longer resolved at the edge of the field.

Figure 3.17 shows a map of the distortion obtained by using the x-y stages and a camera to collect the coordinates of the intersecting lines in the grid ablated grid. The grid has a 3 mm pitch in the object plane, and therefore approximately 1 mm pitch in the ablated image. Although fairly subtle, the predominant distortion is barrel distortion, where the magnification diminishes towards the periphery of the image. The distortion data was then plotted against the Zemax model by subtracting radial position from the centre of the image from the expected position in a perfect rectilinear imaging system with a demagnification of 3. The plot can be seen in Figure 3.18, and although the data follows the general trend predicted by Zemax, there is some discrepancy. The spread of the data can be ascribed to the lens and mask not being perfectly coaxial, and angles between the substrate, lens and mask planes. Although the resolution of the stage encoders are sub-micron, the vision system and camera magnification limit the measurement accuracy to ±5 µm.

The discrepancy between model and data can be resolved by allowing an error in the set up and magnification of the system. The y-axis of the plot is the deviation between the expected and measured position, and calculation of the expected position in an ideal, rectilinear imaging system requires knowledge of the magnification. By adjusting the rectilinear magnification to 3.0075, the model now agrees with the experimental data as shown in

Figure 3.19. This change in magnification corresponds to an error in the >300 mm track length of the imaging system of 350 µm, which is likely given that the position of the optical components were measured by hand with a tape measure.

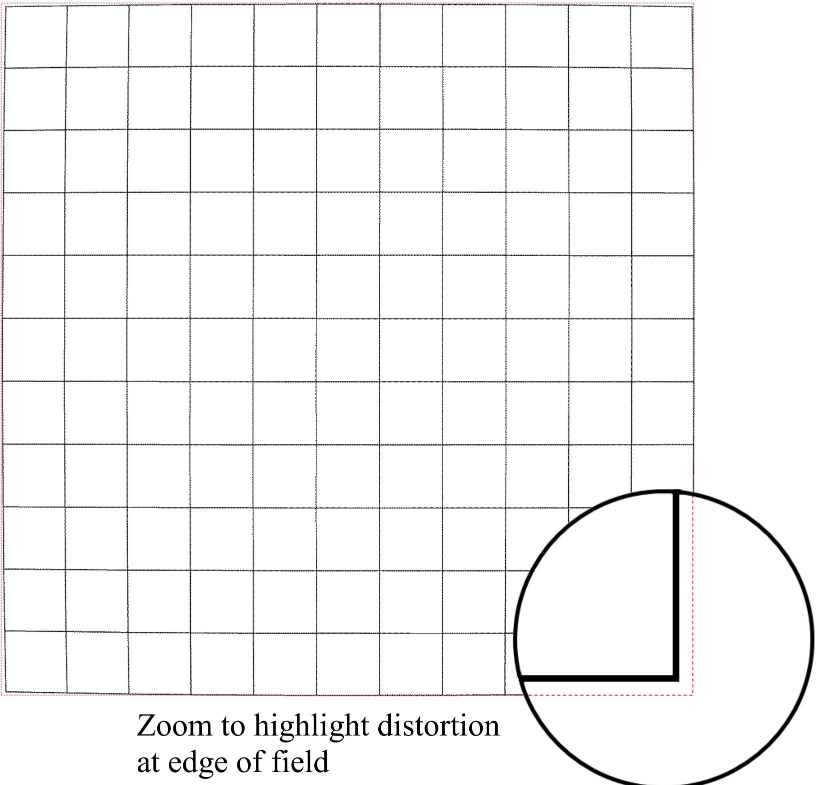

Figure 3.17 Graphic showing the barrel distortion across a 36 mm object imaged with the f53 mm f-theta lens in a finite conjugate imaging system with a demagnification of 3. The grid was plotted by ablating the 36 mm object into a substrate, and collecting the coordinates of intersecting lines using *x-y* stages and a camera. The square surrounding the grid highlights the demagnification of the image is greater at the corners where the separation from the image centre is greatest when compared with the middle of the edges.

3.2.4 Distortion correction at the object plane

Figure 3.16(b) shows that the minimum feature size attainable across the entire image field is ~8 µm. The only feasible solution to improving the field curvature of the lens was to have expensive, custom projection optics designed with a flat field and little distortion. Therefore 8 µm features were the best achievable with the initial set up. However, given the application, it was decided that if the geometric distortion in the image could be corrected, by an inverse distortion applied to the mask in the object plane, this could be sufficient to demonstrate the processes capabilities for feature sizes down to 8 µm L/S. The application requirements for a geometric distortion of less than 5 µm across the image field are due to the fact the chip package has to be bonded to the silicon chip by microbumps on the underside of the silicon. Therefore the features on the chip package need to be well registered with the features on the chip to allow redistribution of the chips I/O signals.

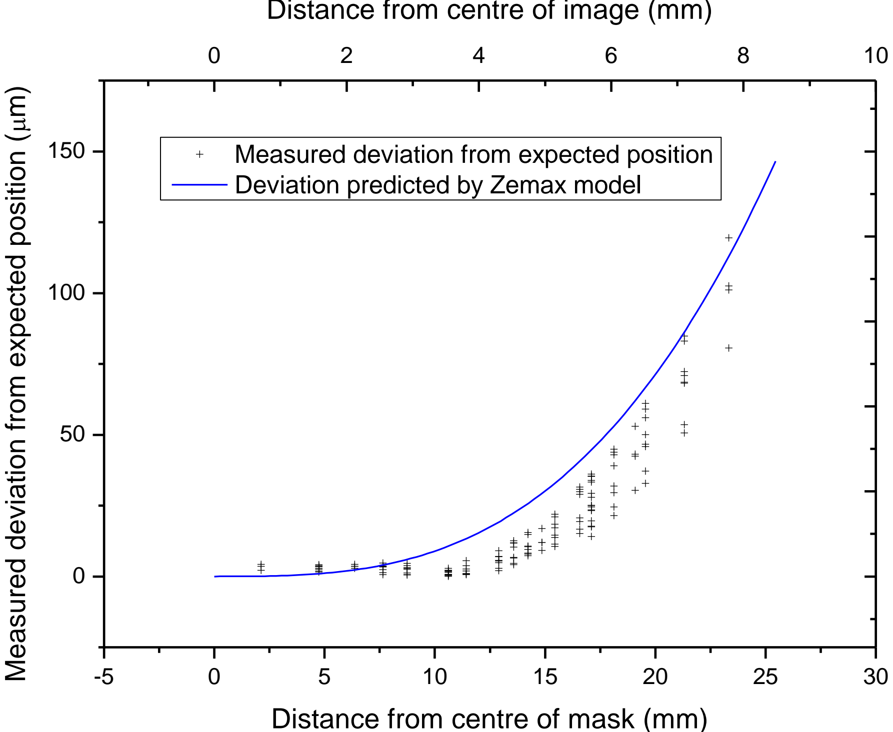

Figure 3.18 Plot showing experimentally measured deviation in the expected position of nodes in a grid for a rectilinear imaging system with a demagnification of 3. The blue line is the deviation predicted by the Zemax model for the f53 mm f-theta lens. The experimental data was collected using stage encoders with sub-micron resolution, however the vision system and camera magnification limit the measurement accuracy to ±5 µm.

Therefore, an attempt was made to fix the positional errors of the features occurring due to the geometric distortion of the lens by altering their position on the mask. From the grid in Figure 3.17 distortion data was entered into an open source program designed to correct distortion in photographic images. The program uses a 3rd order polynomial as an approximation of the distortion as a function of radial distance from the image centre. The coefficients of the polynomial are calculated by inputting the coordinates of curved lines in the image which are straight in the object plane. The polynomial maps distorted pixels to undistorted pixels, so once parameters had been calculated the correction was applied to the circuit to be patterned such that when imaged, the features in the circuit would be in the correct place. A comparison of the circuit and the inverse distorted circuit can be seen in Figure 3.20.

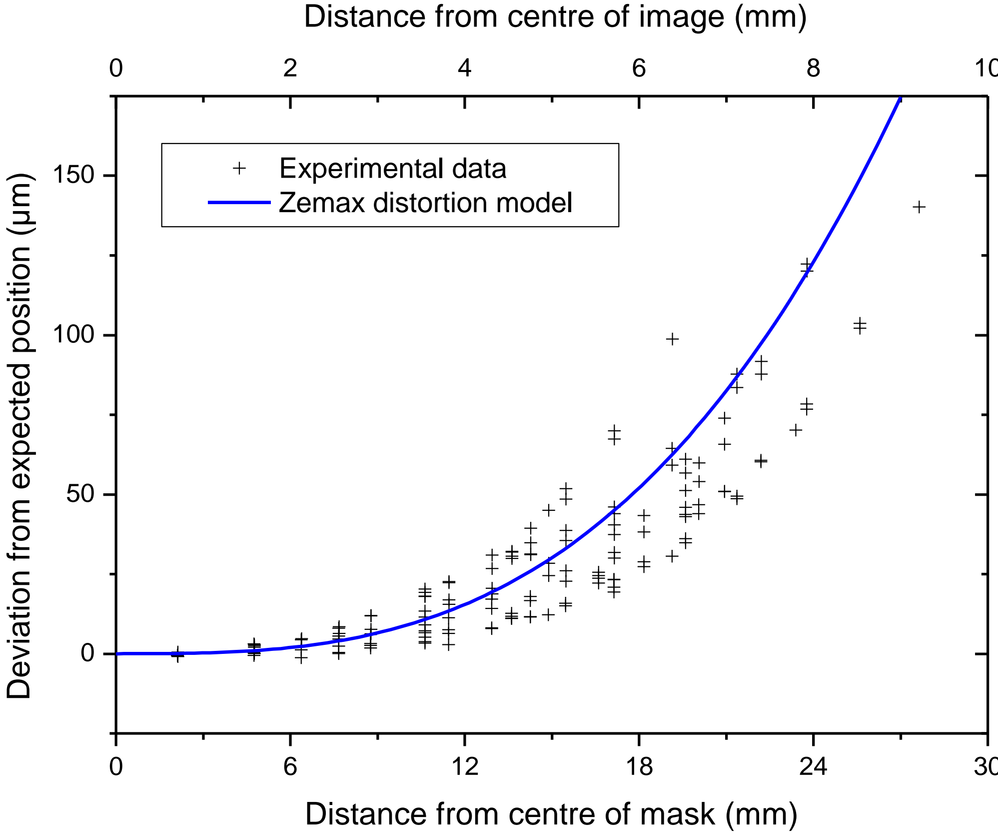

Figure 3.19 Plot showing experimentally measured deviation in the expected position of nodes in a grid for a rectilinear imaging system with a demagnification of 3.0075, where the magnification has been adjusted to align the data with the model, but is well within the bounds of experimental error. The blue line is the deviation predicted by the Zemax model for the f53 mm f-theta lens.

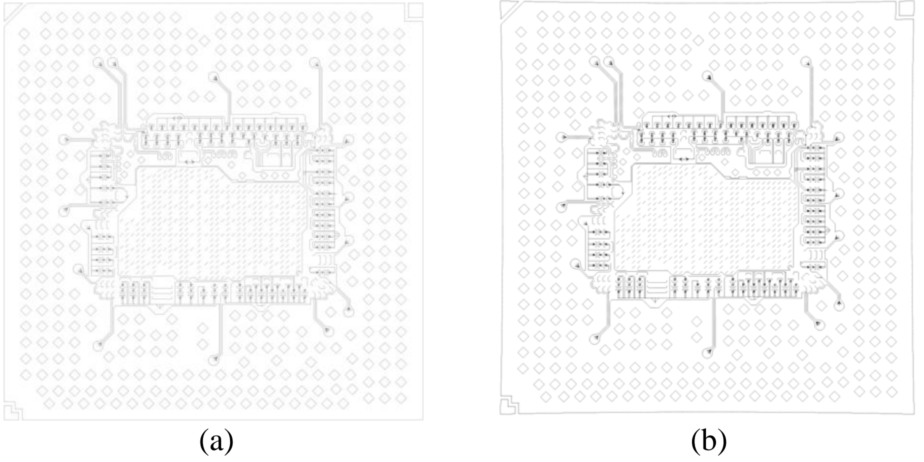

Figure 3.20 (a) The undistorted circuit pattern ~12x12mm in size; (b) the inverse distorted pattern such that when the pattern is imaged by the 53mm focal length f-theta lens, the pattern appears undistorted at the substrate

This methodology had partial success improving, but not completely correcting, the geometric distortion. The images of the inverse distorted circuits had the correct width and height, within measurement errors, at lines passing horizontally or vertically through the image centre. However the corners of the image were 65 μm radially

further from the image centre than anticipated. This meant the final image had a pincushion distortion, although the magnitude of this distortion at the edge of the lens field had been reduced by a factor of 4. Unfortunately it was not possible to complete further iterations to improve the result given the cost and lead time associated with purchasing new photomasks. Ultimately, it was acknowledged that for the project to succeed, custom optics would be required to overcome the aforementioned issues with field curvature, at which point geometric distortion correction would not be needed.

3.2.5 Thermal loading of substrate and lens

It was found early on with the f53 f-theta lens that there were certain aberrations in the ablated image that could only be overcome by scanning the mask in such a way as to increase the time between consecutive shots at a given part of the substrate. This was achieved by scanning the mask multiple times at high speed to build up the required total number of shots. The aberrations included deterioration in image quality and problems with the registration of overlaid features on different parts of the mask when these were scanned with different recipes.

The first and most obvious problem was the difference in laser ablated image quality when scanning the mask at different speeds. Figure 3.21 shows the same resolution chart ablated into a proprietary substrate with different mark speeds. In Figure 3.21(b) the image quality has clearly deteriorated to an unacceptable extent as a result of slowing the scan speed at the mask to increase the shots per area. Initially it was thought that this could be due to thermal loading of the substrate, where the high intensity laser ablation with a lower mark speed was leading to a large heat affected zone reducing the image quality.

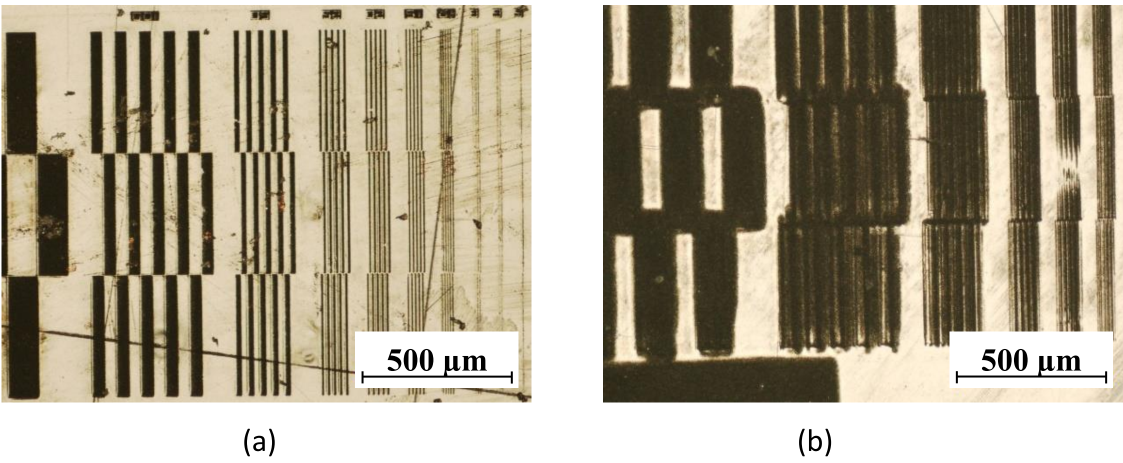

Figure 3.21(a) Resolution chart laser ablated into a proprietary material using a high scan speed and multiple passes of the mask; (b) Resolution chart laser ablated with a low mark speed with a poor image quality.

The error in registration of vias with landing pads across the image field was not, at first, obviously related. Despite checking constant separations of features at the mask plane, it was found it was not possible to perfectly align all vias with all landing pads in an image field, and that there was variation in the error in registration of features across the image field. It was hypothesized that this could be due to a tilt in the mask, lens or substrate plane, causing a change in magnification across the image field. However after further investigation it became apparent that the direction of the mis-registration of vias across the image field was dependent on the direction with which the mask was scanned. This, combined with the fact that the issue could be alleviated by reducing the thermal loading of the lens, and that aberrations appeared in the ablation when scanning the mask at a slow speed, all pointed towards thermal lensing as a likely cause. Because the object is imaged as a sequence of smaller images as the mask is scanned with a particular direction, this leads to the potential to establish thermal gradients within the optical elements of the imaging lens. Holding discussions with the lens maker it became apparent that one of the elements in the multi-element f-theta lens was made of NBK7 as opposed to UV grade fused silica glass. NBK7 is known to be less thermally stable under high average powers due to its much higher coefficient of thermal expansion (CTE), 7-8 ppm K^{-1}, compared to fused silica which has a CTE of 0.5 ppm K^{-1} [80]. As a result the remainder of the preliminary tests were conducted with the f103 mm f-theta lens which contained only UV grade fused silica elements, despite its lower NA.

3.3 Imaging results with the f103 mm f-theta lens

The imaging system with the f103 mm f-theta lens was set up with 3x magnification and a significant amount of work conducted on proprietary materials development for the subsequent copper plating process. All of the materials development and copper plating were done in collaboration with materials and plating companies, and it is not possible to disclose details on the processes used to achieve the following results. However SMI laser ablated features were copper plated, another dielectric layer added, and Figure 3.22 shows the laser ablation of the upper layer of a multilayer chip package well registered with the copper plated structures in the layer below.

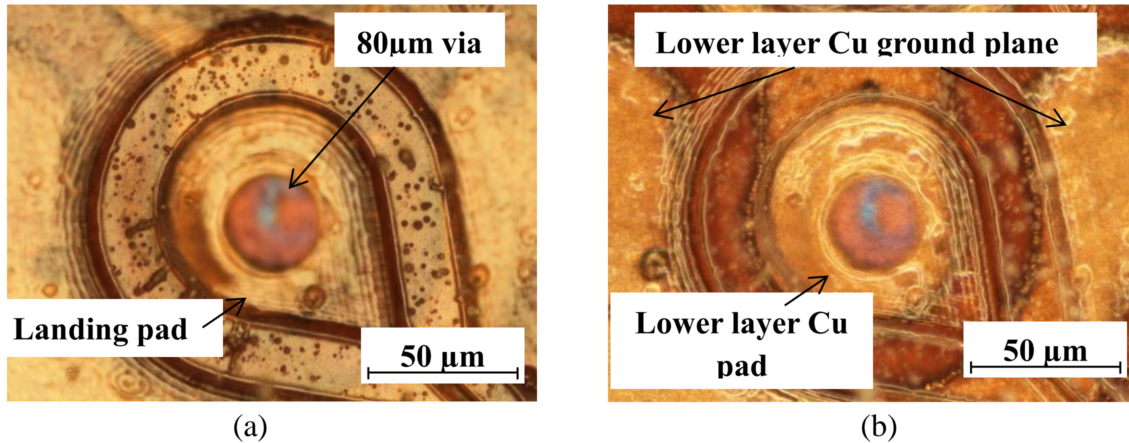

Figure 3.22 (a) Optical microscope image of laser ablation of the top layer of circuitry in a multilayer package above previously laser ablated and copper plated structures; (b) a dark field image of the same area, revealing the copper circuitry below.

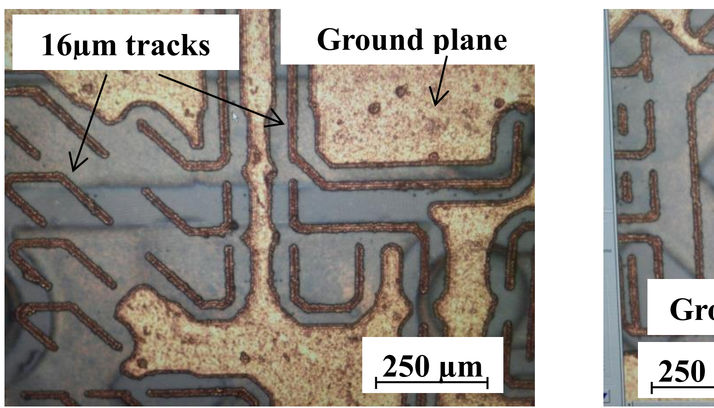

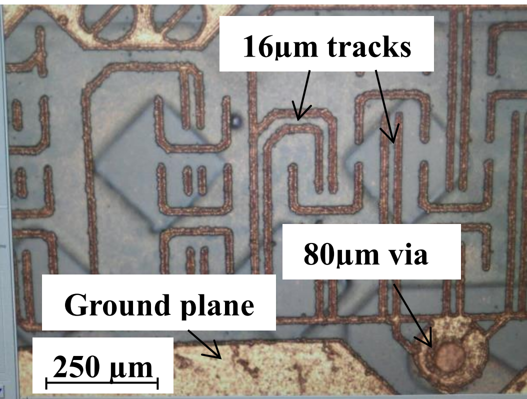

Figure 3.23 Optical microscope images of a copper plated top layer of circuitry well registered above a lower layer of circuitry. For reference, the thinner traces are 16 µm wide.

Figure 3.23 shows optical microscope images taken of 2 layers of laser ablated and copper plated structures taken by the plating collaborator. The vias in the top layer of circuitry are aligned with the landing pads on the lower layer of circuitry. The results

demonstrated, even without upgrading the imaging optics, the potential to fabricate multilayer chip packages with features down to 16 µm L/S.

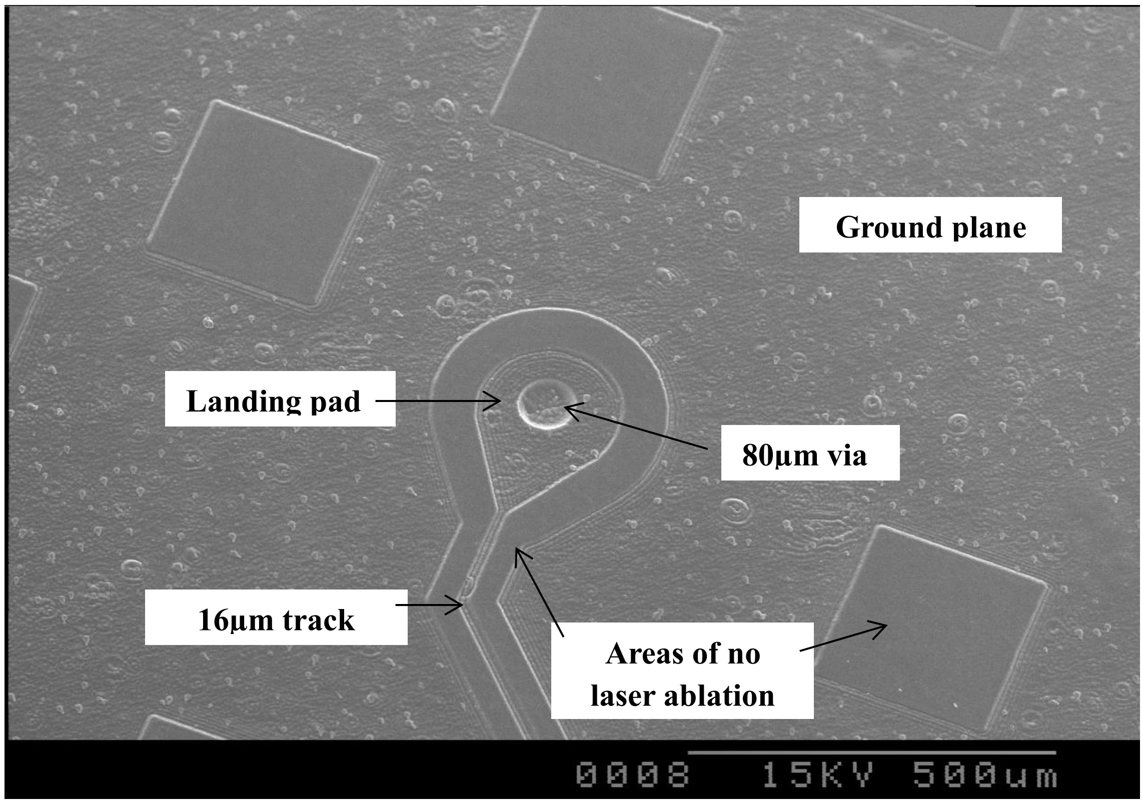

Figure 3.24 SEM micrograph of circuit laser ablated into Kapton with the SMI laser process. The image shows a via well registered with a landing pad, and a ground plane ablated to a uniform depth.

Figure 3.24 shows and SEM micrograph of SMI laser ablation into Kapton during the process development. By tuning the pitch of the lines used to scan the mask, and the speed with which the mask is scanned, it is possible to achieve a uniform ablation depth as demonstrated by the large ground plane region. Scanning the mask multiple times and offsetting each pass also improves the illumination uniformity. The image also shows a blind via well registered with a landing pad. Also noteworthy are the large number of bumps in the ground plane ablation, highlighted in Figure 3.25. These were repeatable on each circuit, which led to the suspicion the defect in the ablation was caused by some defect on the mask. Inspecting the mask on the microscope, the defects turned out to be dust particles on the top surface of the quartz such that they are imaged slightly out of focus at the substrate plane. The observation highlights the need for a clean air flow around the mask and optics to avoid such printed in defects, and to increase the lifetime of the optics.

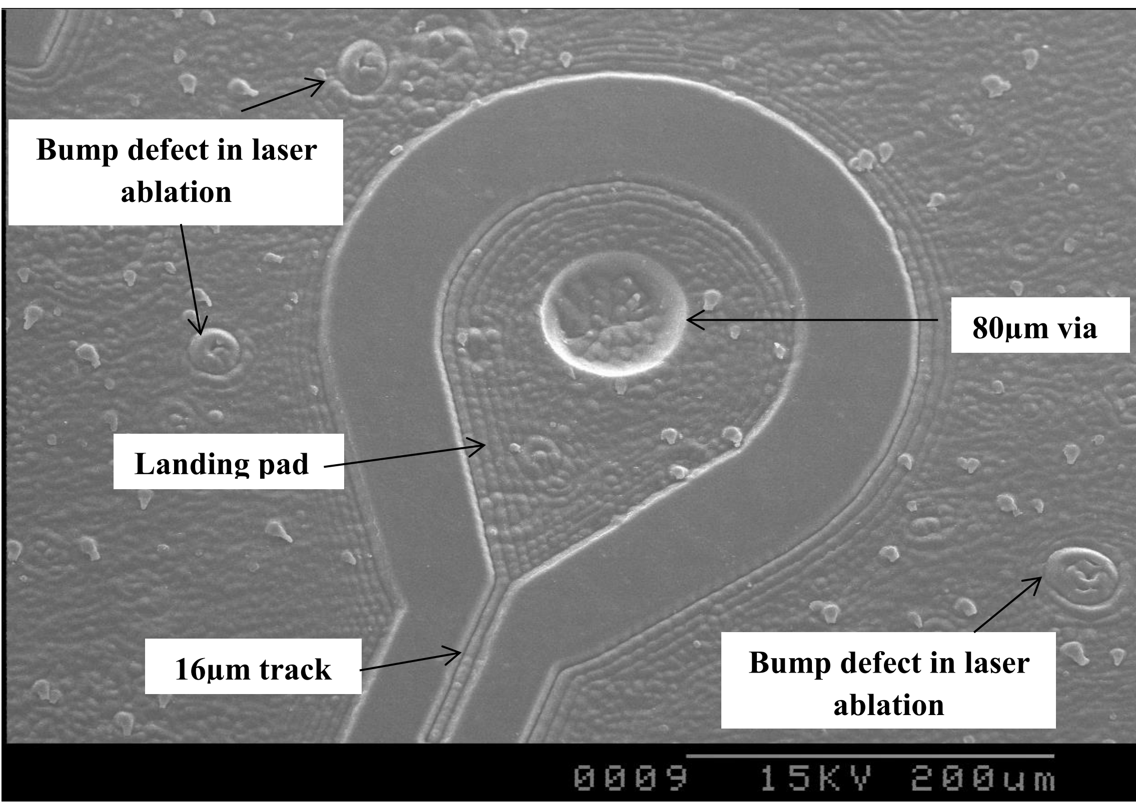

Figure 3.25 SEM image highlighting the defect in ablation caused by dust on the mask obstructing the laser light and being imaged down to the substrate.

3.4 Summary

A test rig was set up to demonstrate the feasibility of the SMI process. Laser ablation of multi-depth structures with resolutions down to 8 µm across a 12 mm × 12 mm image field were shown. Demonstrator chip packages were fabricated in collaboration with a materials company, a plating company and an end user with laser embedded conductors with a minimum feature size of 16 µm L/S. Laser ablation of 4 µm L/S features were demonstrated over a limited field size, however through modelling of the lens performance in Zemax it was established that the field curvature of the lens in a 3x imaging system would prevent attaining this resolution across the entire image field. The feasibility study showed that with the correct optics, it would be possible to provide a cost effective solution to the 1-10 µm technology gap in the advanced chip packaging market by laser embedding conductors. Custom optics would require distortion of less than 5 µm across the flat image field, with a high NA to achieve the required 2-3 µm resolution. The image field of the lens should be ~20 mm × 20 mm to capture the majority of the consumer electronics advanced chip package market.

Chapter 4: Custom Imaging Optics: Design and Installation

The results shown in chapter 3 demonstrate the potential to fabricate laser embedded conductor chip packages, however it is clear that the resolution and distortion of the optics used were not able to address the technology gap for feature sizes between 2-10 μm. In addition, the approximately Gaussian spatial profile of the beam resulted in inefficient use of the laser energy on account of a large portion of the beam having energy below the ablation threshold of the substrate, and with a high peak fluence which increases the risk of mask damage. Finally, the circular beam profile does not tessellate making it more challenging to uniformly illuminate the mask to achieve a constant ablation depth with no periodic depth variation in large features. To address this, an upgrade to the optical system was proposed and implemented including a custom designed projection lens with a flat field and low distortion. Additionally, as part of the upgrade and projection lens design, the illumination of the mask in the mask imaging system was redesigned to give a compact, flexible system with flat top beam profile at the mask plane.

4.1 System schematic and design considerations

To allow flexibility in beam homogeniser choice and to simplify changing and testing different homogenisers after the initial setup, it was decided to image the plane of uniformity formed by an arbitrary homogeniser down to the mask plane. An infinite conjugates imaging system was used, formed of a plano-convex singlet and a telecentric f-theta scan lens. Using a telecentric scan lens means that a double telecentric projection lens can be used to form the image of the mask, and it also limits the size of the first element in the projection lens to approximately the size of the object since the beam deviated across the mask by the scanner is approximately normal to the mask at all points in the scan field. The scan lens also has a flat field in its focal plane which keeps the image of the homogenous beam in focus across the scan field. The use of a double telecentric imaging system gives a more precise definition of magnification which is less sensitive to object and image position. This is key for the application, given that the magnification must be defined to 3 decimal places to give substrates the dimensional accuracy required to accurately register with the microbumps on the chips I/Os. The divergence of the beam after the mask is then defined by the homogeniser system and the lenses in the infinity imaging system, as well as the inherent properties of the multimode beam. Care must be taken to design the system such that the aperture of the scanner and the entrance pupil of the f-theta lens are not overfilled, but that the

divergence at the mask is high enough to obtain the desired numerical aperture on the object side of the projection lens with the optimum partial coherence factor. There are a number of ways to homogenise a multimode laser beam, the most common being microlens arrays and diffractive optic element (DOE) homogenisers. The DOE type homogenisers are less sensitive to alignment in the system, and can generate a more homogenous beam with multimode lasers. The beam homogeneity is improved with multimode lasers by reducing the high intensity speckle occurring due to diffraction effects in beams with long coherence lengths. For these reasons it was decided to use a DOE type homogeniser to form a flat top, square beam profile. The homogeniser used forms a square, flat top plane at the beam waist of a plano-convex singlet. The DOE manufacturer provided the following equation to calculate the square beam size:

$$t = f \times \tan\alpha \tag{4.1}$$

where the width of the square formed, t, is dependent on the diffusion angle of the homogenizer, α, and the focal length of the singlet, f. This introduces another degree of control and flexibility into the system, since both the beam size and the divergence of the beam at the mask can be adjusted by changing the DOE for one with a different diffusion angle, or by changing the focal length of the plano-convex singlet after the DOE. A schematic of the system can be seen in Figure 4.1. The focal length of the second plano-convex singlet can also be adjusted to change the magnification of the infinite conjugates imaging system, and hence the beam divergence at the mask and the filling of the entrance pupil of the f-theta lens and projection lens.

Having planned the illumination system, the lens specification was discussed with Sill Optics, a commercial lens supplier. A proposal was made for a 0.11 NA double telecentric imaging lens with 2-3 μm resolution across its image field. The maximum object size, image size and magnification of the lens required careful consideration with regard to the proposed application. The maximum object size is limited by the availability of metal-on-quartz photomasks. A single photomask is required to have a minimum of two equally sized patterned areas, defining the information for the redistribution of the signal I/Os from the chip and the vias to connect signals in different planes of the package. It is feasible to have this information on two separate masks, with a mechanical solution to align the masks to each other to allow the accurate overlay and registration of the layers. However, in order to reduce the mechanical complexity of the system, and to improve the accuracy of the image overlay, the

information for the redistribution layer and its complimentary via layer was put on the same photomask. Photomasks are standard consumables in the semiconductor industry and chrome and aluminium-on-quartz photomasks are readily available on quartz substrates up to 7×7” in size. The defect free area as defined by the manufacturer of a 7×7” photomask is up to ~164×164mm. Additional space is required between the two layers on the photomask to define features for mask alignment, resolution charts for focusing and any other assembly or tooling marks which may be required on the panel for subsequent process steps. Allowing for some space between features and layers on the mask, to allow for overscan, dictated that the maximum object size at the mask for two equally sized layers on a 7×7” photomask is ~70×70mm.

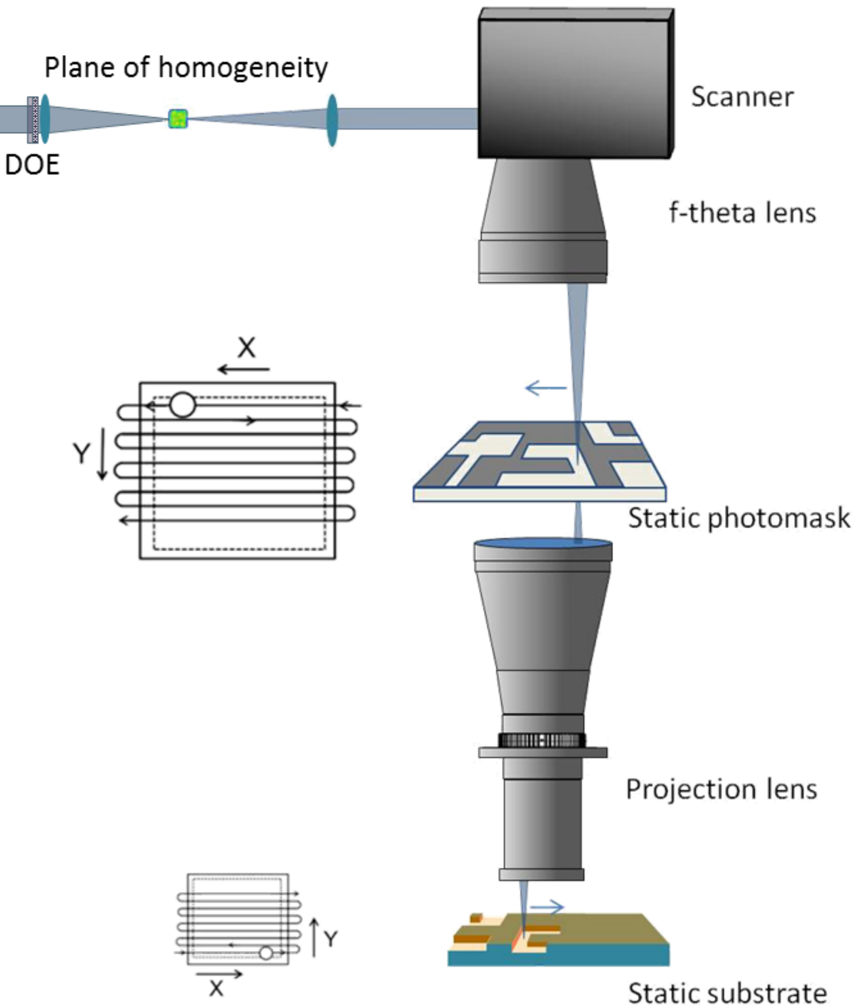

Figure 4.1 Schematic of the SMI system. The beam passed through a DOE and forms a homogenous, square flat top beam at the beam waste of a singlet lens. This plane of homogeneity is then imaged by a singlet and telecentric f-theta lens in an infinite conjugate imaging system down to the plane of the photomask. The beam is rastered across the photomask by the scanner and the image of the photomask is projected onto the substrate by a double telecentric projection lens.

Having calculated the maximum object size based on readily available, low cost photomask sizes, the magnification and image size of the lens was considered with the following constraints. The image size should be as large as possible to capture the largest possible portion of the chip packaging industries. Chip-scale-packages (CSPs) are by definition approximately the same size as the chips they house, and are commonly used in consumer electronics. Thus most of the CSP market can be captured by an image field of ~20×20 mm. There are high end package types such as ball-grid-arrays (BGA) that are commonly around 30×30 mm or larger, and can be as large as 50×50 mm, which are used in high end applications such as graphics processing units (GPUs) and servers. However, because of the limit on the object size, targeting the larger substrate BGA market would require a low magnification imaging system with a demagnification of less than 2. This restricts the fluence at the substrate to below 0.8 J cm^{-2} because of the damage threshold of chrome- and aluminium-on-quartz masks. Photomasks with dielectric coatings can have damage thresholds up to 2 J cm^{-2}, but are significantly more expensive. An optical system with a demagnification less than 2 also increases the challenge of the optical system design to achieve high NA optics with a low demagnification. It was therefore decided to target package sizes below 20×20 mm, with a demagnification of 3.5x in the imaging system, allowing fluences of up to 3 J cm^{-2} at the substrate.

Other constraints on the lens design were total track length and the front and back working distances of the lens. For practical reasons the track length from substrate to scanner was limited to ~1 m. Given that a long focal length, telecentric f-theta was required with a scan field of 70 mm or greater, it was decided to restrict the track length from mask to substrate to ~600 mm to allow room for the f-theta lens and scanner assembly. The projection lens also required a front working distance of greater than 50 mm to allow room for the mechanical mounting of the photomask on a linear stage, and a back working distance of greater than 50 mm to allow room for a debris extraction nozzle to extract fumes and debris from the laser ablation process. Given the small spectral bandwidth of frequency tripled DPSS lasers, it was possible to use an all silica design for the lens without the need to compensate for chromatic aberration with CaF_2 elements, as is the case with some high resolution excimer laser projection lenses.

Based on the above considerations, a custom projection lens was acquired with 0.11 NA across a 20x20 mm image field and a magnification of 3.5x. All other components in

the system were off-the-shelf components, including an f-163 mm f-theta lens with an NA of 0.03 and a scan field of 70x70 mm, a DOE beam homogeniser with a diffusion angle of 0.17° and several singlets to interchange in order to form different spot sizes at the mask.

4.2 Zemax model of the custom imaging lens

Prior to acquiring the lens, a blackbox Zemax lens model was provided by the lens supplier to assess the lens performance. The model was set up with the correct wavelength and ray bundles propagating from defined points in the object field up to a radial distance of 52.5 mm. The plot of the through focus spot diagram can be seen in Figure 4.2. The on-axis plots are indicative of under corrected or positive 3rd order spherical aberrations. However the effect is small and would not impair the lens performance at focus. Also of note are the flares in the spot at the edge of the image field, however the ray density, which is proportional to energy distribution, is low outside the central region. There is also slight astigmatism visible at the edge of the field, with the dense region of the ray bundle having an elliptical shape with a shorter dimension in the y axis at focus, and a shorter dimension in the x axis 20μm inside focus. The spot diagrams for the ray bundles emerging at a radial distance of 40 mm in the object field clearly show elongation in the x and y axes at different focal planes, also indicative of astigmatism.

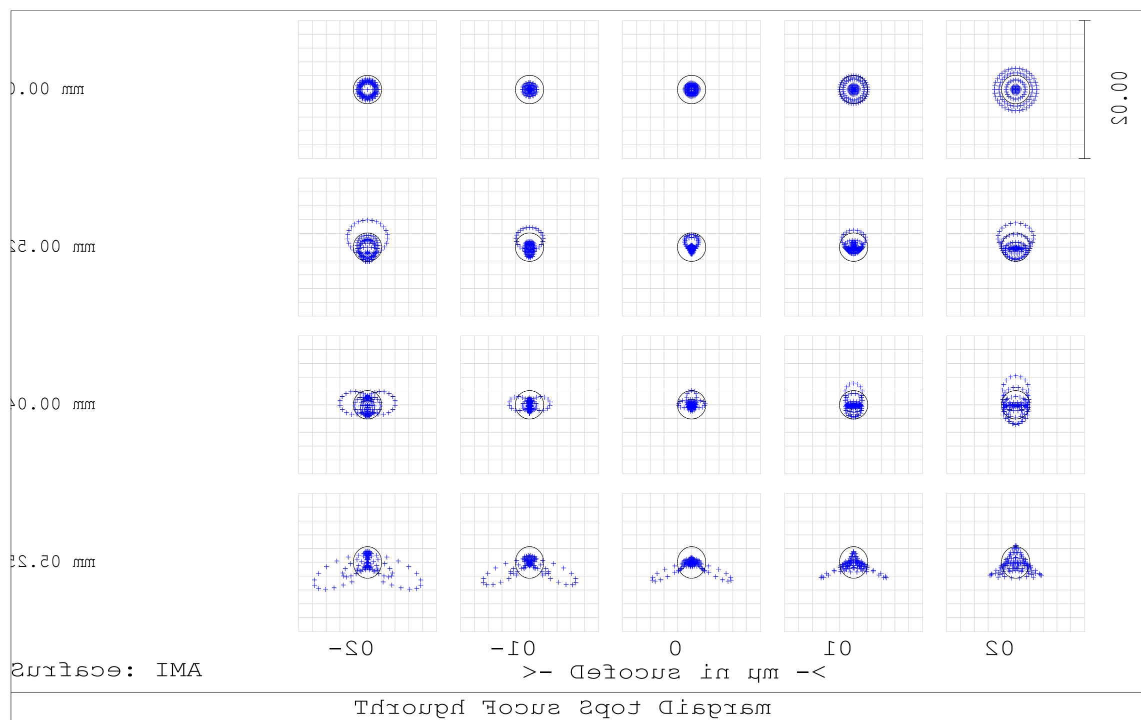

Figure 4.2 Through focus spot diagram generated using black box Zemax model of custom projection lens.

The observations made using the through focus spot diagram can be supported using the transverse ray fan plots shown in Figure 4.3. The tangential ray bundles emerging from within a 40 mm radius of the optical axis in the object field all have predominantly cubic transverse ray fan plots indicative of the slight under corrected spherical aberration observed in the on axis through focus spot diagram. The plots at the edge of the field show the 5th order spherical aberration terms becoming dominant, which begins to become significant in magnitude for marginal rays in the sagittal ray bundle.

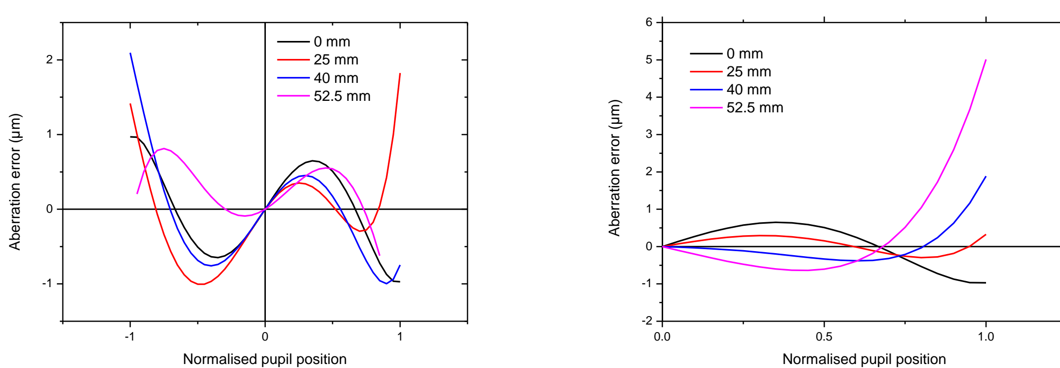

Figure 4.3 Graphs showing the transverse ray fan plots for the tangential and sagittal ray bundles respectively with bundles originating at different points in the object field.

The peak to valley optical path difference (OPD) plots show the magnitude of the OPD is < 0.2 wavelengths inside a 40mm radius of the object field, which suggest the spherical aberration has been sufficiently corrected. However at 52.5 mm the peak to valley OPD is 0.34 wavelengths, again suggesting some spherical aberration at the edge of the field. These observations can be used to explain the modulation transfer function (MTF) shown in Figure 4.4. The graph shows the lens performance is close to diffraction limited for both tangential and sagittal ray bundles originating inside a 40 mm radius in the object field. However there is some departure from this in the ray bundle originating at 52.5 mm, particularly in the sagittal plane as expected from the transverse ray fan plots. The resolution of the optical system is also dependent on the detector, or in this case the substrate. Assuming a homogenous substrate with a given ablation threshold, as long as the modulation transferred by the optical system is great enough such that the maxima in the image plane are above the ablation threshold, and the minima are below the ablation or damage threshold of the substrate, we can consider the feature resolved. It is worth noting that in this case, there could be a lower ablation rate in the smaller features when compared with the larger features due to the lower intensity of light transferred by the optical system. The plot shows modulation transferred at points inside a 40 mm radius in the object field is ~0.6 for 3μm L/S or 167 cycles/mm features and ~0.5 at the edge of the field, which should be great enough to satisfy the above resolution criterion.

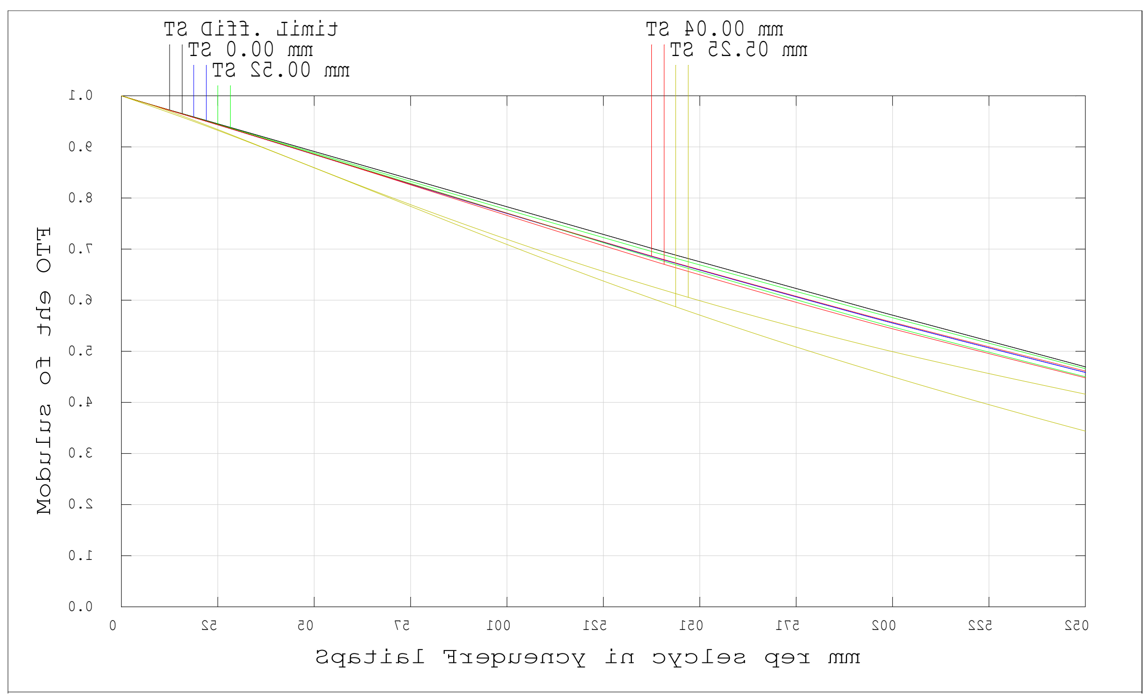

Figure 4.4 Graph showing the modulation transfer function of the custom projection lens for ray bundles in the tangential and sagittal planes originating at the labelled points in the object field.

4.3 System set up with custom projection lens

The optical system was set up as depicted in Figure 4.1, with an f = 500 mm focal length singlet after the DOE, and an f = 160 mm singlet as the first lens in the infinite conjugate imaging system. The beam was expanded prior to the DOE to ~8 mm diameter using a Keplerian telescope to fulfil the input beam diameter requirement of the DOE. The f = 500 mm singlet when used in combination with the 0.17° diffusion angle DOE formed a 1.5 mm spot at the plane of homogeneity, as calculated using equation (4.1). The f = 160 mm singlet then images this plane onto the mask with an approximately 1:1 imaging system when used in combination with the f = 163 mm f-theta lens. Figure 4.5 shows a beam profile taken at the waist of the f = 500 mm lens. The profile was taken with a laser diode current of 100% to allow all modes within the laser to oscillate, since the laser mode structure affects the DOE performance. The profile shows that, despite the error in rotational alignment of the beam with the detector, the full width half maximum of the approximately flat top beam is 1.44±0.02 mm.

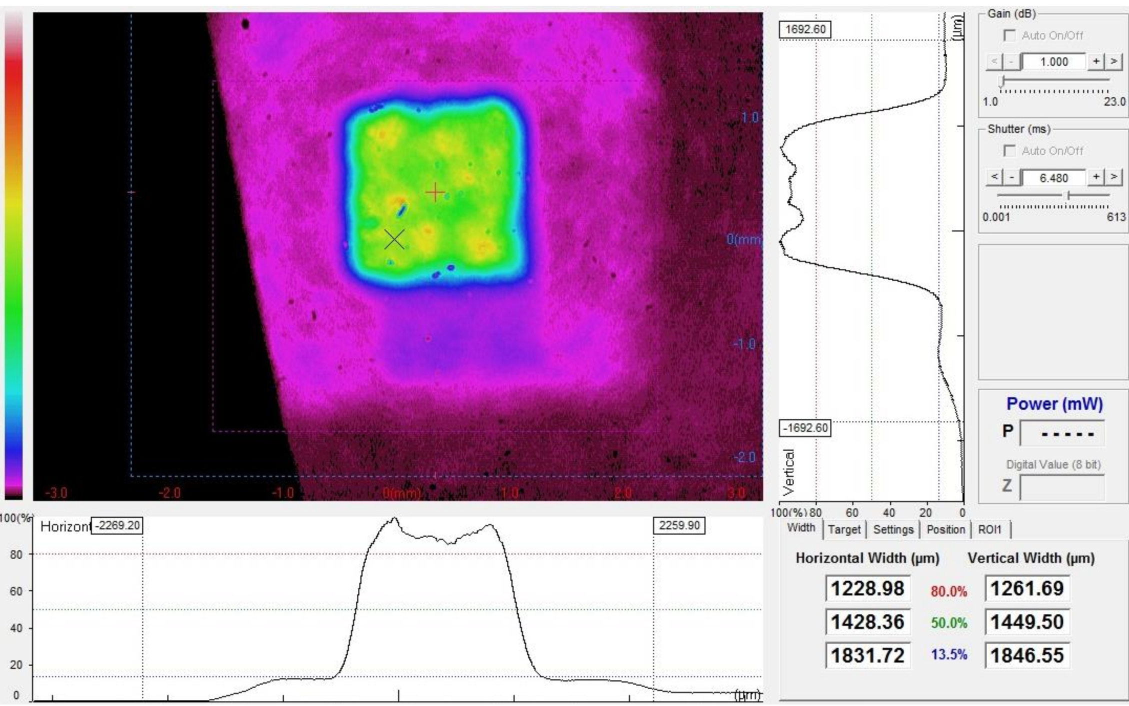

Figure 4.5 Beam profile taken at the beam waist of an f = 500 mm lens preceded by a homgenising DOE. The profile was taken with the laser diode current set to 100%, to allow all modes to oscillate in the cavity. The beam was attenuated prior to the CCD profiler using a high energy mirror, the edge of which can be seen as the absence in scattered light in the left of the image. The X marks the beams peak intensity and the + marks the beam centroid.

Table 4.1 shows the transmission efficiency of the optical components prior to the metal coating on the lower surface of the metal-on-quartz mask. Based on a 16 W average power at 5 kHz, the fluence at the mask is 99 mJ cm^{-2}. This fluence is close to but below the damage threshold of chrome-on-quartz (99 mJ cm^{-2} [43]) and justifies the decision to use the f = 500 mm singlet lens after the DOE in the initial setup to achieve the 1.44 mm spot. To use the CCD beam profiler at 100% laser diode current, the beam was attenuated prior to the sensor using a high energy dielectric mirror, with the dielectric coating optimised for high reflectivity with UV wavelengths. For comparison, Figure 4.6 shows an image of the beam profile in the same plane taken at a low diode current close to the threshold current for lasing. At this diode current there are less transverse electric modes oscillating in the laser cavity which increases the coherence length of the laser. This can be seen in the high intensity speckle in the beam profile which can be attributed to diffraction effects apparent due to the extended coherence length.

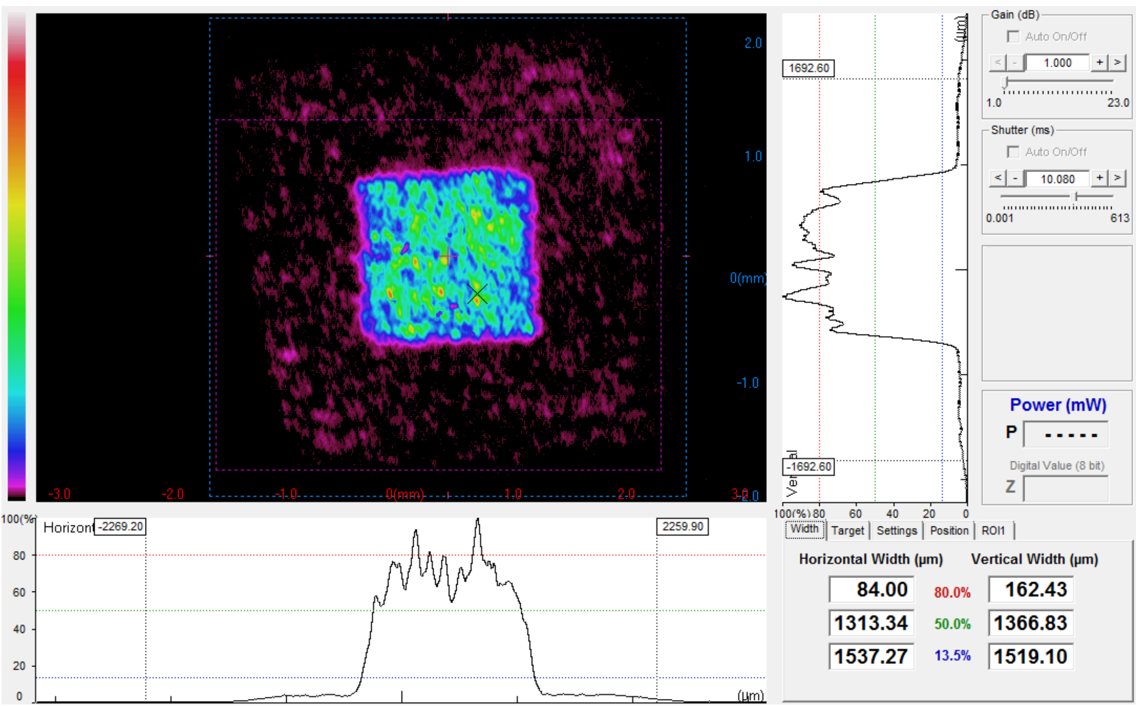

Figure 4.6 Beam profile taken at the beam waist of an $f = 500$ mm lens preceded by the homogenising DOE. The laser diode current was set to close to the threshold for lasing in this image, and diffraction effects can be seen in the image as high intensity speckle in the profile. This is due to the reduced number of modes oscillating within the laser cavity, and the resultant longer coherence length of the generated beam.

Component	Manufacturer quoted transmission efficiency
12x coated lens and mirror surfaces	$0.99^{12} = 0.89$
DOE	0.77
f-theta lens	0.97
Uncoated glass surface of mask	0.96
Portion of energy transmitted from laser to metalized surface of mask	**0.64**

Table 4.1 Transmission efficiency of optical surfaces in the SMI system prior to the metallization on the quartz mask. The fraction of the total original power reaching the metalized surface of the mask, 0.64, was arrived at by taking the product of the fractional loss in each component.

Having tested the DOE at high laser diode current, the subsequent results were collected at a low laser diode current to avoid potential damage of optical components through prolonged exposure to high average power, and to reduce the risk involved with carrying out the experiment. The plane of homogeneity was imaged down to the mask plane using the infinite conjugates imaging system depicted in Figure 4.1 and a profile of the beam taken in approximately the plane of the mask. The profile is shown in Figure 4.7, and it can be seen that the image approximates the profile in Figure 4.6.

Mounting the CCD detector in the plane of the mask was challenging, and the slight elongation of the beam in the vertical direction could well be due to an angle between the plane normal to the beam and the detector.

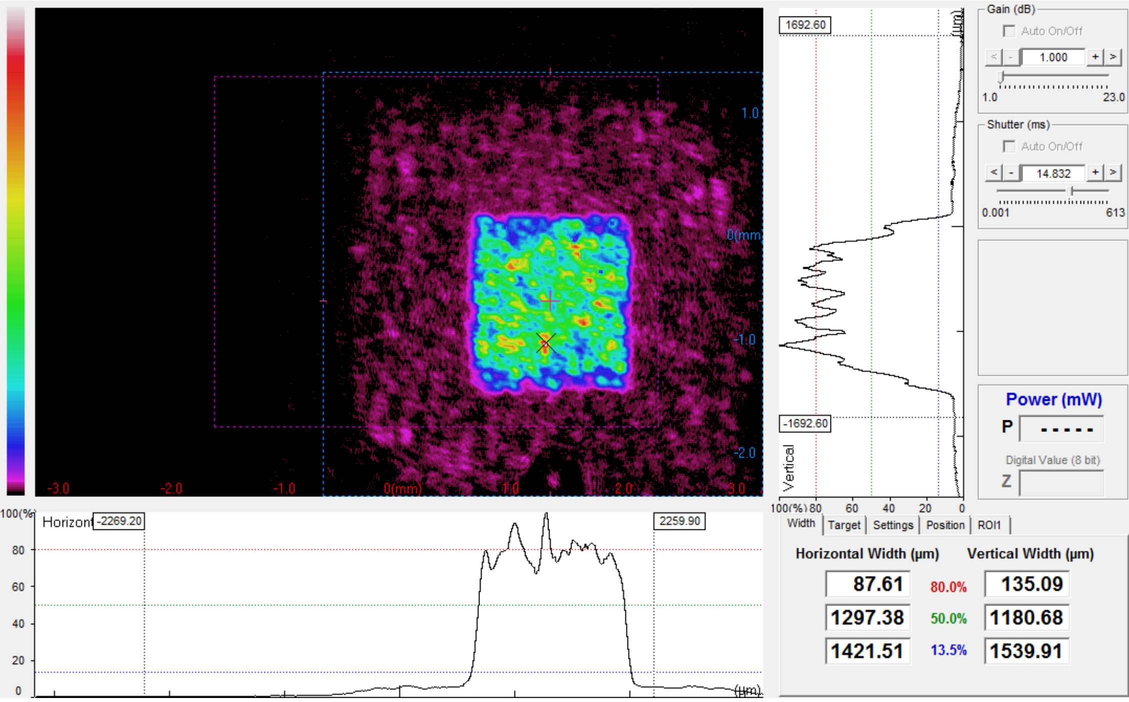

Figure 4.7 Beam profile in the mask plane of the SMI optical system.

Given that the infinite conjugate imaging system was shown to be performing as expected on axis, the beam propagation subsequent to the mask was examined. The beam was expected to have a beam waist at the mask, and then subsequently diverge to illuminate the projection lens as depicted in Figure 4.1. Unexpectedly, the beam was still converging in one axis after the plane of the mask to some point in the body of the lens, preventing the set up being used at high average power for fear of damaging the lens. Images of the beam profile can be seen in Figure 4.8.

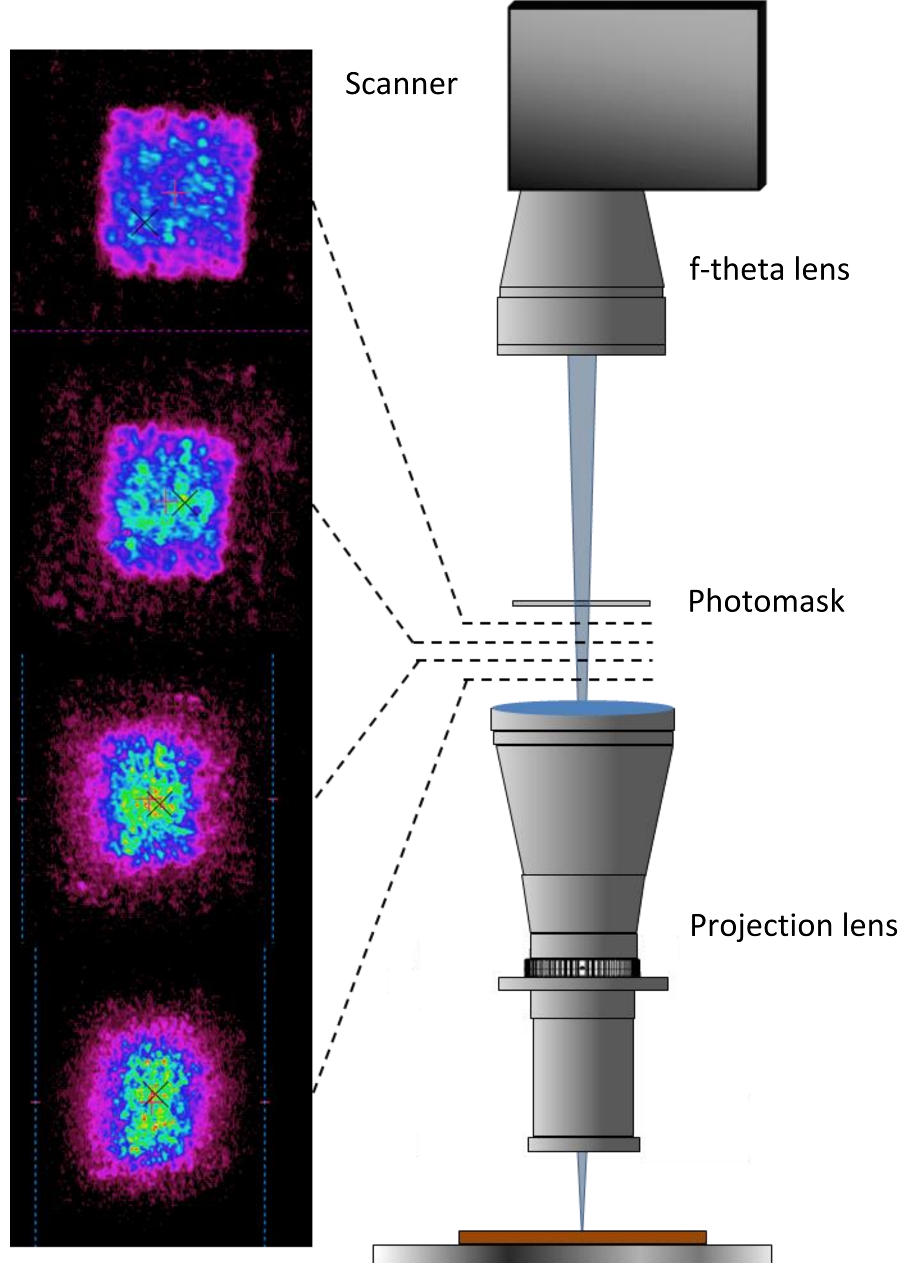

Figure 4.8 Images of the beam profile below the plane of the mask between the mask and the projection lens. There was expected to be a beam waist at the mask plane, which is coincident with the focal plane of the f-theta lens. However the beam was found to be converging in one axis below the plane of the mask.

It was believed the issue might arise from the inadvertent beam reduction brought about by the $f = 500$ mm singlet and the $f = 160$ mm singlet resulting in a reduction in beam size by a factor >3. This could either lead to an underfilling of the entrance pupil of the f-theta lens mounted on the scanner, or a large increase in the beam divergence on account of the additional angles introduced to the beam by the DOE and the small beam diameter. To avoid the issue of the reducing the beam, in part to establish whether this was the cause of the beam waist below the lens, it was decided to remove the

f = 160 mm lens and image the plane of homogeneity directly with the f-theta lens in a finite conjugates imaging system as depicted in Figure 4.9.

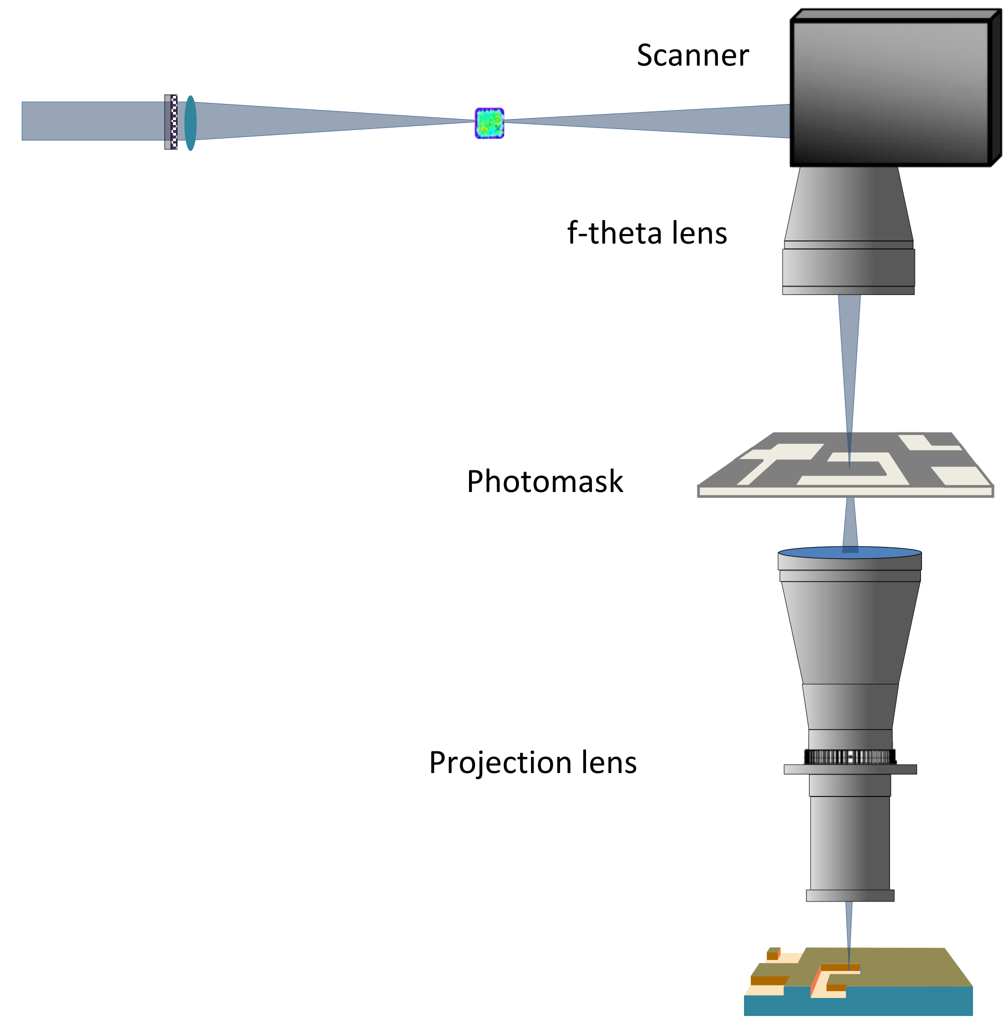

Figure 4.9 SMI system optical set up with a finite conjugate imaging system to image the plane of beam uniformity directly to the mask plane with the f-theta lens.

The system was set up to image the plane with a 1:1 magnification ratio down to the mask, and again beam profiles taken in the mask plane to confirm the imaging system was performing as expected. Figure 4.10 shows the on axis beam profile in the mask plane which confirmed that the imaging system had been set up with approximately the correct magnification. In addition to this, the beam was now divergent after the mask as expected.

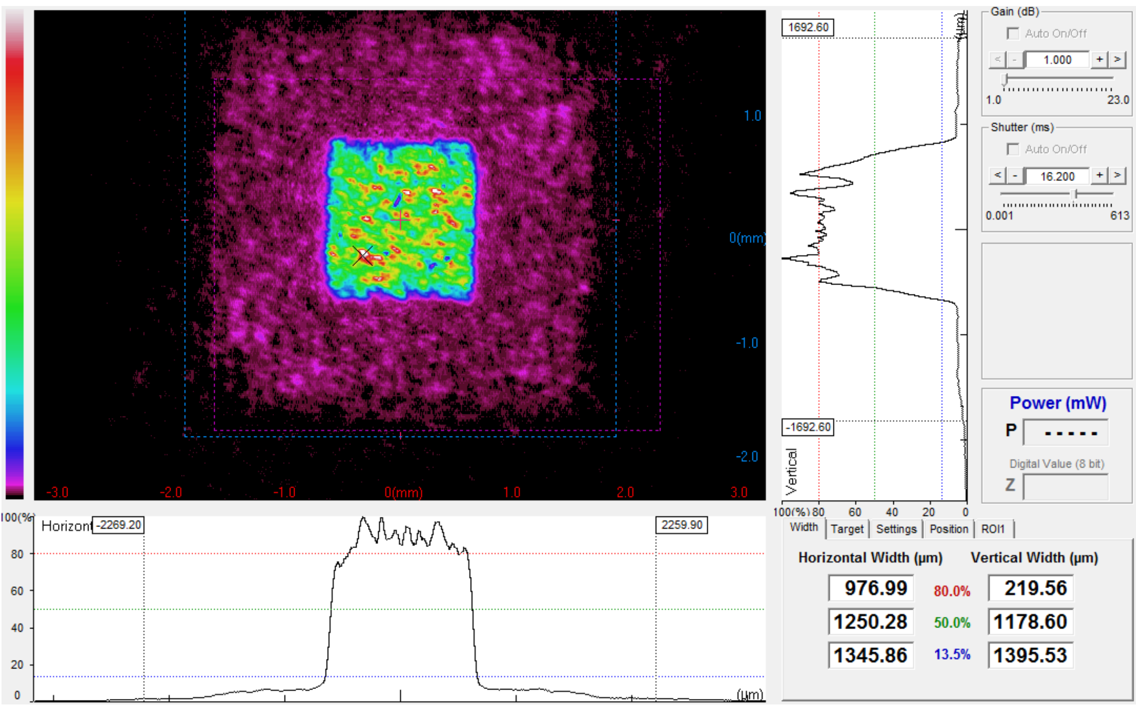

Figure 4.10 On axis beam profile taken at the mask plane of the plane of uniformity imaged by the f-theta lens

The reason for not using a finite conjugate imaging system with the f-theta lens in the initial set up was to avoid using the lens outside of its focal plane, where it is designed to have low distortion and field curvature. To get an idea of the barrel distortion and field curvature of the lens when used in a 1:1 finite conjugates imaging system, beam profiles were taken at several off axis points in the field. The profiles are shown in Figure 4.11 and the distortion is particularly noticeable when the scanner directs the beam to (-35,-35) mm in the scan field. The beam was, however, divergent after the plane of the mask so there was no longer a risk of focusing on an element within the lens. It was therefore decided to proceed with the system alignment and obtain some imaging results with the projection lens until the issue with the infinite conjugates imaging system could be resolved.

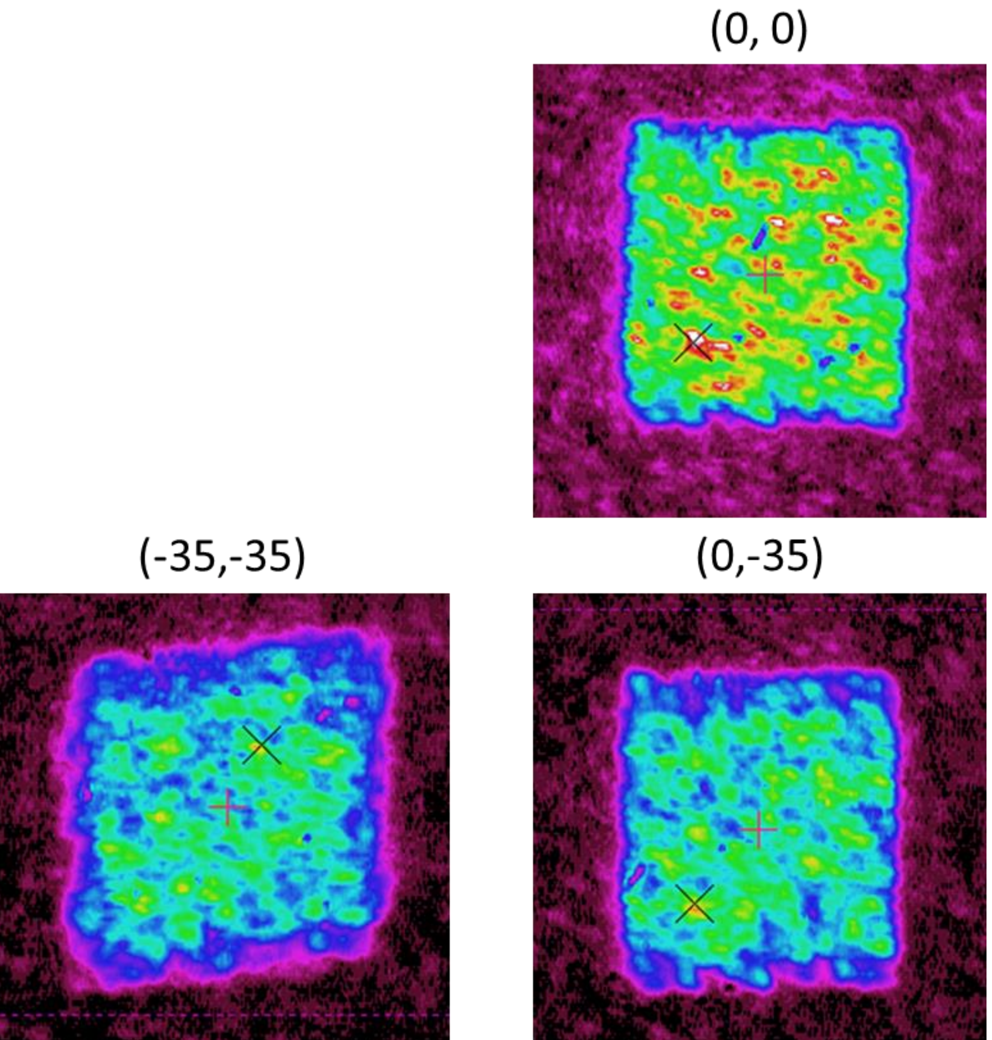

Figure 4.11 Beam profiles taken in the mask plane at different positions in the scanners scan field. Barrel distortion can be seen in the image of the homogenous beam off axis at the (-35,-35) mm position. The X marks the beams peak intensity and the + marks the beam centroid.

4.4 Ablation results with new lens

4.4.1 Alignment and first results

When first aligning the system for use with the new projection lens, the aluminium vacuum chuck, mounted on 3 adjustable points and a supporting point, was levelled using a dial test indicator (DTI). This measures the angular deflection of an arm to a resolution of 2 μm/division. It was noted that the chuck had up to 100 μm bowing such that to maintain focus on a 20x20" panel, adjustments in the z-axis to the lens-substrate separation would be necessary. Having levelled the chuck to the x-y stages, the scanner pitch and yaw were adjusted such that scanner and f-theta lens were held in a plane parallel to that of the chuck to ±0.1 mm m^{-1} using a digital inclinometer. After this, a reflector or reflective substrate was placed on the chuck and again, made parallel to the

x-y stages. Prior to the scanner the beam was aligned to lenses and the DOE using crosshairs centred on the elements and back reflections from the elements to ensure the elements were both centred and normal to the beam. The beam was then aligned using back reflections and a cross hair at the scanner aperture until it entered both centred upon and normal to the scanner aperture. The back reflection from the chuck was then checked, after which back reflections from new elements introduced to the optical axis below the scanner could be examined to ensure the elements were parallel to the reflective substrate, the aluminium chuck and the x-y stages. Prior to inserting the projection lens, a reference mark was aligned to the beam in the substrate plane. The projection lens was inserted into the beam path and was levelled using the back reflections from the protective glass windows on the lens and then centred on the beam by using cross hairs to mark the centre of the lens at both the top and bottom surfaces. It was also ensured that the lens did not deviate the on axis beam path by checking the beam alignment with the reference mark made prior to inserting the lens. Once the projection lens was satisfactorily levelled and aligned to the optical axis, the photomask was inserted at the mask plane. The DTI was used to level the mask to the linear mask stage, after which the pitch and yaw of the stage-mask assembly was adjusted until the mask was normal to the optical axis as determined by using the back reflection of the beam.

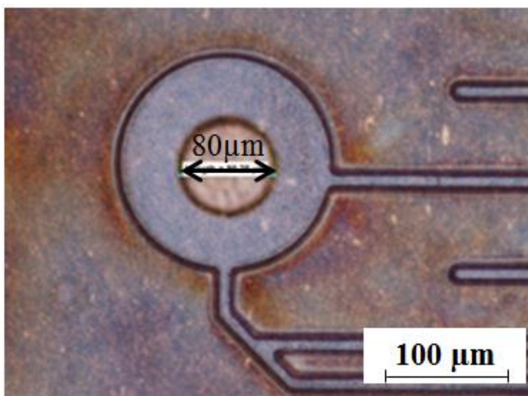

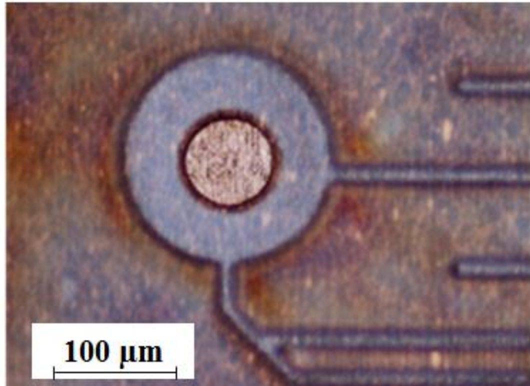

Figure 4.12 Optical micrograph of laser ablation of 16µm signal traces leading to a landing pad and 80µm via. The via has been drilled all the way through the 20µm BTX film to the copper clad laminate below.

Having aligned the system and ensured the substrate, projection lens and mask were parallel; the laser parameters were set to 5 kHz at 100% diode current to achieve a fluence of ~1.2 J cm^{-2} at the substrate. Focusing was done initially by adjusting the projection lens position on a micrometer stage and scanning a resolution chart at each

lens position. The resolution chart had feature sizes below the resolution limit of the lens, so the focus could be judged by examining the laser ablation of the chart to determine the lens position at which the finest features had been ablated. Having found focus, the image of a circuitry layer was overlaid on a via layer using the linear mask stage to achieve ablation to two different depths. The ablation was in an 18 μm BTX film, a proprietary polyimide and epoxy blend by Taiyo Ink, on a copper clad laminate. The optical micrograph in Figure 4.12 shows good registration of the via layer with the landing pad in the circuitry layer. The image on the left focuses on the bottom surface of the circuitry layer of ablation, and shows the 16 μm signal traces to have a flat feature profile ablated to a uniform depth. The image on the right focuses on the bottom surface of the via, which also shows uniform, clean ablation with no damage to the copper. Figure 4.13 shows an SEM micrograph of the same features from a different orientation. The perspective in the image shows the flat bottom feature profile of the 16 μm signal trace, and reveals information about the depth of the ablation, ~7 μm for the traces, pads and ground plane and 18 μm for the via.

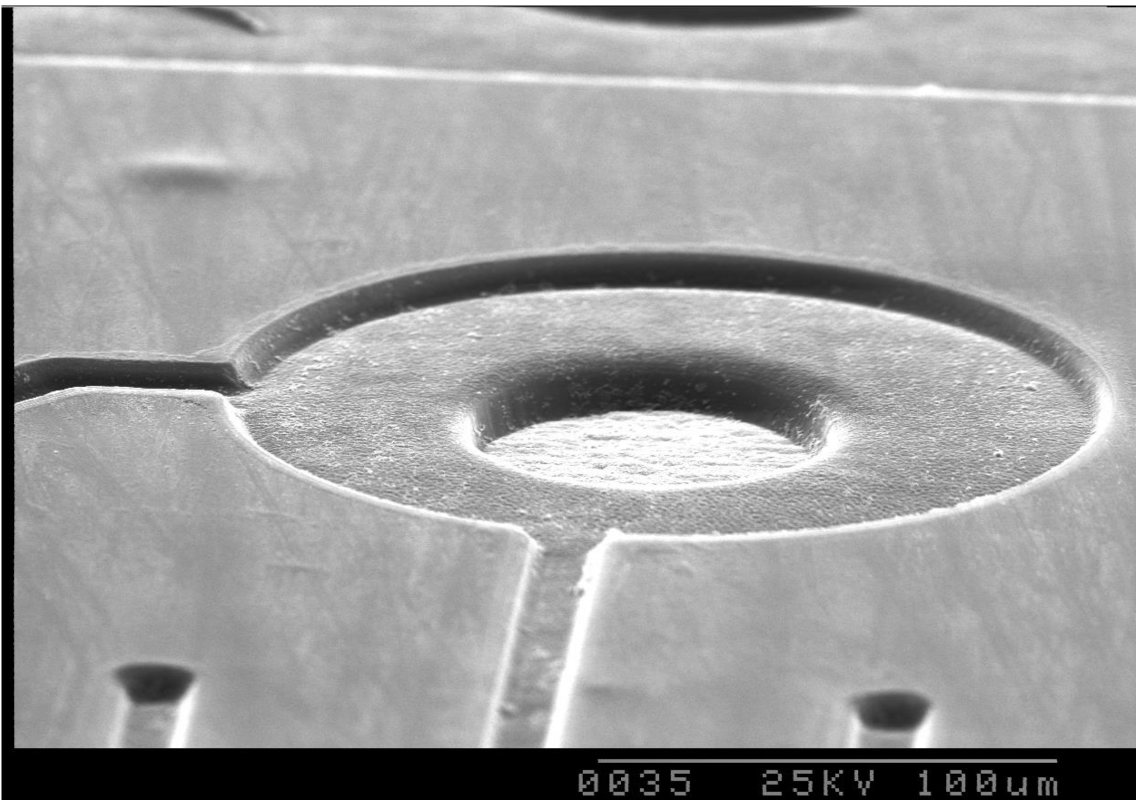

Figure 4.13 SEM micrograph of 16 μm signal traces, a landing pad and an 80 μm via drilled down to the copper layer below. The features are the same as those shown in the optical micrograph in Figure 4.12, and demonstrate good registration between the via and landing pad, a uniform ablation depth and the flat bottom feature profile of the 16 μm signal traces.

Figure 4.14 demonstrates the sample dependent resolution of the lens across a limited field. The optical micrograph shows the resolution chart used for focusing with diminishing line space features, and demonstrates the process can resolve 2 µm L/S features in a commercial polyimide, Kapton.

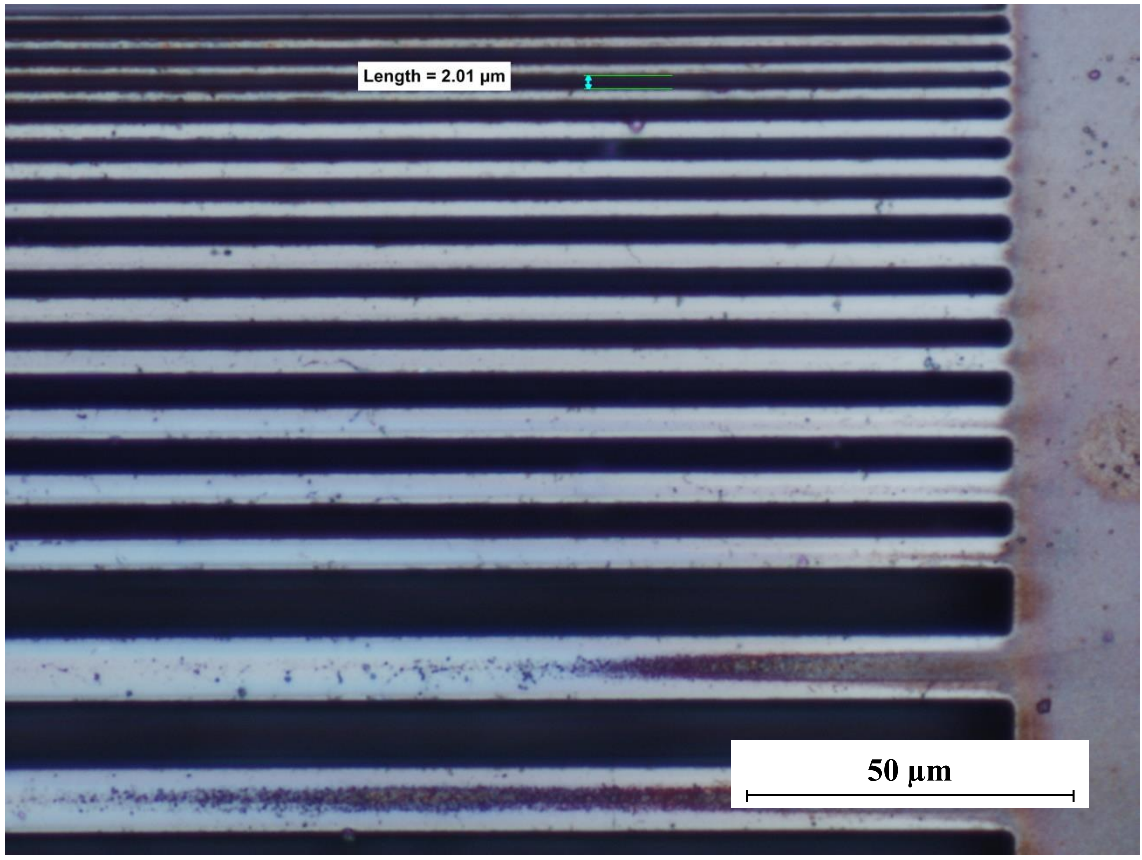

Figure 4.14 Optical micrograph of resolution chart with reducing line space features ablated into Kapton. The finest features at the top of the image are 2 µm L/S at the limit of resolution for the new lenses.

The SEM micrographs in Figure 4.15 show the variety of features that can be laser machined using mask imaging. The large ground plane features in both images would be impractical to make with a focused beam and a direct write approach, taking longer to machine. It would also be extremely challenging, if not impossible, to achieve the same depth uniformity with a focused beam. The micrograph in Figure 4.16 shows a large feature machined by a colleague using quasi-cw, 355nm Paladin laser used in a direct write system with f-theta lens and scanner. The image highlights the difficulty in machining a large area to a uniform depth with a small focused spot, which is not only time inefficient but also of a lower quality. A periodic variation in the ground plane ablation of the image on the left of Figure 4.15 is visible, and consistent with the pitch of the lines used to raster scan the mask. However looking along the edge of the large

square features, it is clear this variation brings about no appreciable difference in ablation depth, and could perhaps be attributed to debris ejected after each pass of the mask. The debris ejected from previous passes would be removed in the laser ablation occurring during subsequent passes, and thus only the debris generated from the laser ablation during the last pass of the mask would be visible at the substrate.

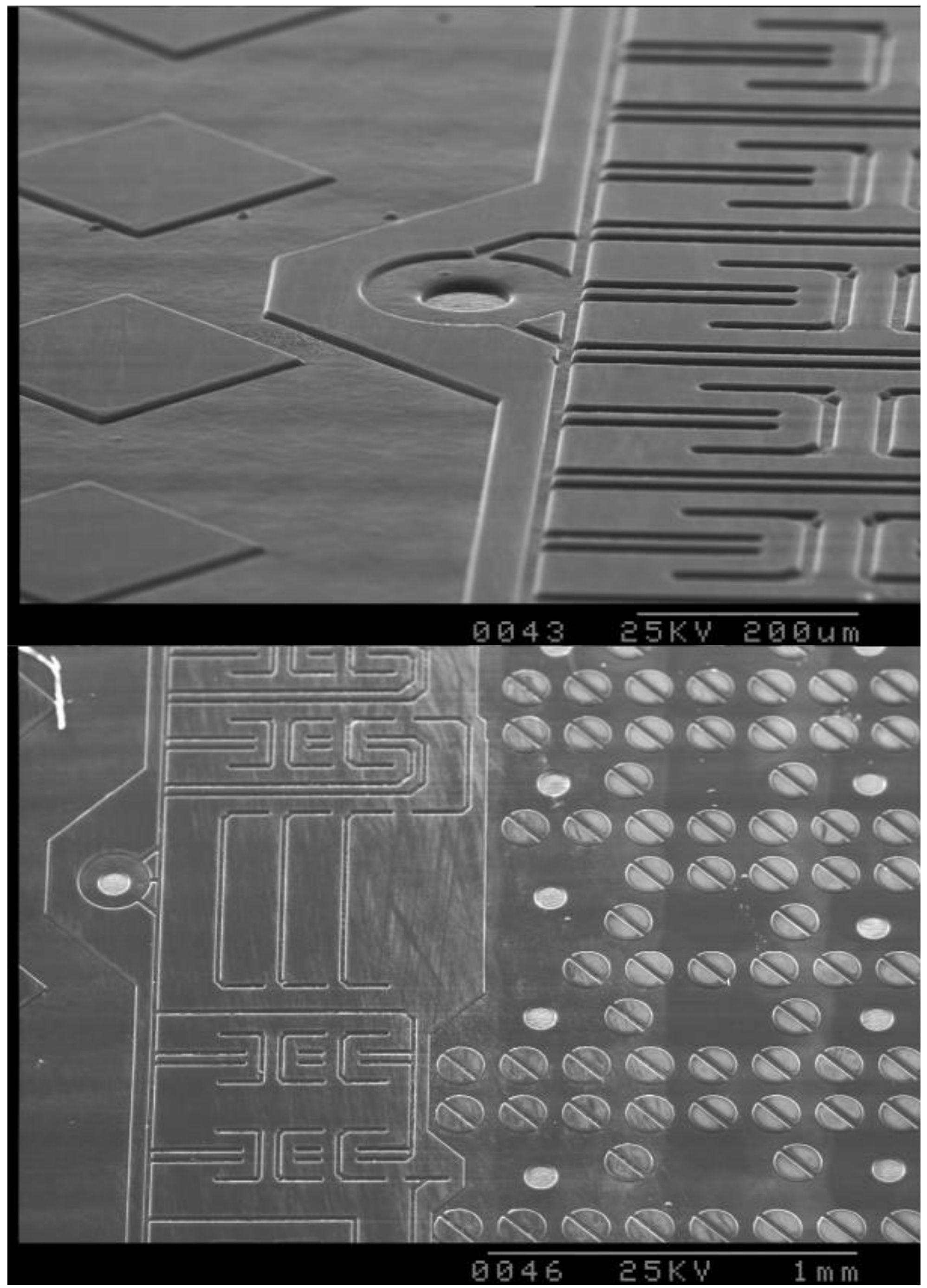

Figure 4.15 SEM micrographs showing ablation of the circuitry an via features, with 16 µm signal traces, 80 µm vias and large, uniformly ablated ground planes.

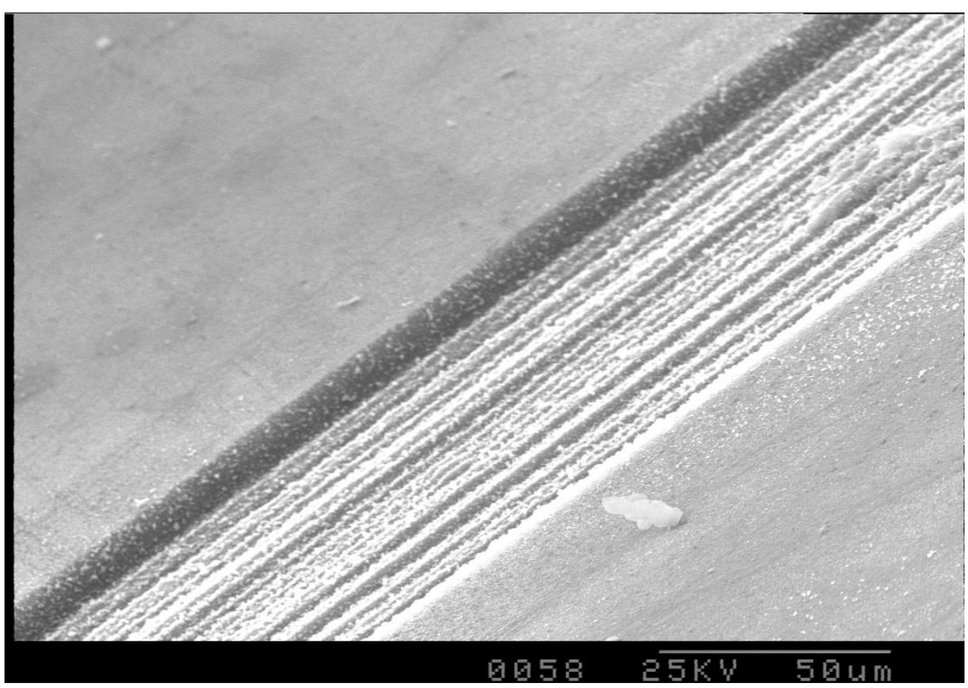

Figure 4.16 Large feature machined by a UV direct write system by overlapping adjacent scribes of a focused beam. The image highlights the difficulty in obtaining good depth uniformity when machining large areas with a comparatively small focused spot.

4.4.2 Selective mask scanning – samples for TPCA show

Having demonstrated very promising results described in Section 4.4.1, a decision at M-Solv was made to promote the SMI technology at the Taiwan Printed Circuit-board Association trade show. To do so, the mask shown in Figure 4.17 was made to demonstrate various features enabled by the SMI system, including the ability to selectively scan small areas of the mask possible due to the small beam size, and then the ability to overlay these features at the substrate plane either by using the linear mask stage or the x-y substrate stage.

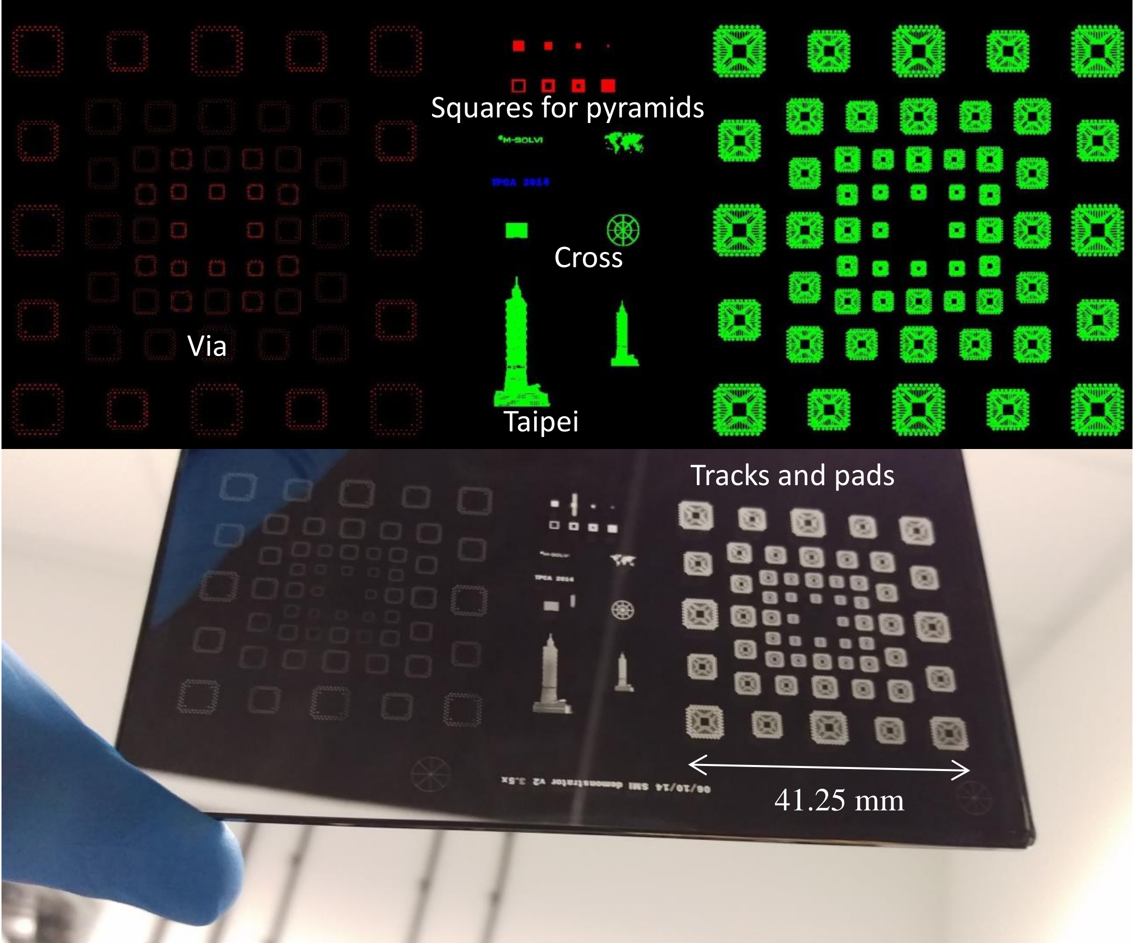

Figure 4.17 CAD file and photograph of the chrome-on-quartz mask used to produce demonstrator samples for the TPCA trade show. The object field of the projection lens is large enough to capture all features in the y-axis; however the mask must be moved relative to the lens on a linear stage to image all features in the x-axis. The data in the CAD image represents transparent regions on the chrome on quartz mask.

Each of the squares shown at the top of Figure 4.17 were raster scanned individually, and the images of each overlaid on top of each other using the linear mask stage to produce pyramid structures. A map of the world, and the Taipai 101 tower, above and below the cross hair feature used to align the mask respectively, were ablated adjacent to the pyramids to demonstrate that there were no restrictions in feature shapes in contrast to a direct write system. The array of circuit tracks and pads were ablated and overlaid with their respective vias, with feature sizes down to 3 µm L/S in the smallest demo devices, and vias down to 10 µm diameter. The text 'M-Solv' and 'TPCA 2014' were then ablated in the centre of the circuitry array. Prior to the ablation, the mask was aligned to the cross hair feature labelled in Figure 4.17. The mask could be moved in the x-direction on a linear stage to centre all the features in x with the lens. By knowing the y offset of the features relative to the cross hair, it was possible to accurately scan each feature, and then arrange the features in the y-axis by using a y-offset on the x-y

substrate stage to account for the offset with regard to the optical axis. A stitched microscope image of all the features arranged and ablated into polyimide on copper can be seen in Figure 4.18.

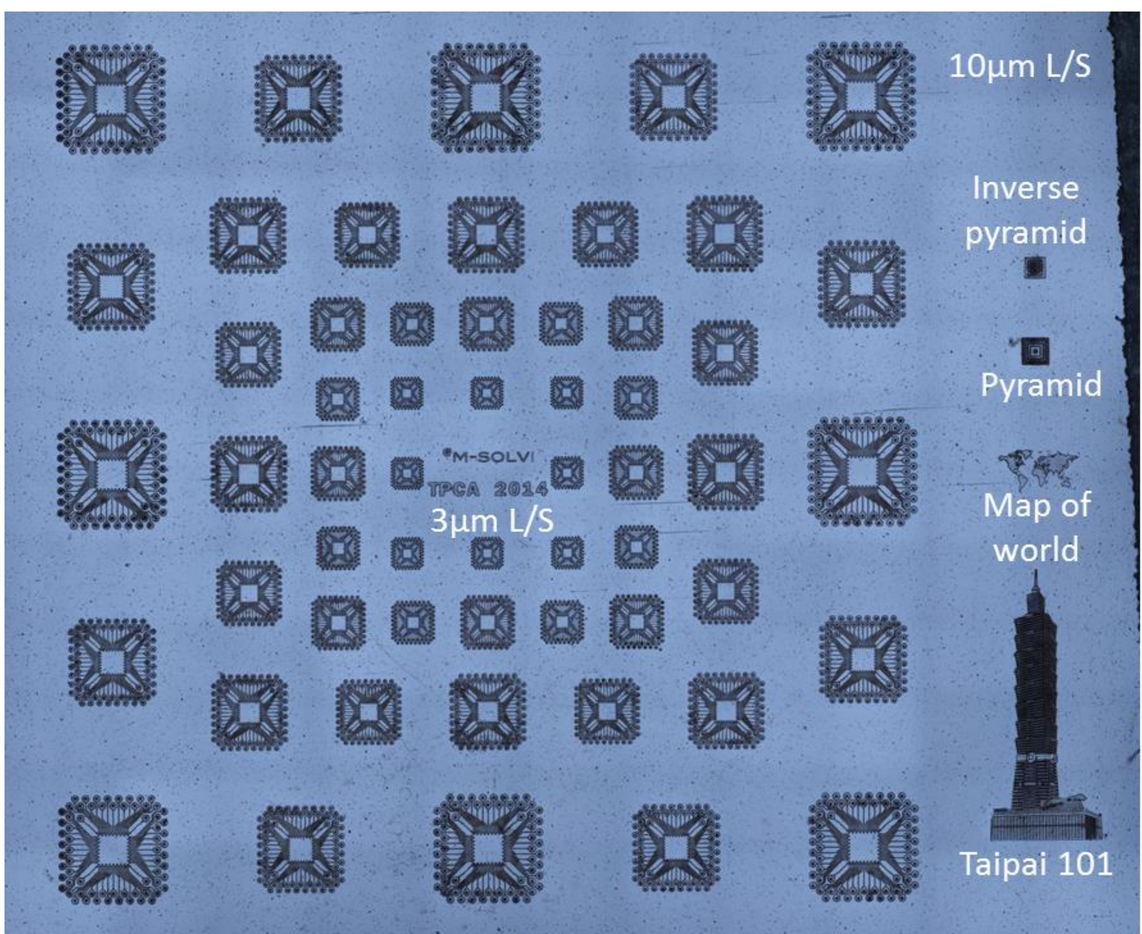

Figure 4.18 Stitched microscope image of the samples handed out at the TPCA trade show. The samples include demonstrator circuits with features down to 3 µm L/S and micromachined pyramids ablated into polyimide on copper. The sample has been cleaned to remove laser ablation debris using tape.

The pyramids shown in Figure 4.19 were both formed by overlaying the image of 4 square apertures. In the case of the inverse pyramid, the square apertures are simply getting smaller, such that only the central region is ablated with each scan of the different apertures. In the case of the other pyramid, there is an opaque chrome square of varying sizes centred on the transparent aperture, such that only the edge of the pyramid is ablated by all 4 scans of the apertures and is therefore the deepest. Although the pyramids are not of any obvious practical use, they demonstrate the accuracy with which one can overlay images using the linear stage in the mask plane, as well as the uniformity of the ablation even with several layers of ablation separated in time. More generally, it highlights the feasibility of overlaying any number of ablation layers, for

complex, multilevel ablation of structures, with the primary constraint being space for the different layers of ablation on the mask.

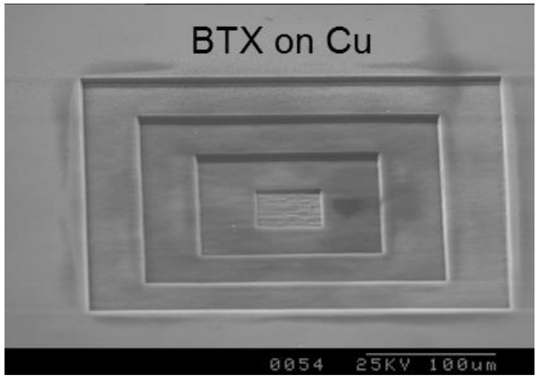

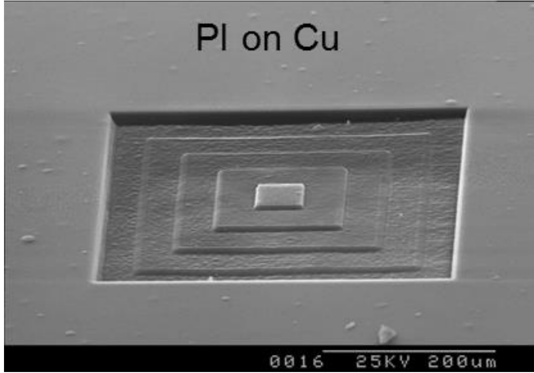

Figure 4.19 SEM micrographs of an inverse pyramid and a pyramid ablated into BTX on copper and polyimide on copper respectively. The pyramids were formed by overlaying the image of different size square apertures in the substrate plane.

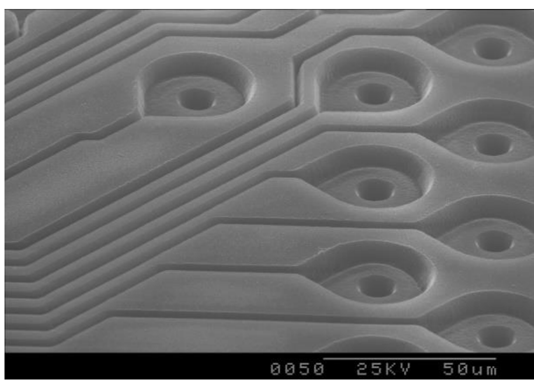

Figure 4.20 Laser ablation of the text ‘M-Solv’ and ‘TPCA 2014’ overlaid on an array of demonstrator devices. The devices surrounding the text have 3 µm L/S traces, as shown in the image on the right, and 10 µm diameter vias.

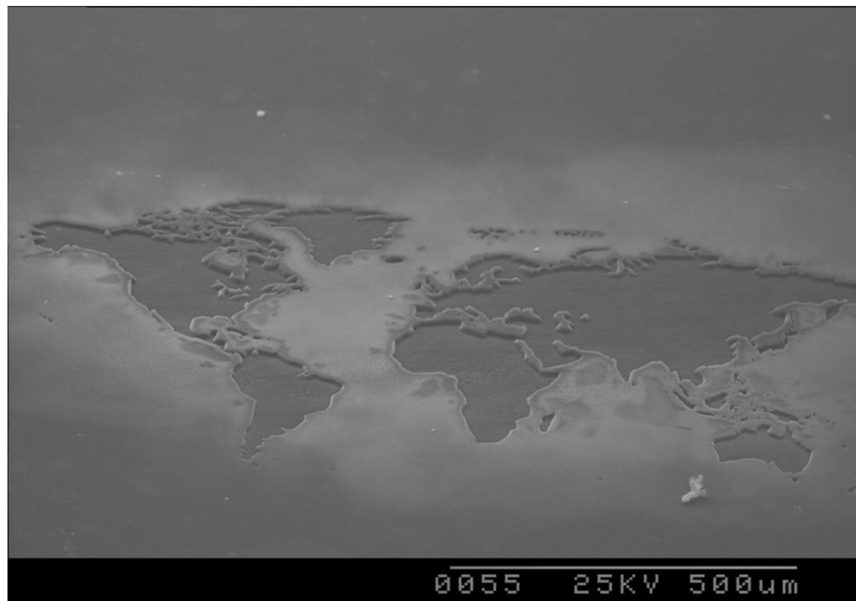

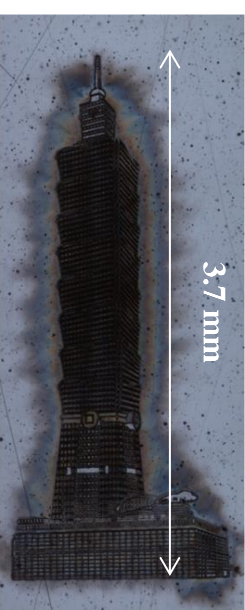

Figure 4.21 Laser ablation of a map of the world and Taipai 101 tower in polyimide on copper. The map demonstrates the uniformity of ground plane ablation, given that the feature size is a factor 2 bigger than the beam size and no stitching effects are visible. Both features demonstrate high resolution ablation of irregular features of any shape.

Figure 4.20 has images of the device array, and the text aligned to it. The image on the right hand side is a close up of the smallest device size, with 3 µm L/S signal traces and 10 µm diameter vias accurately registered with their pads. Figure 4.21 shows a map of the world and the Taipei 101 tower ablated into polyimide. The map of the world demonstrates the uniform ablation of an area larger than the beam with no beam stitching effects visible. The Taipei 101 tower was added to demonstrate that there were no design restrictions in what could be ablated by the SMI system, unlike a direct write system with a focused laser beam. The halo surrounding the Taipei 101 tower is laser ablation debris deposited on the surface of the polyimide. The laser ablation debris is often not an issue for the chip packaging industry, since the samples go through a desmear acid etch process after laser ablation to roughen the surface of dielectrics which improves the adhesion of the copper in the subsequent electroless copper plating process. However the laser ablation debris can be easily removed by a number of cleaning processes. Figure 4.22 shows stitched microscope images of the demonstrator device array handed out at the TPCA show before and after cleaning with an adhesive tape. Alternatively, an ultrasonic bath with isopropyl alcohol (IPA) can be used to clean the samples. Simply wiping the samples with a cloth and IPA removes the laser ablation debris form the surface of the samples, but has a tendency to push and trap the laser ablation debris into the laser ablated features.

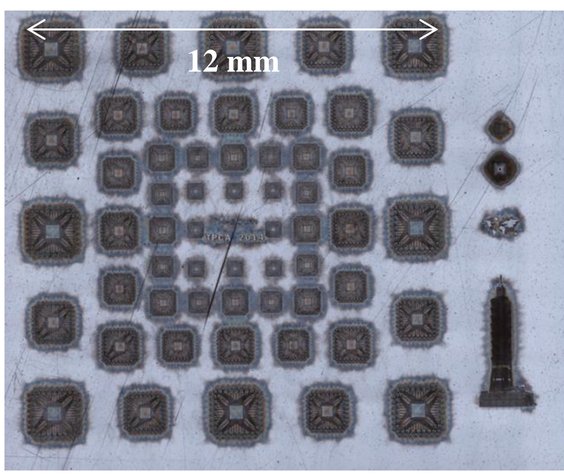

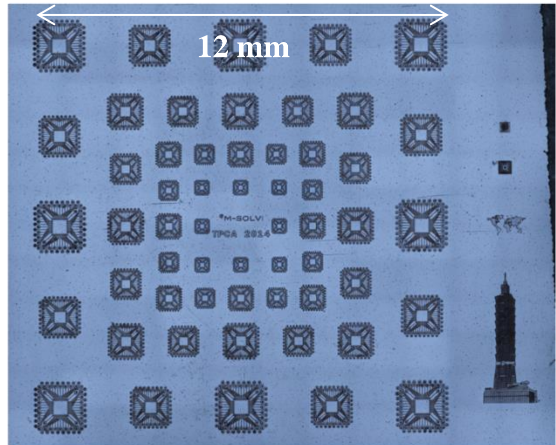

Figure 4.22 Stitched microscope images of demonstrator device samples handed out at the TPCA show taken before and after tape cleaning respectively.

4.4.3 Resolving the issue with infinity imaging system

To avoid the issue of the beam waist below the mask described in section 4.3 thought to be related to the beam reduction brought about by the f = 500 mm lens and the f = 160 mm, it was decided to switch the f = 500 mm lens for an f = 300 mm. This reduced the beam reduction brought about by the two lenses, to better fill the entrance pupil of the f-theta lens. Additionally, since it was not possible to observe the beam propagation inside the scanner, it was decided to move the f = 160 mm singlet as close to possible to the scanner. This reduced the optical path length between the f = 160 mm singlet and the f-theta lens to try to minimise further expansion of the beam due to the divergence of the approximately collimated beam before entering the entrance pupil of the f-theta scan lens.

Using the f = 300 mm singlet after the DOE led to a reduction in the square beam size both in the plane of uniformity and in the mask plane. According to Equation (4.1), the new beam size is 0.89 mm, which brings the fluence in the plane of the mask above the damage threshold of a chrome-on-quartz mask. Using aluminium-on-quartz masks, which reportedly had a higher damage threshold in excess of 250 mJ cm^{-2}, it was both possible to use the f = 300 mm lens and increase the maximum fluence with which a sample could be processed. Feedback from customers indicated that steep side walls with very little taper were beneficial to trace signal integrity, since pointed signal traces can lead to signal emission from the point. Thus the increased range of usable fluences was also useful for tuning feature profile shape, with increased fluences and higher ablation rates known to reduce feature taper angle. The impact of fluence on feature profile is discussed more fully at a later point.

The combination of a larger beam with a lower divergence after the f = 160 mm singlet and a shorter beam propagation path to the f-theta lens resolved the problem of the beam waist near the first element of the projection lens. Additionally it allowed higher fluences to be achieved at the substrate, and thus greater control of feature profile by changing the fluence by changing the pulse energy.

4.4.4 Aperture imaging from the plane of uniformity and beam stitching effects

Having set up the infinity imaging system, it was decided to investigate why beam stitching effects had not been more apparent in ground plane ablation. It had been expected when setting up the system that some artefact from the edge of the beam might be visible in the ablation and depth profile of areas much larger than the beam. It is certainly possible to observe periodic variation in the ablation depth of large features, with the period being consistent with the pitch and mark speed of the raster pattern used to scan the mask, however this was easy to tune out. To investigate whether the absence of beam stitching effects was a result of the sloped edge profile of the top hat beam formed by the DOE, a square aperture was placed at the plane of uniformity and imaged down onto the mask to give the beam sharp edges. Prior to installing the aperture, the imaging performance of the system was tested with the infinite conjugate imaging of the uniform beam to confirm that any change brought about in the beam divergence after the mask had not detrimentally affected the performance of the imaging system by changing the filling of the object side NA of the projection lens. Figure 4.23 shows that the performance of the imaging system is at least as good as with the finite conjugate imaging system by demonstrating 2 μm L/S ablation in an ABF-type build up substrate.

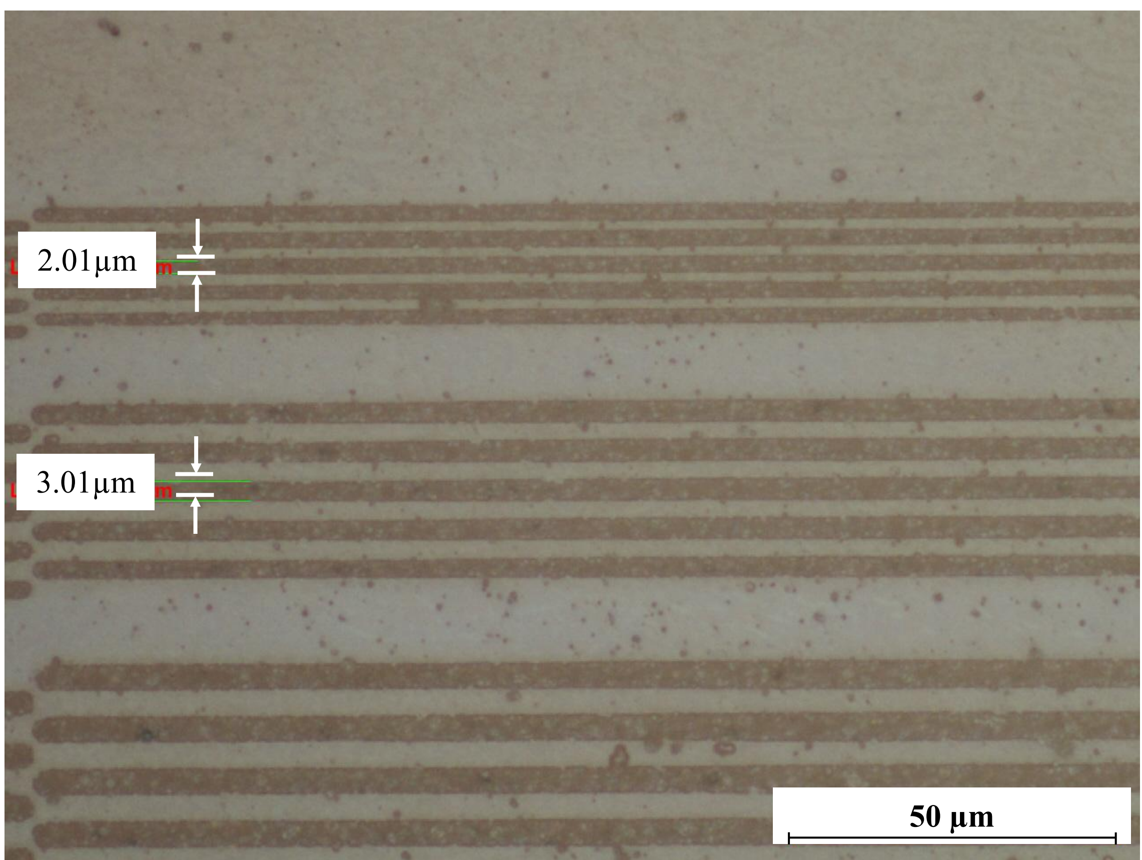

Figure 4.23 Microscope micrograph of resolution chart patterned by SMI after installing the infinite conjugate imaging system of the plane of uniformity. The substrate is an ABF-type substrate of epoxy with glass filler particles. The image demonstrates 2 µm L/S laser ablation of the substrate and good performance of the imaging system. The measurement error is ±0.14 µm.

Having confirmed the imaging system was still performing as expected, the aperture was installed in the plane of uniformity on a micrometer stage, and focused by moving the aperture along the optical axis until the image of the aperture at the mask plane, relayed down to the substrate by the projection lens, was in focus at the substrate plane. A mask was then scanned at less than 1 shot per area both with and without the aperture and images of the laser ablation can be seen in Figure 4.24. On the left hand side of the image, the blue areas between the laser pulses demonstrate the sloped edge of the beam, where there is partial or lower fluence ablation of substrate. In the image on the right hand side, these areas of lower fluence ablation are clearly not present, due to the sharp beam edge brought about by imaging the aperture. The angle of the lines in the image on the right is due to the misalignment of the aperture orientation with the axes of the scanner.

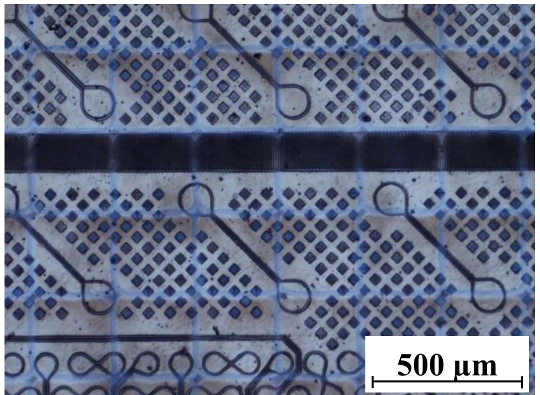

Figure 4.24 Image of a mask scanned at less than 1 shot per area both without (left) and with (right) an aperture imaged onto the mask from the plane of uniformity formed by the DOE. The orientation of the aperture in the image on the right hand side has not been aligned to the axes of the scanner.

The aperture alignment was then corrected and the dimensions of the image of the square aperture calculated so that the mask could be scanned with precisely one shot per area. Figure 4.25 shows the corrected aperture alignment, and the imaged aperture size was measured to be (200±2) µm by (205±2) µm. Thus the mask was scanned with a pitch of 718 µm and a mark speed of 3500 mm s^{-1} such that it was scanned with 1 shot per area as can be seen in Figure 4.26. The beam stitching effects are very apparent, with unacceptable ridges and lines in the laser ablation.

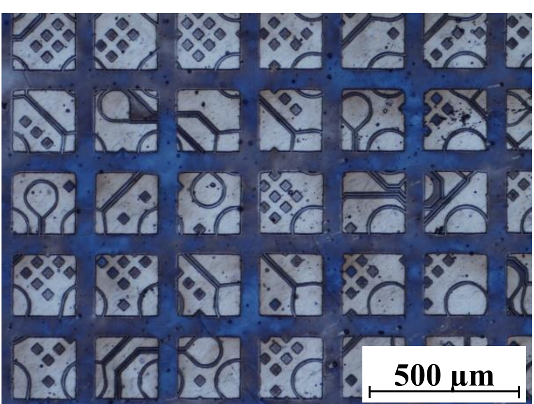

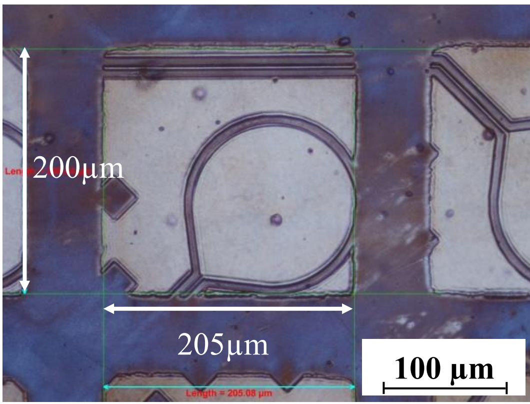

Figure 4.25 Optical micrographs of ablation when the mask is scanned with a square aperture imaged onto the mask. The image on the left shows the orientation of the square aperture has been adjusted such that it is aligned with the axes of the scanner. The image on the right shows the dimensions of square aperture, used to calculate the parameters required to scan the mask with the correct shot overlap.

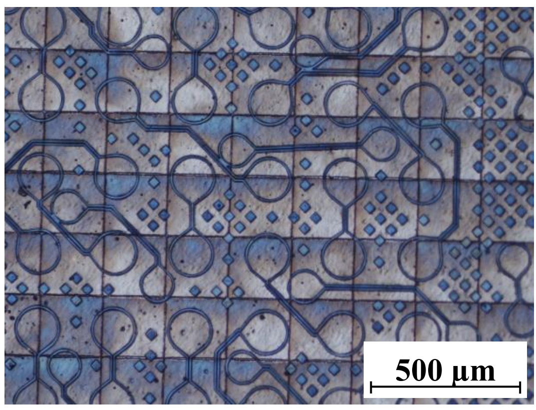

Figure 4.26 Mask scanned with square aperture in beam with 1 shot per area. The beam stitching effects are clearly visible.

The mask was then scanned at 4 shots per area with 2 shots in the horizontal direction and 2 shots in the vertical direction. This was done by both scanning the mask 4 times at 1 shot per area, with each scan of the mask in a 2x2 array with a 0.35 mm pitch, and by halving the pitch and mark speed of the original vector file to put down the 4 shots in a single scan of the mask. The shots were distributed in this fashion in an attempt to homogenise the illumination of the mask and alleviate the stitching effects observed in Figure 4.26. The results can be seen in Figure 4.27, and clearly the pitch in x and y is half that of the 1 shot per area scan shown in Figure 4.26 as expected. The key difference between the 2 images is the amount of laser ablation debris left on the surface of the substrate. In the image on the left, in which the mask was scanned 4 times at 1 shot per area, the debris from the previous scans is removed in each subsequent scan of that mask, such that only the debris generated in the final scan is deposited on the surface. In the image on the right, most of the laser ablation debris from the single pass is deposited on the surface of the ablation. However, the additional shots in both cases have not helped reduce the visibility of the beam stitching effects. Therefore one can conclude that the soft beam edge shown in the beam profile in Figure 4.5 obtained as a result of using the DOE in conjunction with a multimode beam is essential to masking the beam stitching effects to obtain uniform ground plane ablation as shown in Figure 4.21.

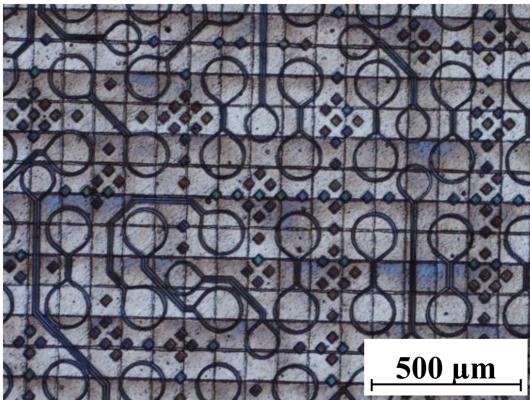

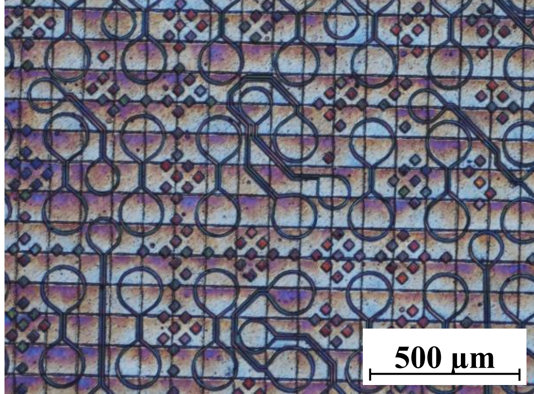

Figure 4.27 Mask scanned with a square aperture in the beam at 4 shots per area. In the image on the left the mask was scanned at 1 shot per area 4 times, with each scan offset in a 2x2 array with a pitch equal to half the spot size. In the image on the right the mask was scanned with 4 shots per area in a single pass of the mask.

4.5 Summary

A custom imaging projection lens and illumination system was specified, and the performance simulated and evaluated using a Zemax ray tracing model. The illumination system was installed and an unexpected beam waist was observed close to the plane of the first element of the projection lens. As a temporary solution, the f-theta lens below the scanner was used in a finite conjugates imaging system to image the plane of beam uniformity formed by the DOE onto the mask. This enabled the production of demonstrator samples to promote the SMI technology, however resulted in non-optimal performance of the f-theta lens since it was being used outside of its focal plane. After the samples had been produced, the illumination system was reverted back to the infinite conjugates imaging system of the plane of uniformity, however with a shorter focal length lens following the DOE. This led to a smaller beam reduction prior to the scanner, and a higher fluence at the mask plane which necessitated the use of Aluminium-on-quartz masks. The imaging system was found to be performing well and an aperture was introduced to the plane of uniformity and imaged onto the mask to investigate the impact of a steep edge to the beam profile. It was found that beam stitching effects become very noticeable when the beam profile has a sharp edge, and that the sloped beam edge formed by the DOE when used in conjunction with a multimode laser is ideal for masking beam stitching effects and obtaining uniform large area ablation. Thus the optimum configuration for the custom imaging lens and illumination system was determined, enabling further investigation of the performance of the imaging system and some of the unique aspects of the SMI approach.

Chapter 5: Characterising the SMI System

Following the set up the custom imaging optics, and the optimisation of the mask illumination in the imaging system, the next step was to assess the performance of the imaging system. The depth of focus and imaging resolution were investigated across the image field. In addition, some of the unique features of the SMI system, not possible with other types of mask imaging systems, were explored. Finally, this chapter concludes by looking at the compatibility of the SMI system with existing mask imaging techniques, including exposing a photoresist and the use of halftone masks for variable depth ablation.

5.1 Imaging Performance of the SMI System

5.1.1 Depth of focus

Wafer level packaging (WLP) is a popular packaging technology. In WLP a redistribution layer can be patterned directly onto an already processed wafer, prior to the wafer dicing, by spinning a polymer passivation layer onto the wafer. The polymer is then patterned and plated using the preferred methodology, which in the context of SMI is laser ablation, and the subsequent plating steps to fill the laser ablated features with copper.

Having obtained some polyimide spun on a polished silicon wafer, a resolution chart was used to focus the image of the mask onto the substrate. Given the extremely high planarity of the polished wafer, it was decided to investigate the depth of focus of the system to determine whether auto-focus equipment would be required to pattern 500×500 mm panel sized substrates. The sample flatness was measured and made parallel to the x-y substrate stage using a DTI. The wafer was levelled until there was <5 µm height variation from one side of the 200 mm wafer to the other. The resolution charts were then scanned at 1 mm intervals to further minimise the effect of any height variation across the substrate. The chart was scanned 5 times around focus, each time changing the substrate to lens separation by 10 µm using the micrometer stage on the lens mount. Images of the 5 ablation sites can be seen in Figure 5.1. At focus, the 2 µm L/S features at the top of the image are well resolved. At ±10 µm the 2 µm L/S features begin to go out of focus, with some erosion and ablation of the areas between the traces. However the 3 µm L/S tracks, although slightly wider, are still acceptably resolved. At +20 µm the image quality has continued to degrade and at +30 µm both 2 µm and 3 µm L/S features are out of focus to an unacceptable extent. Based on the results it was

concluded that the depth of focus for maintaining acceptable ablation of 3 µm L/S features was between ±10 µm and ±20 µm.

Whilst maintaining this degree of flatness over a 500×500 mm panel would be mechanically very challenging in terms of planarity and levelling of the chuck, maintaining this degree of flatness over a 20×20 mm image field is not. It was therefore decided to implement an upgrade to the system which, as well as improving the optomechanics for the projection lens and mask, added a linear Z-wedge stage underneath the chuck and a height sensor such that the lens to substrate separation could be adjusted at each ablation site.

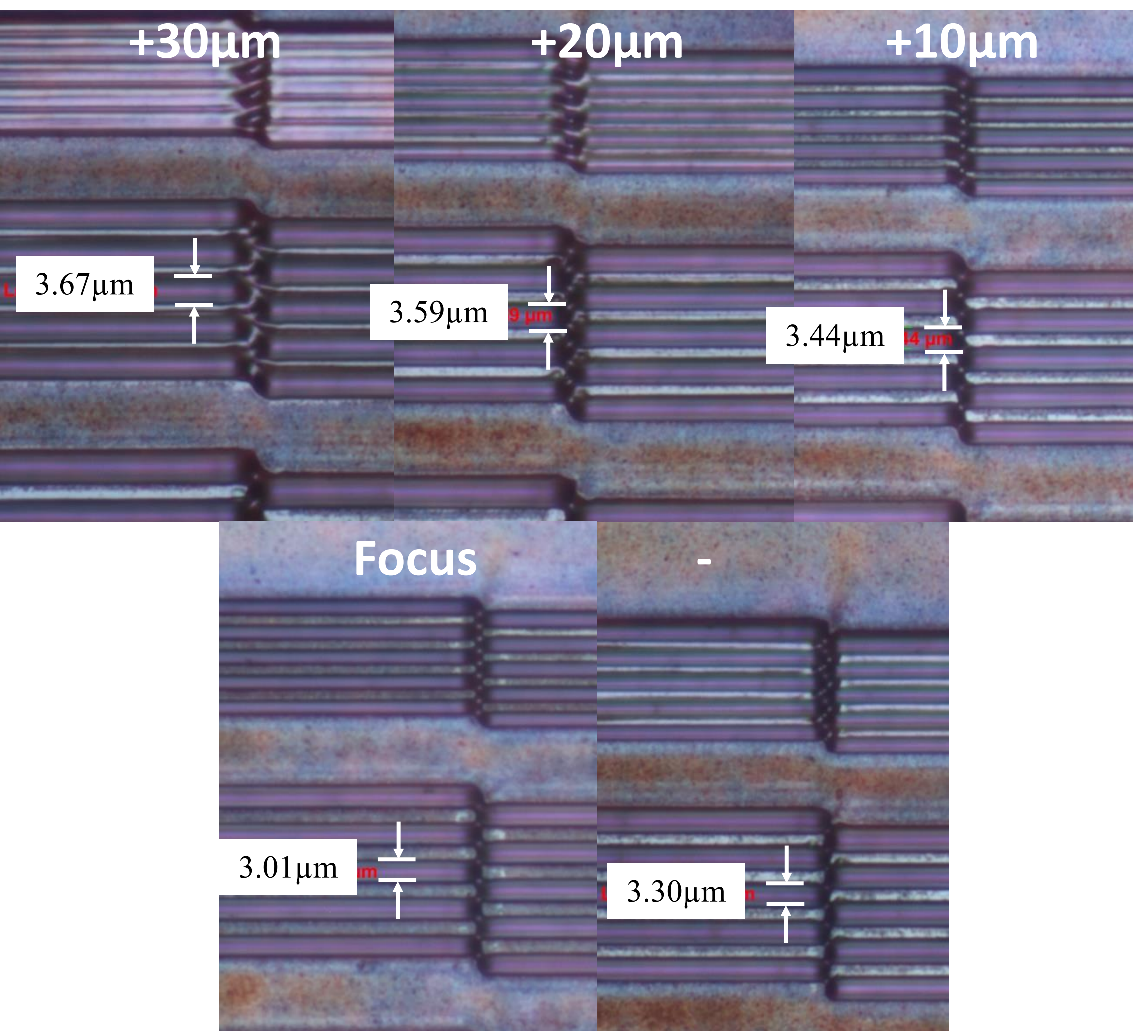

Figure 5.1 Focal scan using the SMI system performed by scanning a resolution chart and then adjusting the lens to substrate separation in 10 µm increments. The focal scan was performed on polyimide spun onto a polished wafer, so the planar substrate gives a reliable estimate of the depth of focus. The measurement error is ±0.14 µm.

Having completed the depth of focus tests, the demonstrator fanout device was ablated into the polyimide on wafer, including microvias through the 10 µm polyimide film.

An image of the laser ablation of the smallest demonstrator device can be seen in Figure 5.2. The diagonal traces in the image are 3 µm L/S and the microvias, which are well registered with the landing pads, are 10 µm in diameter. The results demonstrate the potential to use SMI in WLP. The planarity and smaller size of wafer substrates when compared to panel formats actually reduce the engineering challenges associated with maintaining focus across the sample.

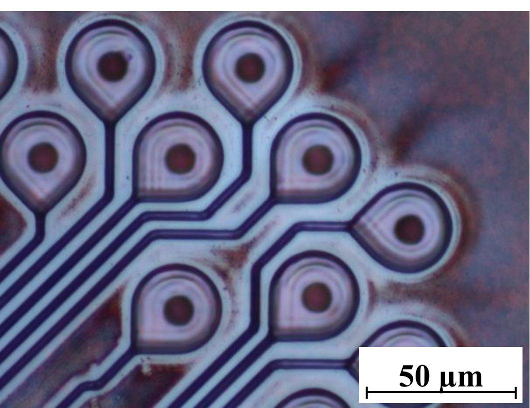

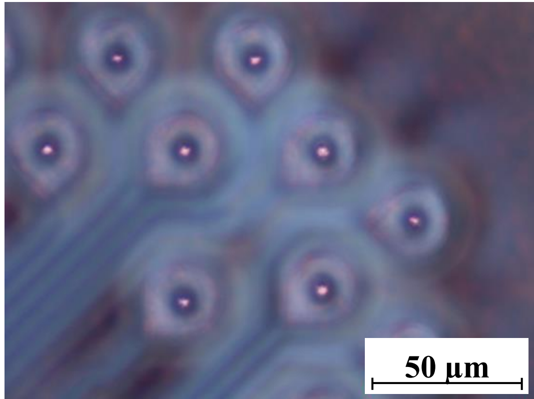

Figure 5.2 Optical micrograph of laser ablation of demonstrator fanout device with 3 µm L/S traces and 10 µm microvias in polymide spun on a silicon wafer. The polyimide film is 10 µm thick. The image on the right focuses on the bottom surface of the vias and shows that all the polyimide has been removed.

5.1.2 Resolution across image field

The capability of the lens to enable laser ablation of 2 µm L/S features across a limited image field has been demonstrated, but in order to deliver a 20×20 mm chip package the lens resolution across its entire image field needed to be investigated. To do this a new photomask was purchased and the CAD data for the mask can be seen in Figure 5.3. The mask has a 3×3 array of resolution charts, spokes, and larger open areas to test ablation uniformity. In hindsight, the mask design could be improved, since the mask is not symmetric about the optical axis and all the lines making up the resolution charts are of the same orientation, making the test less sensitive to aberrations that are dependent on feature orientation such as astigmatism.

ITO on glass was used as a substrate to ensure good substrate planarity. The array of images in Figure 5.4 shows the ablation of each of the finest features in each resolution chart at different points in the image field. The 3 µm L/S features are acceptably resolved in all points of the image field except for in the top right, where the features not well resolved. If this were due to field curvature in the lens, the aberrations would be expected to be symmetric about the optical axis, however other points which are the same radial distance from the optical axis such as the lower right image are clearly

better resolved. This could suggest the anomaly is due to the bowing in the chuck, or perhaps a defect protruding from the chuck's surface such as the burr of a scratch.

Irrespective of the cause, the result justifies the need for the upgraded system with the height sensor and z-wedge. If maintaining focus across an image field is a challenge, achieving this across a 500×500 mm substrate with potential thickness variations and bowing in the chuck would not be possible without some adjustment to the focus.

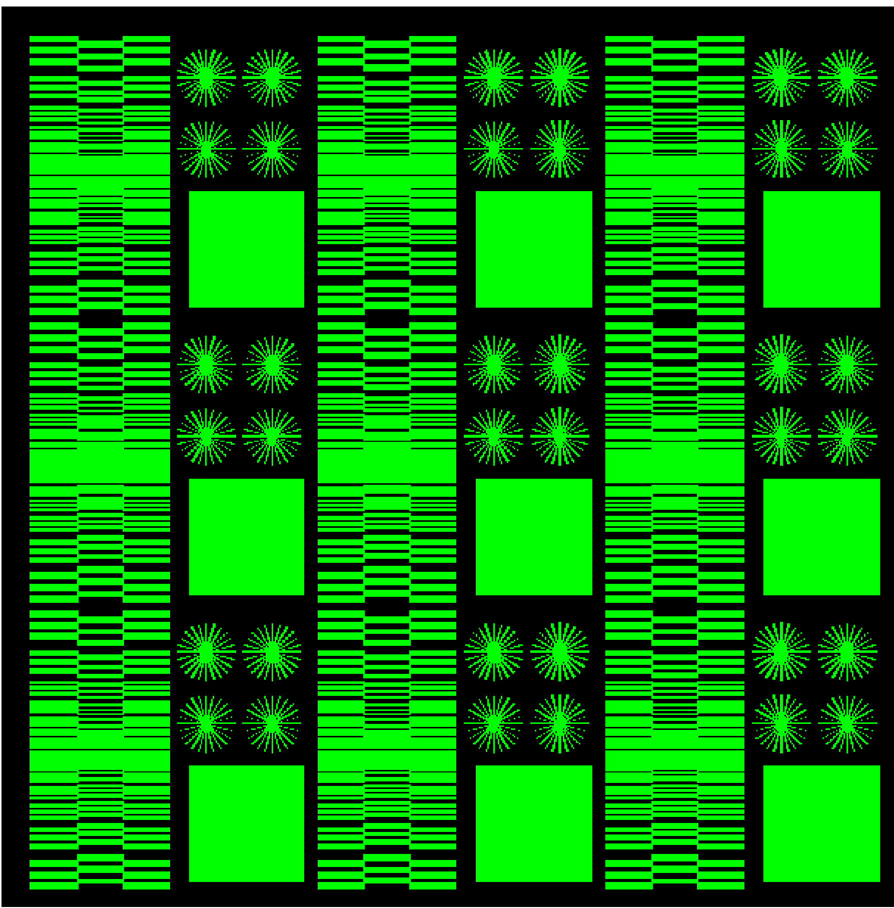

Figure 5.3 CAD data for mask designed to assess lens performance across its image field. The mask contains a 3×3 array of resolution charts, resolution spokes and a large square to test ablation uniformity. Each tile in the array is 5×5 mm.

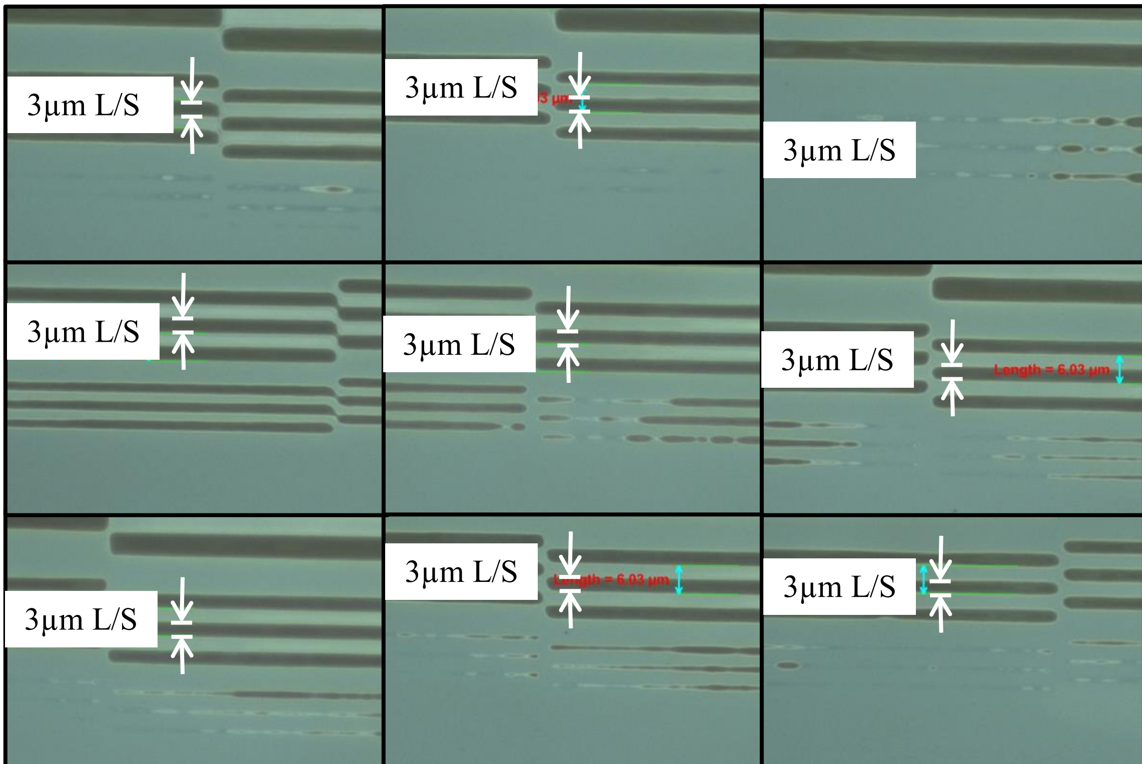

Figure 5.4 Array of optical micrographs of resolution charts ablated in different parts of the image field in a single pass of the mask depicted in Figure 5.3. The figure shows the lens is capable of resolving 3 µm L/S features across the majority of its image field, however with some variation in focus with particularly poor focus in the top right area of the image field. The measurement error is ±0.14 µm.

There is also some evidence of mild astigmatism in the optical system. The effect is exacerbated at defocus, and can be seen in Figure 5.5. The image shows how lines of tangential and radial orientation with respect to the optical axis are resolved differently. Specifically, the lines tangential to the optical axis have not been resolved at all, where as partial ablation can be seen in lines of an equal width (spatial frequency) but different orientation. This aberration is indicative of astigmatism in the optical system, and is in line with the mild astigmatism predicted by the Zemax model of the lens discussed in Section 2.2. It should be noted, however, that this does not affect the ability of the lens to resolve 3 µm features when the image is well focused.

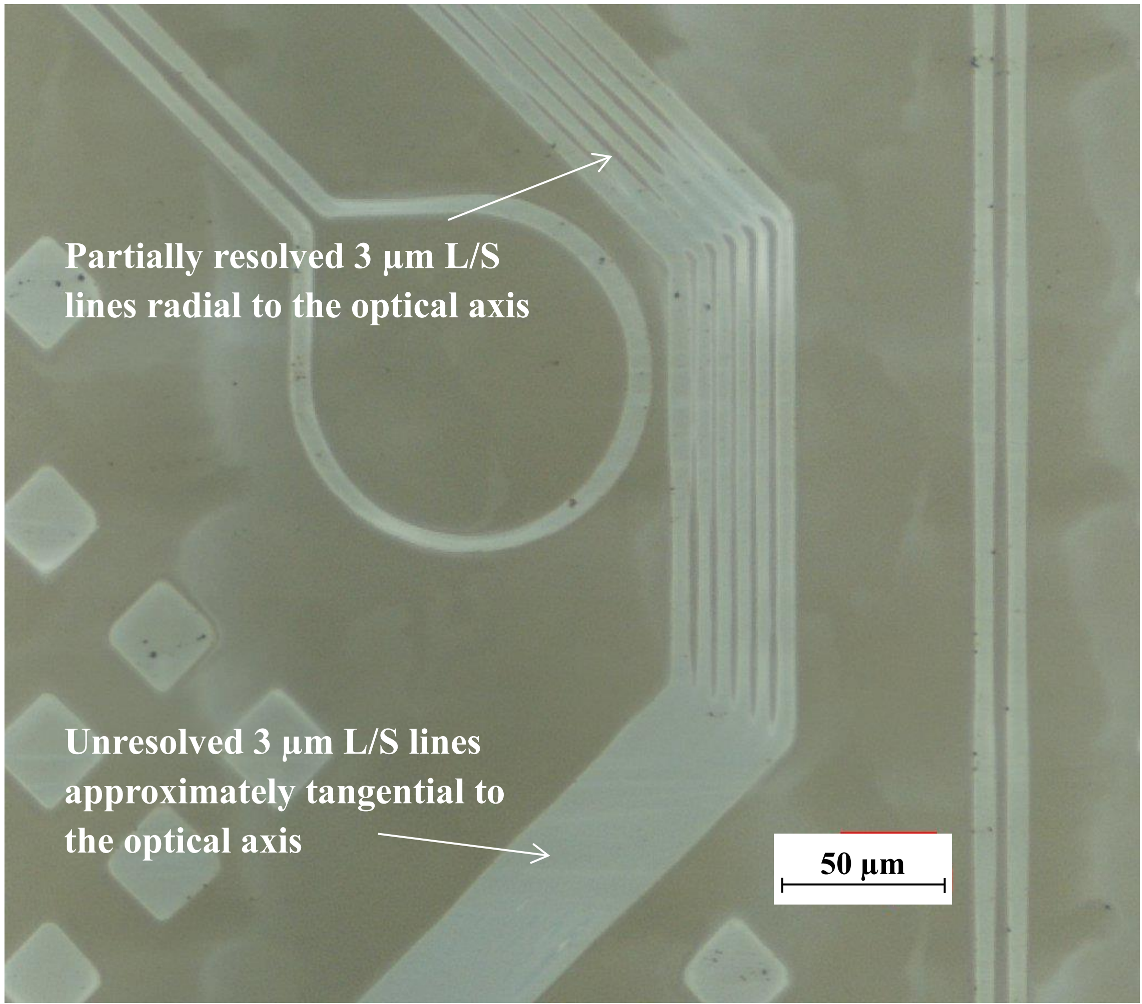

Figure 5.5 Optical micrograph showing evidence of astigmatism in the lens image at defocus. The darker areas in the image represent areas of ITO ablation. The 3 µm L/S features tangential to the optical axis are less well resolved than radial lines. The ablation is in ITO on glass and the mask image has been intentionally defocused to accentuate the astigmatism.

In focus ablation of ITO on glass is shown in Figure 5.6. The ablation has well defined, sharp edges, with removal of all visible ITO in the ablated regions and no damage or delamination of the ITO in the areas adjacent to the ablation. This is due to a number of factors, one being that the glass substrate has low absorption at 355 nm. This means that additional shots can be fired to ensure complete removal of the ITO layer with no risk of damaging or heating the substrate and causing delamination of the ITO in the areas adjacent to the laser ablation. The ITO adhesion to the glass substrate is also very strong, further reducing the risk of delamination. The thin ITO film thickness, ~50 nm, also ensures the ablation has no taper which improves the appearance of the edges. ITO is commonly used as the transparent conductor in capacitive touch panels. Feature sizes of these dimensions are not usually required in conventional touch panel displays, but

interest has been shown in using SMI for patterning transparent, capacitive finger print sensors [81].

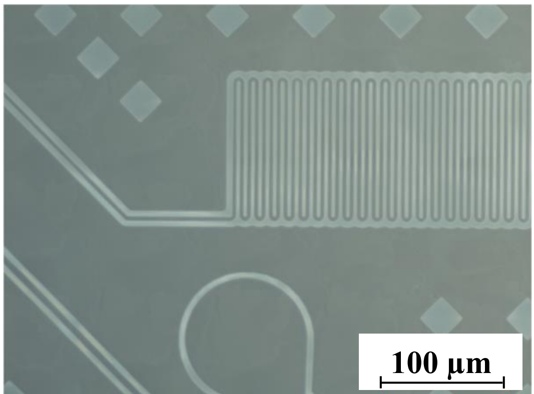

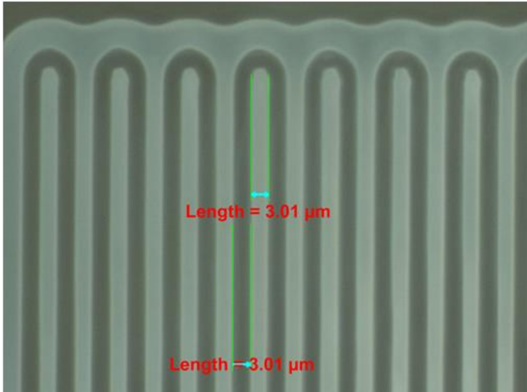

Figure 5.6 Optical micrographs of in Focus ablation of ITO on a glass substrate. The image shows a 3 µm L/S serpentine feature well resolved by the SMI system. The ITO has been ablated in the darker areas of the image. The measurement error is ±0.14 µm.

The imaging performance of the SMI system was assessed following the installation of custom imaging optics. The depth of focus for high quality ablation of 3 µm L/S features was found to be ±10 µm. The resolution across the lens image field was explored, and the lens was found to be able to resolve 3 µm L/S features across the majority of a 15×15 mm image field. The short depth of focus highlights the need for accurate focus control in a production system.

5.2 Variable intensity ablation with the SMI system

A unique property of SMI, when compared to other mask imaging systems discussed in Sections 2.4.2 and 2.5.1, is the ability to have some degree of control over the time between consecutive shots delivered to a given part of the mask and substrate. The relatively high repetition rate DPSS laser, and the accurate and rapid scanning of the mask allowed by the galvanometer scan head, allows the user to change the mask scanning regime to change the period between shots at a given point on the substrate. The mask is scanned with a galvanometer scanner with a certain mark speed, which determines shots in x direction delivered at the repetition rate of the laser. The pitch determines shots delivered in y direction, and the number of bursts of pulses at the repetition rate of the laser. The mask can be scanned a number of times to build up the required number of shots. These 3 parameters determine the intensity profile. The graphic in Figure 5.7 illustrates how energy would be delivered to the substrate over time with 4 Shots Per Area (SPA) per scan, and the start of a 2nd scan of the mask. The mark speed is set so that there are 2 shots in the *x* direction, such that the scanner

mirrors have deflected the beam by a distance equal to half the spot size in the period between pulses. The pitch of the lines in the illumination pattern is then set to half the spot size, such that there are 2 shots in the *y* direction. If the mask were scanned twice at 4 SPA to deliver a total of 8 SPA, this would be denoted (2, 2, 2) such that the product of the numbers gives the total SPA and each number denotes (shots in *x*, shots in y, number of mask scans). The time between shots in a given area also depends on other factors such as the size of the area being scanned at the mask, and whether the area is being scanned with a serpentine or raster scan illumination pattern. However, in general, the higher the first 2 numbers, the more thermal effects become a factor in the laser ablation process because this indicates a large number of shots per area occur per scan of the mask giving the substrate less time to cool down between successive scans.

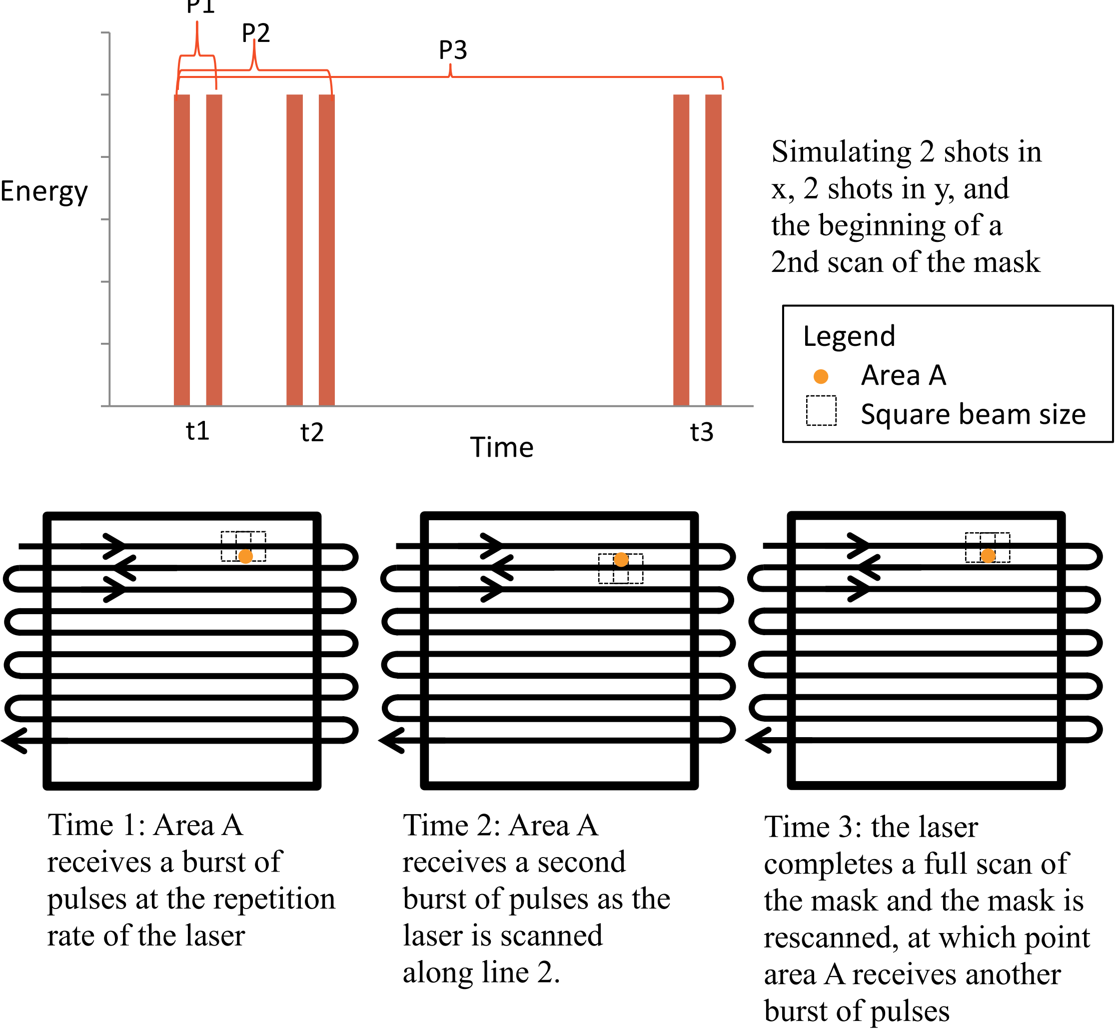

Figure 5.7 A graphic illustrating the intensity control possible with the SMI system. The cartoon graph shows the energy delivered to area A, a given area of the mask or substrate. The mark speed determines how many shots are delivered in the x direction, and the number of pulses in the burst, P1. The pitch determines the shots delivered in

the y direction, and the number of bursts of pulses in P2. The total number of times the mask is scanned with this mark speed and pitch determines how many times P2 is repeated in segment P3.

To investigate the effect of different mask scanning regimes on the ablation quality, a resolution chart was scanned and ablated with the same fluence but different mask scanning regimes into an ABF type build up substrate common in the chip packaging industry. The ABF type substrates are epoxy with small glass filler particles. The ablation of the resolution chart can be seen in Figure 5.8, where the finest scale features at the top of the image are 2 μm L/S. Both charts were scanned with 25 SPA, however the chart on the left was scanned with (5, 5, 1) and the chart on the right with (1, 1, 25). The impact of delivering the 25 shots in a single scan is clear, particularly in the fine scale features. The walls between the channels have completely collapsed for all channels at 6 μm L/S and below. Comparing this with the 25 scans at 1 SPA, despite the 25 SPA delivered to the substrate, there is only trace collapse in some areas of the 2 μm L/S features. By simulating the scanning of the illumination pattern used in the (1, 1, 25) mask scanning regime, the effective repetition rate as seen by a given area of the substrate is estimated to be <100 Hz. This is in contrast to the (5, 5, 1) scan which delivers shots in the x direction at the frequency of the laser, 5 kHz. This lower intensity ablation gives the substrate time to cool between shots, and in this substrate, gives a much better result in the smaller features.

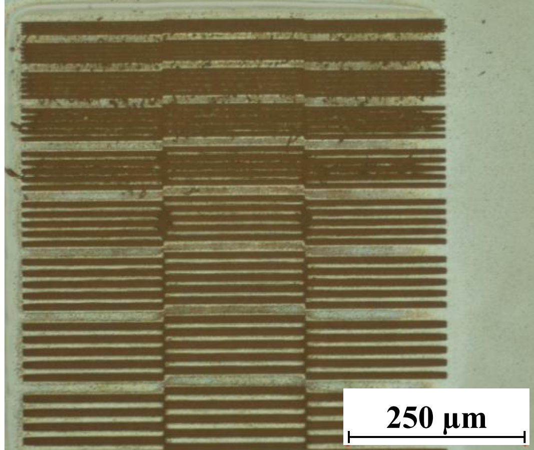

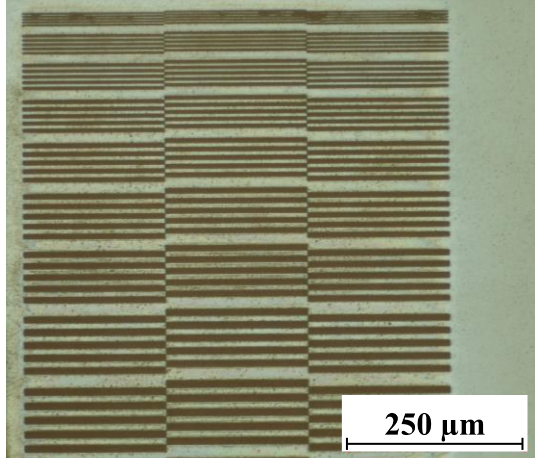

Figure 5.8 Image of ablation of a resolution chart in an ABF type substrate at 2 J cm^{-2} and 25 SPA. In the image on the left, all 25 shots per area were put down in a single scan of the mask, with 5 shots in the x direction and 5 shots in the y direction. In the image on the right, the mask was scanned 25 times at 1 SPA.

Therefore, based on the images in Figure 5.8, one can conclude that for this particular substrate, changing the mask scanning regime to increase the time between consecutive shots in a given part of the substrate reduces the probability of wall collapse of the side walls of the fine line space channels for a given number of shots. Alternatively, it

allows a higher SPA to be delivered without wall collapse compared to higher intensity mask scanning regimes.

Figure 5.9 shows the ablation of the largest, 15 µm L/S, features in the same two resolution charts. Examining the images of the top of the channels, there is little difference between the high intensity (5, 5, 1) mask scanning regime and the low intensity (1, 1, 25) regime. The high intensity ablation has caused the feature to broaden by 0.6 ± 0.2 µm, and there are more debris particles on the sample surface. The depth of the features was measured by focusing on the top and bottom surfaces of the channels and taking readings from the z axis encoder on the optical microscope, and it was found that the ablation depth of the channels scanned with the high intensity regime was significantly greater. The bottoms of the channels in the high intensity regime are narrower than in the (1, 1, 25) regime, but the taper angle of both channels is the same within error, 79±1°, such that the additional narrowing can be attributed to the increased depth of the channel. Therefore for the ablation of features larger than 10 µm L/S in this particular substrate, a higher intensity mask scanning regime is beneficial to the process. It increases the ablation rate (µm/shot) reducing the number of shots required to reach a target depth, and therefore the process time required to pattern a sample. In the example shown, the ablation rate is increased by a factor of ~1.5 from 0.44 µm/shot to 0.64 µm/shot

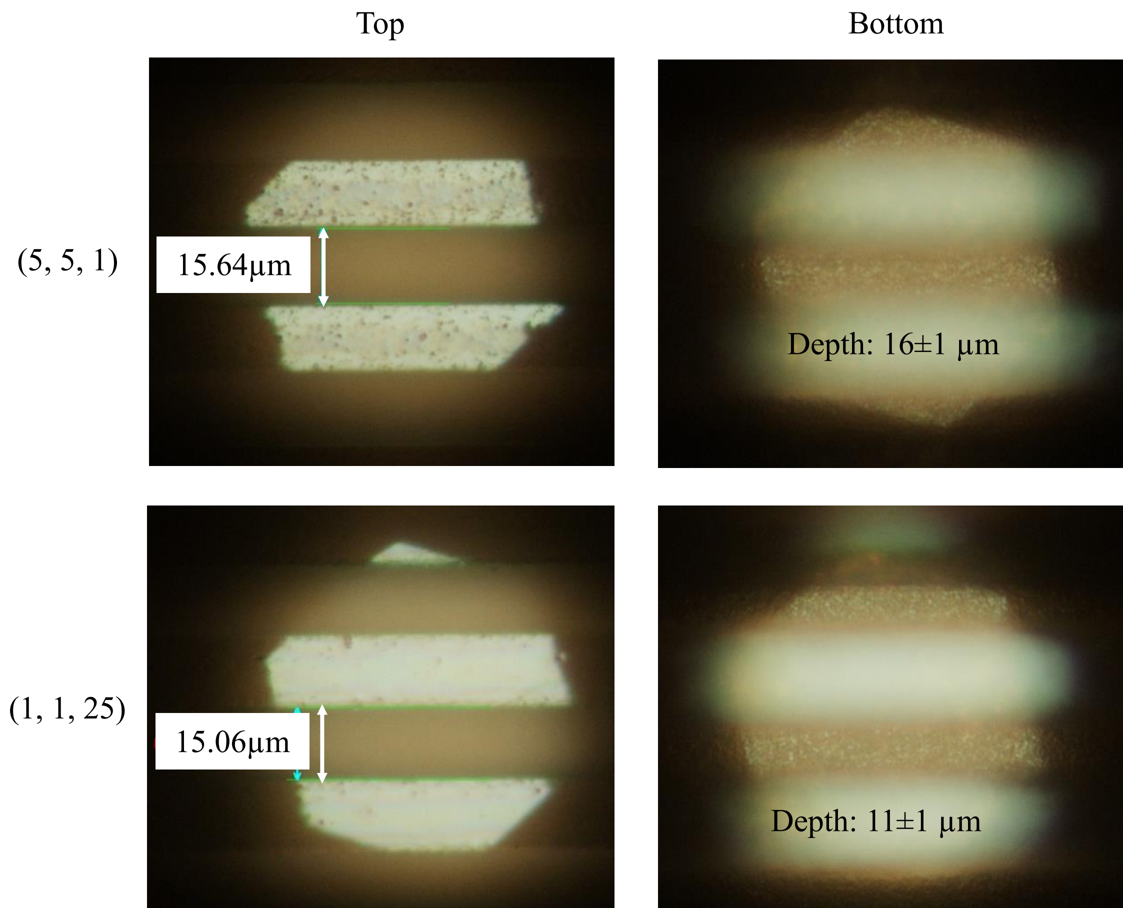

Figure 5.9 Comparison of nominally 15 μm L/S features ablated with the same fluence and total number of shots per area, 2 J cm^{-2} and 25 SPA respectively, but with different mask scanning regimes. The depth, as measured by focusing on the top and bottom of the channels and taking readings from the encoder on the z-axis of the microscope, is significantly greater when delivering all shots in a single scan of the mask and giving the substrate less time to cool.

The response of a material to a given mask scanning regime will vary from material to material. The response of a material depends on its ability to dissipate the incident energy, determined by its thermal properties such as its thermal diffusivity, and the threshold energies in the material such as the melting point. For each substrate the mask scanning regime, in combination with the fluence, needs to be tuned to determine the optimum intensity for the ablation of features of a given size, to a given depth. Figure 5.10 shows the ablation of 2 resolution charts with identical laser parameters and mask scanning regimes in 2 different ABF type substrates made by different manufacturers. Despite the similarities in the composition of the 2 substrates, the substrate in the image on the right shows significantly more erosion to the side walls of fine line space channels.

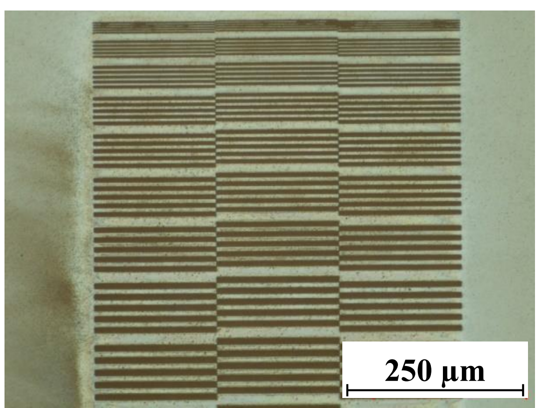

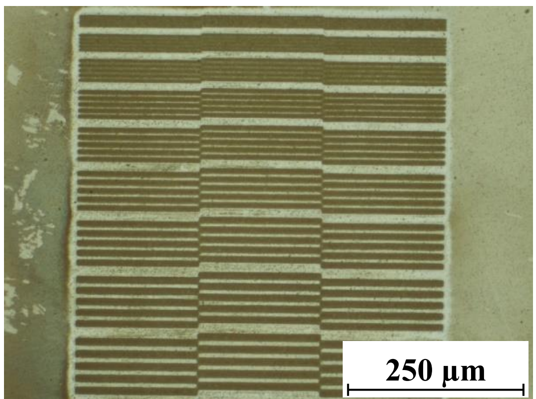

Figure 5.10 Ablation of 2 proprietary ABF type substrates from different manufacturers ablated with the same fluence (2 J cm^{-2}) and mask scanning regime (1, 1, 25) but showing a different response to the laser. Despite the similar composition of the substrates, the side walls of the channels in the substrate on the right are clearly more prone to collapse.

The intensity (W/unit area) can also be tuned by modifying the fluence as well as the mask scanning regime. Figure 5.11 shows how reducing the fluence to lower the intensity of the laser ablation can also help to prevent wall collapse in the laser ablation of fine scale features. Each chart was ablated with the same (1, 1, 100) mask scanning regime to deliver 100 SPA to the same ABF type substrate shown in Figure 5.8 at 2 J cm^{-2}. At 2 J cm^{-2} and 100 SPA, there is now some side wall erosion in all features below 6 µm L/S. Reducing the fluence to 1.5 J cm^{-2}, and therefore reducing the intensity of the laser irradiation, significant side wall erosion now begins to occur for the 3 µm L/S features and below. Stepping down the fluence again to 1 J cm^{-2}, there is no longer any side wall collapse for any of the features down to and including 2 µm L/S despite the high SPA. Despite being able to deliver 100 SPA to the substrate without eroding the side walls of the channels, the ablation depth has become limited by the taper angle of the ablation, such that the fine line space features are very shallow, less than 2 µm deep. This trade-off between depth, fluence and side wall erosion is examined more closely in Section 5.4.

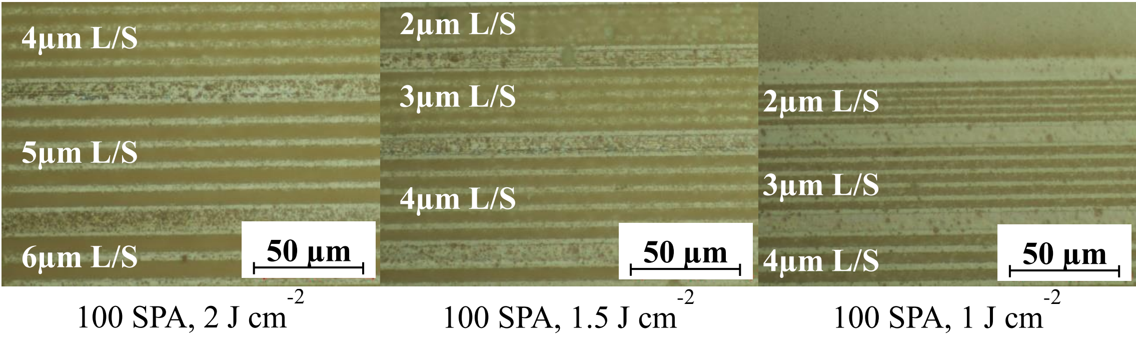

Figure 5.11 Image showing laser ablation of a resolution chart in the same substrate with the same (1, 1, 100) mask scanning regime with different fluences. The fluence was varied by tuning the laser diode current. At 1 J cm^{-2}, there is no erosion of the side walls of the 2 µm L/S features, but the ablated depth is <2 µm.

It has been shown that by changing the intensity, that is the power delivered to a unit area, it is possible to influence the thermal loading of the substrate. Reducing the intensity by changing the mask scanning regime, to increase the time between consecutive shots in a given part of the substrate, it was possible to reduce the probability of the side wall collapse of fine L/S features. Conversely, increasing the intensity by changing the mask scanning regime was shown to increase the ablation depth and ablation rate by 50% in the larger channels spaced further apart, which were not prone to suffering from side wall collapse.

Thus by simply changing the vector file sent to the scanner, it was possible to significantly reduce thermal degradation or significantly improve the ablation rate by controlling the thermal loading of the substrate. Simulation of marking the vector files used by the scanner to illuminate the mask showed the effective repetition rate of the laser as seen by a given part of the substrate could be tuned between <100 Hz and 5 kHz by changing the mask scanning regime. This is something not possible with an excimer laser mask imaging system due to the comparatively low maximum repetition rate of high average power excimer lasers.

5.3 Filler size in ABF substrates

The work in Section 5.2 found that the optimum mask scanning regime for the ablation of fine L/S features in ABF substrates was a low intensity regime, where the time between consecutive shots in a given area of the substrate was maximised. Fixing this as a variable, the impact of filler size on minimum feature size was investigated. Resolution charts and circuit features were ablated into three ABF type substrates with differing filler sizes. Figure 5.12 shows ablation of 7 µm, 5 µm and 3 µm L/S traces in

ABF GX92. The ablation of the 7 µm traces looks reasonably uniform and acceptable because the filler size is a small fraction of the feature width. At 5 µm L/S, the filler size starts to have a noticeable impact on the roughness of the trench, which can impair signal transmission down a conductive track after metallisation. At 3 µm L/S, the larger filler particles begin to protrude approximately half way into the features, unacceptable for high frequency signal transmission. The 5 µm L/S tracks are comparable to the 5 µm tracks shown in Figure 2.11 of excimer laser ablation in ABF GX13.

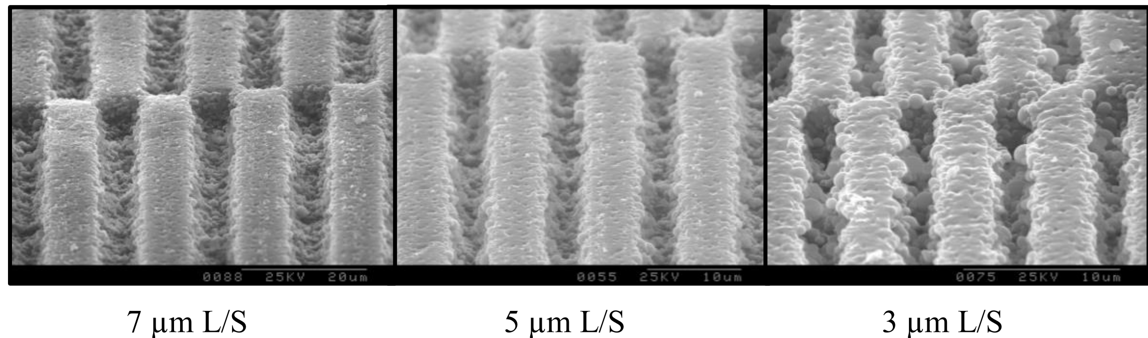

7 µm L/S 5 µm L/S 3 µm L/S

Figure 5.12 SEM micrographs of ablated trenches in an ABF GX92. The largest filler particles are approaching the trench width in the 3 µm L/S tracks, which would lead to poor signal transmission and potentially low yield after metallisation.

Figure 5.13 shows SEM micrographs of laser ablation in Zaristo 520s by Taiyo Ink. This substrate has a mean filler size of 250 nm, and there appears to be an improvement in trench roughness when compared with the images in Figure 5.12. Despite the low mean particles size, however, there are some filler particles with diameters greater than 1 µm visible in the 4 µm and 3 µm L/S trenches. The results highlight the need for the maximum filler particle size, as opposed to the mean, to be less than 10% of the minimum feature size.

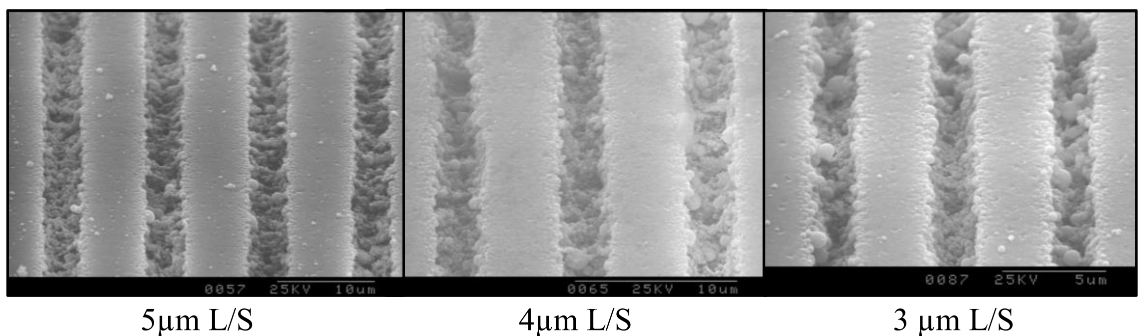

5µm L/S 4µm L/S 3 µm L/S

Figure 5.13 SEM micrographs of ablated trenches in a Zaristo 520s build-up film. The largest filler particles are >1 µm in diameter, which could still lead to poor signal transmission and potentially low yield after metallisation.

Figure 5.14 shows SEM micrographs of 10 µm and 3 µm tracks in a proprietary ABF type substrate. The filler particle sizes were not specified, however it appears in the cross-section that the maximum filler particle size is ~250 nm. The 10 µm tracks have a flat trace bottom and have been ablated to a uniform depth. The nominally 3 µm tracks have broadened to ~4 µm and have been machined to a depth of ~4 µm. The result shows a marked improvement over the other substrates. The investigation highlights the need for fine filler particles in ablative laser processing of ABF type substrates. For a high yield process with low trench roughness, the maximum filler particle diameter should be <10% of the feature width. Using the mean filler particle size to judge substrate suitability can be misleading if the filler particle sizes are normally distributed about the mean. It can be concluded that ablative laser processes are compatible with the silica filled epoxy substrates common in chip packaging, but only if the above criteria regarding filler particle diameters are satisfied.

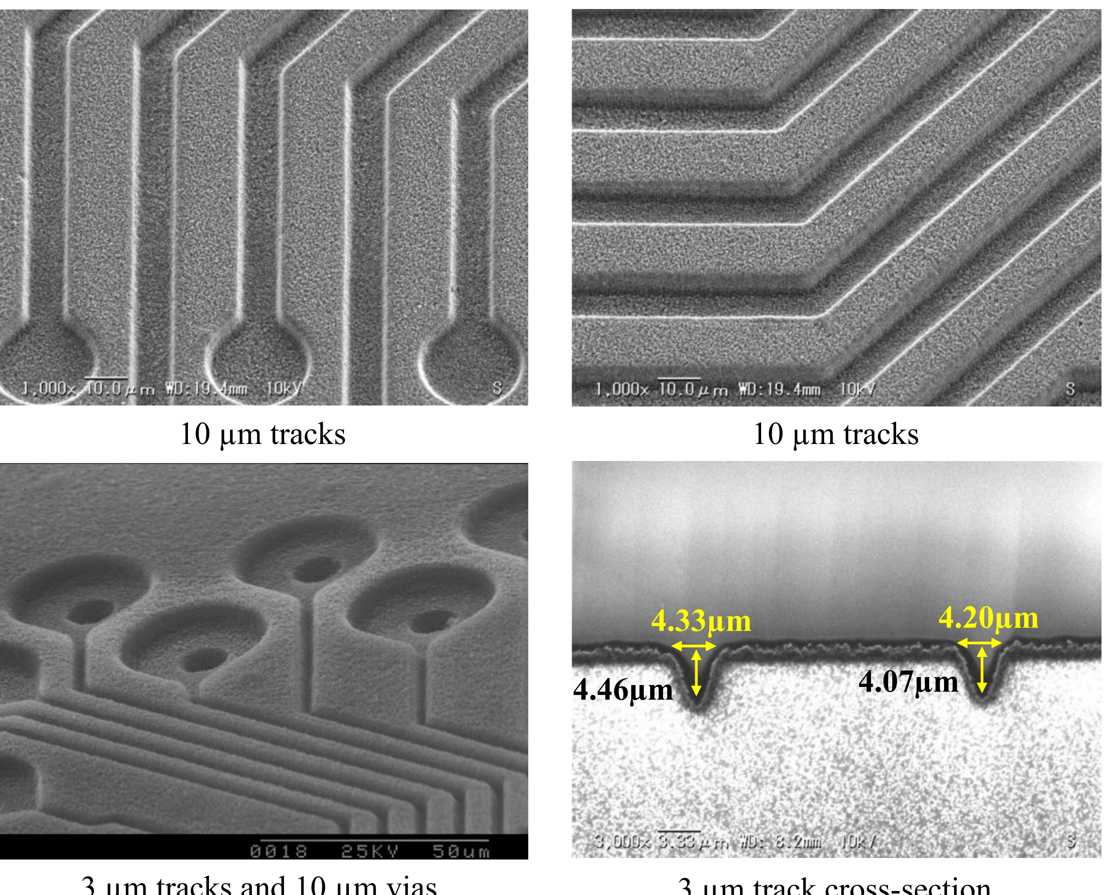

Figure 5.14 SEM micrographs of 10 µm and 3 µm tracks machined with the SMI system in a proprietary ABF type substrate. The 10 µm tracks have been uniformly ablated with a trapezoidal trace profile. The nominally 3 µm tracks have broadened to ~4µm and have a pointed trace profile. All the tracks have a low surface roughness due to the small filler particle size, which improves signal transmission in a conductive track.

5.4 Taper angle, fluence and aspect ratio

In addition to high resolution pattern definition, the feature profile and aspect ratio of the copper structures are also of importance to advanced chip packaging. Both factors influence the volume of copper it is possible to deposit in a trace, which affects the resistance of the conductor. Features with a rectangular profile have a larger cross-sectional area and surface area which reduces the resistance of a current carrying conductor. The feature profile can also detrimentally affect the signal transmission. The feedback from chip package designers was that the conductor cross-section can strongly influence the parasitic capacitance between adjacent current carrying conductors. Specifically, conductors with a triangular cross-section were expected to couple strongly to neighbouring conductors, particularly at high frequencies, which has a detrimental impact on the signal integrity. For this reason it is important to be able to control the profile of the laser ablated grooves, and to this end, an investigation into the effect of laser fluence on taper angle and feature profile was carried out.

The study was conducted in the homogenous build-up film BTX, in part to remove any variation caused by the different sized glass filler particles in ABF substrates. Three laser fluences were investigated to determine the maximum aspect ratio ablation attainable with each. Laser ablation of a chip package at 2 J cm^{-2} and 4 shots per area can be seen in Figure 5.15. Figure 5.15(a) shows an overview of the 3 µm L/S test feature and the surrounding ground plane and package features. The ground plane ablation is to a uniform depth, despite the low number of shots per area, which was achieved by tuning the raster scan pitch and scan speed. Figure 5.15(b) is angled to look into the features. Figure 5.15(c) is an image of the same features shown in Figure 5.15(b) after having machined a cross-section with a focused ion beam (FIB). The features were filled with platinum prior to the cross-section to improve the contrast of the cross-section. The image shows the repeatability in the profile of the feature ablation and the uniformity of the depth across the features. Figure 5.15(d) shows a close up of the cross-section, including measurement of the feature width and depth. It should be noted that the void visible in the middle of a trench is an artefact of the platinum deposition method, and is not related to the laser ablation or any subsequent plating steps. The feature is ~6 µm deep and has broadened to ~4 µm wide. The feature has a rounded profile, acceptable for signal transmission.

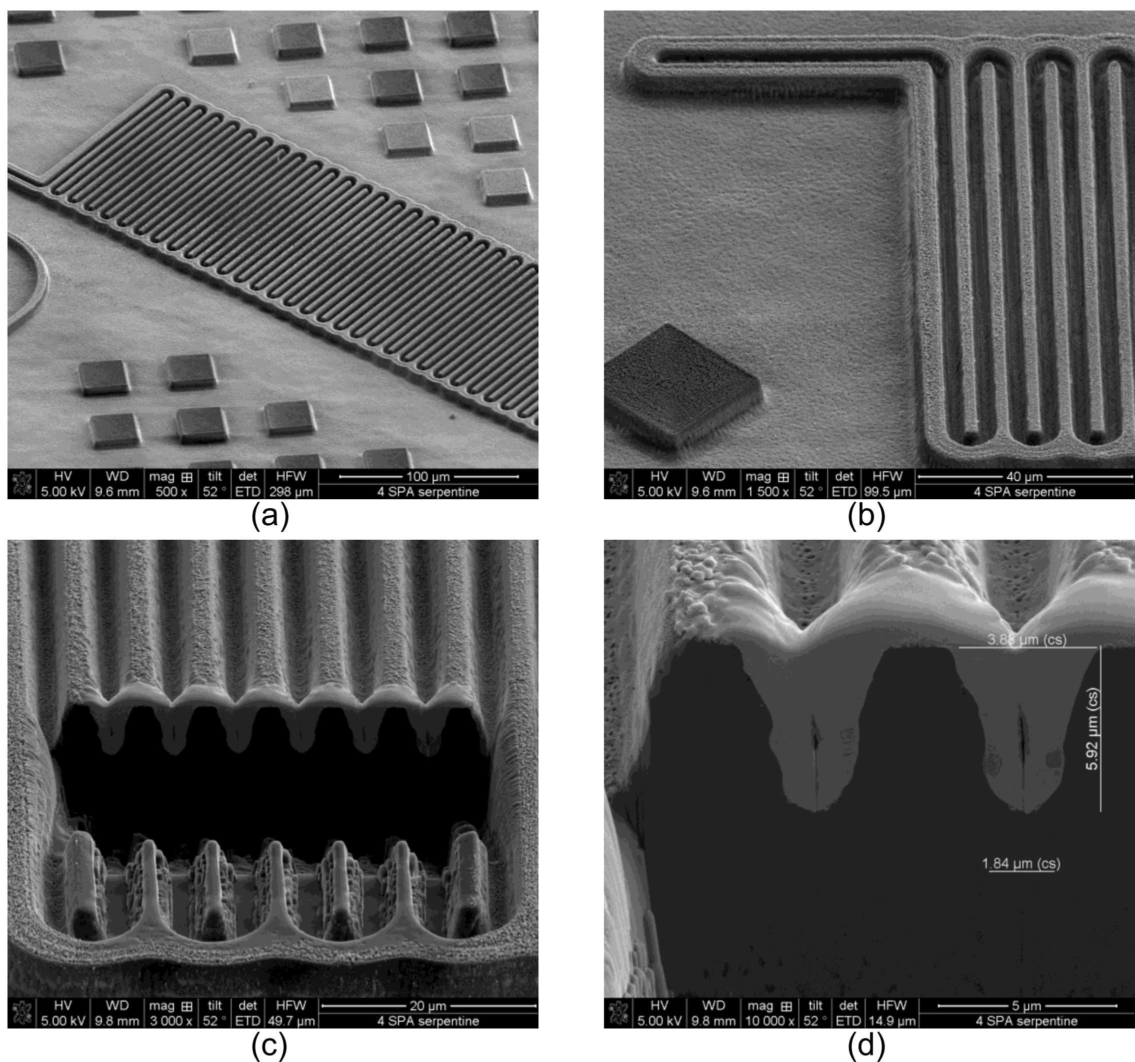

Figure 5.15 SEM micrographs of ablation of a 3 µm L/S serpentine test feature in a chip package. The ablation was done at 4 SPA with a fluence of 2 J cm^{-2}. (a) Overview of 3 µm L/S serpentine feature and surrounding package features. (b) Looking into 3 µm L/S channels. (c) FIB cross-section of channels shown in image (b). The channels have been locally filled with platinum to improve the cross-section definition. (d) Close up of FIB cross-section with measurements of the nominally 3 µm L/S feature.

The shots per area was then increased to 8 SPA by increasing the number of scans of the mask in an attempt to increase the ablation depth and improve the aspect ratio of the laser ablation. Figure 5.16 shows an image of the same nominally 3 µm L/S test feature. The higher number of shots has broadened the features to the point where the top surface of the material between the 3 µm channels has been eroded. Clearly this is unacceptable, and depending on the plating method used, would likely lead to interconnection of all the 3 µm channels over the top of the eroded channel wall. Thus the ablation depth of 3 µm channels at a fluence of 2 J cm^{-2} in the BTX substrate is limited to ~6 µm to prevent erosion of the top surface of the material between the channels.

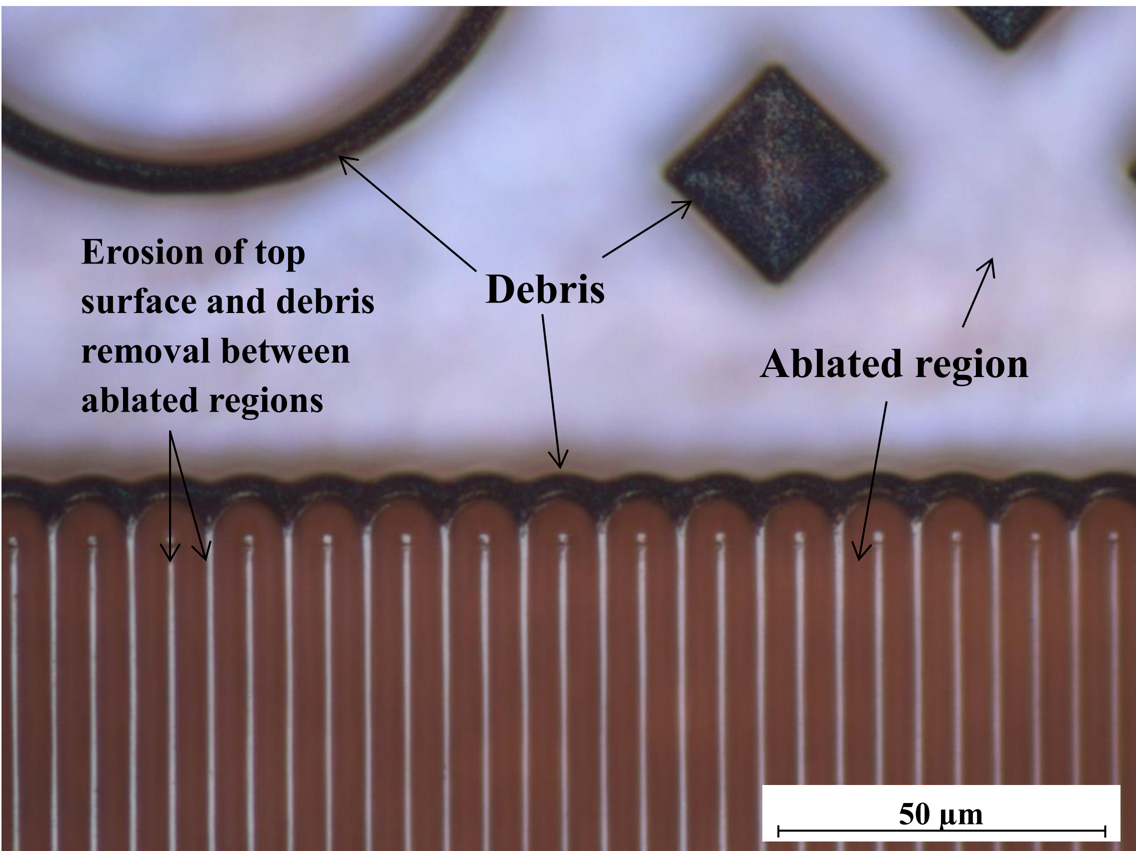

Figure 5.16 Microscope image of ablation of a nominally 3 µm L/S serpentine test feature in a chip package. The ablation was done at 8 SPA with a fluence of 2 J cm^{-2}. The dark material is laser ablation debris re-deposited on the top surface of the substrate. The relatively high fluence and number of shots has broadened the feature width to the point at which the top surface between the 3 µm channels has been eroded.

The fluence was then reduced to 1.5 J cm^{-2} by changing the diode current of the laser. This was to determine if the shots per area could be increased without causing the top surface erosion seen at higher laser intensity. SEM micrographs of the laser ablation at 6 SPA and 1.5 J cm^{-2} can be seen in Figure 5.17. Figure 5.17(a) shows an overview of the nominally 3µm L/S serpentine feature with surrounding pad, signal traces, square support structures and uniform ground plane ablation. Figure 5.17(b) is a close up looking into the nominally 3 µm L/S channels. Debris particles from the laser ablation can be seen on the top surface of the sample. The fact that the debris film remains intact on the top surface of the substrate between the 3 µm L/S channels is an indication that no erosion to the top surface of the substrate between adjacent channels has occurred. Figure 5.17(c) is an SEM image of the same features as in Figure 5.17(b) after platinum deposition within the channels and the machining of a cross-section with FIB. Again, the depth and profile of the ablation shows good uniformity and consistency. Figure 5.17(d) shows a close-up of the cross-section, and includes measurements of the channel dimensions. In comparison with Figure 5.15(d) ablated at the higher fluence,

increasing the number of shots has increased the feature depth by ~2 μm to a depth of 8 μm. However the channel ablation is clearly more tapered, and in combination with the additional depth, this had led to the feature profile beginning to look more pointed. This is expected of ablation of the same substrate at a lower fluence, since less material is removed per pulse. As with the previous result, the feature width has broadened to ~3.5 μm, however this is not to the point at which erosion of the top wall has occurred between the features. Therefore lowering the fluence enabled more shots to be delivered to the substrate without causing erosion of the top surface of the substrate between features. This allowed the 3 μm L/S features to be successfully machined to a greater depth, 8 μm, but at the cost of a more pointed feature profile.

Figure 5.18 shows an image of laser ablation at 8 SPA at a fluence of 1.5 J cm^{-2}. The result is very similar to the ablation shown in Figure 5.16 of the ablation at 2.0 J cm^{-2} and 8 SPA. In both cases the top surface of the substrate between the 3 μm channels has been eroded. There is slightly less erosion to the channel walls in the ablation shown in Figure 5.18, however the key difference between the two results is likely to be the difference in the height of the eroded side walls relative to the undamaged parts of the substrate. The depth of focus of the optical microscope objective used to take the images is approximately ±1 μm, and it can be seen that the eroded channel walls are roughly co-planar with the debris film on the substrate surface, indicating that the extent of the vertical wall erosion cannot be greater than approximately 2 μm.

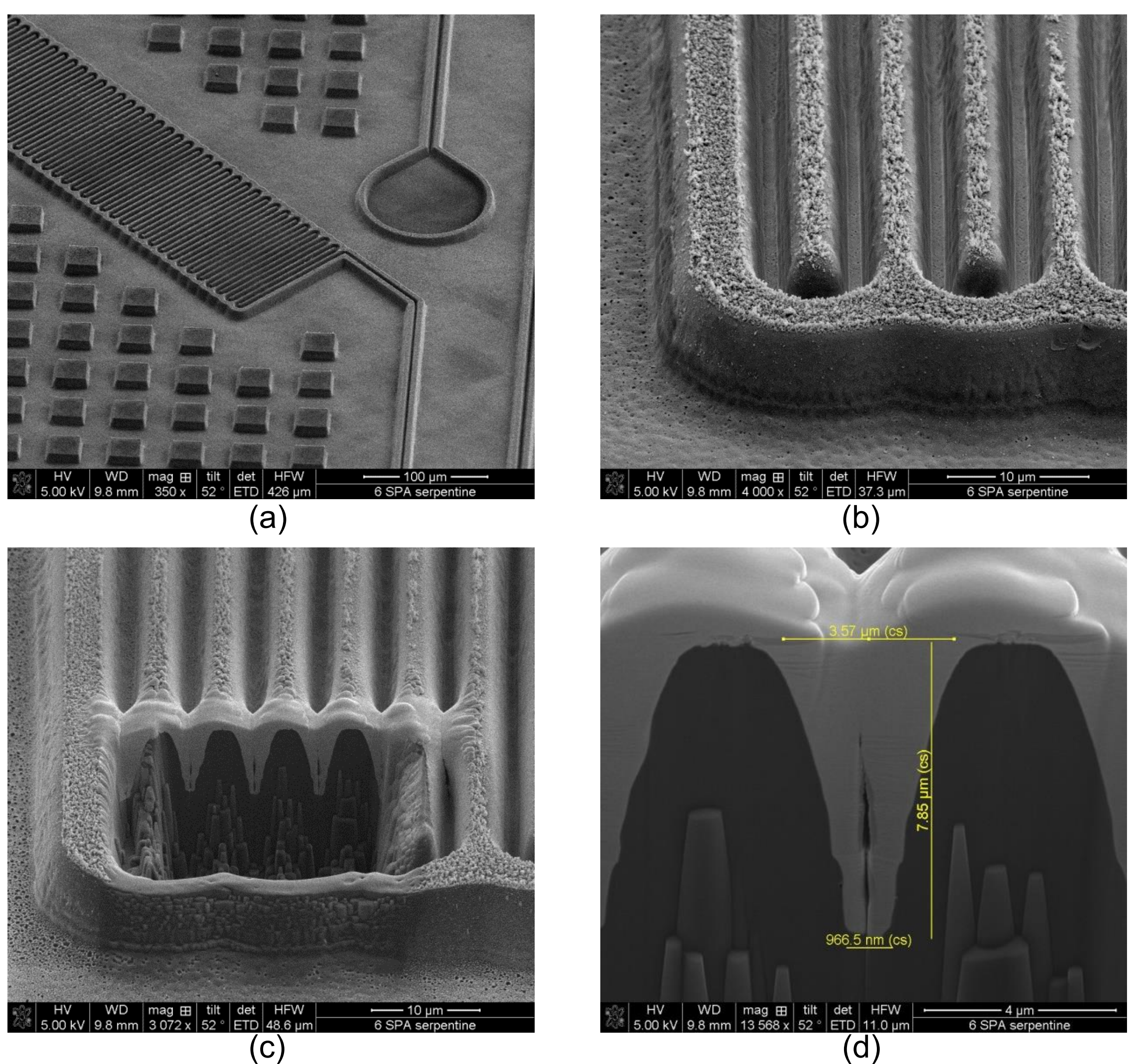

Figure 5.17 Laser ablation of nominally 3 µm L/S at a fluence of 1.5 J cm^{-2} at 6 SPA. (a) Overview of 3 µm L/S serpentine feature and surrounding package features. (b) Looking into 3 µm L/S channels. (c) FIB cross-section of channels shown in image (b). The channels have been locally filled with platinum to improve the cross-section definition. (d) Close up of FIB cross-section with measurements of the nominally 3 µm L/S feature.

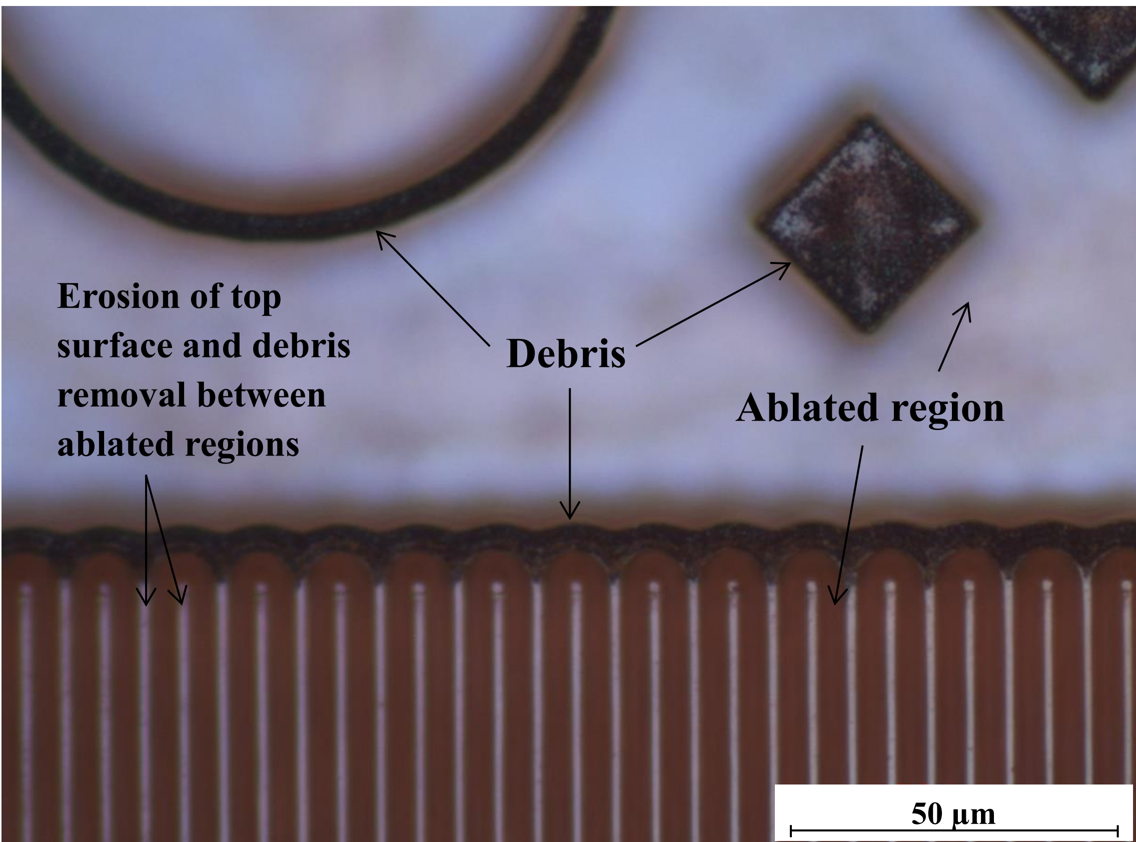

Figure 5.18 Microscope image of ablation of a nominally 3 µm L/S serpentine test feature in a chip package. The ablation was done at 8 SPA with a fluence of 1.5 J cm^{-2}. The dark material is laser ablation debris re-deposited on the top surface of the substrate. The relatively high fluence and number of shots has broadened the feature width to the point at which the top surface between the features has been eroded.

To conclude the experiment, FIB sections were taken of samples processed 16 SPA at 1 J cm^{-2}. Images of the laser ablation can be seen in Figure 5.19. As before, the SPA could be increased without wall collapse of the channels due to the lower fluence. Figure 5.19(a) shows an overview of the nominally 3 µm L/S serpentine test feature and the surrounding features of the chip package. Of particular note is the uniformity of the ground plane. The square uniform spot size at the substrate is ~250 µm, much smaller than the area shown in the image, however there is no perceivable depth variation in the large ground plane areas which could arise from beam stitching and edge effects. The higher the shots per area, the easier it becomes to homogenise the illumination of the mask. By offsetting each subsequent shot, for example in a 4x4 array, any edge effects in the laser ablation arising from the sloped beam profile are averaged out by subsequent shots. Figure 5.19(b) shows a close up of the 3 µm L/S feature and surrounding features, and gives an idea of the aspect ratio of the laser ablation. Figure 5.19(c) and (d) show FIB cross-sections of the nominally 3 µm L/S feature including measurements of the width and depth of the channels. The channels again show good

repeatability in terms of feature profile and depth uniformity, and the additional shots have resulted in an ablation depth of ~11 µm.

Thus reducing the fluence of the laser has enabled the machining of higher aspect ratio channels through a reduction in the intensity of the laser process. The lower intensity process reduces the likelihood of the collapse or erosion of the wall between the two channels, and reduces the broadening of the feature width for a given number of shots per area, however results in a more pointed feature profile. Although the high aspect ratio ablation shown in Figure 5.19 would allow a larger volume of copper to be deposited into the features, reducing the resistance of a copper track, it may result in poorer transmission of the signal down the track due to parasitic losses from the point of the track.

The conclusions of the study are that the maximum ablation depth achievable for fine scale features in the BTX substrate is limited by the erosion of the side walls of the channels and the taper angle of the laser ablation. There is a trade off in that a high intensity, high fluence laser process reduces the taper angle of the laser ablation, however the more energetic material removal reduces the number of shots that can be delivered to the substrate before degradation of the side walls occur. The best compromise was found by reducing the fluence to the point to which a relatively large number of shots per area could be delivered to the substrate without significantly eroding the side walls of the nominally 3 µm L/S channels. The depth of the ablation then becomes limited by the taper angle of the ablation, and the material removal from the bottom of a high aspect ratio trench. This causes the resultant channel to be pointed, and a maximum aspect ratio of ~3:1 was achieved for the nominally 3 µm channels in BTX. This result should be evaluated in the context of chip packaging, where a pointed conductor profile can negatively impact on signal transmission due to signal emission from the point.

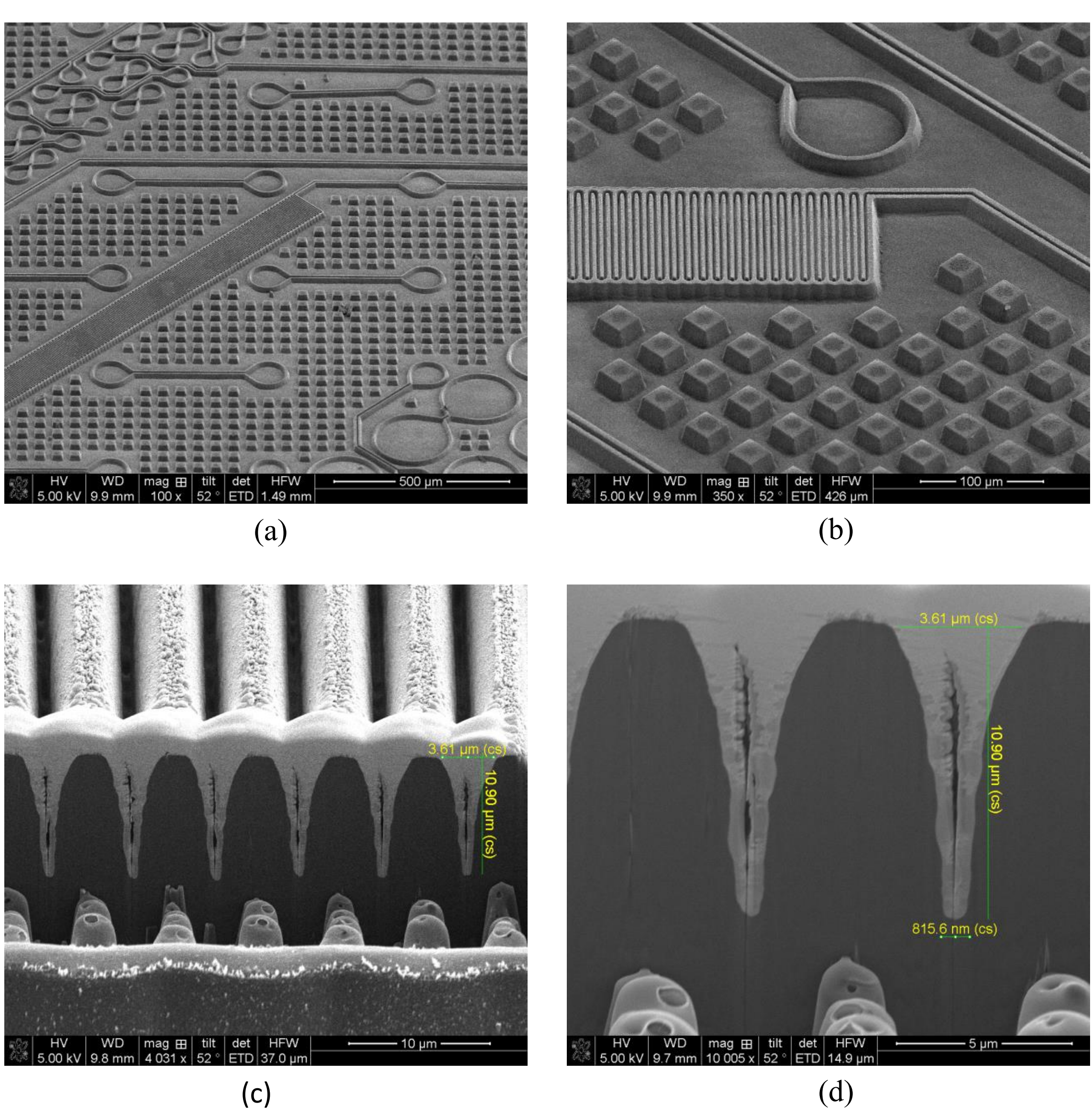

Figure 5.19 Laser ablation of nominally 3 µm L/S at a fluence of 1 J cm^{-2} at 16 SPA. (a) Overview of 3 µm L/S serpentine feature and surrounding package features. (b) Looking into 3 µm L/S channels. (c) FIB cross-section of channels shown in image (b). The channels have been locally filled with platinum to improve the cross-section definition. (d) Close up of FIB cross-section with measurements of the nominally 3 µm L/S feature.

5.5 Imaging from the first plane of uniformity

5.5.1 Limiting resolution

Another unique feature of the SMI system is that there are two image planes, with the possibility to scan or precisely overlay an image from the first plane over an object in the object plane of the projection lens, or the coincident image plane of the f-theta. A schematic of the SMI system is repeated in Figure 5.20 for convenience. By placing an object in the plane of homogeneity, it is possible to image this object down onto the mask plane, positioning the image of the object anywhere within the scan field of the

f-theta lens, and relay this image down to the substrate with the projection lens. Illuminating a mask with a shaped laser beam can also be achieved with an excimer laser system but conventionally there is only one object and image plane. Therefore this normally involves a static aperture held as close as possible to the mask in the object plane, and moving the mask and substrate to form the image. With this methodology, since the aperture and mask plane cannot be coincident, the aperture is necessarily out of focus at the substrate plane, limiting the sharpness of the edge of the shaped beam at the substrate, and the minimum size of features in the aperture plane which can be resolved at the substrate plane [82].

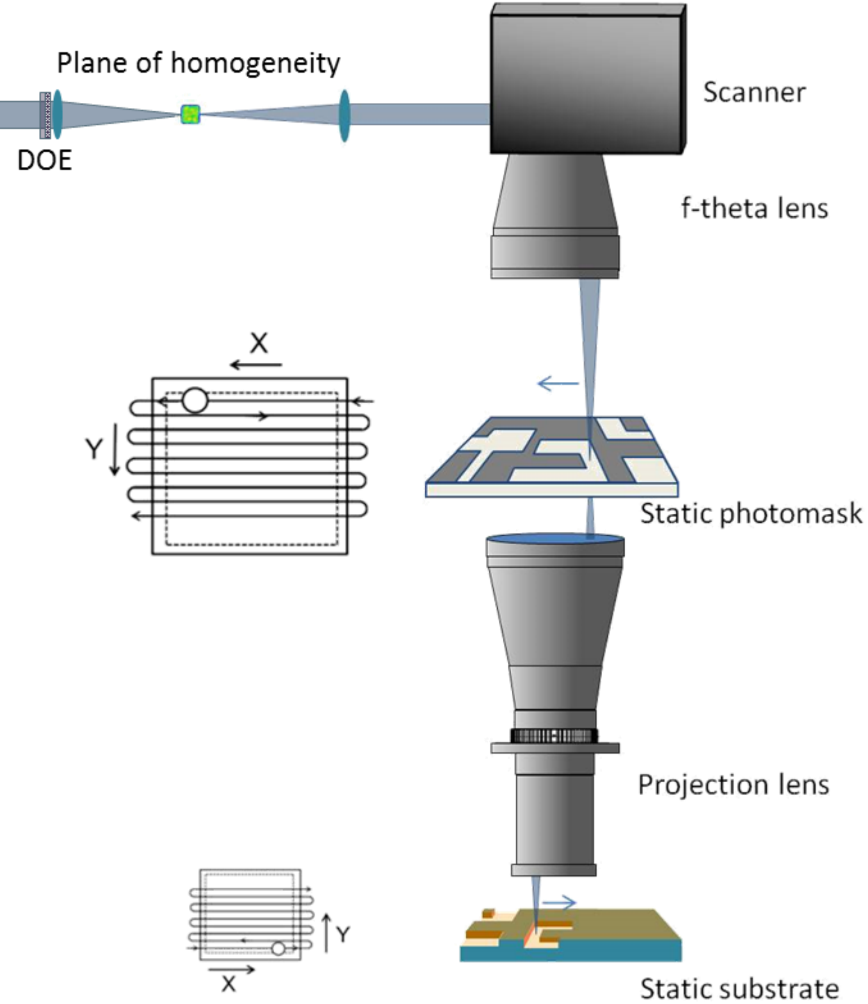

Figure 5.20 Schematic diagram of the SMI system. A DOE forms a square flat top plane at the plane of homogeneity. This plane is imaged down to the mask plane with a 1:1 infinite conjugates imaging system comprising of a singlet and an f-theta scan lens. The projection lens then images this plane down to the substrate.

To test the resolution of imaging from the plane of homogeneity to the mask plane, and then relaying this image down to the substrate, a chrome-on-quartz mask with resolution features was placed in the plane of homogeneity. To focus the image of the

chrome-on-quartz photomask in the plane of homogeneity, the substrate was first put into the focal plane of the projection lens by adjusting the substrate height until the photomask in the object plane of the projection lens was in focus. The photomask was removed from the object plane of the projection lens such that the image of the mask in the plane of homogeneity could be relayed directly down to the substrate. The mask in the plane of homogeneity was mounted onto a micrometer stage allowing accurate adjustment of the mask position along the optical axis. The mask position was then tuned by firing shots through the mask and adjusting the mask position until the image of the mask was in focus at the substrate. Once in focus, the image of this mask was scanned across the object plane of the projection lens using the galvanometer scan head across a 54×54 mm area to test the image resolution across both the scan field of the f-theta lens and the image field of the projection lens. The 54×54 mm area in the object plane of the projection lens corresponds to approximately 15×15 mm in the image plane of the projection lens. The scan speed at the mask and the pitch of the lines in the illumination pattern was set such that there would be no overlap of adjacent shots, but that the shots would cover most of the image field. Images of the laser ablation can be seen in Figure 5.21. The optical micrographs compare the imaging performance of the system on axis and at a point furthest radially from the optical axis. Each square unit represents an image formed and ablated into the substrate by a single pulse from the laser. As can be seen, there is no obvious or significant difference in the image quality in the on and off axis areas.

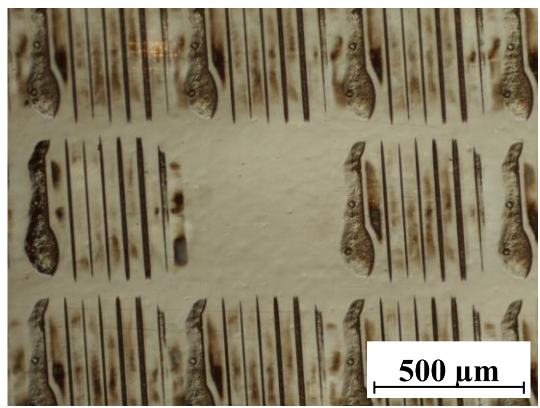

Centre of projection lens image field

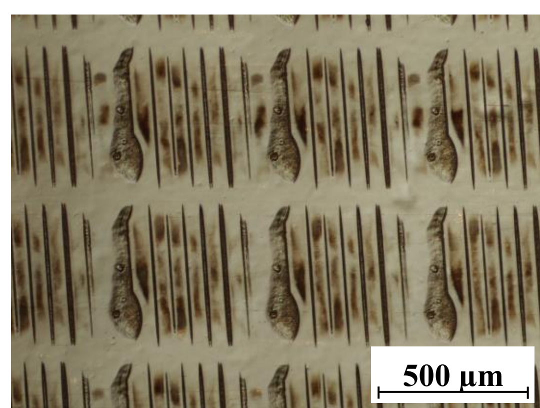

Top right corner of projection lens image field

Figure 5.21 Microscope images taken of ablation achieved by imaging a mask in the plane of homogeneity and scanning this image across the object plane of the projection lens. The projection lens then relays these images to the substrate. Each set of lines within the square border of the beam represents an individual shot from the laser. The optical micrographs compare the imaging performance of the system at the centre and at the edge of the image field.

Taking a closer look at the ablation with a higher magnification objective on the optical microscope, some subtle differences can be seen. Figure 5.22 shows that 7 µm features are resolved even at the limits of the 54×54 mm scan field or 15×15 mm projection lens field. However there is some difference in the reflectivity of the bottom of the trenches. It had been previously observed that the BTX film in which this study was conducted is only strongly reflective when its ablated surface is normal to the incident light. Hence the side walls appear dark brown since little of the incident light is collected by the objective lens on the microscope. If the bottom of the trench is flat, it appears white as in the larger trenches in the bottom left part of the field in Figure 5.22. This implies most of the other features in other parts of the field have a U shaped cross section, rather than a trapezoidal cross section with a flat trench bottom. Despite this, sub 10 µm resolution was demonstrated across a 15×15 mm field imaging from the plane of homogeneity. In chip packaging, this opens up the possibility of drilling vias sequentially through their capture pads in the circuitry part of the mask. When using SMI, the vias are normally drilled by overlaying the circuitry image and the via array image contained on different areas of the same photomask. This requires mounting the photomask on a stage with at least 50 mm travel, and stepping between the two areas on the photomask for each device. Imaging an aperture from the plane of homogeneity to drill a via, by centring the image of the via on the capture pad in the mask plane through use of the scanner, would negate the need to step the mask stage for each device,

improving the process time. The downside to this approach would be that the scanner would require accurate calibration to position the vias accurately in the plane of the mask.

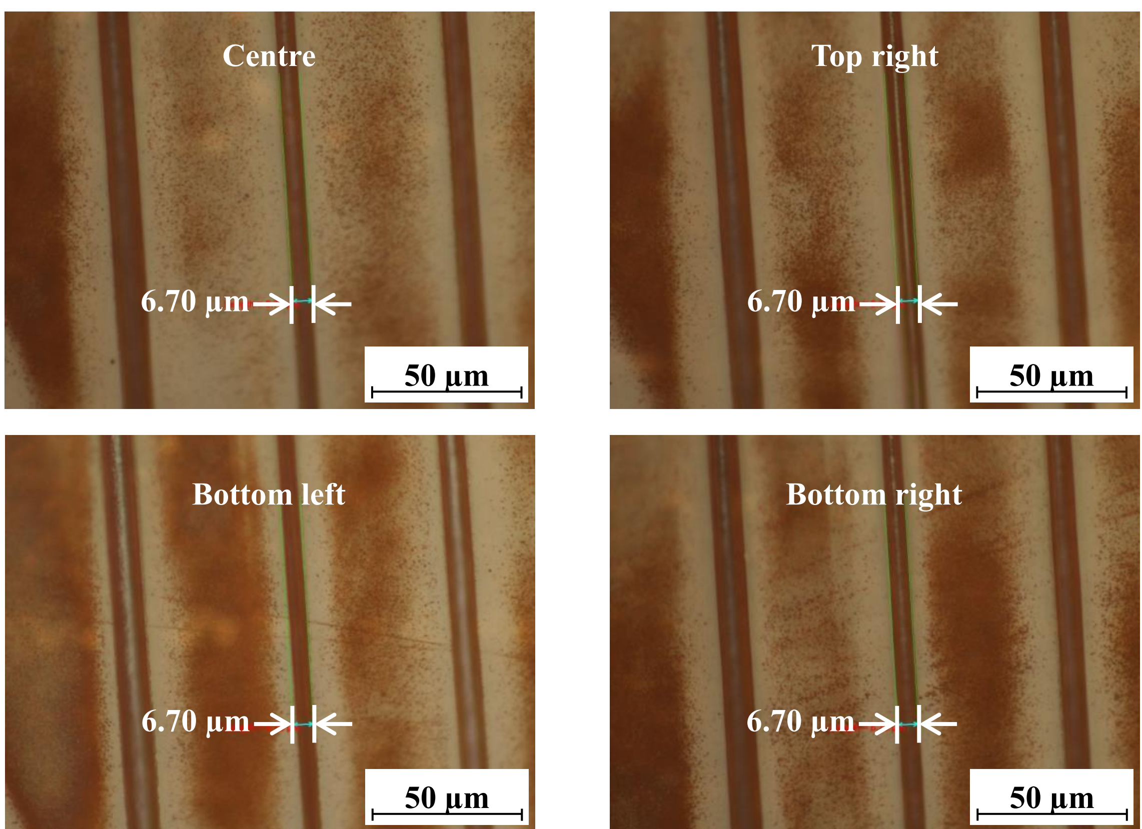

Figure 5.22 Optical micrographs of a resolution chart projected from the plane of homogeneity to different points in the image field of the projection lens. The central trench is 7 µm at all points across the 15×15 mm field. Subtle variation of the taper angle of the ablation can be inferred from the reflectivity of the bottom of the trench. The laser ablated substrate appears white only when normal to the microscope objective. The measurement error is ±0.14 µm.

5.5.2 Overlay of images for micromachining

Having proven it possible to image an object from the first plane of homogeneity to the mask plane, it was decided to briefly investigate if any interesting features could be micromachined by scanning the mask with a shaped beam. A square aperture was placed in the plane of homogeneity to give the beam a hard edge at the mask plane. This hard edge was aligned to a smaller square aperture in the object plane of the projection lens by tuning the scanner offset. By scanning the beam in the direction opposite to the aligned edges at a relatively slow scan speed with multiple shots per area, only one shot is delivered to the material closest to the aligned edge, and progressively more shots are delivered to the material further from that edge. The images in Figure 5.23 show some ramps machined with the SMI system in this fashion.

The direction of the ramp can be reversed by simply scanning the beam in the opposite direction and re-calibrating the beam to aperture edge alignment. Each ramp was machined sequentially and put into the array shown by using x-y stage offsets. The small holes in the surface of the substrate arranged in a line extending from the deeper side of the ramp are due to mask damage in the opaque chrome area of the chrome-on-quartz mask. Pin holes in the chrome were formed when too high a fluence was used in the setup and process development of the ramps.

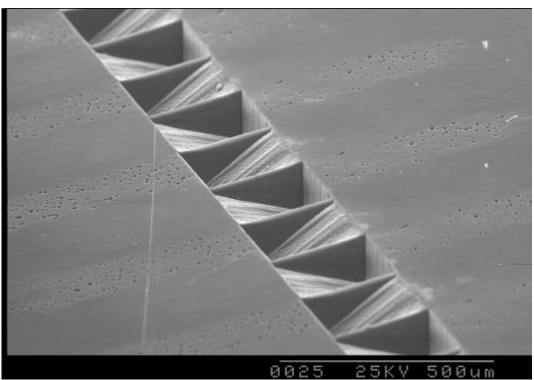

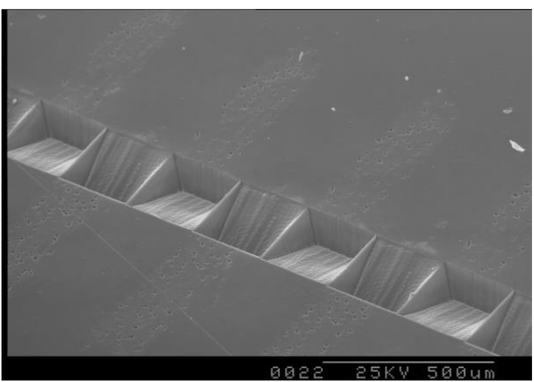

Figure 5.23 SEM micrograph of ramps machined using the SMI system by scanning the image of a square aperture over smaller aperture, and then imaging this aperture down to the substrate with the projection lens.

Imaging from the plane of homogeneity onto the mask plane, and then relaying this image down to the substrate with the projection lens has been demonstrated. The two image planes, whilst not impossible to achieve, are not common with other mask imaging systems. The ability to resolve sub 10 μm features across the field of the f-theta lens and projection lens was confirmed, highlighting the potential to image features from the plane of beam homogeneity through apertures in the mask plane. In the context of chip packaging, this would enable via drilling without a mask stage step for each device, increasing throughput and reducing the required mask size for a given device. This would, however, require accurate calibration of the scanner, not normally required for mask illumination. Scanning the mask with a shaped beam was also explored by inserting a square aperture at the plane of homogeneity. The image of the aperture was aligned to and scanned across a smaller aperture at the mask plane to form ramps in Kapton.

5.6 Selective mask scanning

Raster scanning a limited area of the substrate and being able to accurately define the illuminated area of the mask was briefly discussed in chapter 4, and can reduce process time by avoiding scanning opaque areas of the mask. An extension of this concept, with

certain restrictions on the pattern design, is the ability to only scan areas of the mask in which there are features. A requirement arose for the machining of 3 accurately defined and tightly toleranced slits in a black polyimide substrate for a detector system. The slits were machined in a polyimide sheet, with many parts per sheet. Figure 5.24 shows the CAD data used to manufacture the mask for the project. The green data in the figure represents the transparent regions of the photomask. These transparent regions were narrower than the width of the beam, so the vector file sent to the scanner to machine the part simply consisted of 7 lines which scanned the beam along the transparent parts of the photomask. This is as opposed to raster scanning this entire mask area. Scanning along these lines it was possible to machine through the 25 μm polyimide film with less than 40 SPA.

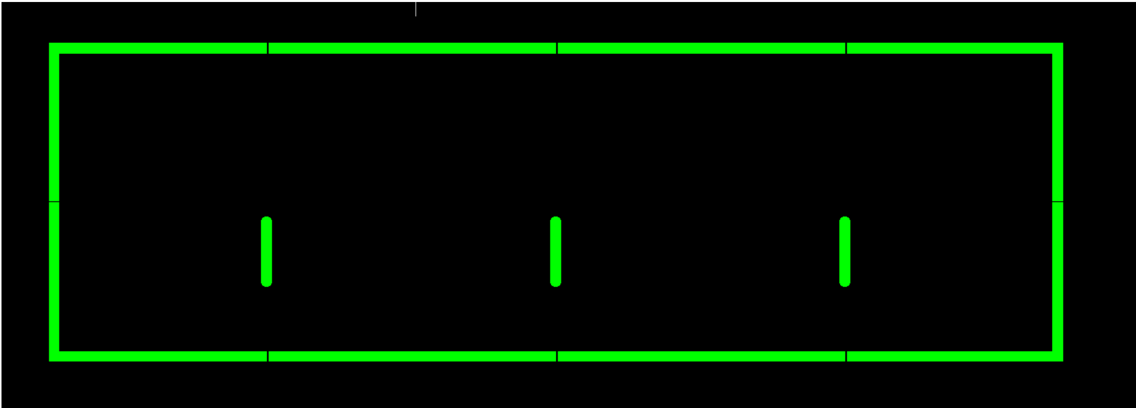

Figure 5.24 CAD data for photomask to micromachine and cut out panel with slits. The cut out section has opaque tabs so that the part remains in place in the polyimide sheet after laser ablation. The green data represents transparent areas of the mask.

Images of the laser ablation can be seen in Figure 5.25. Figure 5.25(a) shows the ablation of one of the slits for use in the detector device. Figure 5.25(b) shows the cut around the edge of the part, including the 20 μm tabs left in place to hold the part within the sheet for shipping. Figure 5.25(c) shows 2 parts held in place by the tabs in Figure 5.25(b), and finally Figure 5.25(d) shows a part that has been removed from the sheet by applying a small force to the part.

Processing the samples with this selective scanning of the mask has the advantage of the dimensional accuracy and precision of a mask imaging system, combined with the speed of a direct write system when marking a simple pattern with a low number of vectors. This reduces the time and laser energy wasted scanning opaque parts of the mask. To demonstrate this, the process times for machining the above part were simulated for both a selective mask scanning regime, and a regime in which an area just

larger than the part in the mask plane is raster scanned. The simulation shows the process time for a selective mask scanning regime, 0.55 s, is almost 3 times faster than the time taken to raster scan the mask, 1.60 s. The amount of time saved depends on the complexity of the mask pattern, and for complex patterns which would require a large number of vectors to selectively illuminate the transparent parts of the mask, raster scanning the mask might be more time efficient.

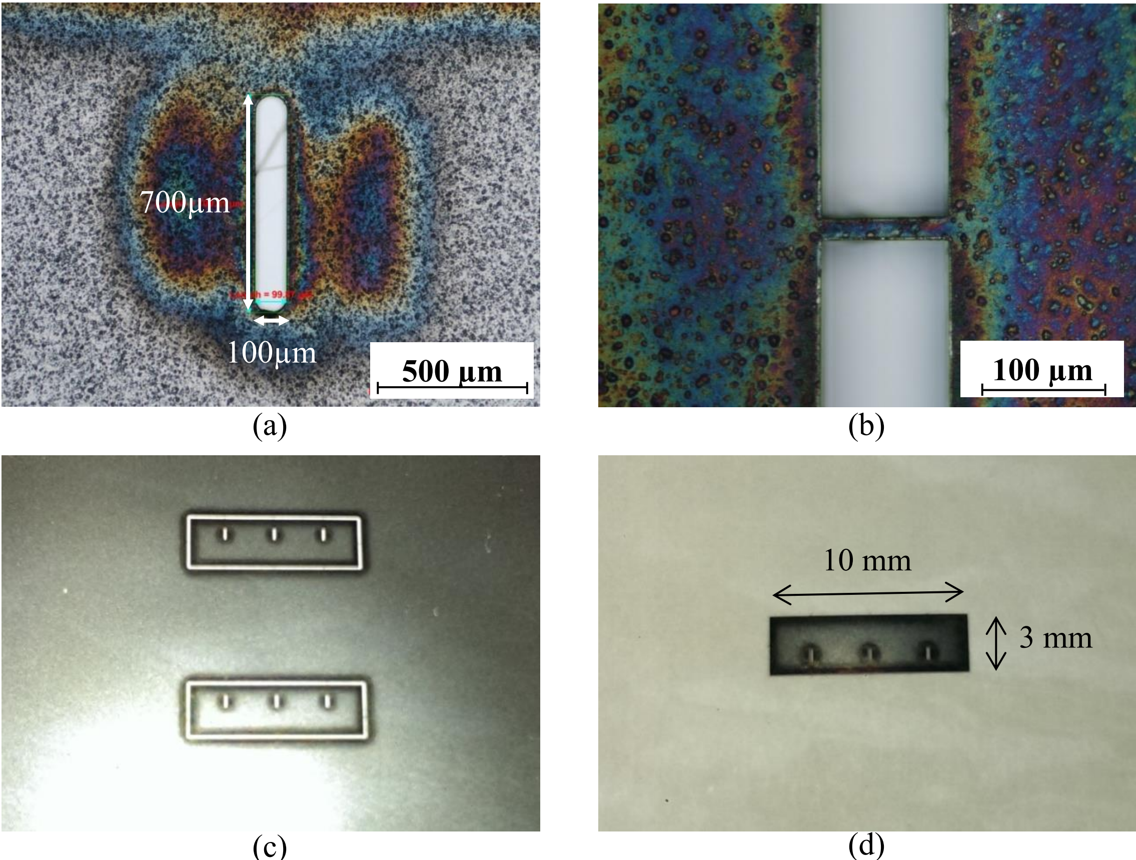

(a) (b) (c) (d)

Figure 5.25(a) slit machined through black polyimide sheet. (b) Tab to keep panel in sheet after cut out. (c) 2 parts machined in black polyimide sheet, held in place by the tabs in image (b). (d) a part after removal from the sheet after application of a small force to break the 20 µm tabs.

Having successfully machined the slits in black polyimide, it was decided to investigate whether a similar, selective illumination of the mask could improve the process time of of a low via density via layer. The circuitry layer on the mask was raster scanned, and the mask stage moved across to overlay the via pattern held on an adjacent part of the photomask. Instead of raster scanning the via layer, each via aperture at the mask plane was illuminated sequentially with a burst of shots. The ablation result can be seen in Figure 5.26. The 80 µm via has been ablated down to the copper clad laminate through

the 18 μm BTX build up film. There is no BTX residue on the copper surface, and the copper has not been damaged on account of the laser fluence of 1 J cm^{-2} being below the damage threshold for the copper clad laminate. Using this technique can improve the process time, but can also be slower than raster scanning the mask depending on the via density. One limitation of the technique is that the vias must be smaller than the beam size, however depending on the fluence required, this is normally the case. With the set up used, the upper limit on the via size would be 400 μm, large for chip packaging. Without editing the illumination vector file and simply using the via coordinates as the drill coordinates for the scanner, using this technique may also result in double exposure of vias in close proximity. This occurs when the vias are less than half the beam size apart. This may cause damage to thin copper pads, however was not an issue for the tests conducted on the copper clad laminate where the copper thickness is 20 μm. In contrast with via formation by aperture imaging from the first plane of beam homogeneity, the technique does not require very accurate scanner calibration, since the beam size is normally much larger than the via. However the sequential via drilling does still require a mask stage step for every device.

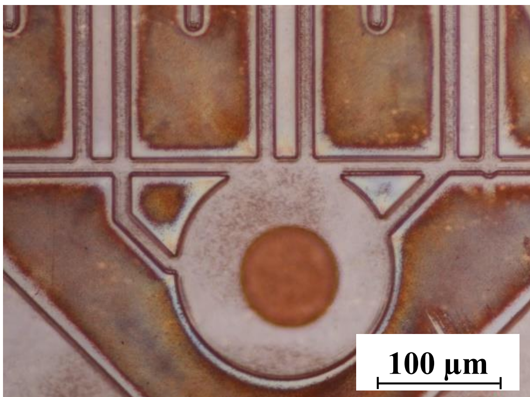

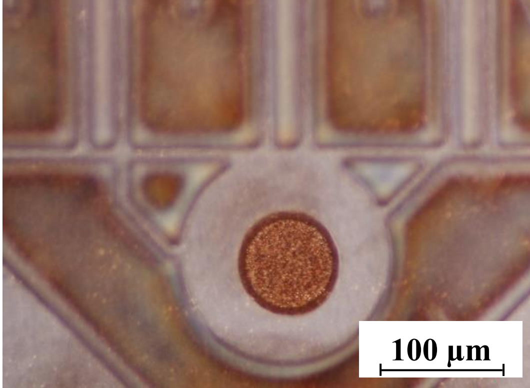

Figure 5.26 Optical micrograph of percussion drilled via machined by sequentially illuminating each via aperture in the mask plane with a burst of laser pulses. The images are focused on the top surface of the substrate (left) and the bottom surface of the via (right). The via has been well registered with the circuitry layer, which was ablated by raster scanning an adjacent part of the photomask.

The ability to selectively illuminate only the transparent areas of the photomask is made possible by a number of related factors unique to the SMI system. The comparatively high repetition rate and low average power of solid state lasers when compared to excimer lasers results in a relatively small pulse energy. This requires a comparatively small beam to achieve the same laser fluence at the mask and substrate as an excimer system. The smaller beam size improves the spatial resolution of the energy delivery by

the high speed galvanometer scanner. This combines the advantages of high positional accuracy of features and sharp edge definition associated with mask imaging, and the more efficient illumination and higher speed of direct write systems when used to ablate very simple patterns with a low number of vectors.

The comparatively high spatial resolution of the energy delivery system enabled by small beam and accurate scanner was also exploited in the imaging of a low via density via layer. Each via was percussion drilled sequentially by illuminating each via aperture sequentially at the mask. A beam size much larger than the via aperture, which is normally the case, means that accurate calibration of the scanner to illuminate the via apertures is not required. This can reduce the process time by avoiding the raster scanning of large opaque areas of the mask in which there are no via apertures. However, above a certain via density threshold, approximately equal to one via per beam size, raster scanning the mask becomes more efficient since multiple vias can be drilled at the same time without the jump and settle times associated with sequential via drilling. The precise jump and settle time depends on a number of factors such as the length of the jump, the specification of the scanner and the focal length of the f-theta lens used with the scanner. However jump and settle times for a 1 mm jump are of the order of 1 ms, so only significantly contribute to the total process time when the number of jumps is high.

5.7 Via drilling with SMI

The only tools currently available for the laser drilling of sub-30 µm vias in high volume production are excimer laser tools, as discussed in Section 2.5.1. The 4 µm micro-via shown in Figure 2.12 represents the current state of the art, with 30 µm vias the best currently achievable with high volume, UV DPSS laser drilling tools. It was expected that the minimum via size machinable by the SMI platform would be of the same order as the minimum trench size, ~3 µm, shown in Section 5.4. To test this, a chrome-on-quartz mask was designed and FIB cross-sections of the smallest micro-vias examined in an SEM. Figure 5.27 shows the resultant images. Figure 5.27(a) shows a nominally 4.5 µm micro-via drilled in the BTX build up film which has broadened to ~5 µm. The volume of material removed by the FIB was not large enough to determine the depth of the hole drilled, however it can be seen that the hole is greater than 5 µm deep. Figure 5.27(b) shows a nominally 3 µm via which has broadened to ~3.5 µm diameter. Again, the bottom of the hole cannot be seen in the cross-section, however the hole is approximately 5 µm deep. The taper angle in both holes is approximately the

same, at (78±2)°. The fluence with which the holes were drilled was limited by the use of the chrome-on-quartz mask, which has a lower damage threshold than aluminium-on-quartz. All holes were drilled with a fluence of approximately 1 J cm^{-2}.

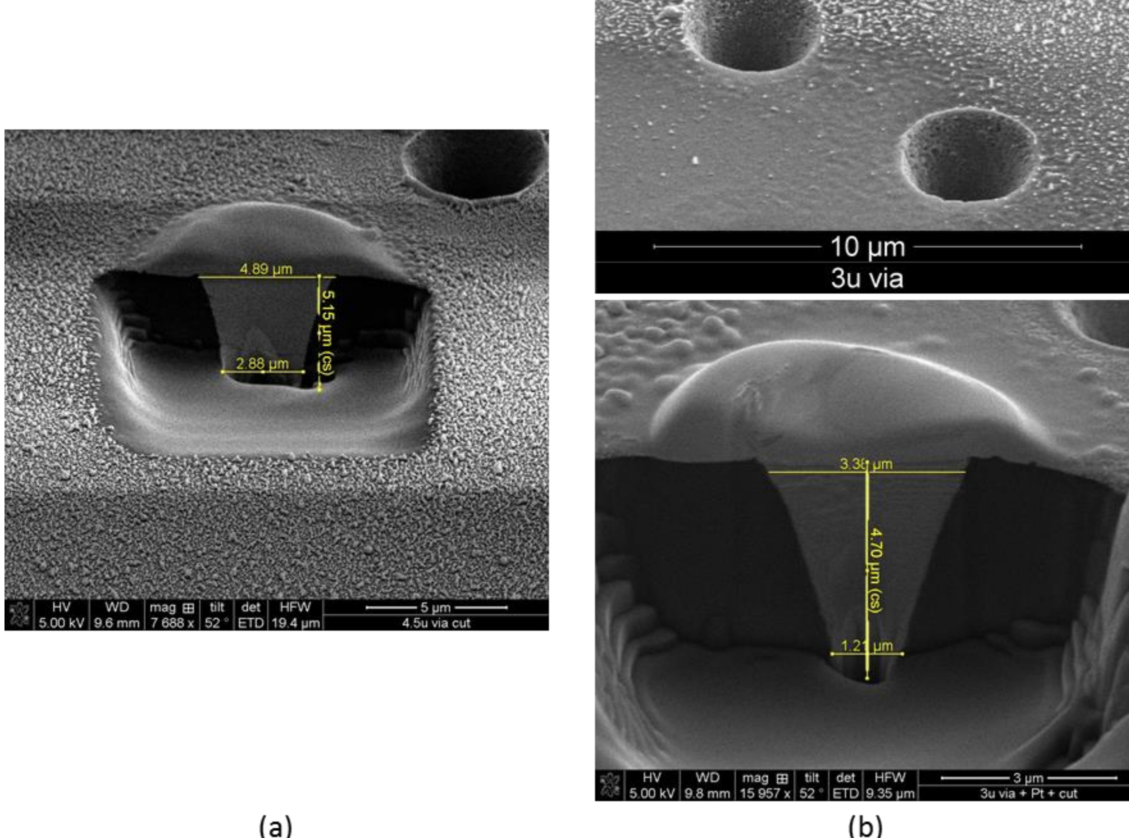

Figure 5.27 SEM micrograph of FIB sections of micro-vias drilled using the SMI laser process in the BTX build up film. (a) 5 µm via >5µm deep. The FIB cross-section was not machined deep enough so the depth of the hole cannot be determined. (b) 3.5 µm via ~5 µm. Again, the bottom of the hole cannot be seen in the FIB cross-section.

The images demonstrate the capability to drill sub-5 µm vias with the SMI process. The results are comparable with those shown in Figure 2.12. In combination with the lower cost of ownership of DPSS laser tool compared to an excimer system (to be discussed in Section 6.1.3) and the selective mask scanning for via drilling discussed in Section 5.6, an SMI process could offer a high throughput, low cost alternative to excimer laser systems for the drilling of sub-30 µm vias.

5.8 SMI compatibility with conventional mask imaging techniques

Having investigated some of the unique features of SMI made possible through accurate scanning of a binary mask with a relatively high repetition rate laser, it was decided to test the compatibility of the SMI system with mask imaging techniques already

developed with other mask imaging systems. These include lamp and excimer laser resist exposure and the use of half tone masks for micromachining with excimer lasers. Images of resist exposure by excimer laser can be seen in Section 2.5.1.

5.8.1 Half tone masks

The half tone mask used was a chrome-on-quartz mask with features below the resolution limit of the optics used to obstruct some of incident laser light in transparent mask areas. This creates a gradient in the fluence at the substrate which can be tuned between a maximum in completely transparent areas of the photomask and a minimum in opaque areas of the mask. The fluences in between are achieved by partial obstruction of the incident light with the sub-resolution chrome pixels. Varying the size and density of these chrome pixels on the photomask enables an effectively continuous range of fluences to be achieved at the substrate with a uniform exposure of the mask.

An image of the mask used to machine a microlens array can be seen in Figure 5.28. The image on the left shows an overview of the top left quadrant of a mask used to establish a fluence gradient to machine a microlens. The mask becomes brighter towards the centre of the circular feature as the density of chrome pixels increases reflecting more light back through the microscope objective. The image on the right was taken with a higher magnification objective, and shows the chrome pixels used to establish the gradient in fluence. The pixel size is increasing towards the bottom right of the image, such that more laser light would be obscured in these areas. The image shows the pixel length is <2 μm in the object plane of the projection lens, which would correspond to a length of <1 μm in the image plane of the lens, well below its resolution limit.

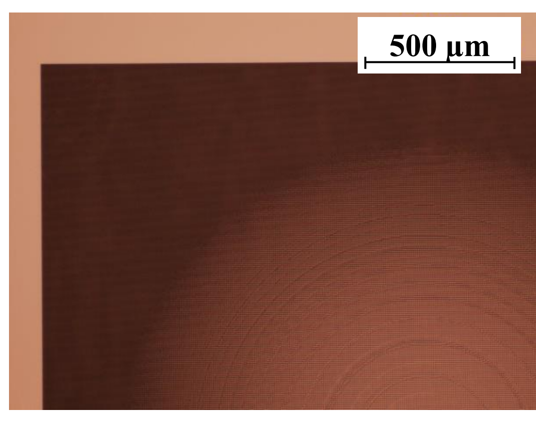

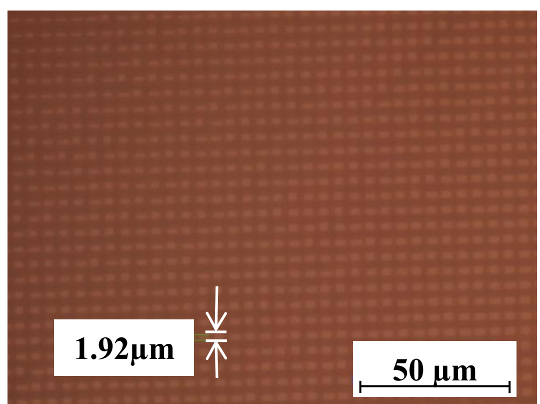

Figure 5.28 Optical micrographs of chrome on quartz half tone mask used to machine microlens arrays. The image on the left shows the macroscopic effect of increasing the density of the sub lens resolution chrome pixels. The lighter areas of the image have a higher density of chrome pixels and the darker areas represent more transparent regions of the mask. The measurement error is ±0.14 µm.

The mask was scanned with a fluence of 100 mJ cm^{-2} and multiple SPA, and the first results can be seen in Figure 5.29. The image of a single microlens was stepped and repeated to form the array. Clearly the mask obstructs some light to form the fluence gradient, so the fluence at the substrate is no longer a factor of the magnification squared greater than the fluence at the mask. The result is of little practical use, since there is no ablation or curvature in the central region of each array element, and there is the cone structure formation around the edge of the array element. This indicates that the beam was attenuated to the extent to which no or very little ablation occurred in the central region. At the edge of each array element, the cone structure formation is a known phenomenon in UV laser ablation of polymers [83] which happens at fluences close to the laser ablation threshold. In Kapton, this is caused by the higher ablation threshold of calcium impurities within the substrate, which subsequently shield the underlying polymer resulting in the cone formation visible in the figure.

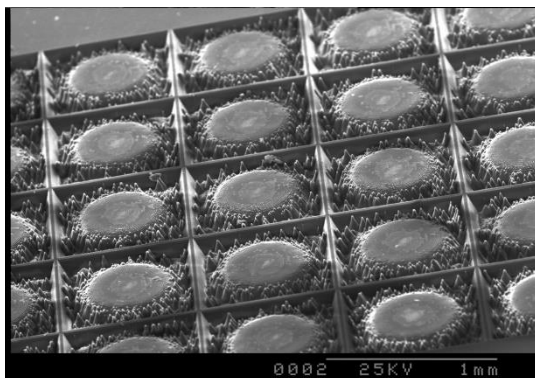

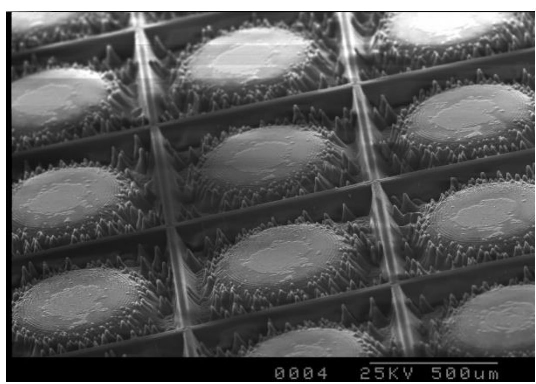

Figure 5.29 SEM micrograph of SMI ablation using half tone mask to ablate a microlens array in Kapton. The array was formed by stepping and repeating the image of a single microlens using x-y stages. The fluence at the mask plane was ~100 mJ cm^{-2}. The cone formation at the edge of each array element occurs due to calcium impurities in the Kapton film which have a higher ablation threshold than the surrounding polymer.

Since this effect was documented to occur at close to the ablation threshold of Kapton, within a narrow range of fluences, the fluence was then increased to ~160 mJ cm^{-2} at the mask plane. This was above the documented damage threshold for chrome-on-quartz masks with excimer lasers, so a low intensity mask scanning regime was used to minimise the risk of damage to the mask. The laser ablation is shown in Figure 5.30. The result is clearly an improvement on Figure 5.29, and looks much closer to what was expected from the microlens array. The higher fluence regions at the outer edge of the array unit have been ablated to a uniform depth, and the pixelated chrome region towards the centre of the mask unit has had the desired effect of creating a fluence gradient varying the etch rate as a function of lens radius at the substrate. There reaches a point however, towards the centre of the microlens, at which the fluence becomes too low, and cone formation begins to occur.

Given that the mask invariably sets up a fluence gradient between the edge and centre of the microlens, and the fluence used for the laser ablation in Figure 5.30 already risked damaging the chrome-on-quartz mask, it was concluded that it would not be possible to ablate a microlens without cone formation in this particular variety of Kapton. Although SMI had been demonstrated to be compatible with half tone masks, shown by the gradient in fluence clearly present in Figure 5.30, to successfully micromachine a microlens array without cone formation would require a high purity polymer.

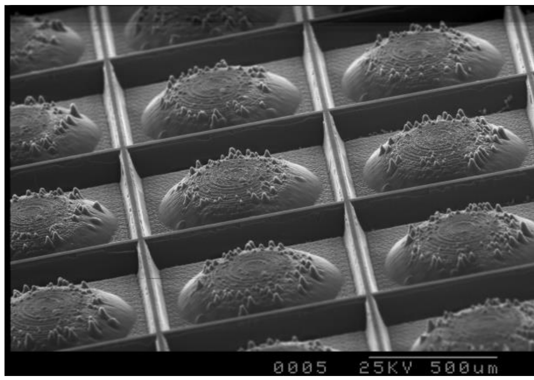

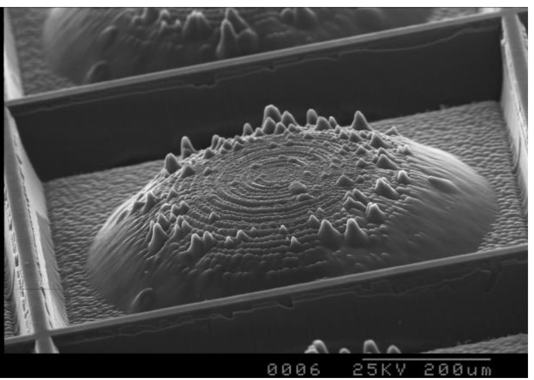

Figure 5.30 SEM micrograph of SMI ablation using half tone mask to ablate a microlens array in Kapton. The array was formed by stepping and repeating the image of a single microlens using x-y stages. The fluence at the mask plane was ~160 mJ cm^{-2}. The cone formation on the lens surface of each array element occurs due to calcium impurities in the Kapton film which have a higher ablation threshold than the surrounding polymer.

To support the idea that the cone formation was due to the calcium impurities in the Kapton film, the half tone mask was imaged onto the BTX build up film substrate which had been used extensively in testing and never shown evidence of cone formation at low fluence. Images of the ablation are shown in Figure 5.31. Indeed there is no cone formation when using the halftone mask with the BTX substrate. BTX had not been used in the initial tests because the film is only 18 µm thick, laminated onto a copper clad laminate. Hence the areas around the edge of the microlens have been ablated to the copper layer below, and the aspect ratio of the microlens is limited by the film thickness and the fixed size of the microlens at the mask plane.

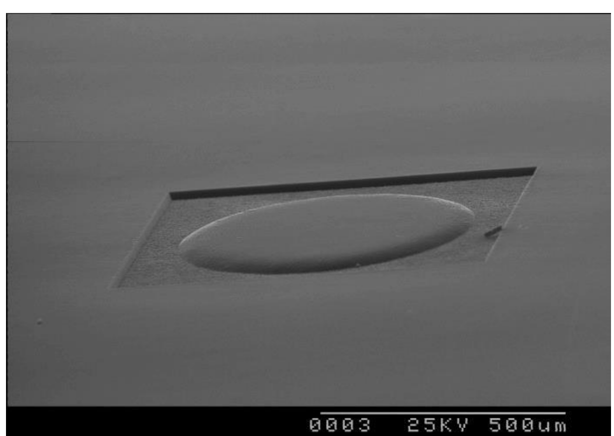

Figure 5.31 SEM micrograph of SMI ablation using half tone mask to ablate a microlens in an 18 µm BTX film on a copper clad laminate.The fluence at the mask plane was ~160 mJ cm^{-2}. There is no evidence of cone formation in the BTX substrate.

It was confirmed that half tone masks could be used to establish a fluence gradient at the substrate with uniform fluence exposure of the mask using the SMI system. This was

used to fabricate a microlens array in Kapton, although calcium impurities in the Kapton led to a defect in the laser ablation. This demonstrates the compatibility of SMI with half tone mask imaging techniques.

5.8.2 Resist exposure

The resolution of the SMI system was also tested for resist exposure. In collaboration with a company with the capability to deposit and develop a resist, and subsequently electrolessly plate the sample, a negative i line resist was deposited on top of a copper seed layer on a PET carrier substrate. The resist was exposed to a range of laser parameters and it was found that the best results were achieved when the material was exposed to a higher intensity. Sites processed with a high intensity had better defined electroless copper plating than low intensity sites with a higher total dose. This suggests the high intensity irradiation improves the cross-linking in the polymer resist. Resists are normally hard baked after development to remove any solvent remaining in the substrate, so a more thermal exposure process might have locally removed the solvent in the exposed areas improving the resist performance.

The sample was then electrolessly plated, and images of the plating results achieved with the optimum exposure parameters can be seen in Figure 5.32. Since the resist was negative, the areas that have been exposed to the laser have cross-linked and become more resistant to removal by the developer. Thus when the resist was developed, only the exposed areas are not removed and remain intact acting as a barrier between the seed layer and the electroless copper plating bath. Therefore electroless copper growth is seeded everywhere but the exposed areas, which appear black in the images. Figure 5.32(a) shows a demonstrator fan out device with 3 µm L/S tracks. Figure 5.32(b) shows the same 3 µm L/S device at a higher magnification. Figure 5.32(c) shows a demonstrator microfluidic device with a 5 µm L/S serpentine pattern exposed, developed, and negatively plated on the carrier PET substrate.

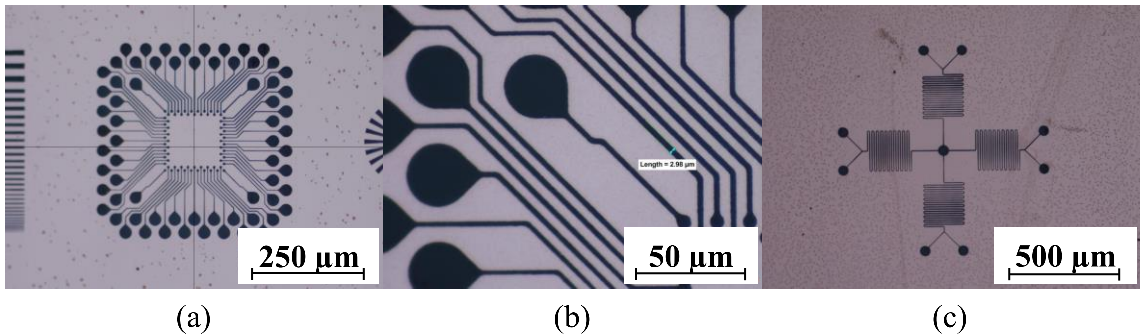

Figure 5.32 Electroless plating results of an optimised exposure dose delivered to a negative resist by the SMI system. The electroless copper is present in the lighter areas of the image. (a) is an image of a 3 µm L/S demonstrator fan out device. (b) shows a higher magnification image of the 3 µm L/S device. (c) shows a demonstator microfluidic pattern with 5 µm L/S serpentine.

Although the plating with the negative resist is of the wrong polarity, the results demonstrate SMI compatibility with long UV wavelength resists for high resolution patterning. The polarity of the resist, or the mask features, could be inverted to obtain 3 µm conductive tracks on a substrate. This could offer a high average power, high throughput alternative to lamps in stepper systems used with i-line resists, however is not a viable alternative to the high average power 193 nm excimer systems, which offer the highest average power in the deep UV.

5.9 Summary

The resolution across the field of the projection lens was tested and it was found that 3 µm features could be resolved across the majority of the image field providing the substrate focus was maintained to within ±10 µm. Varying the intensity of the laser ablation process was explored by changing the mask scanning regime to adjust the thermal loading of the substrate. It was found that the ablation rate of features greater than 10 µm wide could be increased by using a high intensity mask scanning regime, and that a low intensity mask scanning regime could improve the resolution of fine scale features. This feature is unique to the SMI system due to the comparatively low maximum repetition rate of high power excimer lasers, approximately 300 Hz.

The relationship between fluence and taper angle was investigated, and the maximum aspect ratio of 3 µm L/S features found to be ~3:1. Scanning the mask with a shaped laser beam was explored, and ramps were micro-machined in Kapton to demonstrate a potential application. The high spatial and temporal resolution of the SMI illumination system was investigated in the micro-machining of some apertures for a detector. The case study shows that selectively illuminating the transparent areas of the photomask

can significantly reduce the process time. Finally, the SMI system was shown to be compatible with half tone mask laser ablation and resist exposure, broadening the range of applications which might be able to adopt the technology.

Chapter 6: Evaluation of SMI

It has been shown that the SMI system can be used to achieve high quality laser ablation of organic dielectrics of a comparable quality to excimer laser systems. This chapter aims to critically evaluate the performance, throughput and cost of an SMI production system in comparison with an excimer production system. It goes on to compare the cost of a manufacturing process flow of an ablative SMI tool with the current SAP technologies, and qualitatively assesses the likelihood of the adoption of SMI technology within advanced packaging and other industries.

6.1 Comparison of SMI and excimer laser systems for high resolution ablation

6.1.1 Performance

In terms of the quality of laser ablation excimer and SMI systems are comparable. The minimum feature size it is possible to laser ablate to a depth at least equal to the feature width across a reasonable field is around 2 μm. The most economical excimer wavelength for mass production is 308 nm because of the cost and lifetime of the XeCl gain medium, the high average power attainable, and the higher ablation rates achievable with longer wavelengths. Based on this the resolution of XeCl excimer system should be a factor 1.15 better than the most economical UV solid state laser wavelength, 355 nm. However, in practise, the minimum feature size achievable is dependent largely on how much is invested in the projection optics, and the NA of the projection lens. Not only this, but due to the fact that XeCl lasers have two spectral peaks in the emission wavelength at 307.96 nm and 308.25 nm [42], high resolution 308 nm lenses require calcium fluoride lens elements as well as fused silica elements to overcome chromatic aberrations in the projection lens image. This can significantly increase the cost and complexity of the lens design. This is in contrast to lenses designed for 355 nm which require only fused silica elements due to the comparatively narrow spectral line width of the laser.

There are also a limited number of materials which have both strong absorption at 308 nm and weak absorption at 355 nm. With these materials, high quality ablation is possible with excimer systems due to the small optical penetration depth which limits the size of the heat affected zone. However, at 355 nm, due to the low absorption, these materials will typically melt when irradiated with high fluences meaning the machining of fine scale features is not possible, and large features would have a heat affected zone.

PET is one such material, which can be machined at 308 nm, but not at 355 nm without the addition of absorption enhancing additives.

Excimer lasers also offer the highest average power in the UV, with up to 300 W available in commercial models for industry. Frequency tripled, multimode, DPSS lasers are lower power, for example Lee Laser manufacture a multimode 55 W model and Powerlase manufacture a 180 W model. However the throughput and transmission efficiency of illumination optics is higher in solid state lasers meaning the percentage of the total laser power reaching the substrate is higher. High efficiency DOEs can have diffraction efficiencies specified at over 90%, such that the transmission efficiency of an SMI production system is estimated to be ~71% as shown in Table 6.1.

This is compared to excimer systems, where the percentage of laser power delivered to the substrate is typically between 40-60%. This is partly due to the poor spatial coherence of the laser, which has a comparatively high divergence particularly in the long axis of the beam. Excimer lasers are also very large, meaning the laser is normally kept adjacent to the process head. This normally results in a relatively long beam path from the laser to the process head, which coupled with the poor spatial coherence of the laser beam, results in a significant loss of power between the laser and the substrate.

A number of DPSS lasers would be required to match the throughput of a 300 W excimer system, however because the cost per watt of laser power of a DPSS laser is lower, the capital cost of DPSS laser system will always be less. The fact that multiple lasers are required would mean that a production tool with 4 DPSS lasers lends itself more naturally to multiple process heads, with two 55 W lasers illuminating each head. This further reduces the cost of ownership of a solid state laser tool by approximately halving the stage step times per device. Based on the factors above, analysis suggests a two head, 220 W SMI system would have a higher throughput than a single head 300 W excimer system. This claim is justified in Section 6.1.2.

Component	Manufacturer quoted transmission efficiency
12x AR coated lens and mirror surfaces	$0.995^{12} = 0.94$
DOE	0.91
f-theta lens	0.97
Uncoated glass surfaces of mask	0.92
Projection lens	0.93
Fraction of power delivered from laser to substrate	**0.71**

Table 6.1 Transmission efficiency of optical components in an SMI production tool. The fraction of the total original power from the laser being delivered to the substrate, 0.71, was arrived at by taking the product of the fractional loss in each component.

6.1.2 Machine architecture and throughput comparison

Accurate throughput simulation of a production tool is difficult, and depends on the ablation rate for the specific substrate, panel size, devices per panel and the machine architecture. To enable a fair comparison, throughput information for a 300 W excimer production system was obtained for a specific fluence, lens field, wafer size and required shots per area. To simplify the comparison, it was assumed the same fluence, etch rate and total number of shots per area are required for each laser system. This is despite the fact that longer wavelengths are typically associated with longer optical penetration depths and therefore higher ablation rates [39].

An SMI throughput model was developed for a substrate of the same size, with the same number of devices and the same lens field to remove these variables from the throughput comparison. The throughputs for various machine architectures were analysed by M-Solv, including single head and dual head architectures with multiple lasers for each projection head. A two head SMI production tool with four 55 W lasers (2 lasers and 110 W per head) was found to provide the best compromise between high throughput, low cost and relatively low engineering complexity. The mechanical design team at M-Solv then put forward the model seen in Figure 6.1. The two production heads pattern two panels simultaneously on two separate but synchronised tables sharing common rails. It was decided this would be easier to implement in terms of engineering complexity than having multiple heads on a single panel. With two heads per panel, the masks and projection heads must be aligned to each other as well as the substrate, increasing the complexity of the system, the number of stages required and therefore accentuating Abbe errors on the system. The separation between the projection heads on the system would have to be a multiple of the device pitch on the panel, constraining the panel layout, or be adjustable, again increasing complexity.

Having two 110 W heads gives a higher throughput than a single 220 W head because two devices are positioned in a single stage step time, effectively halving the stage step times between devices. It also halves the power per head, which reduces the power handling requirements placed on the coatings of the optical components in the system. This also has the potential to increase optical component lifetime, particularly compared to excimer laser systems which have shorter wavelengths and pulse energies a factor of 100 times higher.

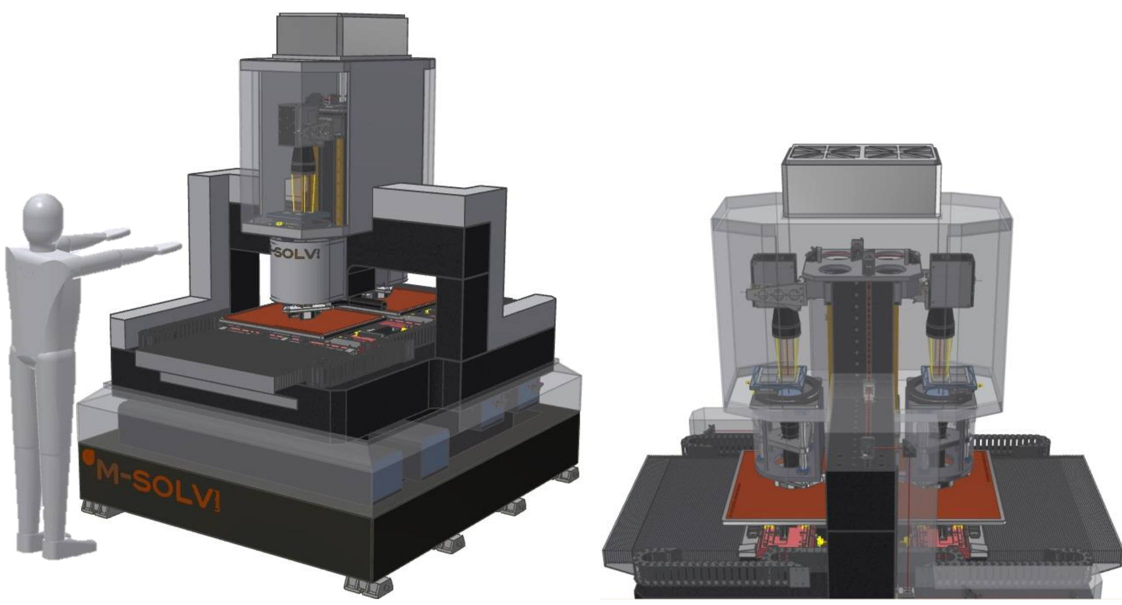

Figure 6.1 Proposed SMI system architecture where four 55 W multimode lasers, which can be seen under the tables in the image on the left, feed two SMI optical systems.

Based on the above system architecture, an SMI production tool throughput was compared to the excimer laser system. Input variables were fixed to deliver the same fluence and shots per area to the substrate as with the excimer analysis. The comparison suggests that for this particular substrate size and device layout, with the defined ablation depth and ablation rate, the 220 W SMI production tool would have a throughput ~1.6 times higher in terms of wafers/hour than the 300 W excimer system. The specific input variables cannot be discussed as they would reveal commercially sensitive information regarding the excimer production system.

6.1.3 Cost of ownership

The difference in cost of ownership of an excimer laser system and a DPSS laser system is largely due to the capital cost and running costs of the lasers. The initial cost and running costs of the laser systems were estimated based on list prices and manufacturer information obtained in 2014/2015. The running costs of excimer laser systems scale

per laser pulse, and are expected to be approximately \$30 per million laser pulses. Simulating an excimer laser production tool operating at 300 Hz, and allowing for time in production when the laser is not firing, for example when stepping between devices, or load and alignment times, it is estimated that the laser fires 332 000 shots/hour such that the running costs are ~ \$9.96/hour. Combined with the depreciation of the laser over a 5 year period with 8000 hours/year, at a capital cost of ~\$3300/W of laser power, this comes to \$34.71/hour for the 300 W laser ownership costs alone. This excludes higher costs associated with running the excimer system compared to a solid state laser system, such as shorter life time of optics on account of the shorter UV wavelength and higher pulse energy, more expensive projection optics due to the calcium fluoride elements and the larger footprint of the tool on account of the laser size which would require approximately 1.5 times more floor space in a production clean room. The cost per unit area of clean room floor space is not estimated here as it depends on a large number of variables including the class of the clean room, the total floorspace and height of the clean room and the country in which the cleanroom is located. Infrastructure costs associated with handling and transportation of gases are also ignored.

In contrast, the main cost associated with running a solid state laser system is the replacement of the laser diode used to pump the gain medium, which scales with time not pulses delivered. Diode lifetimes are expected to be ~25000 hours, so need to be replaced approximately every three years in full time production. The running costs including all spare parts for the 4 lasers required to achieve a 220 W, dual head, SMI production system would be \$5.28/hour. This is approximately half the cost per hour for an excimer laser. The cost per watt of laser power is approximately \$2100/W, but the total watts required on the system are also less because of the more efficient delivery of laser power to the substrate, and the increased tool throughput obtained through multiplexing with multiple heads. Again, writing off the capital expenditure over 5 years with 8000 hours/year, the combined cost of ownership including the initial capital and parts cost is \$17.83/hour. This analysis suggests the cost of ownership of the lasers alone is approximately half that of an excimer system.

The above information is summarised in Table 6.2, showing the total cost of ownership of an SMI system is expected to be less than half that of an excimer system. This factors in the higher device throughput achieved at lower capital and running costs. In

both cases, the calculation includes: a five year equipment write off period with 8000 hours per year; approximate utility costs including factory space, water, air and electricity and excludes operator costs.

Relative	SMI Tool	Excimer tool
Relative machine price	1×	2×
Relative consumables cost	1×	2×
Relative throughput rates	1.5×	1×
Relative cost of ownership	**1×**	**2.5×**

Table 6.2 Summary of relative cost of SMI DPSS laser tool and an excimer laser mask projection tool.

6.2 Cost comparison of SMI with conventional SAP technologies

The SMI process compares very favourably in terms of cost of ownership to excimer laser systems. Currently, however, excimer laser ablation is not in common use in the chip packaging industry. A more meaningful comparison might therefore be with conventional SAP technologies in which resist is exposed on a 2 µm copper seed layer with an LDI tool and the subsequent laser via drilling. Such a comparison is challenging since process steps must be added and removed, and the whole supply chain must now be considered rather than the direct comparison possible with the two laser ablation tools.

A comprehensive cost of ownership analysis of the different process flows was carried out by a collaborator, with input information on the cost and throughput rates on laser ablation equipment from M-Solv. The throughput of an LDI tool is much higher than a laser ablation tool, simply because the total energy per unit area required to expose a resist is much lower than that needed for laser ablation. In an SAP process, however, the resist exposure is preceded by copper plating the seed layer and drilling of the vias, and is followed by development of the resist, pattern plating of the conductive channels, stripping of the resist and the etching of the seed layer.

Taking this into consideration, the analysis found that the total cost of ownership for a patterned panel – also taking into account the throughput rates of the tools – was 33% higher for an SMI ablation than for conventional SAP methods. This is based on panel plating the laser ablated grooves and etching or planarising the panel to reveal the circuitisation. This is compared to 64% higher with an excimer laser based ablation process. However the comparison is not like for like, since both the excimer process and the SMI process reduce the minimum feature size possible. This improves the performance of the package and can potentially lead to a reduction in the number of

layers required for a given package. Reducing the number of build-up layers required would, of course, significantly reduce the cost.

In addition to this, the planarization step to reveal the circuitry after panel plating in the ablative manufacturing process is costly. The analysis found that if a process were developed where the copper seed layer could be selectively deposited in the laser ablated channels, such that electroless copper would only be deposited in the laser ablated areas, the cost could be reduced significantly by removal of the planarization step. Such a process would be 87% of the cost of current SAP processes when used in conjunction with SMI ablative laser technology. Using an excimer laser system in conjunction with this plating methodology would still be 18% more costly than current SAP processes.

The argument for adopting SMI laser ablation technology with fully additive plating methodologies seems simple given the improved performance and reduced cost. There are, however, barriers to the introduction of this manufacturing technology into the chip packaging industry. The semiconductor and micro-electronics industry has been driven by the increased demand for smart phones over the past decade. This is a high volume, low margin market which requires high yield manufacturing technologies to ensure good profitability. This makes the industry risk averse, so the adoption of new manufacturing technologies and process flows without a proven and established record for yield and reliability can be slow.

The industry requires new manufacturing methods to address the technology gap between the current state of the art in SAP and semiconductor production technology. There are alternatives to laser ablation, however, such as projection imaging steppers used with photoresists, or photo-imageable dielectrics which can be structured by mask imaging and development. There are drawbacks to these technologies, such as cost or electrical and mechanical properties of photo-imageable dielectrics, however the use of high resolution steppers and photolithography in the semiconductor industry has been common place for many years. It remains to be seen what technology IC substrate and interposer manufacturers will adopt, however there might be a preference for proven and familiar technologies regardless of the economic implications and impact on device performance.

6.3 SMI for micro-via drilling and micromachining

To realise the full benefit of fine line space tracking in an advanced package, there also needs to be a reduction in the via size to reduce the required capture pad size for the via. This increases the number of I/Os it is possible to redistribute from the chip in a given layer, and thus reduces the total number of layers required. For this reason, it makes sense to form the circuitisation with the same tool used to drill the micro-vias, which is only possible if the circuitisation is formed by an ablative laser process. Forming the two features on the same platform improves the achievable registration between the two features, reducing the size of the capture pads required which allow a tolerance for misalignment between imaging and via drilling tools.

If the circuitisation is formed through use of a stepper and a resist, however, there is still need for sub-30 μm via drilling which is the best currently available on high throughput, frequency tripled, solid state laser drilling tools. The only current alternative is mask imaging with an excimer laser, which can achieve sub-5 μm vias over the required package size. The SMI platform offers a lower cost alternative for the high volume laser drilling of sub-5 μm vias regardless of the technology used to form the circuitisation in the package. Since the laser drilling of micro-vias is already the industry standard, and the only option currently available for high throughput drilling of sub-30 μm vias is also a mask imaging technology, the introduction of SMI technology for high throughput drilling of micro-vias is likely to meet less resistance.

There might also be other industries in which the high resolution structuring of polymers or thin metal films is required and ablative excimer laser technologies are incumbent. Such industries, where introduction of SMI technology would not require the introduction of new process flows and methodologies, might be more receptive to the introduction of the SMI process. These industries might include sensing, biotechnology, microfluidics and inkjet nozzle drilling, among others.

6.4 Summary

An SMI production system offers comparable ablation quality and higher throughput than an excimer laser system. Excimer systems operating at 248 nm and 308 nm do have a better theoretical resolution than a 355 nm solid state laser system, and might also benefit from a shorter pulse length in some materials. An SMI system enables selective mask scanning, which reduces the laser energy wasted illuminating opaque areas of the mask and reduces process time. SMI also provides some control of the

repetition rate of consecutive shots delivered to a given area of the substrate, which can be tuned to improve the ablation quality or the ablation rate of the substrate. Regardless of whether the chip packaging industry chooses laser ablation as the preferred methodology for reducing feature sizes in chip packages, SMI represents a low cost alternative to excimer lasers for high resolution laser ablation. Enabling the use of multimode solid state lasers in mask imaging applications reduces the cost of high resolution laser ablation by enabling the use of a less expensive laser technology with a mature, well developed optical system.

Chapter 7: Further Work and Conclusions

7.1 Further work

The high resolution structuring of glass is of interest to a number of industries including the advanced chip packaging industry. The structuring of thin glass would enable the embedding of conductors in glass for 2.5D interposer applications. Glass is appealing to the chip packaging industry because of its mechanical and electrical properties, and the fact that the coefficient of thermal expansion of glass can be tuned to match that of silicon. Glass processing with femtosecond lasers has been the subject of much research [84, 85], and is able to direct write microfluidic channels and waveguides in the bulk of transparent materials. The very high peak power of ultrafast lasers induces non-linear absorption in the transparent material at the focal point of the laser. Forming structures in the bulk of the glass is of no benefit to chip packaging, however, and would complicate the plating process. Additionally, for the formation of surface features in the glass, femtosecond lasers are less reliable and lower power than multimode nanosecond lasers. Used in direct write systems, they also suffer from the same limitations discussed in Section 2.5.2 in terms of ablation of large areas with a focused spot.

Laser Induced Backside Wet Etching (LIBWE) has also received much attention from researchers, and involves the structuring of transparent materials by placing the backside of the substrate in contact with a strongly absorbing liquid. Trenches 7 μm wide and 420 μm deep have been demonstrated in UV transparent materials through mask projection with a KrF excimer laser [86]. The machining of glass with 355 nm nanosecond lasers at etch rates of up to around 3 μm/pulse with fluences achievable with the SMI system has also been demonstrated [87]. It would be of great interest to see if it were possible to structure glass to a high resolution with features commonly found in chip packaging using SMI in a LIBWE process. The high planarity of glass substrates would also make the planarization step to reveal the circuitry after panel plating of the substrate easier and faster.

Further work could also be done to optimise the illumination of the imaging system. This could be done empirically by testing DOE homogenising elements with different diffraction angles and singlets to keep the beam size and fluence constant at the mask, but change the beams divergence after the mask. Increasing the beam divergence after the mask would increase the filling of the entrance pupil of the projection lens, which could affect the imaging performance and partial coherence factor of the imaging system.

Bow tie mask scanning regimes could be explored in conjunction with conformal mask scanning to extend the addressable area of the projection optics without stitching errors. This would require high accuracy stages and some development of the system integration to allow synchronisation of the scanner commands with the stage motion.

It might also be of interest for other applications to develop SMI systems for the fundamental and second harmonic frequencies of Nd:YAG DPSS lasers. This would enable well defined, sharp images of photomasks to be projected onto substrates at 1064 nm and 532 nm, which might be more appropriate or cost effective in applications with substrates strongly absorbing at those wavelengths. As femtosecond and fourth harmonic 266 nm lasers become more reliable and powerful, these might also be interesting candidates for light sources in an SMI system. Femtosecond lasers used in conjunction with SMI would allow high precision micromachining of transparent substrates such as glass. A 266 nm laser would decrease the power and throughput of an SMI system in comparison to a 355 nm, but would improve the theoretical resolution limit of the optical system and would allow the machining of substrates transparent at 355 nm but absorbing at 266 nm such as PET.

7.2 Conclusions

In this thesis I have developed the SMI system which enables the use of a multimode solid state laser in a mask projection imaging system. I have taken the system from a conceptual stage, tested its feasibility on a proof-of-concept system, and specified the optical design of the prototype lab system. Having designed and installed the prototype lab system, I have characterised the system performance and assessed its applicability to addressing a technology gap in the chip packaging market.

Having set up the proof-of-concept system, I demonstrated it was possible to raster scan a binary mask with a galvanometer scan head and form the image of the mask with an f-theta lens. I then specified upgrades to the opto-mechanics on the system, including the mounting of the photomask on a linear stage and demonstrated the overlay of two adjacent areas of the mask in the substrate plane to machine vias in a circuitry layer. I used the system to laser ablate a two layer panel level fan-out chip package in collaboration with a plating company, a materials company and an assembly company. This demonstrated the feasibility of using the SMI process to laser ablate circuit features for a chip package.

Despite the successful production of the 2 layer chip packages, I found the optical aberrations in the f-theta lens when used in a finite conjugate projection imaging system were too great to image feature sizes below 10 μm across a 15×15 mm optical field. I modelled the lens performance in Zemax, and correlated the model results with the ablation results I had obtained on the proof-of-concept system. The two optical aberrations most pertinent to the resolution of fine scale features across an optical field with a high degree of spatial accuracy were the field curvature and the distortion. The model suggested the field curvature was already several hundred microns at a radial distance of 10 mm from the optical axis, consistent with the loss of focus I observed at the edge of the optical field in the laser ablation. I concluded that the f-theta lens did not have the required optical performance for the machining of sub-10 μm features across a 15×15 mm optical field. This meant that to address the technology gap in the chip packaging market, a new optical system with custom projection optics would have to be specified and designed.

In discussions with a lens supplier, I specified the design of a new telecentric illumination system and a double telecentric, high NA projection lens. The new illumination system included a DOE which formed a square, homogenous beam at the focal plane of a singlet lens. The image of the homogenous beam was relayed to the mask plane by an infinite conjugate imaging system consisting of a second singlet lens and a telecentric f-theta lens mounted to the scanner. I designed the illumination system this way to allow control of the beam fluence and divergence at the mask plane by interchanging the singlets or DOE, as well as to negate the need for a field lens and limit the size of the first element in the projection optics. I then modelled the performance of the projection optics in Zemax and confirmed the optics were suitable for the application. I installed the new optical system and I found that the system could resolve 2 μm L/S features in a resolution chart. I found the beam homogeneity greatly improved the uniformity of large area ablation, and I demonstrated the laser ablation of a variety of features relevant to chip packaging including large ground plane areas, fine scale tracks, landing pads and vias. I also investigated the optimum beam profile for the mask illumination by placing an aperture in the first plane of homogeneity formed by the DOE. I found that the sharp edge of the aperture in the beam profile accentuated beam stitching affects at the substrate, and that the shallow edge to the beam energy profile formed by the DOE was optimum for uniform ablation of large areas.

Having installed the new optical system, I characterised its performance and explored the novel aspects of the SMI system. I discovered that the small beam and high repetition rate of the laser gave a relatively high spatial and temporal resolution to the mask illumination. This meant the mask could be selectively illuminated, significantly improving the process time for simple parts with a small number of features. The high temporal resolution of the SMI illumination system gives control of the time between successive shots in a given part of the substrate. I demonstrated that this could be used to improve the ablation quality of fine scale features, or improve the ablation rate of larger features not prone to thermal collapse. I showed that the SMI system was compatible with mask imaging applications developed with other laser sources, such as resist exposure and half tone masks. I also explored illuminating the mask with a shaped beam profile to micro-machine ramps in Kapton, and highlighted the potential to laser ablate vias without a photomask by imaging a circular aperture through landing pads in the circuitry layer photomask.

I then compared the SMI system to an excimer system, focusing on metrics of performance, throughput and cost of ownership. I outlined the system architecture for an SMI production tool, modelled its throughput and compared this with an excimer production system for chip packaging. The comparison suggests that through multiplexing, an SMI production tool would have a higher throughput. Entering the data into a cost of ownership model, I found that the cost of ownership of an SMI production system was less than half that on an excimer system. This is due largely to the lower purchase and running costs of the laser technology, and the lower total laser power required to achieve a higher throughput.

In this work I have demonstrated it is possible to perform high resolution laser ablation by using a multimode diode pumped solid state laser system to illuminate a mask in a projection imaging system. I have shown that the ablation results are comparable to the current state of the art in high throughput, high resolution laser ablation: excimer laser systems. Further, I have highlighted some of the performance advantages attainable by high resolution scanning of a binary mask with a high repetition rate laser. Finally, I have put forward the economic argument for adoption of the technology, which compares favourably with the current state of the art because of the lower cost of the employed laser technology.

References

[1] (2012). *International Technology Roadmap for Semiconductors*. Available: http://www.public.itrs.net/

[2] E. Beyne, "Multilayer thin-film technology enabling technology for solving high-density interconnect and assembly problems," *Nuclear Instruments and Methods in Physics Research Section A: Accelerators, Spectrometers, Detectors and Associated Equipment,* vol. 509, pp. 191-199, 2003.

[3] R. Huemoeller, "Advancements in Interposer Assembly," in *5th Annual Global Interposer Technology Workshop GIT 2014*, Georgia Institute of Technology, Atlanta, 2014.

[4] R. K. Cavin, P. Lugli, and V. V. Zhirnov, "Science and Engineering Beyond Moore's Law," *Proceedings of the IEEE,* vol. 100, pp. 1720-1749, 2012.

[5] J. Fjelstad, *Flexible Circuit Technology*, 4th ed. Seaside: BR Publishing Inc., 2011.

[6] Y. Zhang, C. Q. Liu, and D. Whalley, *Direct-write Techniques for Maskless Production of Microelectronics: A Review of Current State-of-the-art Technologies*, 2009.

[7] E. D. Williams, R. U. Ayres, and M. Heller, "The 1.7 kilogram microchip: Energy and material use in the production of semiconductor devices," *Environmental Science & Technology,* vol. 36, pp. 5504-5510, Dec 2002.

[8] J. van den Brand, R. Kusters, M. Barink, and A. Dietzel, "Flexible embedded circuitry: A novel process for high density, cost effective electronics," *Microelectronic Engineering,* vol. 87, pp. 1861-1867, 2010.

[9] E. D. Blackshear, M. Cases, E. Klink, S. R. Engle, R. S. Malfatt, D. N. de Araujo, S. Oggioni, L. D. LaCroix, J. A. Wakil, G. G. Hougham, N. H. Pham, and D. J. Russell, "The evolution of build-up package technology and its design challenges," *Ibm Journal of Research and Development,* vol. 49, pp. 641-661, Jul-Sep 2005.

[10] E. Beyne, R. Van Hoof, T. Webers, S. Brebels, S. Rossi, F. Lechleiter, M. Di Ianni, and A. Ostmann, "High density interconnect substrates using multilayer thin film technology on laminate substrates (MCM-SL/D)," *Microelectronics International,* vol. 18, p. 36, 2001.

[11] M. Kuniba, "Semiconductor Package Substrates, Technology Trends and Forecast," Gartner Inc.2002.

[12] W. J. Greig, *Integrated Circuit Packaging, Assembly and Interconnections*. New York: Springer, 2007.

[13] R. R. Tummala, "Emerging Opportunities and Challenges for Interposers," in *5th Annual Global Interposer Technology Workshop GIT 2014*, Georgia Institute of Technology, Atlanta, 2014.

[14] T. H. J. van Osch, J. Perelaer, A. W. M. de Laat, and U. S. Schubert, "Inkjet Printing of Narrow Conductive Tracks on Untreated Polymeric Substrates," *Advanced Materials,* vol. 20, pp. 343-345, 2008.

[15] K. Cheng, M. H. Yang, W. W. W. Chiu, C. Y. Huang, J. Chang, T. F. Ying, and Y. Yang, "Ink-jet printing, self-assembled polyelectrolytes, and electroless plating: Low cost fabrication of circuits on a flexible substrate at room temperature," *Macromolecular Rapid Communications,* vol. 26, pp. 247-264, Feb 2005.

[16] P. J. Smith, D. Y. Shin, J. E. Stringer, B. Derby, and N. Reis, "Direct ink-jet printing and low temperature conversion of conductive silver patterns," *Journal of Materials Science,* vol. 41, pp. 4153-4158, Jul 2006.

[17] H. H. Lee, K. S. Chou, and K. C. Huang, "Inkjet printing of nanosized silver colloids," *Nanotechnology,* vol. 16, pp. 2436-2441, Oct 2005.

[18] A. Kamyshny, M. Ben-Moshe, S. Aviezer, and S. Magdassi, "Ink-jet printing of metallic nanoparticles and microemulsions," *Macromolecular Rapid Communications,* vol. 26, pp. 281-288, Feb 2005.

[19] M. C. Dang, T. M. Dung Dang, and E. Fribourg-Blanc, "Inkjet printing technology and conductive inks synthesis for microfabrication techniques," *Advances in Natural Sciences: Nanoscience and Nanotechnology,* vol. 4, p. 015009, 2013.

[20] K. Y. Shin, M. Lee, H. Kang, K. Kang, J. Y. Hwang, J. M. Kim, and S. H. Lee, "Characterization of Inkjet-Printed Silver Patterns for Application to Printed Circuit Board (PCB)," *Journal of Electrical Engineering & Technology,* vol. 8, pp. 603-609, May 2013.

[21] H. Meier, U. Loffelmann, D. Mager, P. J. Smith, and J. G. Korvink, "Inkjet printed, conductive, 25 mu m wide silver tracks on unstructured polyimide," *PHYSICA STATUS SOLIDI A-APPLICATIONS AND MATERIALS SCIENCE,* vol. 206, pp. 1626-1630, 2009.

[22] H. Holden, *The HDI Handbook*, 1st Edition ed. Seaside: BR Publishing Inc., 2009.

[23] R. Barbucha, M. Kocik, J. Mizeraczyk, G. Koziol, and J. Borecki, "Laser direct imaging of tracks on PCB covered with laser photoresist," *BULLETIN OF THE POLISH ACADEMY OF SCIENCES-TECHNICAL SCIENCES,* vol. 56, pp. 17-20, 2008.

[24] X. Dai, C. Kim, R. Willecke, and P. S. Ho, "In-Situ Mapping and Modeling Verification of Thermomechanical Deformation in Underfilled Flip-Chip Packaging Using Moiré Interferometry," *MRS Online Proceedings Library Archive,* vol. 445, p. 167, 1996.

[25] D. Manessis, L. Boettcher, A. Ostmann, R. Aschenbrenner, H. Reichl, and Ieee, *Innovative Approaches for Realisation of Embedded Chip Packages - Technological Challenges and Achievements*, 2009.

[26] H. Matsumoto, M. Unrath, H. B. Zhang, and B. Hainsey, "Laser Direct Ablation for Patterning Printed Wiring Boards Using Ultra-fast Lasers and High Speed Beam Delivery Architectures," *JOURNAL OF LASER MICRO NANOENGINEERING,* vol. 8, pp. 315-320, 2013.

[27] R. Brown, *RF/microwave Hybrids : Basics, Materials, and Processes*. Boston: Kluwer Academic Publishers, 2003.

[28] S. Franssila, *Introduction to Microfabrication*, 2nd ed. Chichester, UK: John Wiley & Sons, 2010.

[29] R. Zoberbier, M. Arendt, H. Hichri, and J. Hansen. (2015) SUSS MicroTec's Unique DSC300 Gen2 Platform – Combined Projection Lithography Performance with Advantages of Full-field Exposure. *Suss Report 2015*.

[30] J. H. Lau, "The future of interposers for semiconductor IC packaging," *Chip Scale Review,* vol. 18, pp. 32-36, 2014.

[31] K. Yang, H. Hichri, and R. Zoberbier, "Suss Solutions for Large Format Patterning: UV Scanning Lithography and Excimer Laser Ablation " in *SEMI Packaging Tech Seminar*, Vila do Conde, Portugal, 2015.

[32] M. Y. Norio Michigami, Masahiro Kawamura, Osamu Kuze, Shigeo Nakamura, "High-performance Printed Ciircuit Board Production Equipment for Ultra-High Density Multi-layer Wiring," *Hitachi Review,* vol. 60, pp. 216-221, 2011.

[33] R. Huemoeller, S. Rusli, S. K. Kuchibhotla, L. Wojcik, and et al., "Unveiling the Next Generation in Integrated Circuit Substrate Circuit Formation," *CircuiTree,* vol. 20, pp. 12-12,14,16,18, June 2007.

[34] F. Liu, C. Nair, V. Sundaram, and R. R. Tummala, "Advances in embedded traces for 1.5µm RDL on 2.5D glass interposers," 2015, pp. 1736-1741.

[35] R. Huemoeller, S. Rusli, S. Chiang, T. Chen, D. Baron, L. Brandt, and B. Roelfs, "Unveiling the Next Generation in Substrate Technology," Amkor Technology, Inc, Unimicron Technology Corporation, Atotech GmbH, 2007.

[36] D. Baron, "Laser Embedded Circuit Technology (Via^2) - A Comprehensive Wiring Solution for Advanced IC Substrates in the Sub- 10µm L/S range," presented at the The 12th Electronic Circuits World Convention, Taipei, Taiwan, 2011.

[37] R. Zoberbier, "Excimer Laser Ablation: A Novel Patterning Technology for Wafer Level Packages," presented at the SEMICON Taiwan, Taipei, Taiwan, 2013.

[38] D. Baron, "Via 2-laser embedded conductor technology 2008 The 3rd impact and 10th emap joint conference," 2008, pp. 106-109.

[39] D. Bäuerle, *Laser Processing and Chemistry*, 4th ed. Berlin: Springer-Verlag, 2011.

[40] R. Paetzel, "Comparison Excimer Laser - Solid State Laser," Lambda Physik AG, Goettingen, Germany, 2002.

[41] R. Delmdahl and J.-L. Tapié, "Excimer lasers drive large-area microprocessing," *Applied Surface Science,* vol. 258, pp. 9123-9127, 2012.

[42] D. Basting and G. Marowsky, *Excimer Laser Technology*: Berlin, Heidelberg : Springer Berlin Heidelberg, 2005.

[43] P. Rumsby, E. Harvey, D. Thomas, and N. Rizvi, *Excimer laser patterning of thick and thin films for high density packaging* vol. 3184, 1997.

[44] J. Meijer, "Laser beam machining (LBM), state of the art and new opportunities," *Journal of Materials Processing Technology,* vol. 149, pp. 2-17, 2004.

[45] R. Huemoeller, S. Rusli, S. Chiang, T. Chen, D. Baron, L. Brandt, and B. Roelfs, "Unveiling the next generation in substrate technology," presented at the 12th Annual Pan Pacific Microelectronics Symposium, Hawaii, USA, 2007.

[46] M. Töpper, K. Hauck, M. Schima, D. Jaeger, and K.-D. Lang, "A sub-4 µm Via Technology of Thin film Polymers using Scanning Laser Ablation," presented at the 65th Annual IEEE Electronic Components and Technology Conference, 2015.

[47] C. Abbott, R. M. Allott, B. Bann, K. L. Boehlen, M. C. Gower, P. T. Rumsby, I. Stassen Boehlen, and N. Sykes, "New techniques for laser micromachining MEMS devices," 2002, pp. 281-288.

[48] K. L. Boehlen and I. B. Stassen Boehlen, "Laser micromachining of high-density optical structures on large substrates," 2004, pp. 118-126.

[49] D. J. Meier, A. Boenke, L. Herbst, and G. Spiecker, "LDP For Low Cost Flex A fast reel-to-reel process allows direct patterning of thin metal films on a variety of flex substrates," *PRINTED CIRCUIT DESIGN AND MANUFACTURE,* vol. 22, pp. 36-41, 2005.

[50] Z. Illyefalvi-Vitéz, "Laser processing for microelectronics packaging applications," *Microelectronics Reliability,* vol. 41, pp. 563-570, 2001.

[51] R. Rozman, B. Kmetec, B. Podobnik, D. Kovačič, and E. Govekar, "Optimisation of direct laser structuring of printed circuit boards," *Applied Surface Science,* vol. 254, pp. 5524-5529, 2008.

[52] B. Zhang and K. C. Yung, "Frequency-tripled Nd:YAG laser ablation in laser structuring process," *Optics and Lasers in Engineering,* vol. 44, pp. 815-825, 2006.

[53] F. E. Livingston, L. F. Steffeney, and H. Helvajian, "Tailoring light pulse amplitudes for optimal laser processing and material modification," *Applied Surface Science,* vol. 253, pp. 8015-8021, 2007.

[54] A. Piqué, S. A. Mathews, B. Pratap, R. C. Y. Auyeung, B. J. Karns, and S. Lakeou, "Embedding electronic circuits by laser direct-write," *Microelectronic Engineering,* vol. 83, pp. 2527-2533, 2006.

[55] S. R. I. Gabran, R. R. Mansour, and M. M. A. Salama, "Maskless pattern transfer using 355nm laser," *Optics and Lasers in Engineering,* vol. 50, pp. 710-716, 2012.

[56] M. R. Nowak, A. J. Antończak, P. E. Kozioł, and K. M. Abramski, "Laser prototyping of printed circuit boards," *Opto-Electronics Review,* vol. 21, pp. 320-325, 2013.

[57] K. C. Yung and B. Zhang, "Analysis of process parameters of laser structuring with Taguchi method," *Applied Physics A,* vol. 101, pp. 385-392, 2010.

[58] H. J. Booth, "Recent applications of pulsed lasers in advanced materials processing," *Thin Solid Films,* vol. 453–454, pp. 450-457, 2004.

[59] B. Tan, S. Panchatsharam, and K. Venkatakrishnan, "High repetition rate femtosecond laser forming sub-10 µm diameter interconnection vias," *Journal of Physics D: Applied Physics,* vol. 42, p. 065102, 2009.

[60] B. Zhang and K. C. Yung, "Feasibility of the 248 nm Excimer laser in the laser structuring of fine circuit lines on printed circuit board," *The International Journal of Advanced Manufacturing Technology,* vol. 33, pp. 1149-1158, 2006.

[61] L. Urech, T. Lippert, C. R. Phipps, and A. Wokaun, "Polymer ablation: From fundamentals of polymer design to laser plasma thruster," *Applied Surface Science,* vol. 253, pp. 6409-6415, 2007.

[62] B. S. Shin, J. Y. Oh, and H. Sohn, "Theoretical and experimental investigations into laser ablation of polyimide and copper films with 355-nm Nd:YVO4 laser," *Journal of Materials Processing Technology,* vol. 187–188, pp. 260-263, 2007.

[63] W. K. C. Yung, J. S. Liu, H. C. Man, and T. M. Yue, "355 nm Nd : YAG laser ablation of polyimide and its thermal effect," *Journal of Materials Processing Technology,* vol. 101, pp. 306-311, Apr 2000.

[64] P. Gordon, B. Balogh, and B. Sinkovics, "Thermal simulation of UV laser ablation of polyimide," *Microelectronics Reliability,* vol. 47, pp. 347-353, 2007.

[65] B. Balogh, P. Gordon, R. Berenyi, and Z. Illyefalvi-Vitez, "Effect of patterned copper layer on selective polymer removal by 355 nm laser," *4th IEEE International Conference on Polymers & Adhesives in Microelectronics & Photonics, 2004. POLYTRONIC 2004,* p. 237, 2004.

[66] K. C. Yung, D. W. Zeng, and T. M. Yue, "High repetition rate effect on the chemical characteristics and composition of Upilex-S polyimide ablated by a UV Nd:YAG laser," *Surface and Coatings Technology,* vol. 160, pp. 1-6, 2002.

[67] R. Rozman, I. Grabec, and E. Govekar, "Influence of absorption mechanisms on laser-induced plasma plume," *Applied Surface Science,* vol. 254, pp. 3295-3305, 2008.

[68] A. Bogaerts, Z. Y. Chen, R. Gijbels, and A. Vertes, "Laser ablation for analytical sampling: what can we learn from modeling?," *Spectrochimica Acta Part B-Atomic Spectroscopy,* vol. 58, pp. 1867-1893, Nov 2003.

[69] B. Sinkovics, P. Gordon, and G. Harsányi, "Computer modelling of the laser ablation of polymers," *Applied Thermal Engineering,* vol. 30, pp. 2492-2498, 2010.

[70] I. Bozsóki, B. Balogh, and P. Gordon, "355nm nanosecond pulsed Nd:YAG laser profile measurement, metal thin film ablation and thermal simulation," *Optics & Laser Technology,* vol. 43, pp. 1212-1218, 2011.

[71] M. Eyett and D. Bäuerle, "Influence of the beam spot size on ablation rates in pulsed-laser processing," *Applied Physics Letters,* vol. 51, p. 2054, 1987.

[72] T. Lippert, "UV Laser Ablation of Polymers: From Structuring to Thin Film Deposition," in *Laser-Surface Interactions for New Materials Production: Tailoring Structure and Properties*, A. Miotello and M. P. Ossi, Eds., ed Berlin, Heidelberg: Springer Berlin Heidelberg, 2010, pp. 141-175.

[73] M. Knowles, G. Rutterford, D. Karnakis, and A. Ferguson, "Micro-machining of metals, ceramics and polymers using nanosecond lasers," *International Journal of Advanced Manufacturing Technology,* vol. 33, pp. 95-102, 2007.

[74] E. G. Gamaly, "The physics of ultra-short laser interaction with solids at non-relativistic intensities," *Physics Reports,* vol. 508, pp. 91-243, 2011.

[75] R. Le Harzic, N. Huot, E. Audouard, C. Jonin, P. Laporte, S. Valette, A. Fraczkiewicz, and R. Fortunier, "Comparison of heat-affected zones due to nanosecond and femtosecond laser pulses using transmission electronic microscopy," *Applied Physics Letters,* vol. 80, p. 3886, 2002.

[76] M. Bolle, K. Luther, J. Troe, J. Ihlemann, and H. Gerhardt, "Photochemically assisted laser ablation of doped polymethyl-methacrylate," *Applied Surface Science,* vol. 46, pp. 279-283, 1990.

[77] J. Ihlemann, M. Bolle, K. Luther, and J. Troe, "Near-UV laser ablation of doped polymers," 1991, pp. 1011-1019.

[78] J. Ihlemann, "Micro patterning of fused silica by laser ablation mediated by solid coating absorption," *Applied Physics A,* vol. 93, pp. 65-68, 2008.

[79] J. M. Liu, "Simple technique for measurements of pulsed Gaussian-beam spot sizes," *Optics Letters,* vol. 7, pp. 196-198, 1982.

[80] G. W. C. Kaye and T. H. Laby, *Tables of physical and chemical constants*, 16th ed. Essex, England ; New York: Longman, 1995.

[81] T. Feng, V. Prakash, and W. Shi, "Touch panel with integrated fingerprint sensors based user identity management," *2013 IEEE International Conference on Technologies for Homeland Security (HST),* p. 154, 2013.

[82] N. H. Rizvi and P. Apte, "Developments in laser micro-machining techniques," *Journal of Materials Processing Tech.,* vol. 127, pp. 206-210, 2002.

[83] A. Miotello and P. M. Ossi, *Laser-Surface Interactions for New Materials Production: Tailoring Structure and Properties. [eBook]*: Berlin, Heidelberg : Springer Berlin Heidelberg, 2010.

[84] R. R. Gattass and E. Mazur, "Femtosecond laser micromachining in transparent materials," *Nat Photon,* vol. 2, pp. 219-225, 2008.

[85] G. D. Valle, R. Osellame, and P. Laporta, "Micromachining of photonic devices by femtosecond laser pulses," *Journal of Optics A: Pure and Applied Optics,* vol. 11, p. 013001, 2009.

[86] Y. Kawaguchi, T. Sato, A. Narazaki, R. Kurosaki, and H. Niino, "Rapid prototyping of silica glass microstructures by the LIBWE method: Fabrication of deep microtrenches," *Journal of Photochemistry and Photobiology A: Chemistry,* vol. 182, pp. 319-324, 2006.

[87] Z. Q. Huang, M. H. Hong, K. S. Tiaw, and Q. Y. Lin, "Quality Glass Processing by Laser Induced Backside Wet Etching," *JOURNAL OF LASER MICRO NANOENGINEERING,* vol. 2, pp. 194-199, 2007.